

**Petrology and geochemistry of a suite of felsic
orthogneisses and its enclaves from the northern
part of the North Purulia Shear Zone:
Implications for the crustal evolution of the east
Indian Shield during the Proterozoic time**



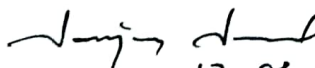
*Thesis submitted to Jadavpur University
for the degree of
Doctor of Philosophy (Science)*

By
Somdipta Chatterjee
Department of Geological Sciences
Jadavpur University
2024



CERTIFICATE FROM THE SUPERVISORS

This is to certify that the thesis entitled “**PETROLOGY AND GEOCHEMISTRY OF A SUITE OF FELSIC ORTHOGNEISSES AND ITS ENCLAVES FROM THE NORTHERN PART OF THE NORTH PURULIA SHEAR ZONE: IMPLICATIONS FOR THE CRUSTAL EVOLUTION OF THE EAST INDIAN SHIELD DURING THE PROTEROZOIC TIME**” submitted by **Sri. Somdipta Chatterjee**, who got his name registered on **20.02.2018** for the award of Ph. D. (Science) degree of Jadavpur University, is absolutely based upon his own work under the supervision of **Professor Pulak Sengupta** and **Professor Sanjoy Sanyal** and that neither this thesis nor any part of it has been submitted for either any degree / diploma or any other academic award anywhere before.


17. 01. 2024

Supervisor

Prof. Sanjoy Sanyal

Department of Geological Sciences

Jadavpur University

Kolkata 700032



Dr. Sanjoy Sanyal
Professor
Dept. of Geological Sciences
Jadavpur University
Kolkata - 700032, India


17/1/24

Supervisor

Prof. Pulak Sengupta

Department of Geological Sciences

Jadavpur University

Kolkata 700032



Dr. Pulak Sengupta
Professor
Dept. of Geological Sciences
Jadavpur University
Kolkata - 700032, India

To my parents

Acknowledgements

I would like to extend my heartfelt gratitude and appreciation to the people who helped me bring this work into reality.

I would like to thank my supervisors, Prof. Pulak Sengupta and Prof. Sanjoy Sanyal, for their constant support and guidance. I am indebted to my supervisors for their immense patience and for providing constant motivation that boosted my courage to overcome obstacles during my research work.

I would like to thank Prof. Subrata Karmakar for his support, which has significantly enhanced my work.

I am grateful to Dr. Tapabrata Sarkar for his valuable suggestions as the Research Advisory Committee subject expert.

I would also like to thank Dr. Shyamal Sengupta for providing valuable guidance.

I would like to acknowledge the Council of Scientific & Industrial Research (CSIR) for providing financial support, which has made my work possible.

I would like to acknowledge the EPMA lab of IIT Kharagpur and the Geological Survey of India. I would like to thank the Department of Earth Sciences at the Indian Institute of Technology, Kanpur, for providing me the opportunity to analyse samples. I would also like to thank Susmita Mondal, Geological Survey of India, Kolkata, for helping me with the fieldwork.

I would like to express my gratitude to Jadavpur University for providing me with all the research facilities, including the Scanning Electron Microscope facilities. Additionally, I would like to sincerely thank all the faculty, researchers and staff members of the Department of Geological Sciences for their support and cooperation.

I would also like to specially thank Dr. Subham Mukherjee for guiding me and being a great co-worker. I would also like to thank Dr. Shreya Karmakar and Dr. Enakshi Das for being great co-workers and seniors. I would like to thank Dr. Anindita Dey, Dr. Satabdi Das, Nivedita Lahiri, Dr. Sayan Biswas, and Mohai Menul Hassan for being helpful and supportive seniors.

Acknowledgements

I would also like to sincerely thank my labmate Dr. Sirina Roy Choudhury for guiding me and being a great senior. I would like to thank Arimita for being a fantastic lab mate and helping me in many ways. I also thank Dr. Nandini Chattopadhyay for being a very supportive senior. I would like to thank Sourav, Shreyasi and Nilanjan for being wonderful labmates and juniors.

I would like to express my deepest thanks to Kasturi for her constant patience and support during hard times.

Most importantly, I would like to thank my parents and grandmother for their immense sacrifice and constant motivation. I would also like to thank my other family members for their constant support.

Somdipta Chatterjee
Department of Geological Sciences
Jadavpur University, Kolkata

Contents

Abstract	I-III
Chapter 1: Introduction	1-8
1.1 Objectives of this study	3
1.2 Methodologies	4
1.3 Thesis Layout	4
Chapter 2: Geological Background	9-32
2.1 Extent and boundary of CGGC	9
2.2 Classification of CGGC	10
Chapter 3: Lithology of the area	33-47
3.1 Country rock of the area	33
3.2 Intrusive felsic orthogneisses	36
3.3 Enclave suite of rocks	39
3.4 Intrusive metamafic dykes	42
3.5 Structural relations	46
Chapter 4: Magmatic petrogenesis and metamorphic evolution of the migmatitic felsic gneiss	48-68
4.1 Petrography	48
4.2 Mineral chemistry	50
4.3 Geochemistry	57

4.4 Magmatic temperature	62
4.5 Mineral evolution and physical condition of metamorphism	62
Chapter 5: Magmatic and metamorphic evolution of the metaporphyritic charnockite and biotite gneiss	69-118
5.1 Petrography	69
5.2 Phase chemistry	77
5.3 Whole rock Geochemistry	87
5.4 Estimation of Magma temperature	96
5.5 Petrogenetic modelling of the charnockite-granite association	98
5.6 Physical conditions of metamorphism	109
Chapter 6: High pressure metamorphism and partial melting of mafic granulite	119-160
6.1 Petrography	119
6.2 Mineral chemistry	127
6.3 Metamorphic evolution	144
6.4 Physical conditions of metamorphism	147
Chapter 7: Origin of clinopyroxene-ilmenite symplectites in mafic granulites	161-189
7.1 Petrography	162
7.2 Phase compositions	166
7.3 Modelling the formation of Cpx ₂ -Ilm symplectites using CSpace and XMapTools	175

7.4 Physical conditions of metamorphism	180
Chapter 8: Metamorphic evolution of the metamafic dykes	190-205
8.1 Petrography	190
8.2 Phase chemistry	192
8.3 Mineral evolution during metamorphism	199
8.4 Physical condition of metamorphism	200
Chapter 9: Discussion	206-264
9.1 Petrogenetic evolution of various lithounits	206
9.2 Tectono-thermal events in the CGGC in the backdrop of the present study	232
9.3 Correlation between CGGC and Proterozoic Indian landmass in context with supercontinental cycle	237
Appendix	265-266
Supplementary Material	267-268
Publication	269

ABSTRACT

A suite of meta igneous rocks having mafic and felsic compositions from the least studied northern part of the North Purulia Shear Zone of the Chotanagpur Granite Gneiss Complex (CGGC) have been investigated. The migmatitic mafic granulite with layered to patchy leucosomes, the oldest lithocomponent of the studied area, occurs as enclaves within the migmatitic felsic orthogneisses. The internal fabric of the mafic granulite is discordant with and cut across by the gneissic fabric of the enclosing gneissic rocks. The migmatitic felsic orthogneisses are intruded by the protoliths of a suite of megacrystic metaporphyritic charnockite that grades to biotite gneiss (Ferroan granitoids). The metaporphyritic charnockite contains pods of migmatitic felsic gneiss, suggesting repeated felsic magmatism and deformation. The metaporphyritic charnockites are intruded by a suite of metamafic dykes.

Interpreting the field and petrological attributes, as well as observations from the modelling study, suggest that layered and patchy leucosomes in the mafic granulite were caused by dehydration melting of amphibole-bearing protolith at the culmination of high-pressure metamorphism (~13-14 kbar and 800-900 °C along a geothermal gradient of ~19°C/km.). Observed and predicted melt compositions suggest that the leucosomes that are presumed to be quenched melt have the composition of trondjemite. This study, therefore, provides a viable mechanism for the formation of TTG (Tonalite-Trondjemite-Granodiorite) suites. The sequence of reaction textures that variably replaced the granoblastic assemblage (garnet+clonopyroxene+plagioclase+titanite) that developed at the culmination of metamorphism defines a steeply decompressive P-T path (~13 to 7 kbar). The high-pressure metamorphism, the geometry of the retrograde P-T path and the inferred geothermal gradient of 19°C/km at the culmination of metamorphism are consistent with a clockwise (CW) retrograde P-T path that is common in a continent-continent collision setting. The mafic granulite of the studied area joins the regional high-pressure metamorphism in the CGGC, which is dated to be of Palaeoproterozoic age. A low proportion of leucosomes vis-a-vis extensive growth of amphibole throughout the mafic granulite and evidence from pseudosection are consistently suggestive of fluid infiltration-driven metamorphism that led to the formation of amphibole-rich selvages and hydration of the mafic granulite.

The mafic granulite develops a rare occurrence of rod-like intergrowths of clinopyroxene-ilmenite that variably replace titanite at contact with porphyroblastic garnet. The garnet proximal to the clinopyroxene-ilmenite intergrowth is variably replaced with symplectic clinopyroxene-plagioclase or a rind of plagioclase. Textural modelling study suggests that the decomposition of garnet+titanite forms ilmenite-clinopyroxene intergrowth. The presence of small granules of halogen-rich apatite within the ilmenite-clinopyroxene is consistent with a fluid-mediated process. Thermodynamic modelling in the NCFMAST (+H₂O) system demonstrates that the clinopyroxene-ilmenite symplectite was formed during the tectonic exhumation of the host mafic granulites. Relative to Fe, Mg, and Ca, Ti was less mobile, and its mobility was restricted within the confines of titanite being replaced by the clinopyroxene-ilmenite symplectite.

The geochemistry of the migmatitic felsic gneiss suggests that the magmatic protolith of the rock had I-type granite affinity that is commonly seen in the continental arc setting. The porphyritic structure and relict igneous textures of metaporphyritic charnockite, that intruded the migmatitic felsic gneiss support that the protolith of the megacrystic rock was emplaced as magmatic charnockite. Geochemically, metaporphyritic charnockite and associated biotite gneiss are ferroan, calc-alkalic, and meta- to peraluminous in composition. Variations of major and certain trace elements of both rock types show a similar trend with increasing silica content and maficity. This feature is consistent with the well-studied A-type granitoids of different parts of CGGC. The petrological attributes of the two suites of rocks do not support the mobility of elements beyond a few mm. Open system phase equilibrium modelling in the NCKFMASHTO system suggests that fractional crystallisation is responsible for the observed geochemical trends and is considered to be the likely mechanism for the formation of protolith of the metaporphyritic rocks and the biotite gneiss. The modelling study under different P-T, aH₂O, and fO₂ conditions suggests that the ambient aH₂O and fractional crystallisation primarily controlled the stabilisation of orthopyroxene in the magmatic stage. Fractionation of anhydrous minerals, including orthopyroxene, increased the aH₂O of the melt and triggered the crystallisation of orthopyroxene-free biotite granitoid (the protolith of biotite gneiss).

The petrological attributes of the migmatitic felsic gneiss suggest that the dominant metamorphism (M2) culminated at 700-800 °C; 7.5-8 kbar along a geothermal gradient of 26-28 °C/km, which is distinctly hotter than the high-pressure metamorphism (M1) that are recorded in the mafic granulite enclaves. Frozen-in reaction textures support a steeply decompressive retrograde P-T path that can be traced to 600 °C, 6 kbar. The ferroan granitoid

suites and the metamafic dykes also share a similar retrograde P-T path. The geometry of the retrograde P-T path is consistent with a continent-continent collision event that superposed on the felsic rocks whose protoliths were formed in grossly different tectonic regimes. The mafic dyke that intruded all the felsic orthogneisses has escaped M2 high-grade metamorphism but bears the impress of amphibolite facies (M3) metamorphism and deformation. Integrating the inputs from the studied area with the published information, it is demonstrated that the magmatic and metamorphism imprints in the CGGC happened in response to the formation and breakup of the Proterozoic supercontinental cycles.

Chapter 1

Introduction

The continental crust of the present day is the endproduct of episodic assembly, accretion and disintegration of crustal blocks known as supercontinental cycle (Damian Nance and Brendan Murphy 2013; Condie 2021; Mitchell et al. 2021). Studies show that the supercontinental cycles are linked with the evolution of the Earth's lithospheric, hydrospheric and atmospheric evolution (Hoffman and Schrag 2002; Bradley 2011; Hannisdal and Peters 2011; Chowdhury et al. 2017). Several studies proposed that the Proterozoic Eon records three such episodes of assembly and breakup of supercontinents, including Columbia (Meert and Santosh 2017; Zhao et al. 2017), Rodinia (Li et al. 2008; Pant and Dasgupta 2017) and Gondwanaland (Meert and Van Der Voo 1997). Understanding the processes along the orogenic belts that mark the locations along which different crustal blocks merged/disintegrated during the supercontinental cycle holds the key to understanding the birth and demise of supercontinents (reviewed in Condie 2021). The Indian landmass preserves multiple such past orogenic belts that record the dynamics of Earth's history over 3500 Ma (reviewed in Nance et al. 2014). The Chotanagpur Granite Gneiss Complex (CGGC) is presumed to be the eastern extension of the roughly WSW-ENE trending orogenic belt, known as the Central Indian Tectonic Zone (CITZ; (Acharyya 2003; Bhowmik 2019)) is perceived to be the suture zone along which the Greater Indian Landmass was formed (Acharyya 2003; Roy and Hanuma Prasad 2003; Bhowmik et al. 2012) but the timing and process of suturing of remain highly debated (reviewed in Bhowmik 2019; Mukherjee et al. 2019b; Deshmukh and Prabhakar 2020).

The study of the lithounits of CGGC can thus provide crucial information about the crustal evolution of the orogenic belts. The CGGC is comprised of a vast amount of felsic orthogneisses with minor enclave suite of supracrustals and metabasic rocks (Sanyal and Sengupta 2012; Mukherjee et al. 2019b) and records a significant amount of felsic magmatism throughout the Proterozoic Eon (Saikia et al. 2017; Mukherjee et al. 2018;

Chakraborty et al. 2019; Mukherjee et al. 2019a; Chakraborty et al. 2022; Sequeira et al. 2022) that shaped the crustal evolutionary history of the CGGC. Although several studies have been conducted during the last decade, especially from the northern and north-eastern parts of the CGGC, as well as from the southern part of the North Purulia Shear Zone (NPSZ) (reviewed in Mukherjee et al. 2019b), the northern part of NPSZ remains relatively unexplored. The granitic rocks can be utilised in deciphering tectonic conditions of magmatism and can thus provide significant information on crustal evolution (Pearce et al. 1984; Eby 1992; Pearce 1996). The ferroan (A-type) granites characterise felsic rocks with Fe enrichment and high alkali, silica, and HFSEs, along with low H₂O and elevated magmatic temperature (~900°C) and are associated with extensional tectonic regimes (Clemens et al. 1986; Whalen et al. 1987; Eby 1992; Patiño Douce 1997; Anderson et al. 2003; Bonin 2007; Frost and Frost 2011; Dall'Agnol et al. 2012). In contrast, I-type granites are more magnesian (Frost et al. 2001; Frost and Frost 2008a) with relatively lower magmatic temperatures (Miller et al. 2003) and are commonly associated with convergent tectonic setup (Chappell and White 1992; Pearce 1996). Orthopyroxene bearing granitic magmatism also provides critical insights into understanding the evolutionary history of the earth's crust (Zhao et al. 2023). The felsic magmatism of CGGC is accompanied by multiple episodes of orogenic pulses (Mukherjee et al. 2019b), where early phases of metamorphism are often obliterated. The study of the enclave suite of rocks is crucial as they provide the best probability of preserving early metamorphic tectonothermal events. On the other hand, later intrusive rocks can help delineate polymetamorphism, as these are usually not affected by early metamorphic processes before the intrusion.

The area in and around Massanjor (24°15';87°15', – 24°00';87°30'), Jharkhand, the area of this study, exposes an ensemble of metamorphosed igneous rocks having both felsic and mafic compositions. The studied area is a E-SE extension of the rocks of the CGGC exposed in the Jashidihi-Deoghar area. The studied area that falls in the IB domain of the CGGC (Sanyal and Sengupta 2012; Mukherjee et al. 2019) offers a unique opportunity to unravel the sequence of magmatism and metamorphism that shaped the CGGC during the proterozoic time. A detailed study of the rocks of the study area in the light of modern methods of petrology is not available. Nevertheless, a preliminary study (Ray Barman et al. communicated in Acharya 2003) describes a big body of porphyritic charnockite from the study area. This raises the question of whether this rock represents magmatic charnockite pluton reported from other parts of the world (Frost and Frost 2008b; Zhao et

al. 2023). Furthermore, a small communication (Kole et al. 2016) reports a rare intergrowth of ilmenite and clinopyroxene in the mafic granulite from the study area. The origin of ilmenite-clinopyroxene intergrowth is a unique petrological phenomenon, and the factors that control the development of the symplectite remain elusive. Together with the published geological information from Jashidihi-Deoghar area, comprehensive petrological information from rocks exposed in and around the Massanjor area will help better understand the evolution of the CGGC in the light of the supercontinental cycles of the Proterozoic time. In this backdrop detail, petro-geochemical investigations of the metaigneous rocks from the Massanjor and the adjoining areas are undertaken with the following objective.

1.1 Objectives of this study:

- ❖ To establish the sequence of formation /reconstitution of the different lithologies with particular emphasis on the meta-igneous rocks
- ❖ To understand the petrogenetic processes, including the condition of partial melting, physical conditions of metamorphism and the P-T path followed by the mafic granulite during the evolution of the complex
- ❖ To decipher the nature of the melt composition and the probable tectonic setting of emplacement of the magmatic protolith of the felsic orthogneiss
- ❖ To trace the petrogenetic history and possible tectonic setting of emplacement of the magmatic protolith of the metaporphyratic charnockite and its relations with the biotite gneiss.
- ❖ To reconstruct the metamorphic and deformational events that affected the metafelsic rocks (migmatitic felsic gneiss, metaporphyratic charnockite, biotite gneiss) and metamafic dyke. Attempts will be made to reconstruct the exhumation history of these rocks.
- ❖ To understand the mechanism, physicochemical conditions and scale of mass transport that led to the formation of rare Cpx-Ilm symplectite in mafic granulites.
- ❖ Integrating all the information of this study with the published information, a holistic evolutionary model for the CGGC will be developed and compared with other parts of the Indian shield areas. The implications of this study will be discussed in light of the supercontinental cycles during the Proterozoic time.

1.2 Methodologies:

Several methods are applied to fulfil the above-discussed objectives. These include,

- ❖ Detailed field work and lithological mapping of the study area.
- ❖ Systematic sampling of each rock type from the study area.
- ❖ Thin section preparation from the various litho units for petrographic study.
- ❖ Detailed petrographic study of each rock type to understand textural relations from the various mineral assemblages.
- ❖ Detailed electron microprobe analysis of each rock type using wave dispersive spectrometry (WDS) to obtain phase composition and elemental X-ray intensity map (wherever present).
- ❖ Systematic major and trace element, bulk composition analysis from various lithounits using XRD (major element) and ICP-MS (trace element)
- ❖ Open system phase equilibria modelling for modelling magmatic processes (wherever done)
- ❖ Phase equilibria modelling and conventional thermobarometry to obtain P-T conditions of metamorphism.
- ❖ Textural modelling to obtain mass-balanced mineral reaction using Cspace and XMaptools software (wherever done)

1.3 Thesis Layout:

- ❖ In Chapter 2, already available geological and geochronological information from different parts of the CGGC is compiled.
- ❖ Chapter 3 deals with the lithological and structural aspects of the study area.
- ❖ Chapter 4 describes the petrography, mineral chemistry, geochemical characteristics and metamorphic conditions of the Migmatitic felsic gneiss.
- ❖ Chapter 5 comprises a detailed study of petrography, mineral chemistry, geochemistry and phase equilibria modelling (of both magmatic and metamorphic evolution) of the metaporphyritic charnockite and biotite gneiss.
- ❖ Chapter 6 encompasses the metamorphic evolution of the enclave suite mafic granulite with petrology and phase chemistry combined with phase equilibria modelling.

- ❖ Chapter 7 deals with the rare occurrence of Ilmenite clinopyroxene symplectite in the mafic granulite.

Observations made from Chapter 7 has been published as:

Chatterjee, S., Karmakar, S., Mukherjee, S., Sanyal, S. & Sengupta, P. (2023). Origin of clinopyroxene-ilmenite symplectites in mafic granulites from eastern parts of the Chotanagpur granite gneissic complex, East Indian shield. *American Mineralogist*, 108(12), 2308-2322. <https://doi.org/10.2138/am-2022-8715>

- ❖ Chapter 8 deals with the metamorphism of the late intrusive (meta) mafic dykes.

References:

- Acharyya, S.K. (2003) The Nature of Mesoproterozoic Central Indian Tectonic Zone with Exhumed and Reworked Older Granulites. *Gondwana Research*, 6, 197–214.
- Anderson, I.C., Frost, C.D., and Frost, B.R. (2003) Petrogenesis of the Red Mountain pluton, Laramie anorthosite complex, Wyoming: implications for the origin of A-type granite. *Precambrian Research*, 124, 243–267.
- Bhowmik, S.K. (2019) The current status of orogenesis in the Central Indian Tectonic Zone: A view from its Southern Margin. *Geological Journal*, 54, 2912–2934.
- Bhowmik, S.K., Wilde, S.A., Bhandari, A., Pal, T., and Pant, N.C. (2012) Growth of the Greater Indian Landmass and its assembly in Rodinia: Geochronological evidence from the Central Indian Tectonic Zone. *Gondwana Research*, 22, 54–72.
- Bonin, B. (2007) A-type granites and related rocks: Evolution of a concept, problems and prospects. *Lithos*, 97, 1–29.
- Bradley, D.C. (2011) Secular trends in the geologic record and the supercontinent cycle. *Earth-Science Reviews*, 108, 16–33.
- Chakraborty, K., Ray, A., Chatterjee, A., Deb, G.K., and Das, K. (2019) Neoproterozoic granitic activity in syn-collisional setting: Insight from petrology, geochemistry, and zircon–monazite geochronology of S-type granites of the Chotanagpur Granite Gneissic Complex, eastern India. *Geological Journal*, 54, 3112–3147.
- Chakraborty, K., Ray, A., Chakraborti, T.M., Deb, G.K., Mandal, A., Kimura, K., and Mukhopadhyay, S. (2022) Petrology, geochemistry and U–Pb zircon geochronology of alkali granites of Jhalda, eastern India and their possible linkage to Rodinia Supercontinent. *Journal of Earth System Science*, 131, 253.
- Chappell, B.W., and White, A.J.R. (1992) I- and S-type granites in the Lachlan Fold Belt. *Earth and Environmental Science Transactions of the Royal Society of Edinburgh*, 83, 1–26.
- Chowdhury, P., Gerya, T., and Chakraborty, S. (2017) Emergence of silicic continents as the lower crust peels off on a hot plate-tectonic Earth. *Nature Geoscience*, 10.
- Clemens, J.D., Holloway, J.R., and White, A.J.R. (1986) Origin of an A-type granite :

- Experimental constraints. *American Mineralogist*, 71, 317–324.
- Condie, K. (2021) Earth as an Evolving Planetary System.
- Dall’Agnol, R., Frost, C.D., and Rämö, O.T. (2012) IGCP Project 510 “A-type Granites and Related Rocks through Time”: Project vita, results, and contribution to granite research. *Lithos*, 151, 1–16.
- Damian Nance, R., and Brendan Murphy, J. (2013) Origins of the supercontinent cycle. *Geoscience Frontiers*, 4, 439–448.
- Deshmukh, T., and Prabhakar, N. (2020) Linking collision, slab break-off and subduction polarity reversal in the evolution of the Central Indian Tectonic Zone. *Geological Magazine*, 157, 340–350.
- Eby, G.N. (1992) Chemical subdivision of the A-type granitoids: petrogenetic and tectonic implications. *Geology*, 20, 641–644.
- Frost, B.R., and Frost, C.D. (2008a) A Geochemical Classification for Feldspathic Igneous Rocks. *Journal of Petrology*, 49, 1955–1969.
- (2008b) On charnockites. *Gondwana Research*, 13, 30–44.
- Frost, B.R., Barnes, C.G., Collins, W.J., Arculus, R.J., Ellis, D.J., and Frost, C.D. (2001) A geochemical classification for granitic rocks. *Journal of Petrology*, 42, 2033–2048.
- Frost, C.D., and Frost, B.R. (2011) On Ferroan (A-type) Granitoids : their Compositional Variability and Modes of Origin Fe-index. *Journal of Petrology*, 0, 1–15.
- Hannisdal, B., and Peters, S. (2011) Phanerozoic Earth System Evolution and Marine Biodiversity. *Science (New York, N.Y.)*, 334, 1121–1124.
- Hoffman, P.F., and Schrag, D.P. (2002) The snowball Earth hypothesis: testing the limits of global change. *Terra Nova*, 14, 129–155.
- Kole, L., Sanyal, S. Sengupta, P. (2016) Textural modeling of a high pressure mafic granulite from parts of the Chotanagpur Granite Gneiss Complex (CGGC), India: Evidence for rapid exhumation of a former lower crust. International conference on Electron Microscopy & XXXVII Annual Meeting of EMSI (2-4 June), Varanasi, India. P:84-85.
- Li, Z.X., Bogdanova, S. V, Collins, A.S., Davidson, A., De Waele, B., Ernst, R.E., Fitzsimons, I.C.W., Fuck, R.A., Gladkochub, D.P., Jacobs, J., and others (2008) Assembly, configuration, and break-up history of Rodinia: A synthesis. *Precambrian Research*, 160, 179–210.
- Meert, J.G., and Santosh, M. (2017) The Columbia supercontinent revisited. *Gondwana Research*, 50, 67–83.
- Meert, J.G., and Van Der Voo, R. (1997) The assembly of Gondwana 800-550 Ma. *Journal of Geodynamics*, 23, 223–235.
- Miller, C.F., McDowell, S.M., and Mapes, R.W. (2003) Hot and cold granites: Implications of zircon saturation temperatures and preservation of inheritance. *Geology*, 31, 529–

532.

- Mitchell, R., Zhang, N., Salminen, J., Liu, Y., Spencer, C., Steinberger, B., Murphy, J., and Li, Z.-X. (2021) The Supercontinent Cycle. *Nature Reviews Earth & Environment*, 2, 12–28.
- Mukherjee, S., Dey, A., Sanyal, S., and Sengupta, P. (2018) Tectonothermal imprints in a suite of mafic dykes from the Chotanagpur Granite Gneissic complex (CGGC), Jharkhand, India: Evidence for late Tonian reworking of an early Tonian continental crust. *Lithos*, 320–321, 490–514.
- Mukherjee, S., Dey, A., Sanyal, S., Ibanez, M., and Pulak, M. (2019a) Bulk rock and zircon geochemistry of granitoids from the Chotanagpur Granite Gneissic Complex (CGGC): implications for the late Paleoproterozoic continental arc magmatism in the East Indian Shield. *Contributions to Mineralogy and Petrology*, 174, 1–17.
- Mukherjee, S., Dey, A., Sanyal, S., and Sengupta, P. (2019b) Proterozoic crustal evolution of the Chotanagpur granite Gneissic Complex, Jharkhand-Bihar-West Bengal, India: Current status and future prospect. *Springer Geology*, 7–54.
- Nance, R.D., Murphy, J.B., and Santosh, M. (2014) The supercontinent cycle: A retrospective essay. *Gondwana Research*, 25, 4–29.
- Pant, N., and Dasgupta, S. (2017) An introduction to the crustal evolution of India and Antarctica: The supercontinent connection. Geological Society, London, Special Publications, 457, SP457.14.
- Patiño Douce, A.E. (1997) Generation of metaluminous A-type granites by low-pressure melting of calc-alkaline granitoids. *Geology*, 743–746.
- Pearce, J. (1996) Sources and settings of granitic rocks. *International Union of Geological Sciences*, 19, 120–125.
- Pearce, J.A., Harris, N.B.W., and Tindle, A.G. (1984) Trace Element Discrimination Diagrams for the Tectonic Interpretation of Granitic Rocks. *Journal of Petrology*, 25, 956–983.
- Roy, A., and Hanuma Prasad, M. (2003) Tectonothermal events in Central Indian Tectonic Zone (CITZ) and its implications in Rodinian crustal assembly. *Journal of Asian Earth Sciences*, 22, 115–129.
- Saikia, A., Bibhuti, G., Tatiana, K., Liudmila, L., Tamara, B., and Mansoor, A. (2017) Geochemical and U–Pb zircon age characterisation of granites of the Bathani Volcano Sedimentary sequence, Chotanagpur Granite Gneiss Complex, eastern India: vestiges of the Nuna supercontinent in the Central Indian Tectonic Zone. Geological Society, London, Special Publications, 457, 233–252.
- Sanyal, S., and Sengupta, P. (2012) Metamorphic evolution of the Chotanagpur Granite Gneiss Complex of the East Indian Shield: current status. Geological Society, London, Special Publications, 365, 117–145.
- Sequeira, N., Bhattacharya, A., and Bell, E. (2022) The ~1.4 Ga A-type granitoids in the “Chottanagpur crustal block” (India), and its relocation from Columbia to Rodinia? *Geoscience Frontiers*, 13, 1138.

- Whalen, J.B., Currie, K.L., and Chappell, B.W. (1987) A-type granites: geochemical characteristics, discrimination and petrogenesis. *Contributions to Mineralogy and Petrology*, 95, 407–419.
- Zhao, K., Xu, X., and Erdmann, S. (2017) Crystallisation conditions of peraluminous charnockites: constraints from mineral thermometry and thermodynamic modelling. *Contributions to Mineralogy and Petrology*, 172, 26.
- Zhao, K., Xu, X., Klemm, R., He, Z., and Zhang, X. (2023) A review of the genetic mechanisms generating igneous charnockite: CO₂ flushing and crystal-melt segregation in mushy reservoirs. *Earth-Science Reviews*, 237, 104295.

Chapter 2:

Geological Background

2.1 Extent and boundary of CGGC

The CGGC constitutes the northern block of the East Indian Shield, extending through the states of Chattisgarh, Jharkhand, Bihar and West Bengal (reviewed in Mahadevan 2002; Acharyya 2003; Mukherjee et al. 2019). It is an east-west trending, sub-arcuate belt covering an area of over 1,00,000 square kilometres. The northern boundary of the CGGC is covered by Quaternary sediments of the Indo-Gangetic alluvium, which also partitions it from the Tertiary Himalayan rocks and the Paleoproterozoic rocks that are interlaced with them throughout the lower part of the Lesser Himalaya. The southern margin of CGGC occurs the Mesoarchean Singhbhum craton separated by a Mesoproterozoic mobile belt named North Singhbhum Fold Belt (NSFB). An east-west to ENE–WSW trending crustal scale brittle–ductile shear zone, known as the Tamar–Porapahar–Khatra Fault Zone (Mahadevan 2002) or the South Purulia Shear Zone (Mazumdar 1988), defines the border between CGGC and NSFB. Mesozoic volcanics from Rajmahal Trap cover the terrain's northeastern edge, while sediments from the Bengal Basin demarcate the eastern boundary. The Central Indian tectonic zone (CITZ *sensu stricto*), which comprises the Paleoproterozoic volcano-sedimentary sequence of Mahakoshal belt in its north and Meso- to Neoproterozoic rocks of the Sausar mobile belt in its south (Acharyya and Roy 2000), lies to the west of CGGC. The Mahakoshal rocks are partitioned from the CGGC at its northwest corner by an ENE–WSW brittle–ductile shear zone comprising fault breccia and mylonite. This fault forms the eastern part of the Son–Narmada South Fault (Mazumdar 1988; Roy et al. 2002). The younger Gondwana

sediments of Son-Narmada and Mahanadi graben of the Permian to mid-Cretaceous age conceal the contact between the Sausar belt and CGGC. However, the younger Gondwana sediments of Son-Narmada and Mahanadi graben of the Permian to mid-Cretaceous age cover a significant portion of this western boundary (Mahadevan, 2002). Vindyan sediments also cover a portion of the north-western margin of CGGC.

2.2 Classification of CGGC

The main obstacle to a comprehensive classification of the CGGC is the lack of detailed petrological, lithological, and geochronological data. The scarce and scattered distribution of exposures due to urbanisation and tropical weathering further complicates the issue. Earlier studies (Mahadevan 2002; Sanyal and Sengupta 2012) have classified the CGGC into five blocks based on the Chotanagpur plateau and the Gondwana deposits (Permian-mid Cretaceous). However, the classification of Precambrian CGGC on the basis of younger Phanerozoic sediments and related geomorphic features appears improbable. Nevertheless, in the last decade, a substantial amount of geological and geochronological data has been published from the various regions of CGGC. Mukherjee et al. (2019) reclassified the CGGC into three E-W domains (from south to north, Domain I, Domain II and Domain III; Fig. 2.1), based on lithological, metamorphic, and geochronological characteristics into primarily three east-west domains. Three major lineaments dissect the CGGC; among these, the South Purulia Shear Zone (SPSZ) and Monghyr- Saharsa Ridge Fault roughly coincide with the southern and northern boundaries of the CGGC, respectively (Fig. 2.1). The other major lineament is the Gondwana Boundary Faults (Mukherjee et al. 2019b) (GBF; Fig. 2.1). The Gondwana Boundary Faults that confine the exposure of Gondwana deposits of Damodar Valley, run through Domain I of the CGGC (Mandal 2016). Based on GBF, Mukherjee et al. (2019) subdivided Domain I into Domain IA (north) and IB (south) despite any major lithological or geochronological break. Though no tectonic lineament separates Domain II from Domain I and Domain III, it is a unique litho unit due to an abundance of mica-bearing pegmatite intrusive (the Bihar Mica Belt; BMB).

Salient petrological and geochronological characteristics of the domains have been described in detail in the section that follows. The geochronological data from each domain in the CGGC is compiled in Table 2.1.

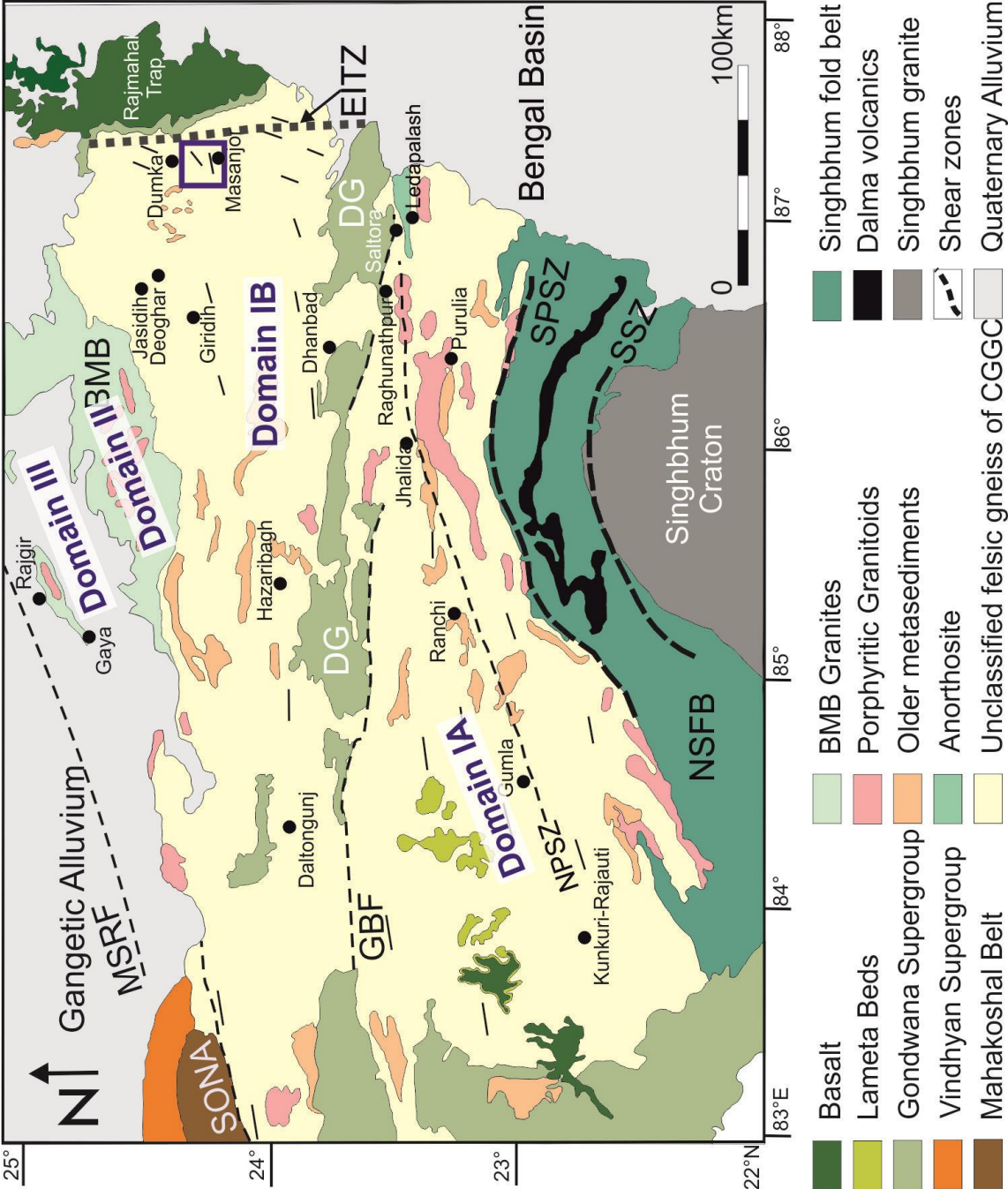


Fig. 2.1: Geological map of the CGGC modified after Mukherjee et al., (2019)) showing the threefold subdivisions. From south to north CGGC is divided into: Domain I, II and III. Domain I is again subdivided into Domain IA and IB.

2.2.1 Domain IA

Domain IA is the southernmost part of the CGGC and GBF, and the South Purulia Shear Zone confines this domain in the north and south, respectively. The geological information clusters around the Raghunathpur-Adra-Ranchi areas in the central part, the Bankura-Saltora- Bero area in the east and the Raikera- Kunkuri region in the western part of the domain (Fig. 2.1).

Numerous researchers have conducted in-depth studies on the petrology and geochronology of the rocks exposed in the Bankura, Saltora, and Bero (West Bengal) area (Manna and Sen 1974; Roy 1977; Bhattacharyya and Mukherjee 1987; Sen and Bhattacharyya 1993; Mukherjee et al. 2005; Chatterjee et al. 2008; Maji et al. 2008). The predominant rock type in the area is migmatitic felsic orthogneisses, which are variably deformed. The felsic orthogneisses hold enclaves of mafic granulite and calc-silicate gneisses, and they are intruded by massif-type anorthositic rocks (Bengal anorthosite). High grade metapelitic rocks and migmatitic quartzofeldspathic rocks are exposed in the easternmost part, near Saltora-Santuri-Bero. The metamorphic grade ranges from granulite to amphibolite facies. However, the available data has not demonstrated any consistent variations in the estimated metamorphic conditions along any geographic direction. The rocks in this region are folded to east-west closing folds, and an E-W trending axial planar fabric dips steeply towards the north (Maji et al. 2008). Maji et al. (2008) have denoted three deformation (D_{1-3}) phases accompanied by four metamorphic events (M_{1-4}) from the region.

The earliest tectonic event (M_1) occurred at ~1700 Ma, deduced from the chemical dating of monazite (Chatterjee et al. 2010). M_1 has been identified as a granulite facies metamorphic event with an estimated P-T condition of ~5–6 kbar and ~750–850 °C and led to the formation of migmatitic banding in the orthogneisses (S1, corresponding to D_1 ; Sen and Bhattacharyya 1993; Maji et al. 2008). The early granulite facies assemblage was primarily replaced by successive deformation (D_2 - D_3) and metamorphism (M_2 - M_3 : estimated to be an amphibolite facies event) episodes over ~1300-1100 Ma (Maji et al. 2008). Between the D_1 and D_2 deformation events, at approximately 1550 Ma (U-Pb zircon dating; Chatterjee et al. 2008), a massif-type anorthosite body known as "Bengal Anorthosite" intruded the area around Saltora (Bhattacharyya and Mukherjee 1987; Chatterjee et al. 2008; Maji et al. 2008). The fourth metamorphic event (M_4 : Maji et al.

2008) occurred between 1000-950 Ma (U-Pb zircon dating: Chatterjee et al. 2008; Th-U-Pb monazite dating: Chatterjee et al. 2010) is inferred to be the most pervasive metamorphic event. Maji et al. (2008) constrained peak metamorphic P-T conditions of 650 ± 50 °C at 4-5 kbar, while Chatterjee et al. (2010) constrained high-grade conditions ~850-900°C and 8.5-11 kbar from gabbro-anorthositic rocks. Near Kankarkhari (West Bengal), nepheline-bearing syenite and carbonatite have intruded migmatitic felsic orthogneisses and got deformed and metamorphosed subsequently (Goswami and Bhattacharyya 2008; Das et al. 2017, 2019). Although the timing of the nepheline-bearing syenite intrusion has not been constrained, studies indicate that the intrusion occurred in post-Grenvillian times. These intrusive bodies had been deformed and metamorphosed under amphibolite grade P-T (~700–750 °C and ~10 kbar) conditions (Das et al. 2019). A late Tonian–early Cryogenian tectonothermal event documented by several workers correlates well with the event. Late Tonian ages (~900-820 Ma) are recorded from overgrowths on older monazites by Maji et al. (2008) and Chatterjee et al. (2010).

The area around Raghunathpur (West Bengal; Fig. 2.1) comprises various generations of felsic orthogneisses (porphyritic and deformed granitoids), metapelitic and calcareous enclaves (Dunn 1929; Baidya et al. 1987, 1989; Ray Barman et al. 1994; Goswami and Bhattacharyya 2008, 2014; Karmakar et al. 2011). The intrusion of non-porphyritic granite at 1178 ± 61 Ma (Rb–Sr whole rock isochron age, Ray Barman et al. 1994) is concurrent with the growth of S1, during initial deformation (D1) (Goswami and Bhattacharyya 2008). Subsequently, porphyritic granite emplaced at 1071 ± 64 Ma (Rb–Sr whole rock age; Ray Barman et al. 1994; Goswami and Bhattacharyya 2014) before D2. Geochemical features classify these porphyritic granites as shoshonitic to high K-calc alkaline and have been inferred to have formed by mixing of mantle-derived mafic magma and crustal melts and subsequent fractional crystallisation within a continental collisional set-up (Goswami and Bhattacharyya 2014). Chakraborty et al. (2019) reported the intrusion of syn-collisional granite in the Raghunathpur-Bero-Ramchandrapur area. Near Jhalda Chakraborty et al. (2022) reported ~966 Ma Alkali granite intrusion. Near Adra, mafic granulites and Mg–Al granulites occur as enclaves within the migmatitic felsic gneiss. The metamorphic P-T culminate at ~870 °C and 11 kbar, followed by a steeply decompressive P-T path (Karmakar et al. 2011). Mg–Al granulites and migmatitic felsic gneiss constrain the age of metamorphism between ~990-940 Ma (Karmakar et al. 2011). Goswami and Bhattacharyya (2008) constrained similar temperatures (~800 °C) and lower pressures (6.5-

7.5 kbar), suggesting that the M1 event occurred over both D1 and D2. Karmakar et al. (2011) also constraints younger ages (850–775 Ma) that are consistent with those obtained by Baidya et al. (1987) (870 ± 40 Ma: K–Ar biotite of porphyritic granite and 810 ± 40 Ma: K–Ar muscovite of leucogranite) from Jaipur, West Bengal. Despite the lack of petrological characterisation, these youngest age clusters are assumed to be associated with the third deformational event D3.

Lithounits exposed in the south-central part of the terrain, south of Ranchi, consist of garnetiferous migmatitic felsic gneiss, pelitic schist, minor calc-silicate units and intrusive porphyritic granite (Rekha et al. 2011). The litho-package resembles rock types of the eastern part. Zircon and monazite ages from the migmatitic felsic gneiss and metapelites constrain an early Neoproterozoic (944 ± 9 Ma and 921 ± 18 Ma) age of metamorphism. The emplacement ages of younger granites (928 ± 23 Ma) with older inherited components (1072 ± 17 and 1239 ± 66 Ma) were also constrained by Rekha et al. (2011).

The litho units of the Raikera-Kunkuri region in southwest Chhattisgarh constitute various granitic bodies, pelitic schist (with chlorite, biotite and hornblende schist), quartzite and dolerite dykes/sills (reviewed in Singh and Krishna 2009). At 1005 ± 51 Ma, two-mica bearing grey granites that were formed from juvenile crustal sources ($SrI \approx 0.7047$ and low high field strength elements) intruded the crust (Singh and Krishna 2009). However, the high SrI (~ 0.7539) and younger Rb-Sr isochron age of 815 ± 47 Ma determined from the pink granite suggest a late metasomatic event associated with the Y-mineralization in the region (Singh and Krishna 2009). The intrusion of calc-alkaline shosonitic lamprophyre intrusion at ~ 944 Ma is reported from the Simdega area (Kumar et al. 2023).

2.2.2 Domain IB

Domain IB represents a crudely E-W trending region between the GBF in the south and Domain II in the north. Geological information from this domain mainly concentrates on Daltonganj, Jasidih, Deoghar, Dumka and Masanjore. Felsic orthogneiss of variable mineral assemblage and compositions that underwent granulite facies metamorphism, with varying degrees of partial melting, is the country rock of the domain. Enclaves of metamorphosed mafic, pelitic, felsic and calcareous rocks are enclosed in the country rock. Granulite grade rocks are preserved predominantly in the eastern part. The overall strike of the domain varies from EW to NW-SE; however, in the northeast, it becomes N-S. At least

three sets of deformation have been identified (Ghosh and Sengupta 1999; Sanyal and Sengupta 2012; Mukherjee et al. 2019b).

In the eastern part, near Dumka, Masanjore, the dominant rock type is a migmatitic felsic gneiss. This migmatitic felsic gneiss encloses enclaves of Mg-Al granulites, khondalites (garnet-sillimanite gneiss), mafic granulites, and calc-silicate granulite. The emplacement age of the migmatitic country rock is 1624 ± 5 Ma (Acharyya 2003). A porphyritic charnockite intrudes the orthogneissic country rock and contains enclaves of the latter within it (Sanyal and Sengupta, 2012). The foliation preserved in the enclave suite of rocks has been inferred to have been formed during D1, while The E-W foliation of the host felsic gneiss and subsequent refolding of the foliation represents D2 and D3 deformation (Sanyal and Sengupta 2012). The emplacement of the porphyritic granite has been constrained during 1515 ± 5 Ma (Acharyya 2003). Mg-Al granulites of the region have undergone ultra-high temperature (UHT) metamorphism (>900 °C, > 8 kbar) (Sanyal and Sengupta 2012).

Most of the geological and geochronological information is documented from the region between Deoghar-Dumka (Jharkhand). The region's country rock, a magmatic felsic orthogneiss, consists of pelitic granulite, mafic granulites, calc-silicate granulites, and augen gneiss enclaves that range in size from meters to kilometres. The host rock migmatitic felsic gneiss exhibits dominant N-S trending migmatitic bandings (S2), defining the regional fabric. This fabric swerves around the enclosing enclaves. The earliest fabric of the area (S1) (discordant with S2) is defined by the pelitic granulite enclaves that contain thick leucosomes (Dey et al. 2019b). This earliest metamorphic event in the area (M1) was characterised by Dey et al. (2019) as a granulite facies metamorphism that culminated at > 850 °C and medium pressure (~ 8 -9 kbar) and was followed by a sharp decompression. Following this, the region experienced a second metamorphism (M2), which led to the folding of S1 in the pelitic granulites, the formation of migmatitic bandings (S2) in the felsic gneiss, and the emergence of a second generation of migmatitic foliation in the pelitic granulites (Mukherjee et al. 2017; Dey et al. 2019b). The estimated P-T conditions of the second metamorphism (M2) have been evaluated to be $\sim 800 \pm 50$ °C and ~ 9 -14 kbar (Chatterjee et al. 2008; Mukherjee et al. 2017; Chatterjee 2018; Dey et al. 2019b). The mafic granulites in the region record high pressure granulite facies peak metamorphic condition of 12 ± 1 kbar and 800 ± 50 °C, followed by a steeply decompressive path that defines a clockwise P-T path corresponding to continent-continent collision (Dey et al.

2019a). Roy Choudhury et al. (2023) constrained the age of metamorphism of the calc-silicate enclaves between 1060-970 Ma. Mafic dykes (now metamorphosed to amphibolites) intruded the host felsic gneiss and cut across the S2 foliation. Following this, the third tectonothermal event in the region is represented by the folding of the S2 foliation and the mafic dykes by two sets of coaxial folding (with N-S axial plane) (Ghosh and Sengupta 1999; Sanyal and Sengupta 2012; Mukherjee et al. 2017, 2018b). Along the axial planes of the folded S2/dykes, a N-S trending foliation forms (S3). Locally, the S3 foliation is folded into open folds with E-W axial plane (Ghosh and Sengupta 1999; Sanyal and Sengupta 2012; Mukherjee et al. 2017, 2018b). The P-T conditions of this third tectonothermal event (M3) have been evaluated to be $\sim 700^{\circ}\text{C}$ and ~ 7.5 kbar from the Mafic dykes in the region. Bhattacharjee et al. (2012) reported the intrusion of a gabbro-anorthositic body within the felsic country rock that metamorphosed together during this M2-D2 event. The P-T condition estimated from anorthositic body varies over a wide range of $\sim 511\text{--}915^{\circ}\text{C}$ and $5.0\text{--}7.5$ kbar (Bhattacharjee et al. 2012). Chatterjee et al. (2010) have described the "Eastern Indian Tectonic Zone (EITZ)," a highly tectonised zone at the easternmost boundary that trends N-NE. The authors have constrained the peak metamorphic P-T condition for this event at 11.3 kbar and 800°C , followed by an isothermal pressure increase to 12.7 kbar and retrogression to 9 kbar and 730°C which they associated with the shearing and anatexis event along EITZ.

The oldest known magmatic event is the emplacement of a porphyritic granite (now augen gneiss) in a continental arc setting between approximately 1710 and 1635 Ma (Mukherjee et al. 2019a). Geochemical features characterise the event as I-type granite magmatism (Mukherjee et al. 2019a). Detailed detrital zircon study has constrained the age of sedimentation of the metapelite protoliths between $\sim 1700\text{--}1650$ Ma (U-Pb zircon ages from Dey et al. 2017 and Pb-Pb isotopic ages from Singh et al. 2001). Further, the source of sediments is inferred to be from Archaean/ Palaeoproterozoic terranes (Rekha et al. 2011; Dey et al. 2017). U-Pb zircon and monazite age dating constrain the timing of M1 metamorphism from the metapelites between $\sim 1680\text{--}1580$ Ma (Dey et al. 2019b). A similar age of the Palaeoproterozoic metamorphism has been documented by Rekha et al. (2011) from metapelites and quartzo-feldspathic gneiss. Similar ages for the M1 metamorphism are obtained from Th-U-total Pb chemical ages from monazites by Chatterjee et al. (2010) ($\sim 1684\text{--}1659$ Ma) and Sanyal and Sengupta (2012) ($\sim 1628\text{--}1518$ Ma). The host migmatitic felsic gneiss is geochemically characterised as ferroan (A-type) granites. The emplacement

age of the ferroan (A-type) granites has been constrained to Mesoproterozoic times during ~1470-1350 Ma) in a continental rift setting (Dey et al. 2017; Mukherjee et al. 2018a, 2022; Sequeira et al. 2022). The extensional tectonism is linked with the breakup of the Columbia supercontinent (Mukherjee et al. 2018a; Sequeira et al. 2022). The source of the Mesoproterozoic ferroan magmatism is linked to the high-temperature partial melting of the Paleoproterozoic crustal source (augen gneiss) with limited mantle component (Mukherjee et al. 2018a, 2022). The compositional variation of the ferroan granites is predominantly influenced by fractional crystallisation (Mukherjee et al. 2018a, 2022). Ray Barman et al. (1994) constrained the ages of syenite and charnockite (1457 ± 63 Ma and 1331 ± 125 Ma) from the Dumka-Jamua area of Jharkhand by Rb–Sr whole rock ages. Zircon and monazite dating constrain the age of the M2 metamorphic event at ~1000–930 Ma (Chatterjee et al. 2008, 2010; Rekha et al. 2011; Mukherjee et al. 2017; Dey et al. 2019b). Chatterjee et al. (2010) constrained the timing of the tectonothermal event of the EITZ at ~870-650 Ma. The third (amphibolite facies) metamorphic event (M3) occurred between 920 and 880 Ma, as constrained by zircon and monazite dates (Chatterjee and Ghose 2011; Sanyal and Sengupta 2012; Mukherjee et al. 2018b).

In and around Dhanbad and Hazaribag, west of Jasidih, the general strike of the litho-units varies between E-W and NW-SE. Lithological exposures in parts of Dhanbad districts comprise amphibolite facies banded gneisses, with enclaves of olivine-orthopyroxene bearing metanorites, hornblende bearing schists and gneisses and quartzites (Roychowdhury, 1979). Sarangi and Mohanty (1998) identified three sets of folding and the E-W to NW-SE trending axial planar foliation corresponding to the second deformation event. Amphibolites, calcareous and pelitic rocks constitute the lithounits of Hazaribagh (Jharkhand). The dominant fabric is defined by E-W trending schistosity. Three distinct folding generations have been identified, with the first two being coaxial and tight, and the third being an open fold (RoyChowdhury 1979; Mahadevan 2002). The youngest age has been obtained from biotite-K-feldspar from a migmatite by whole rock Rb–Sr isochron date 481 ± 18 Ma (Pandey et al. 1986b, 1986a).

The litho package in the Daltonganj area comprises migmatites and granite gneiss that are interbedded with graphite-bearing pelitic schists, quartzites, and limestones and are intruded by mafic-ultramafic, anorthositic-komatiitic rocks (Bhattacharya et al. 2010). High grade conditions from granite gneiss corresponding to the formation of gneissic

foliation have been constrained at high grade conditions of 850–800 °C (Chatterjee and Ghose 2011). the granite gneisses were intruded by Non-foliated granitic/granodioritic rocks (Rode 1947; Ghose 1983; Mazumdar 1988). The ultramafic rocks contain fluorite, magnetite and base metal mineralisation (Ghose 1983; Soni et al. 1991; Sinha and Bhattacharya 1995). The granulite facies metamorphism and partial melting have been evaluated between ~2–6 kbar and ~650–800 °C metapelites (Srivastava and Ghose 1992). Granitic magmatism is constrained at 1741 ± 65 Ma by the granite gneiss's whole-rock Rb–Sr dating (Ray Barman et al. 1994). The granitic rock subsequently underwent high grade metamorphism and anatexis at 975 ± 67 Ma. Three stages of deformation events (D1–D3) occurred in the granite gneiss and metapelitic lithounits (Lahiri and Das 1984; Patel 2007). Calc-silicate rocks in the Tatapani area give rise to the uncommon assemblage of vesuvianite + grossular garnet + diopside + wollastonite + quartz that formed at < 4 kbar and 590–650°C, in the presence of highly aqueous fluid (Patel 2007).

2.2.3 Domain II

The ENE-WSW trending the Bihar Mica belt (BMB), sandwiched between Domain III (in the north) and GBF (in the south), exposes a distinct lithological package of this domain. The litho-units comprise a metasedimentary sequence that includes conglomerates, micaceous quartzites, hornblende schists, and calc-silicate rocks. These metasedimentary units with local conglomerate bases overlie high-grade rocks of the CGGC (Ghose and Mukherjee 2000). Occasionally, economic-grade base-metal mineralisation appears to be associated with carbonate metasediments (Ghose 1992). Based on Pb–Pb galena dates of base metal deposits, sedimentation ages in the BMB have been determined to be ~ 1700–1650 Ma (Singh et al. 2001). Rb–Sr whole-rock age of a migmatitic granite gneissic basement from south of BMB constrains an age of 1717 ± 102 Ma (Mallik et al. 1991). Large bodies of granitoid rocks, dolerite dykes, gabbro anorthosite, and mica pegmatites (sometimes rich in rare earth elements and/or rare metals) intrude the entire lithological ensemble. Three folding stages (D1, D2, and D3) were documented in the meta-sedimentary package; the first two folds are the most prominent and result in E–W trending axial planar foliation, whilst the third fold is weaker and less widespread. Though most of the granite intrusions cluster between 1300–1100 Ma (syn- to post-D2), the oldest emplacement dates back to ~1600 Ma (Misra and Dey 2002; Rb–Sr mineralisochron and whole-rock ages; Pandey et al. 1986a). The estimated P–T conditions

for the granite pluton emplacement during the post-collisional extensional setting are approximately 5 kbar and $>1000^{\circ}\text{C}$ (Misra and Dey 2002). Furthermore, the distinctively high Sr/I ratio of these BMB plutons points to their origin in sialic crustal sources (Misra and Dey 2002). Several generations of mica-bearing granite–pegmatites intruded pre-D2 to post-D3 (Mahadevan 2002). The oldest REE-rare metal-bearing mica pegmatites of the BMB were emplaced 960 ± 50 Ma (Pb/Pb age; Vinogradov et al., 1964) and 910 ± 20 Ma (U–Pb and Pb/Pb ages of the Columbite–Tantalite minerals; Krishna et al., 2003). Lal et al. (1976) constrained the fission-track ages of garnet (830 Ma), muscovite (760 Ma), biotite (590 Ma) and apatite (590 Ma) from mica pegmatites, suggesting that the rocks of this area had not received any significant thermal pulse, implying cratonization, since 590 Ma (Lal et al. 1976).

2.2.4 Domain III

This domain is situated north of BMB and comprises lithounits of migmatitic quartzo-feldspathic gneisses and meta-supracrustals, forming the gneissic basement for the sedimentary deposits of the Munger and Rajgir group. The boundary between the basement gneiss and the sedimentary deposits is demarcated by a conglomerate horizon (Ghose and Mukherjee, 2000). The supracrustals comprise low-grade quartzites and phyllites, associated with felsic and mafic-ultramafic intrusives. Porphyritic granitoids form the basement of the sedimentary units near Gaya, while near Bhagalpur, biotite gneiss is the basement (Chatterjee and Ghose 2011). The geochemical characteristics of the porphyritic granites suggest these are extensional (A-type) magmatism (Yadav et al. 2016). The banded iron formation (BIF), chert bands, garnet-mica schist, and mafic intermediate volcanics constitute the volcano-sedimentary sequence surrounding Bathani village (Saikia et al. 2014). Bimodal volcanism comprising basalt of tholeiitic affinity and intermediate-felsic magmatism of calc-alkaline trend indicates an island-arc setting (Saikia et al. 2014, 2017). The age of emplacement of the granitic plutons from this volcano-sedimentary sequence is constrained by U-Pb zircon dating at 1737–1664 Ma (Saikia et al. 2017). Though Paleoproterozoic imprints of magmatism are prominent in the central and western parts of the domain, the Neoproterozoic overprinting is insignificant. Neoproterozoic ages are documented from the eastern part near Bhagalpur from biotite-granodiorite gneiss, which constrained dates of 557 ± 99 Ma, 768 ± 11 Ma and 929 Ma (Chatterjee and Ghose 2011). While the earlier metamorphism suggests granulite grade condition, the latter correlates with shearing linked with EITZ (Chatterjee et al. 2010).

Table 2.1: Available geochronological information on tectonothermal events in the CGGC.

Domain IA					
Age (Ma)	Method	Area	Rock type	Event	Reference
595	U-Pb monazite	S margin of N-CGGC	Metapelite	hydrothermal alteration	Chatterjee et al. (2010)
784	U-Pb monazite	S margin of N-CGGC	blastoporphyratic granite	magmatic/metamorphism+anatexis/E-W compression	Chatterjee et al. (2010)
810± 40	K-Ar muscovite	Purulia	alkali feldspar-rich leucogranitoid	magmatism	Baidya et. al.(1987)
815±47	Rb–Sr whole rock	Raikera-Kunkuri region,Jashpur district, Chhattisgarh	granite	age of metasomatism	Singh and Krishna (2009)
825-818	U-Pb monazite	Bero-Saltora	metapelite	metamorphic	Maji et.al. (2008)
850-775	U-Pb monazite	puruliya	migmatitic gneiss	deformation event	Karmakar et. al. (2011)
859	U-Pb monazite	S margin of N-CGGC	Metapelite	metamorphism+anatexis/E-W compression	Chatterjee et al. (2010)
860-830	U-Pb monazite	S margin of N-CGGC	blastoporphyratic granite	magmatic/metamorphism+anatexis	Chatterjee et al. (2010)
870± 40	K-Ar biotite	Purulia	porphyritic biotite granitoid	magmatism	Baidya et. al. (1987)
921	U-Pb monazite	South of Ranchi	Foliated granite	metamorphism	Rekha et al. (2011)
921	U-Pb monazite	South of Ranchi	metapelite	metamorphism	Rekha et al. (2011)
923	U-Pb zircon	South of Ranchi	quartzofeldspathic gneiss xenolith	metamorphism	Rekha et al. (2011)
928	U-Pb zircon	South of Ranchi	Foliated granite	metamorphism	Rekha et al. (2011)
937	U-Pb monazite	S margin of N-CGGC	Metapelite	older thermal event??	Chatterjee et al. (2010)
942 - 944	U-Pb apatite; titanite	Simdega	Lamprophyre	emplacement	Kumar et al. (2023)
944	U-Pb monazite	South of Ranchi	quartzofeldspathic gneiss xenolith	metamorphism	Rekha et al. (2011)
946	U-Pb monazite	S margin of N-CGGC	Metapelite	older thermal event??	Chatterjee et al. (2010)
947±27	U-Pb zircon	Saltora	anorthosite	granulite metamorphism	Chatterjee et.al. (2008)
965	U-Pb monazite	S margin of N-CGGC	blastoporphyratic granite	older thermal event??	Chatterjee et al. (2010)
966	U-Pb Zircon	Jhalda	Alkali granite	Magmatism	Chakraborty et al. (2022)
990-940	U-Pb monazite	Purulia	High Mg–Al granulite, migmatitic gneiss	high grade event with decompression	Karmakar et. al. (2011)

Table 2.1 contd.:

1000	U-Pb Zircon	Purulia	Megacrystic granite gneiss; pink granite	magmatic	Chakraborty et al. (2019)
1000	U-Pb monazite	Purulia	Garnetiferous granite gneiss	metamorphism	Chakraborty et al. (2019)
1005±51	Rb-Sr whole rock	Raikera-Kunkuri region, Jashpur district, Chhattisgarh,	granite	emplacement age	Singh and Krishna (2009)
1021-967	U-Pb monazite	Bero-Saltora	metapelite, foliated granite	metamorphic/magmatic	Maji et.al. (2008)
1025	U-Pb zircon	South of Ranchi	quartzofeldspathic gneiss xenolith	metamorphism	Rekha et al. (2011)
1059±104	Rb-Sr whole rock	Kailash nath gufa	Alkali Syenite	magmatism	Krishna et al. (1996)
1065±74	Rb-Sr whole rock	Marne	Pink Granite	magmatism	Krishna et al. (1996)
1071± 64	Rb-Sr whole rock	Murguma-Purulia-Raghunathpur	hypersthene granite	retrogression in amp facies with ITD	Ray Barman et.al.(1994)
1072	U-Pb zircon	south of Ranchi	Foliated granite	metamorphism	Rekha et al. (2011)
1138±193	Rb-Sr whole rock	Kailash nath gufa	Diorite	magmatism	Krishna et al. (1996)
1176	U-Pb monazite	Bero-Saltora	metapelite	metamorphic	Maji et.al. (2008)
1178± 61	Rb-Sr whole rock	Murguma-Purulia-Raghunathpur	migmatite	retrogression in amp facies with ITD	Ray Barman et.al.(1994)
1200-1100	U-Pb monazite	puruliya	migmatitic gneiss	older tectonothermal events	Karmakar et. al. (2011)
1239	U-Pb zircon	south of Ranchi	Foliated granite	metamorphism	Rekha et al (2011)
1331±42	Rb-Sr whole rock	Nagam	granite		Krishna et al. (1996)
1422-1305	U-Pb monazite	S margin of N-CGGC	Metapelite	older thermal event??	Chatterjee et al (2010)
1550±12	U-Pb zircon	Saltora	anorthosite	magmatic	Chatterjee et.al.(2008)
1717-1446	U-Pb monazite	S margin of N-CGGC	blastoporphyratic granite	older thermal event??	Chatterjee et al. (2010)
1737-1664	U-Pb zircon				Saikia et al. (2017)
1800	U-Pb monazite	Purulia	migmatitic gneiss	inherited	Karmakar et. al. (2011)
1870-1691	U-Pb monazite	S margin of N-CGGC	blastoporphyratic granite	older thermal event??	Chatterjee et al. (2010)
1754±116	Rb-Sr whole rock				Dhurandhar et al. (2005)

Table 2.1 contd.:

Domain IB					
Age	Method	Area	Rocktype	Type of age	Reference
481±18	Bt and K-feldspar Rb–Sr isochron			metamorphism?	Pandey et al.(1986)
560	U–total Pb xenotime	NE CGGC	Biotite–granodiorite gneiss?	metamorphism?	Chatterjee & Ghose (2011)
649	U–Pb monazite	E margin of N- CGGC	quartzofeldspathic gneiss	magmatic/metamorphism+anatexis/E-W	Chatterjee et al. (2010)
650–600	Th–U–total Pb monazite	E CGGC	Quartzo-feldspathic gneiss, metapelite	Metamorphism/ hydrothermal	Chatterjee et al. (2010)
850	Monazite	Daltanganj	high-grade gneiss		Kumar et al. (2022)
850-750	U–Pb monazite	Dumka-Deoghar	metapelitic enclave	metamorphism	Sanyal et. al. (2007)
872-838	U–Pb monazite	E margin of N- CGGC	quartzofeldspathic gneiss	magmatic/metamorphism+anatexis/E-W	Chatterjee et al. (2010)
876	U–Pb monazite	E margin of N- CGGC	quartzofeldspathic gneiss	magmatic/metamorphism+anatexis/E-W	Chatterjee et al. (2010)
876-784	U–Pb monazite		pelitic granulites		Chatterjee et al. (2018)
902	U–Pb zircon	deoghar-Dumka	felsic gneiss	Metamorphism	Mukherjee et al. (2017a)
910	U–Pb monazite	Dumka	Metapelite	Metamorphism	kekna et al. (2011)
937	U–Pb monazite	E margin of N- CGGC	garnet–sillimanite bearing metapelite	older thermal event??	Chatterjee et al. (2010)
943	U–Pb zircon	deoghar-Dumka	felsic gneiss	Metamorphism	Mukherjee et al. (2017)
945	U–Pb monazite	Dumka	metapelite	Metamorphism	kekna et al. (2011)
948 ± 22, 951 ± 2.7	U–Pb zircon	deoghar-Dumka	felsic gneiss	Metamorphism	Mukherjee et al. (2018)
950± 20	U–Pb monazite	Dumka	metapelite granulite	retrogression	Chatterjee et al. (2008)
954	U–Pb monazite	E margin of N- CGGC	blastoporphyratic granite	older thermal event??	Chatterjee et al. (2010)
965-930	U–Pb monazite	E margin of N- CGGC	quartzofeldspathic gneiss	older thermal event??	Chatterjee et al. (2010)
974-895	U–Pb monazite		Mica schist and Granitoids	metamorphism	Sequeira and Bhattacharya
970–950	U–Pb zircon	Dumka	metapelite	high-temperature granulite facies metamorphism	Dey et al. (2019c)
972 ± 28	U–Pb monazite	Daltanganj	granulite rock	metamorphism	Kumar and Diwedi (2019)
975±67 Ma	U–Pb monazite	Daltanganj	granitic gneiss	granulite metamorphism	Chatterjee & Ghosh (2011)
978	Monazite	Daltanganj	high-grade gneiss	metamorphism	Kumar et al. (2022)
979-942	U–Th–Pbmonazite	Dumka- Deoghar	quartzofeldspathic and pelitic gneiss	metamorphism	Sanyal et al. (2007)
995 ± 24	U–Pb monazite	Dumka	metapelite granulite	high grade metamorphism	Chatterjee et.al. (2008)

Table 2.1 contd.:

1009	U-Pb zircon	Dumka	metapelite	metamorphic	Rekha et al. (2011)
1045	U-Pb zircon	N CGGC	Granite	Magmatism	Wanjari et. al. (2012)
1060-970	U-Pb Zircon	Dumka-Deoghar	calcsilicate enclave	metamorphism	Roy Choudhury et al. (2023)
1118-1088	U-Pb monazite	Dumka-Deoghar	metapelitic enclave	metamorphism	Sanyal et al. (2007)
1119 Ma,	Rb-Sr whole rock	Chianki	gneissic granite		Sarkar et al.(1986)
1183	U-Pb monazite	E margin of N-CGGC	garnet-sillimanite bearing metapelite	older thermal event??	Chatterjee et al. (2010)
1190 ± 26	U-Pb monazite	Dumka	metapelite granulite	high grade metamorphism	Chatterjee et.al.(2008)
1270	U-Pb zircon	Dumka	metapelite	?	Rekha et al. (2011)
1272	U-Pb monazite	E margin of N-CGGC	blastoporphyratic granite	older thermal event??	Chatterjee et al. (2010)
1278	U-Pb monazite	E margin of N-CGGC	garnet-sillimanite bearing metapelite	older thermal event??	Chatterjee et al. (2010)
1331± 125	Rb-Sr whole rock	Jamua-Dumka		isobaric cooling age	Ray Barman et al. (1994)
1333	U-Pb zircon	Dumka	metapelite	?	Rekha et al. (2011)
1377	U-Pb zircon	Dumka	metapelite	?	Rekha et al. (2011)
1424 ± 64	U-Pb monazite	Daltanganj	felsic gneiss	emplacement	Kumar and Diwedi (2019)
1434 ±18	U-Pb monazite	Daltanganj	high-grade gneiss	emplacement	Kumar et al. (2022)
1435	U-Pb zircon	Dumka	metapelite	?	Rekha et al (2011)
~1469-1446	U-Pb zircon	Dumka-Deoghar	felsic gneiss	Magmatism	Mukherjee et al. (2018)
1447±11	U-Pb zircon	Dumka-Deoghar	felsic gneiss	Magmatism	Mukherjee et al. (2017)
1450-1350	U-Pb zircon	Dumka-Deoghar	felsic gneiss	emplacement	Sequeira et al. (2022)
~922	U-Pb zircon	Dumka-Deoghar	felsic gneiss	metamorphism	Sequeira et al. (2022)
1457±63	Rb-Sr whole rock	Jamua-Dumka	syenite	high grade meta with partial melting	Ray Barman et.al.(1994)
1462	U-Pb zircon	Dumka	metapelite	?	Rekha et al. (2011)
1480	U-Pb monazite	Dumka	metapelite	?	Rekha et al. (2011)
1515 ±5	U-Pb zircon	mor valley	massive charnockites	Intrusion age	Acharyya (2003)
1522±71 Ma	Rb-Sr whole rock		migmatite	magmatism	Mallik et al.(1991)

Table 2.1 contd.:

1580±33 Ma	Rb–Sr whole rock		migmatite	magmatism	Mallik et al.(1991)
1599±33 Ma	Rb–Sr whole rock		migmatite	magmatism	Mallik et al.(1991)
1624 ±5	U-Pb zircon	mor valley	hypersthene gneiss	crystallization age	Acharyya (2003)
1649	U-Pb zircon	Dumka	metapelite	high grade metamorphism	Rekha et al. (2011)
1628-1518	U-Pb monazite	Dumka-Deoghar	metapelitic enclave	metamorphism	Sanyal et al. (2007)
1629 ± 6	U-Pb zircon	Daltanganj	mafic granulite	emplacement	Kumar et al. (2021)
1638 ± 22	U-Pb zircon	Daltanganj	pelitic granulite	metamorphism	Kumar et al. (2021)
1680–1580	U-Pb zircon	Dumka	metapelite	high-temperature granulite facies metamorphism	Dey et al. (2019c)
1660-1270	U-Pb monazite	Dumka-Deoghar	metapelitic enclave	metamorphism?	Sanyal et al. (2007)
1700-1650	U-Pb zircon	Dumka-Deoghar	metapelitic enclave	sedimentation	Dey et al. (2017)
1710-1635	U-Pb zircon	Dumka-Deoghar	Augen Gneiss	Emplacement	Mukherjee et al. (2019)
1720	U-Pb monazite	E margin of N-CGGC	garnet–sillimanite bearing metapelite	older thermal event??	Chatterjee et al. (2010)
1741±65 Ma	Rb–Sr whole rock	northwest CGC	granite	?	Ray Barman et.al.(1994)
1824-1659	U-Pb monazite	E margin of N-CGGC	quartzofeldspathic gneiss	older thermal event??	Chatterjee et al. (2010)
1870-1720	U-Pb monazite	Dumka-Deoghar	metapelitic enclave	UHT metamorphism	Sanyal et al. (2007)
2600-1900	U-Pb zircon	Dumka	metapelite	detrital	Rekha et al. (2011)

Table 2.1 contd.:

Domain II					
Age	Method	Area	Rocktype	Type of age	Reference
590	Apt Fission Track	BMB	Mica Pegmatite	cooling age	Nand Lal (1976)
595	Bt Fission Track	BMB	Mica Pegmatite	cooling age	Nand Lal (1976)
760	mus Fission Track	BMB	Mica Pegmatite	cooling age	Nand Lal (1976)
830	grt Fission Track	BMB	Mica Pegmatite	cooling age	Nand Lal (1976)
855±25	Mica Rb-Sr	Bhallupahari-Nirupahari	Mica Pegmatite	Intrusion age	Pandey et al. (1986b)
910±19	U-Pb, Pb-Pb	Dhajua, Jharkhand	Pegmatite Cb-Ta	Intrusion age	Krishna et al. (2003)
960±50	Pb-Pb	Pichili	Pegmatite columbite-tantalite, Samarskite, monazite)	Intrusion age	Vinogradov et al. (1964)
1086-850	K-Ar		Granitoids		Sarkar (1980)
1020±46	Rb–Sr whole rock	BMB	Granite	emplacement	Mallik et. al. (1991)

Table 2.1 contd.:

1100-700 Ma	Fission track mica		Mica Pegmatite	cooling age	Mehta & Nagpal (1971)
1242±34	Rb–Sr whole rock	Binda-Nagnaha	Granite-gneiss		Pandey et al.(1986a)
1238±33	Rb–Sr whole rock	BMB	Granite	emplacement	Mallik et. al. (1991)
1285±108	Rb–Sr whole rock	BMB	Migmatitic Granite gneiss	emplacement	Mallik et. al. (1991)
1300–1100 Ma	Rb–Sr whole rock	BMB	Granite gneiss-Migmatite		Pandey et al.(1986a, b)
1590±30	Rb–Sr whole rock		Granitoids	emplacement	Pandey et al. (1986b)
1700–1650	Pb/Pb age of galena	metasediments		sedimentation age	Singh et. al. (2001)
1717±102	Rb–Sr whole rock	S of BMB	migmatitic granite gneiss		Mallik et. al. (1991)

Table 2.1 contd.:

Domain III					
Age (Ma)	Method	Area	Rocktype	Event	Reference
557±99	U-Pb xenotime	Bhagalpur	biotite–granodiorite gneiss	?	Chatterjee and Ghosh (2011)
768±11	U-Pb uraninite	Bhagalpur	biotite–granodiorite gneiss	metamorphism along EITZ	Chatterjee and Ghosh (2011)
929	U-Pb xenotime	Bhagalpur	biotite–granodiorite gneiss	granulite metamorphism	Chatterjee and Ghosh (2011)
1044±35	U-Pb zircon	Bathani	granite	emplacement	Wanjari et al. (2012)
1337±26	Rb–Sr whole rock	Sonbhadra	granite	emplacement	Wanjari et al. (2012)
1583±50	U-Pb xenotime	Gaya	porphyritic granite	cooling of granite	Chatterjee and Ghosh (2011)
1697±17	U-Pb Monazite	Gaya	porphyritic granite	emplacement	Chatterjee and Ghosh (2011)
1737-1664	Rb–Sr whole rock	Gaya	granite	emplacement	Saikia et al. (2017)

References:

- Acharyya, S., and Roy, A. (2000) Tectonothermal history of the Central Indian Tectonic Zone and reactivation of major faults/shear Zones. *Journal of the Geological Society of India*, 55, 239–256.
- Acharyya, S.K. (2003) The Nature of Mesoproterozoic Central Indian Tectonic Zone with Exhumed and Reworked Older Granulites. *Gondwana Research*, 6, 197–214.

- Baidya, T.K., Chakravorty, P.S., Drubetskoy, E., and Khiltova, V.J. (1987) New geochronologic data on some granitic phases of the Chhotanagpur granite gneiss complex in the north-western Purulia district, West Bengal. *Indian Journal of Earth Sciences*, 14, 136–141.
- Baidya, T.K., Maity, N., and Biswas, P. (1989) Tectonic Phases and Crustal Evolution in a Part of the Eastern Chotanagpur Gneissic Complex. *Journal of Geological Society of India*, 34.
- Bhattacharjee, N., Ray, J., Ganguly, S., and Saha, A. (2012) Mineralogical study of gabbro-anorthosite from Dumka, Chhotanagpur Gneissic Complex, Eastern Indian Shield. *Journal of the Geological Society of India*, 80, 481–492.
- Bhattacharya, D.K., Mukherjee, D., and Barla, V.C. (2010) Komatiite within Chhotanagpur Gneissic Complex at Semra, Palamau District, Jharkhand: Petrological and geochemical fingerprints. *Journal of the Geological Society of India*, 76, 589–606.
- Bhattacharyya, P.K., and Mukherjee, S. (1987) Granulites in and around the Bengal anorthosite, eastern India; genesis of coronal garnet, and evolution of the granulite-anorthosite complex. *Geological Magazine*, 124, 21–32.
- Chakraborty, K., Ray, A., Chakraborti, T.M., Deb, G.K., Mandal, A., Kimura, K., and Mukhopadhyay, S. (2022) Petrology, geochemistry and U–Pb zircon geochronology of alkali granites of Jhalda, eastern India and their possible linkage to Rodinia Supercontinent. *Journal of Earth System Science*, 131, 253.
- Chatterjee, N. (2018) An assembly of the Indian Shield at c . 1 . 0 Ga and shearing at c . 876 – 784 Ma in Eastern India : Insights from contrasting P-T paths , and burial and exhumation rates of metapelitic granulites. *Precambrian Research*, 317, 117–136.
- Chatterjee, N., and Ghose, N.C. (2011) Extensive Early Neoproterozoic high-grade metamorphism in North Chotanagpur Gneissic Complex of the Central Indian Tectonic Zone. *Gondwana Research*, 20, 362–379.
- Chatterjee, N., Crowley, J.L., and Ghose, N.C. (2008) Geochronology of the 1.55Ga Bengal anorthosite and Grenvillian metamorphism in the Chotanagpur gneissic complex, eastern India. *Precambrian Research*, 161, 303–316.
- Chatterjee, N., Banerjee, M., Bhattacharya, A., and Maji, A.K. (2010) Monazite chronology, metamorphism–anatexis and tectonic relevance of the mid-Neoproterozoic Eastern Indian Tectonic Zone. *Precambrian Research*, 179, 99–120.
- Das, S., Dasgupta, N., Sanyal, S., Sengupta, S., Karmakar, S., and Sengupta, P. (2017) Dolomitic carbonatite from the Chotanagpur Granite Gneiss Complex: a new DARC

- (Deformed Alkaline Rocks and Carbonatite) in the Precambrian shield of India. *Current Science*, 113, 1038–1040.
- Das, S., Sanyal, S., Karmakar, S., Sengupta, S., and Sengupta, P. (2019) Do the deformed alkaline rocks always serve as a marker of continental suture zone? A case study from parts of the Chotanagpur Granite Gneissic complex, India. *Journal of Geodynamics*, 129, 59–79.
- Dey, A., Mukherjee, S., Sanyal, S., and Sengupta, P. (2017) Deciphering Sedimentary Provenance and Timing of Sedimentation From a Suite of Metapelites From the Chotanagpur Granite Gneissic Complex, India: Implications for Proterozoic Tectonics in the East-Central Part of the Indian Shield, 453–486 p.
- Dey, A., Karmakar, S., Mukherjee, S., Sanyal, S., Dutta, U., and Sengupta, P. (2019a) High pressure metamorphism of mafic granulites from the Chotanagpur Granite Gneiss Complex, India: Evidence for collisional tectonics during assembly of Rodinia. *Journal of Geodynamics*, 129, 24–43.
- Dey, A., Karmakar, S., Ibanez-Mejia, M., Mukherjee, S., Sanyal, S., and Sengupta, P. (2019b) Petrology and geochronology of a suite of pelitic granulites from parts of the Chotanagpur Granite Gneiss Complex, eastern India: Evidence for Stenian - Tonian reworking of a late Paleoproterozoic crust. *Geological Journal*, 55, 2851–2880.
- Dunn, J.A. (1929) The geology of north Singhbhum including parts of Ranchi and Singhbhum districts. *Geological Survey of India, Memoir*, 54, 1–280.
- Ghose, N.C. (1983) Geology, tectonics and evolution of the Chhotanagpur granite gneiss complex, Eastern India. *Recent Researches in Geology*, 10, 211–247.
- (1992) Chhotanagpur gneiss-granulite complex Eastern India: Present status and future prospect. *Indian Jour. Geol.*, 64, 100–121.
- Ghose, N.C., and Mukherjee, D. (2000) Chotanagpur gneiss–granulite complex, Eastern India — akaleidoscope of global events. In A.N. Trivedi, B.C. Sarkar, and N.C. Ghose, Eds., *Geology*.
- Ghosh, S.K., and Sengupta, S. (1999) Boudinage and composite boudinage in superposed deformations and syntectonic migmatization. *Journal of Structural Geology*, 21, 97–110.
- Goswami, B., and Bhattacharyya, C. (2008) Tectonothermal evolution of Chhotanagpur Granite Gneiss Complex from northeastern part of Puruliya district, West Bengal, eastern India, 80, 41–54.
- Goswami, B., and Bhattacharyya, C. (2014) Petrogenesis of shoshonitic granitoids, eastern

- India: Implications for the late Grenvillian post-collisional magmatism. *Geoscience Frontiers*, 5, 821–843.
- Karmakar, S., Bose, S., Sarbadhikari, A.B., and Das, K. (2011) Evolution of granulite enclaves and associated gneisses from Purulia, Chhotanagpur Granite Gneiss Complex, India: Evidence for 990-940Ma tectonothermal event(s) at the eastern India cratonic fringe zone. *Journal of Asian Earth Sciences*, 41, 69–88.
- Krishna, V., Sastry, D.V.L.N., Pandey, B.K., and Sinha, R.P. (2003) U-Pb and Pb-Pb ages on columbite-tantalite minerals from pegmatites of Bihar mica belt, Jharkhand, India. *Indian Society for Mass Spectrometry*, India.
- Kumar, D., Rao, N.V.C., Tripathi, A., Belyatsky, B., Prabhat, P., Rahaman, W., and Satyanarayanan, M. (2023) U-Pb Neoproterozoic age and petrogenesis of a calc-alkaline shoshonitic lamprophyre from Simdega area, Chhotanagpur Gneissic Complex (Eastern India): Implication for the evolution of the Central Indian Tectonic Zone and Rodinia tectonics. *Chemical Geology*, 631, 121512.
- Lahiri, G., and Das, S. (1984) Petrology of the area east of Daltonganj, Palamau district, Bihar. *Geol. Soc. India*, 25, 490–504.
- Lal, N., Saini, H.S., Nagpaul, K.K., and Sharma, K.K. (1976) Tectonic and cooling history of the Bihar Mica Belt, India, as revealed by fission-track analysis. *Tectonophysics*, 34, 163–180.
- Mahadevan, T.M. (2002) *Geology of Bihar & Jharkhand*. Geological Society of India, Bangalore.
- Maji, A.K., Goon, S., Bhattacharya, A., Mishra, B., Mahato, S., and Bernhardt, H.-J. (2008) Proterozoic polyphase metamorphism in the Chhotanagpur Gneissic Complex (India), and implication for trans-continental Gondwanaland correlation. *Precambrian Research*, 162, 385–402.
- Mallik, A.K., Gupta, S.N., and Barman, T.R.. (1991) Dating of early Precambrian granite greenstone complex of the eastern India Precambrian shield with special reference to Chotonagpur Granite gneiss complex. *Records of the Geological Survey of India*, 124, 20–21.
- Mandal, P. (2016) Shear-wave splitting in Eastern Indian Shield: Detection of a Pan-African suture separating Archean and Meso-Proterozoic terrains. *Precambrian Research*, 275, 278–285.
- Manna, S.S., and Sen, S.K. (1974) Origin of garnet in the basic granulites around Saltora, W. Bengal, India. *Contributions to Mineralogy and Petrology*, 44, 195–218.

- Mazumdar, S.K. (1988) Crustal evolution of the Chotanagpur gneissic complex and the Mica Belt of Bihar. In D. Mukhopadhyay, Ed., Precambrian of the Eastern Indian Shield. Geological Society of India.
- Misra, S., and Dey, S. (2002) Bihar Mica Belt Plutons-an Example of Post-Orogenic Granite from Eastern Indian Shield. Geological Society of India; Volume 59, Issue 4, April 2002.
- Mukherjee, D., Ghose, N.C., and Chatterjee, N. (2005) Crystallisation history of a massif anorthosite in the eastern Indian shield margin based on borehole lithology. *Journal of Asian Earth Sciences*, 25, 77–94.
- Mukherjee, S., Dey, A., and Sanyal, S. (2017) Petrology and U – Pb geochronology of zircon in a suite of charnockitic gneisses from parts of the Chotanagpur Granite Gneiss Complex (CGGC): evidence for the reworking of a Mesoproterozoic basement during the formation of the Rodinia supercontinent. Geological Society, London, Special Publications, 457.
- Mukherjee, S., Dey, A., Ibanez-mejia, M., Sanyal, S., and Sengupta, P. (2018a) Geochemistry , U-Pb geochronology and Lu-Hf isotope systematics of a suite of ferroan (A-type) granitoids from the CGGC : Evidence for Mesoproterozoic crustal extension in the east Indian shield. *Precambrian Research*, 305, 40–63.
- Mukherjee, S., Dey, A., Sanyal, S., and Sengupta, P. (2018b) Tectonothermal imprints in a suite of mafic dykes from the Chotanagpur Granite Gneissic complex (CGGC), Jharkhand, India: Evidence for late Tonian reworking of an early Tonian continental crust. *Lithos*, 320–321, 490–514.
- Mukherjee, S., Dey, A., Sanyal, S., Ibanez, M., and Pulak, M. (2019a) Bulk rock and zircon geochemistry of granitoids from the Chotanagpur Granite Gneissic Complex (CGGC): implications for the late Paleoproterozoic continental arc magmatism in the East Indian Shield. *Contributions to Mineralogy and Petrology*, 174, 1–17.
- Mukherjee, S., Dey, A., Sanyal, S., and Sengupta, P. (2019b) Proterozoic crustal evolution of the Chotanagpur granite Gneissic Complex, Jharkhand-Bihar-West Bengal, India: Current status and future prospect. *Springer Geology*, 7–54.
- Mukherjee, S., Dey, A., Choudhury, S.R., and Mayne, M.J. (2022) Effect of source heterogeneity, melt extraction and crystal separation on the composition of a suite of ferroan (A-type) granites from parts of the Chotanagpur Granite Gneissic Complex (CGGC), India. *Lithos*, 430–431, 106875.
- Pandey, B.K., Upadhyay, D.L., and Sinha, K.K. (1986a) Geochronology of Jajawal-

- Binda-Nagnaha granitoids in relation to uranium mineralisation. *Indian J. earth Sci.*, 13, 163–168.
- Pandey, B.K., Gupta, J.N., and Lall, Y. (1986b) Whole rock and mineral Rb-Sr isochron ages for the granites from Bihar mica belt of Hazaribagh, Bihar, India. *Ind. Jour. Earth Sci.*, 12, 157–162.
- Patel, S.C. (2007) Vesuvianite-wollastonite-grossular-bearing calc-silicate rock near Tatapani, Surguja district, Chhattisgarh. *Journal of Earth System Science*, 116, 143–147.
- Ray Barman, T., Bishui, P.K., Mukhopadhyay, K., and Ray, J.N. (1994) Rb-Sr geochronology of the high-grade rocks from Purulia, West Bengal and Jamua-Dumka sector, Bihar. *Indian Minerals*, 48, 45–60.
- Rekha, S., Upadhyay, D., Bhattacharya, A., Kooijman, E., Goon, S., Mahato, S., and Pant, N.C. (2011) Lithostructural and chronological constraints for tectonic restoration of Proterozoic accretion in the Eastern Indian Precambrian shield. *Precambrian Research*, 187, 313–333.
- Rode, K.P. (1947) On charnockitic rocks of Palamau, Bihar, India. *Schweiz. Min. Petr. Mitt*, 28, 288–302.
- Roy, A., Sarkar, A., Jeyakumar, S., Aggrawal, S.K., and Ebihara, M. (2002) Mid-Proterozoic Plume-Related Thermal Event in Eastern Indian Craton: Evidence from Trace Elements, REE Geochemistry and Sr - Nd Isotope Systematics of Basic-Ultrabasic Intrusives from Dalma Volcanic Belt. *Gondwana Research*, 5, 133–146.
- Roy, A.K. (1977) Structure and metamorphic evolution of the Bengal anorthosite and associated rocks. *journal of geological society, India*, 18, 203–223.
- Roy Choudhury, S., Dey, A., Mukherjee, S., Sengupta, S., Sanyal, S., Karmakar, S., and Sengupta, P. (2023) Formation of aluminous clinopyroxene-ilmenite-spinel symplectic assemblage in a regionally metamorphosed calc-silicate granulite from the Chotanagpur Granite Gneiss Complex, East Indian shield. *Lithos*, 442–443, 107058.
- RoyChowdhury (1979) Annual general report of the Geological survey of India, for the year 1972-73. *Rec. Geol. Surv. India*, 107, 147–151.
- Saikia, A., Gogoi, B., Ahmad, M., and Ahmad, T. (2014) Geochemical constraints on the evolution of mafic and felsic rocks in the Bathani volcanic and volcano-sedimentary sequence of Chotanagpur Granite Gneiss Complex. *Journal of Earth System Science*, 123, 959–987.
- Saikia, A., Bibhuti, G., Tatiana, K., Liudmila, L., Tamara, B., and Mansoor, A. (2017)

- Geochemical and U–Pb zircon age characterisation of granites of the Bathani Volcano Sedimentary sequence, Chotanagpur Granite Gneiss Complex, eastern India: vestiges of the Nuna supercontinent in the Central Indian Tectonic Zone. Geological Society, London, Special Publications, 457, 233–252.
- Sanyal, S., and Sengupta, P. (2012) Metamorphic evolution of the Chotanagpur Granite Gneiss Complex of the East Indian Shield: current status. Geological Society, London, Special Publications, 365, 117–145.
- Sarangi, S., and Mohanty, S.P. (1998) Structural studies in the Chhotanagpur Gneissic Complex near Gomoh, Dhanbad district, Bihar. *Indian Journal of Geology*, 70, 73–80.
- Sen, S.K., and Bhattacharyya, A. (1993) Post-peak pressure– temperature–fluid history of the granulites around Saltora, West Bengal. *Proceedings of the National Academy of Sciences of India*, 63(A), 282–306.
- Sequeira, N., Bhattacharya, A., and Bell, E. (2022) The ~1.4 Ga A-type granitoids in the “Chottanagpur crustal block” (India), and its relocation from Columbia to Rodinia? *Geoscience Frontiers*, 13, 1138.
- Singh, R.N., Thorpe, R., and Kristic, D. (2001) Galena Pb isotope data of base metal occurrences in the Hesatu-Belbathan Belt, Eastern Precambrian Shield, Bihar. *Journal of the Geological Society of India*, 57, 535–538.
- Singh, Y., and Krishna, V. (2009) Rb-Sr Geochronology and Petrogenesis of Granitoids from the Chhotanagpur Granite Gneiss Complex of Raikera-Kunkuri Region, Central India. *Journal of the Geological Society of India*, 74, 200–208.
- Sinha, A.K., and Bhattacharya, D.K. (1995) Geochemistry of the magnetite deposits around Sua, Palamau district, Bihar. *Geol. Soc. India*, 46, 313–316.
- Soni, S., Mukherjee, A.B., and Sengupta, D.K. (1991) A New Fluorite Deposit in the Palamau District, Bihar and the Associated Iron-Fluorine-Tungsten Skarns and Hornfelses. *Journal of Geological Society of India*, 38.
- Srivastava, S.C., and Ghose, N.C. (1992) Petrology of the highgrade gneisses and granites around Chianki, south of daltonganj, district Palamau, Bihar. *Indian Jour. Geol.*, 64, 122–142.
- Vinogradov, A., Tugarinov, A.L., Zhykov, C., Stapnikova, N., Bibikova, E., and Khorre, K. (1964) Geochronology of Indian Precambrian. In Report of the 22nd International Geological Congress pp. 553–567.

Yadav, B.S., Wanjari, N., Ahmad, T., and Chaturvedi, R. (2016) Geochemistry and petrogenesis of Proterozoic granitic rocks from northern margin of the Chotanagpur Gneissic Complex (CGC). *Journal of Earth System Science*, 125, 1041–1060.

Chapter 3:

Lithology of the area

The study area is located in the eastern margin of the CGGC (well within Domain IB), in and around Massanjore (Fig. 2.1). As discussed in the last chapter, overall, the lithology of CGGC is mainly dominated by a variety of felsic rock units that are deformed and metamorphosed. Resembling most of the CGGC, different types of deformed and metamorphosed granitoids dominate the lithology of the area. The country rock is the migmatitic felsic gneiss. It contains several intrusive (felsic orthogneisses and metamafic dyke) and enclave suites (mafic granulite, metapelite) of rocks. The lithological disposition of the various litho-units is represented in Figure 3.1. The various litho-units and their mutual relation have been described in detail below.

3.1 Country rock of the area:

It is evident from the lithological map (Fig. 3.1) that the migmatitic felsic gneiss is the dominant rock type in the study area. It is a medium to fine grained rock that exhibits prominent gneissic banding (Fig. 3.2.a-b). The gneissic banding constitutes alternate quartz + plagioclase + K-feldspar rich and orthopyroxene + garnet + biotite + amphibole rich layers. Relatively coarse-grained leucosomal segregations are also present along the gneissic banding (Fig. 3.2.c-d). The gneissic banding and leucosomal segregations representing the regional S2 fabric are often folded (Fig. 3.2.b-d) and develop axial planar fabric (S3). The leucosomal segregations are often garnetiferous (Fig. 3.2.d), and these garnets are coarse grained (~0.5-1 cm).

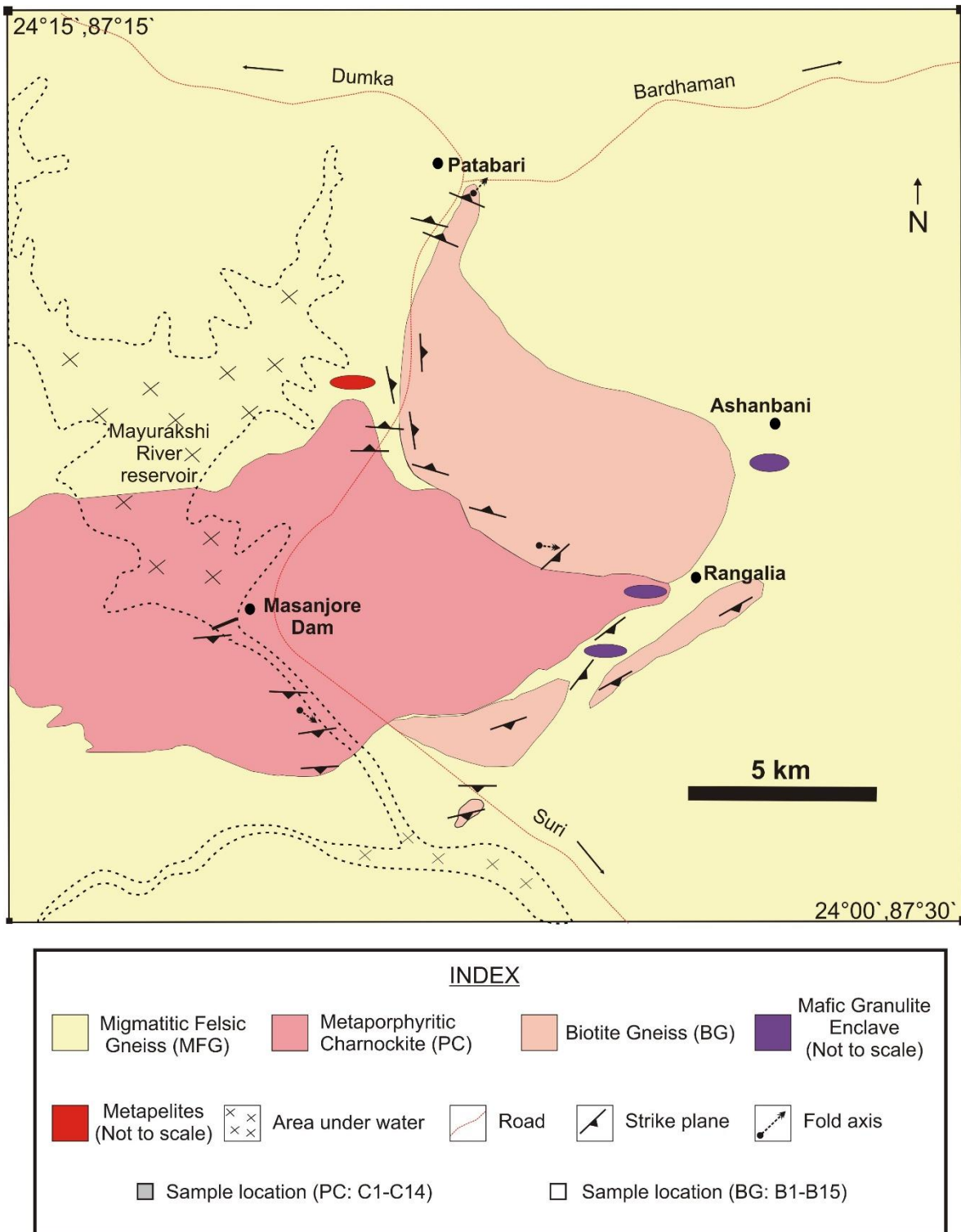


Figure 3.1: (a) Lithological map of the study area showing Masanjore and the adjoining areas adapted and modified after the Geological and mineral map/ district resource map of Dumka district, Jharkhand (Geological Survey of India, year 2009),

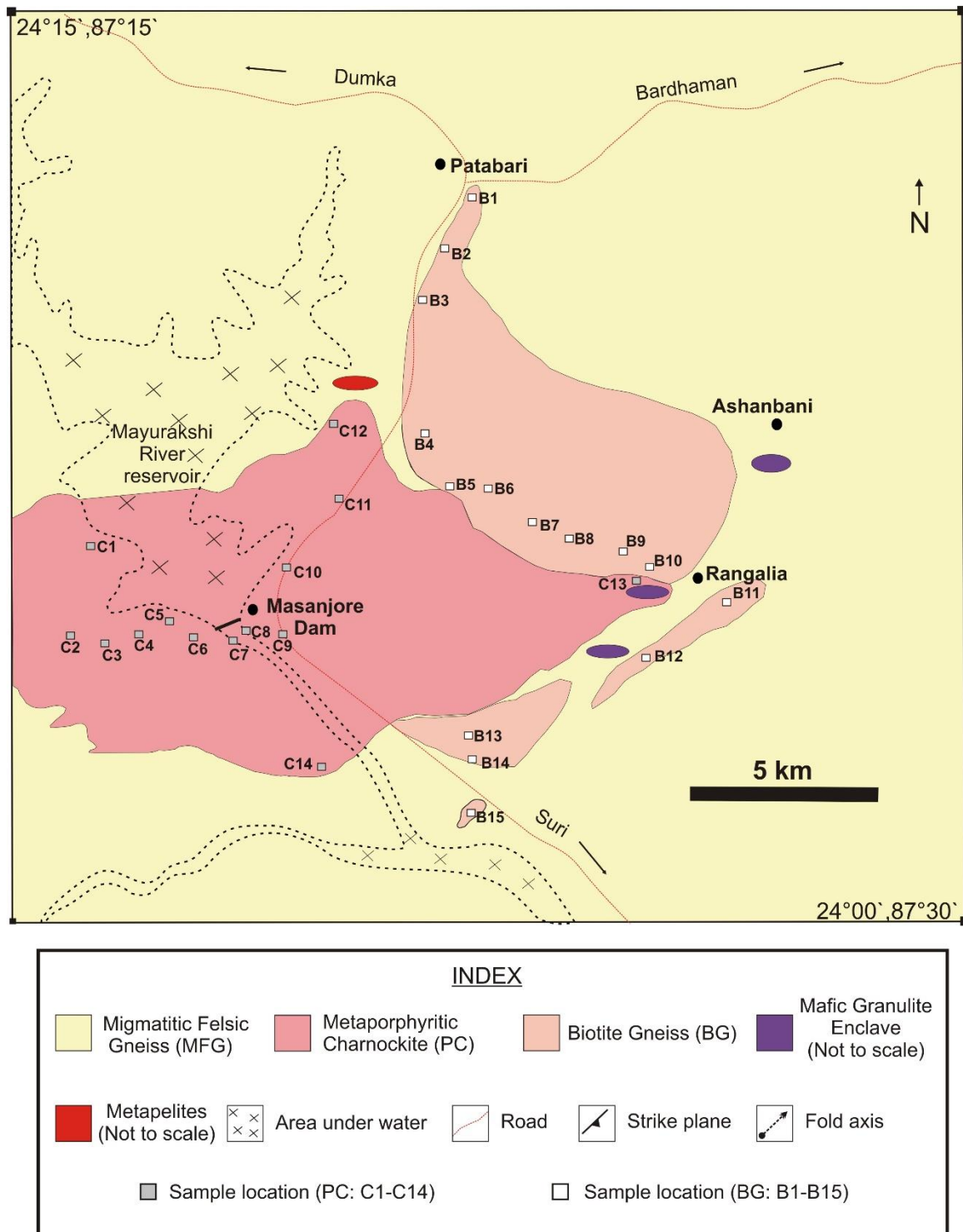


Figure 3.1(continued): (b) Lithological map showing the studied metaporphyrritic charnockite and biotite gneiss sample locations.

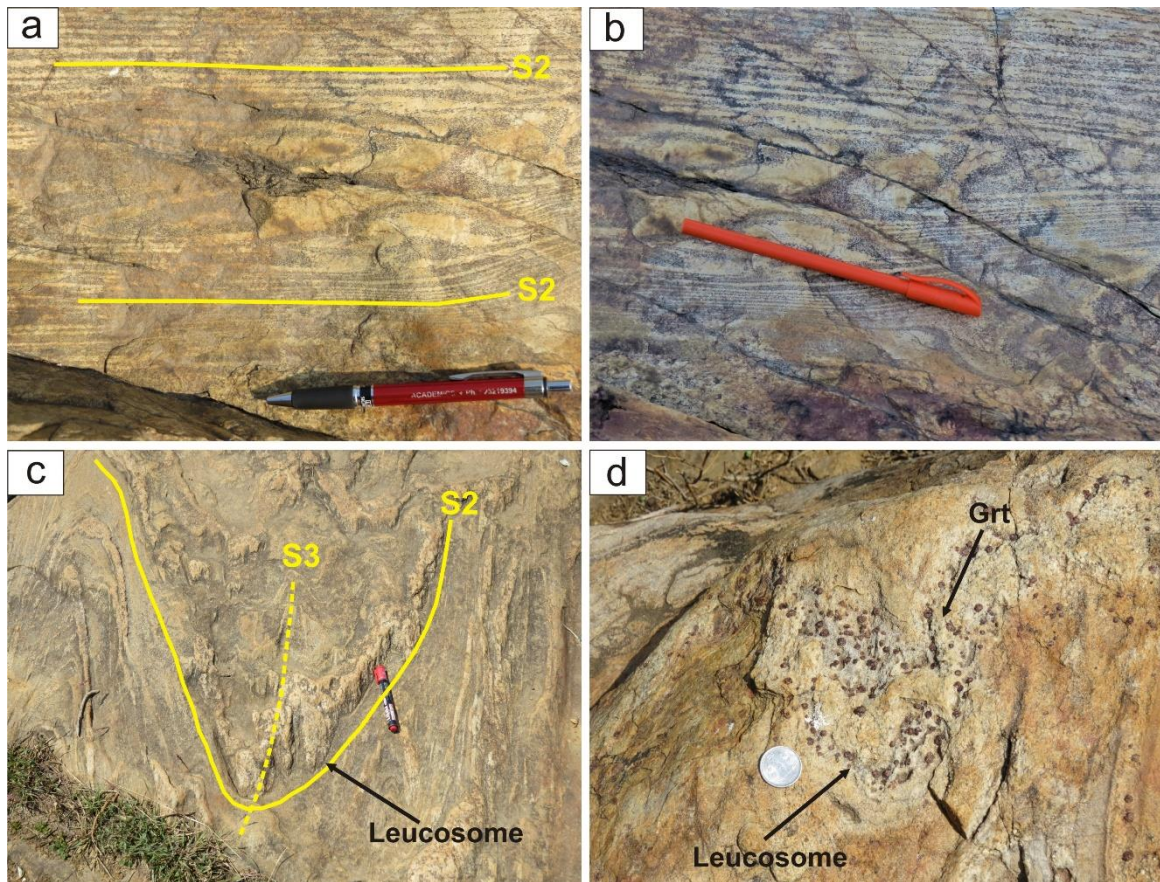


Figure 3.2: (a) The migmatitic felsic gneiss exhibits prominent gneissic banding; it defines the regional S2 foliation. (b) The gneissic banding is folded, defining the F3 folds. (c) Coarse-grained leucosomal segregations along the gneissic banding are folded and develop axial planar fabric S3. (d) The leucosomal segregations often contain coarse-grained garnets (~0.5-1 cm).

3.2 Intrusive felsic orthogneisses:

Metaporphyritic charnockite:

The rock type is predominantly coarse grained, and the porphyritic nature is defined by feldspar (both plagioclase and K-feldspar) embedded in a medium- to fine-grained matrix (Fig. 3.3.a-d). Though both plagioclase and K-feldspar are present, the abundance of plagioclase is undoubtedly more. In some locations, these feldspar grains are deformed (Fig. 3.3.c-d), giving them a proper augen shape. The augen-shaped feldspar grains are oriented along the S2 fabric (3.3.c). Relatively undeformed plagioclase frequently exhibits typical euhedral and lath shapes and a clear, simple twined plane (Fig. 3.3.a-b).

Besides feldspar, orthopyroxene is also observed (Fig. 3.3.d). Though the rock units are deformed and metamorphosed, unlike the host rock, these granitoids do not exhibit any evidence of migmatisation or leucosome formation.

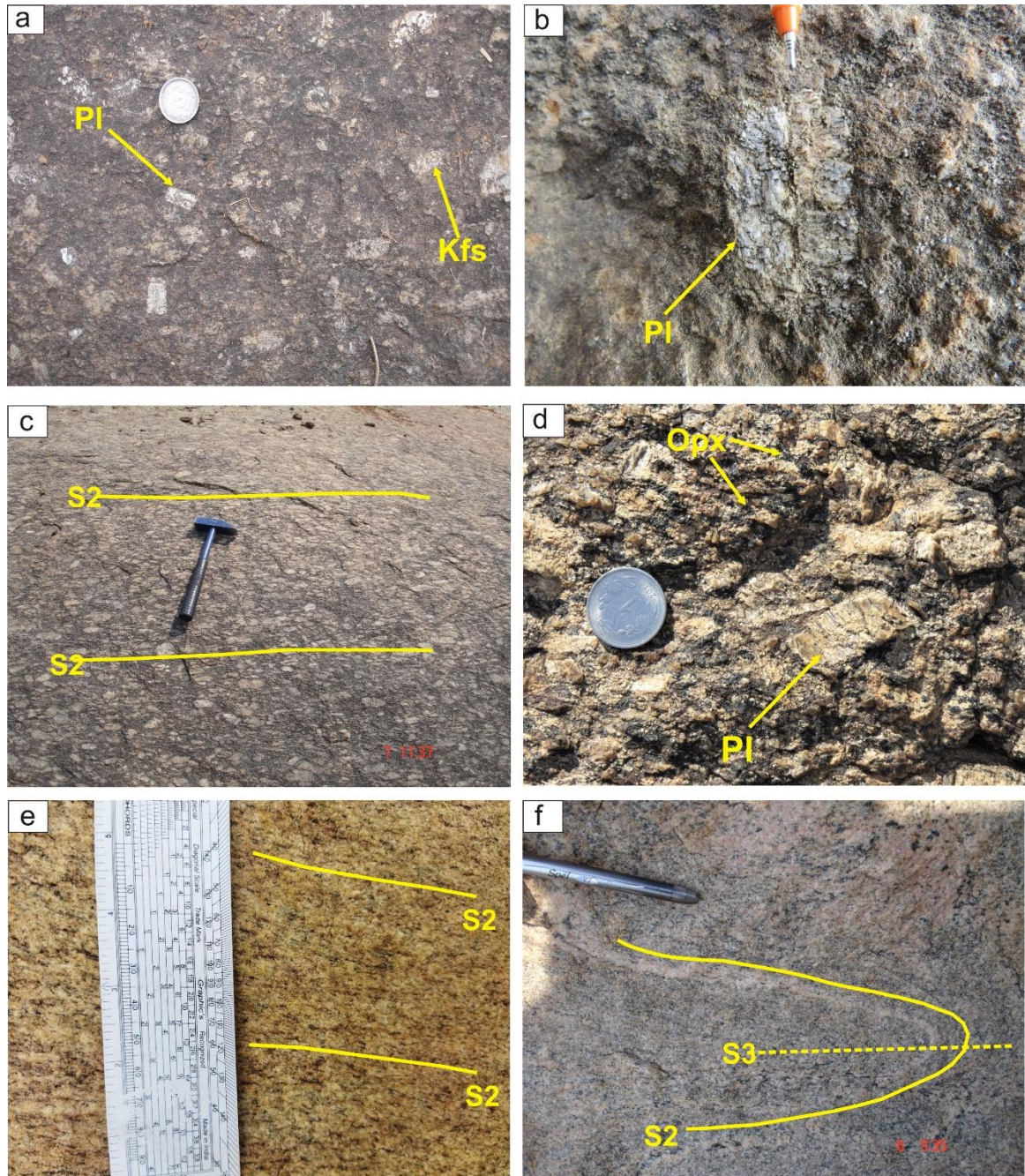


Figure 3.3: (a) Relatively undeformed plagioclase in metaporphyritic charnockite frequently exhibits typical euhedral and lath shapes. (b) Undeformed plagioclase displays clear, simple twinned plane. (c-d) The feldspar grains are deformed, giving them a proper augen shape and feldspar augens are oriented along the S2 fabric; orthopyroxene is also observed. (e) In the biotite gneiss, fine-grained biotites define the foliation (S2) in the rock. (f) The gneissic banding (S2), defined by quartz and biotite-rich layers, is folded, and axial planar fabric (S3) (defined by biotite) develops.

Biotite gneiss:

The biotite gneiss (BG) is fine-grained and more leucocratic compared to the metaporphyratic charnockite (Fig. 3.3.e-f). Fine-grained quartz, K feldspar, plagioclase, biotite and garnet comprise the mineral assemblage of the biotite gneiss. Fine-grained biotites are oriented to define the foliation (S2) in the rock (Fig. 3.3.e). The gneissic banding (S2), defined by quartz and biotite-rich layers, is often folded, and axial planar fabric (S3) develops. S3 foliation is also characterised by biotite.

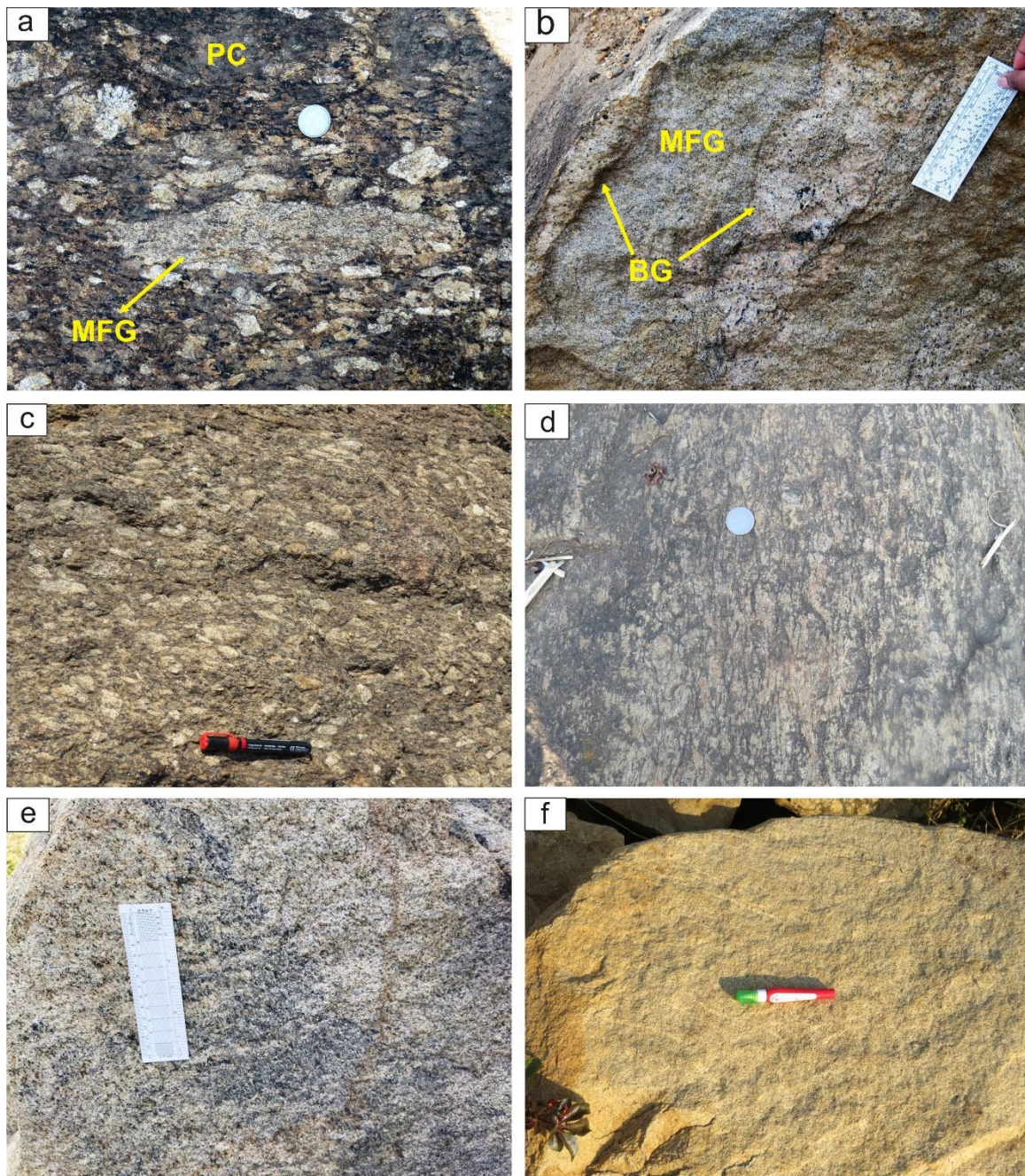


Figure 3.4: (a) Migmatitic felsic gneiss is present as enclaves within metaporphyratic charnockite. (b) Tongs of biotite gneiss intruded within the migmatitic felsic gneiss. (c) Away from the contact (between metaporphyratic charnockite and biotite gneiss), near the core of the charnockitic pluton, the rock is coarse-grained. (d) Near the contact region, the charnockite is comparatively more leucocratic and finer-grained. (e-f) The biotite gneiss near the contact (e) is relatively less leucocratic and coarser-grained than away from the contact (f). MFG: Migmatitic felsic gneiss; BG: Biotite gneiss; PC: Metaporphyratic charnockite.

Lithological relation:

Enclaves of the foliated migmatitic felsic gneiss are present within metaporphyratic charnockite (Fig. 3.4.a), confirming its intrusive nature within the country. Similarly, biotite gneiss intrudes within the gneissic country rock, as evidenced by tongs of biotite gneiss within the migmatitic felsic gneiss (Fig. 3.4.b). According to the field disposition and lithological mapping, biotite gneiss is present along the boundary of metaporphyratic charnockite, and they share a contact (Fig. 3.1). Near the contact region, the charnockite is comparatively more leucocratic and finer-grained (Fig. 3.4.d) than away from the contact, (near the core of the charnockitic pluton; Fig. 3.4.c). On the other hand, the biotite gneiss near the contact (Fig. 3.4.e) is comparatively less leucocratic and coarser-grained than away from the contact (Fig. 3.4.f). The gradual change of both granitoids represents a gradational contact between the two.

3.3 Enclave suite of rocks

Mafic granulite:

The mafic granulite in the studied area occurs as pods and lenses of different dimensions within both metaporphyratic charnockite and migmatitic felsic gneiss. The latter rocks contain rafts of the mafic granulites of different dimensions (Fig. 3.5.b-c). The pervasive foliation of these felsic orthogneisses swerved around the mafic granulite rafts (Fig. 3.5.b). The mafic granulite enclave has an internal fabric (S1) that is abruptly truncated against the foliation (S2) of the felsic orthogneiss (Fig. 3.5.c). Based on mineralogy and structure, the rock is divided into two major components: melanosome and leucosome. The melanocratic matrix comprises medium to coarse-grained aggregates of pyroxene, plagioclase and garnets (~1-2 cm) (Fig. 3.5.a). The leucosomes of variable size, shape and mineralogy occur as continuous and discontinuous layers and pods of varying thickness.

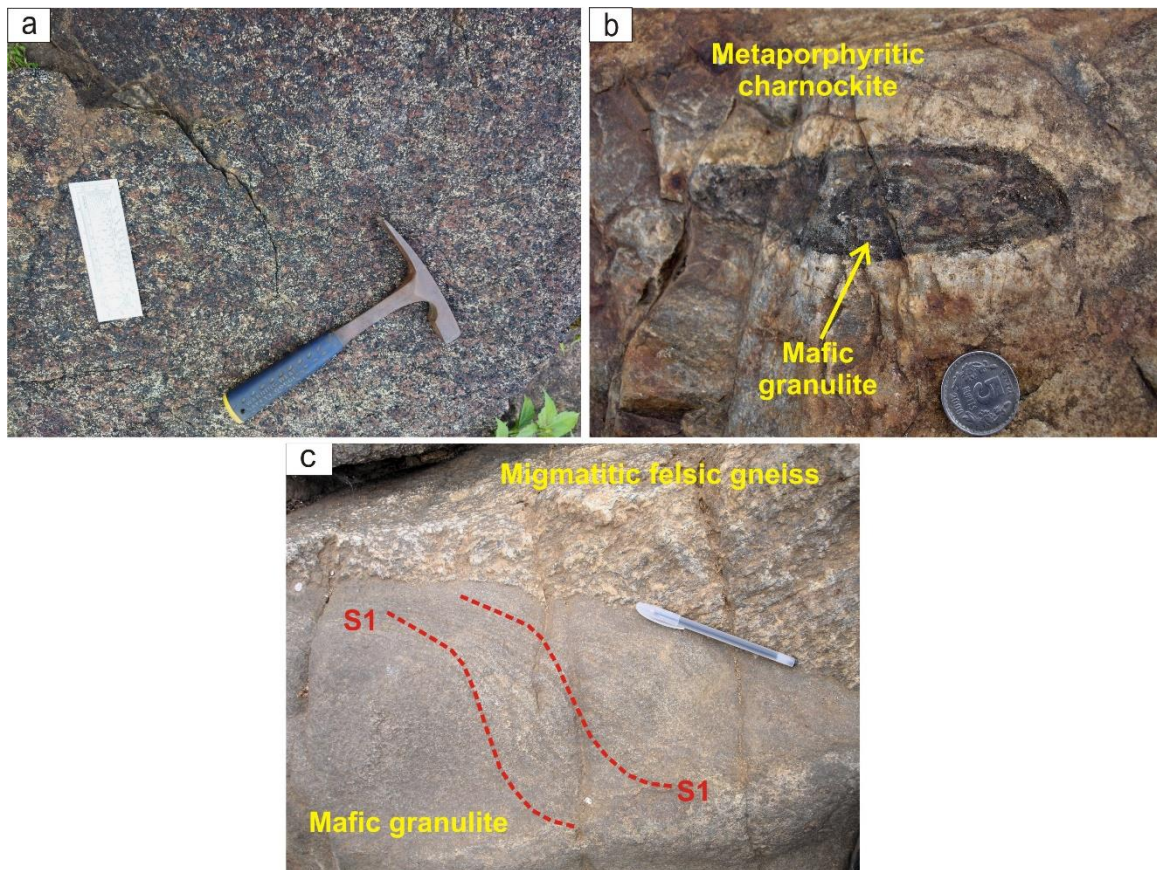


Figure 3.5: (a) The melanocratic matrix of the mafic granulite comprises medium to coarse-grained aggregates of pyroxene, plagioclase and garnets. (b) The mafic granulite is present as an enclave within the metaporphyritic charnockite, and the pervasive foliation (S2) swerves around the mafic granulite rafts. (c) The mafic granulite enclave has an internal fabric (S1) that is discordant with the foliation of the enclosing felsic orthogneiss the foliation (S2) specially at the centre of the enclaves, while at the margin, it has transposed along the host gneiss foliation.

Based on field features, four types of leucosomes are identified. Type I leucosomes show small (~1 cm) patches, commonly around large (1-2 cm) euhedral to subhedral garnet porphyroblasts (Fig. 3.6.a). These leucosomal patches are elongated (Fig. 3.6.b) and grades to thin, discontinuous stringers to continuous leucosome layers that define foliation (Fig. 3.6.c-d). These leucosomal segregations are often relatively thicker and contain large eu- to subhedral garnets (Fig. 3.6.e-f). Type II leucosomes are thin, contain rare garnet and form a network around small patches of the melanocratic matrix that interconnects thin leucosomal layers of Type I (Fig. 3.7.a-b). The Type III leucosomes resemble the Type I as they form leucosomal bands parallel to foliation and leucosomal pods. However, relative to Type I, the Type III leucosomes are distinctly

thicker but are devoid of large grains of garnet (Fig. 3.7.c-d). Compared to Type I, the leucosomal pods are larger in size and are not associated with garnet grains. Type IV leucosome form laterally continuous (~1-2 meters) veins within the melanosome (Fig.

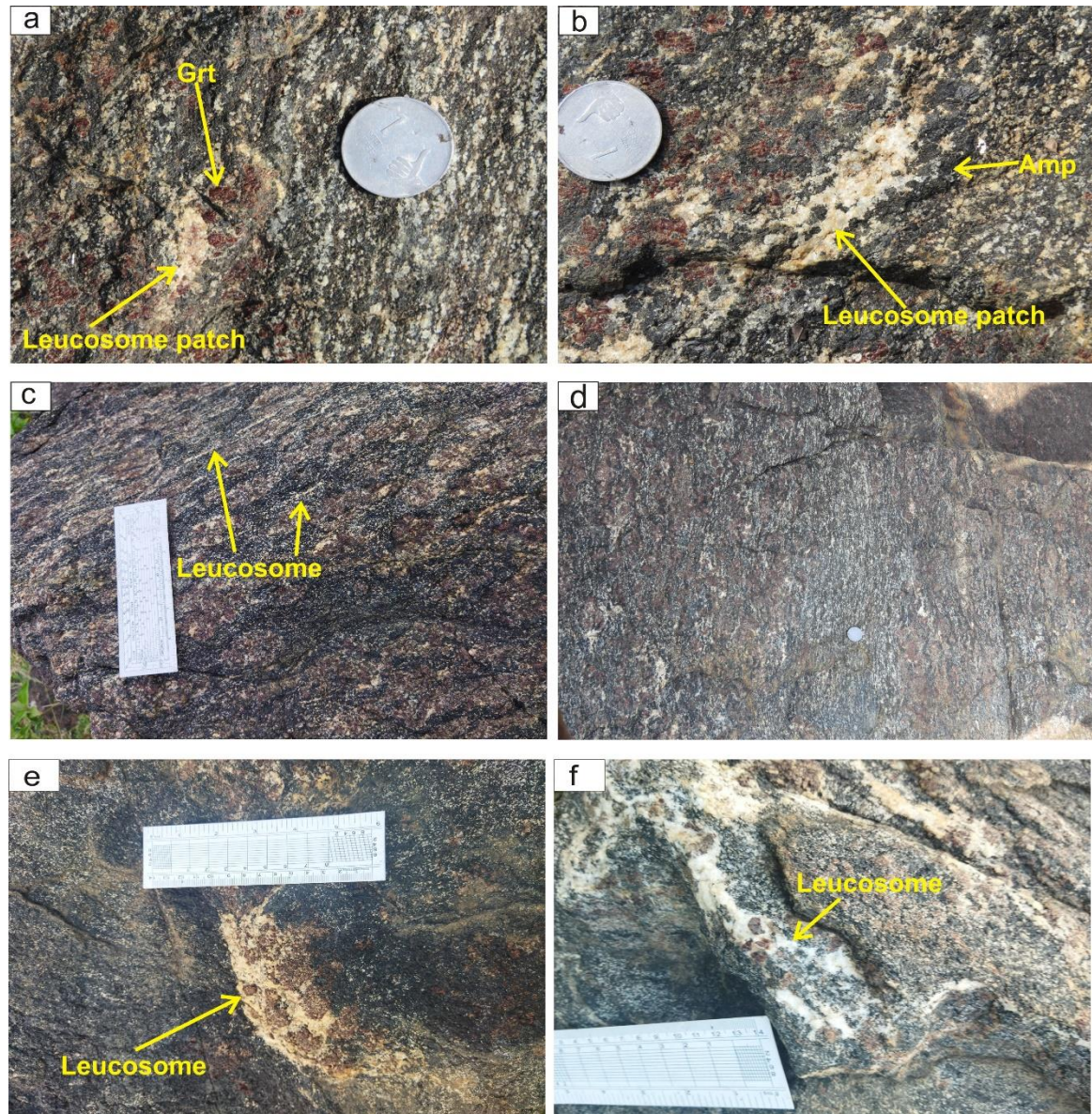


Figure 3.6: (a) Type I leucosomes of the mafic granulite show small (~1 cm) patches, commonly around large (1-2 cm) euhedral to subhedral garnet porphyroblasts. (b-d) The leucosomal patches are elongated (b) and grade to thin, discontinuous stringers (c) to continuous leucosome layers that define foliation (d). (e-f) The leucosomal segregations are often relatively thicker and contain large eu- to subhedral garnets.

3.8.a) and are rich in garnet. Locally, the abundance of garnet reaches up to ~40 vol%. In the central part, these garnet grains are mostly euhedral to subhedral in shape, whereas garnet is elongated along the margin of the veins and makes a high angle with the vein wall

(Fig. 3.8.b). Though these veins are ~2-3 cm thick, at places these are relatively thicker (~3-6 cm).

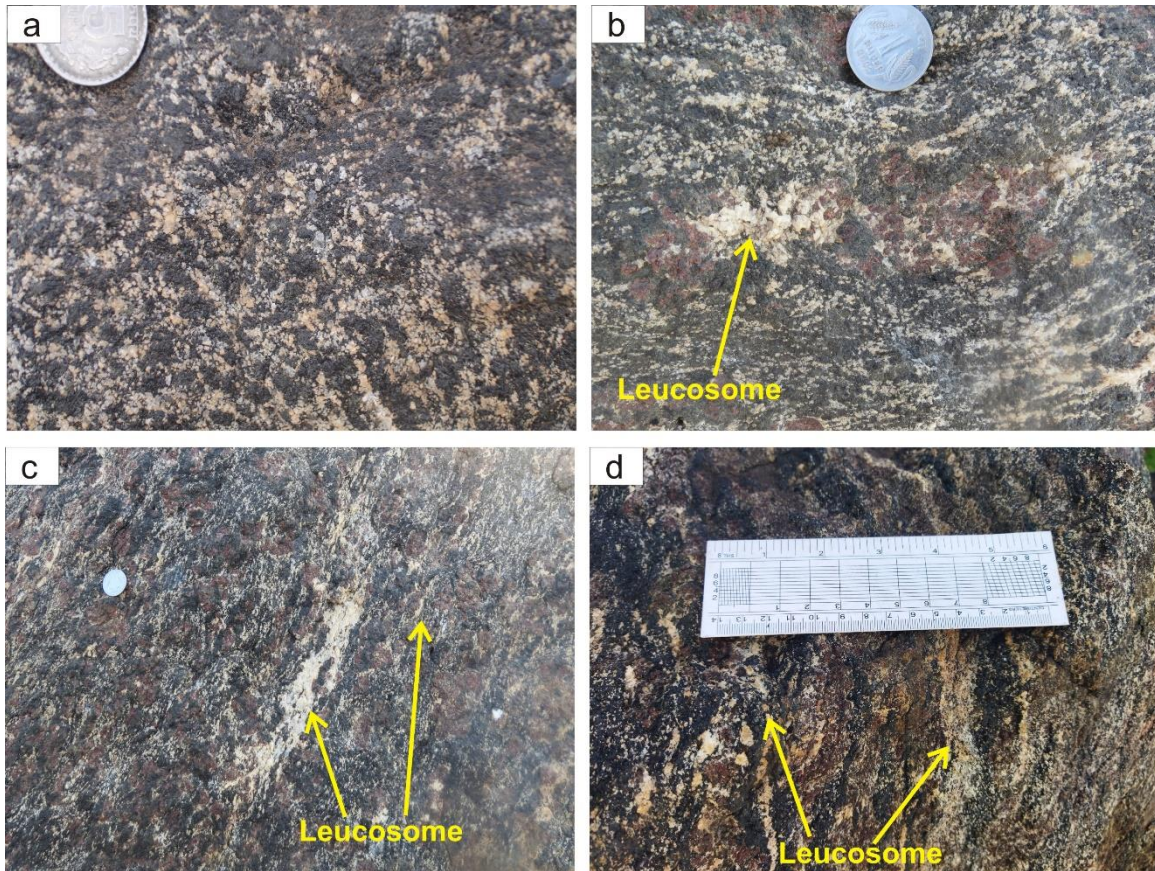


Figure 3.7: (a) Type II leucosomes are thin and form a network around small patches of the melanocratic matrix (b) These networks interconnect thin leucosomal layers of Type I. (c-d) The Type III leucosomes form leucosomal bands parallel to foliation (c) and leucosomal pods (d), but relative to Type I, the Type III leucosomes are distinctly thicker but are devoid of large grains of garnet.

Leucosomal segregations are commonly separated from the melanosome matrix by coarse-grained amphibole selvage (Fig.3.8.a-d). Locally, the amphibole-rich selvages thicken and nearly completely replace the leucosomes (Fig.3.8.c-d). In amphibole-rich domains, coarse garnet megacrysts are often rimmed by thick rind or occur as skeletal grains within the coarse aggregates of haphazardly oriented amphibole (Fig. 3.8.e-f). A thin rind of plagioclase often separates the skeletal garnet from amphibole (Fig. 3.8.f). Owing

to the extensive development of amphibole, the exact proportion of leucosomes could not be measured.

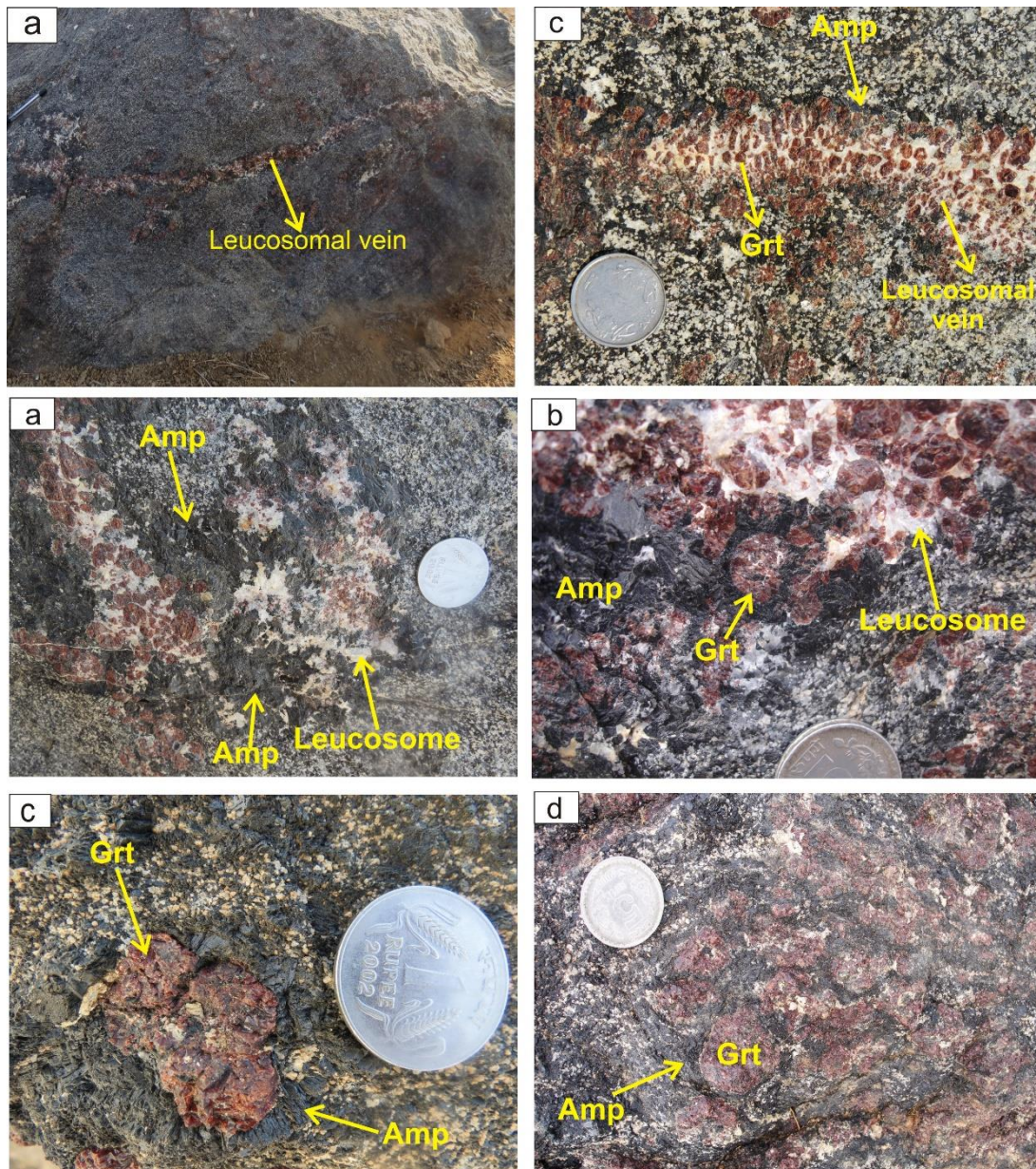


Figure 3.8: (a) Type IV leucosome form laterally continuous (~1-2 meters) veins that are rich in garnet. (b) In the central part of Type IV leucosomal veins, garnet grains are mostly euhedral to subhedral in shape, whereas garnet is elongated along the margin of the veins and makes a high angle with the vein wall. The amphibole-rich selvages separate the leucosomal veins from melanosome. (c-d) The amphibole-rich selvages nearly completely replace the leucosomes along the boundary. (e-f) In amphibole-rich domains, coarse garnet megacrysts are rimmed by thick rind of amphibole (e) and occur as skeletal grains within the coarse aggregates of haphazardly oriented amphibole (f).

Metapelites:

The metapelitic enclave comprises two different varieties. One variety is fine-grained, where the fabric of the metapelite is defined by biotite (Fig. 3.9.a-b). It contains coarse-grained (~1-2 cm) garnet. These coarse grained garnets are rimmed by leucosomal segregation (Fig. 3.9.a). Stromatic leucosomal bands of variable thickness are present along the foliation and also cut the foliation at a low angle (Fig. 3.9.b). These stromatic leucosomal bands often contain coarse grained garnets or clusters of garnets (Fig. 3.9.b). Apart from garnet, these stromatic bands include biotite and are often rimmed by a thin selvage of biotite (Fig. 3.9.b). The other variety of metapelite is present as isolated ground-level exposures (Fig. 3.9.c-d). These metapelitic units exhibit relatively coarser grain sizes and are more melanocratic than the other variety. These are devoid of leucosomal segregation. These metapelites constitute fine-grained garnet and cordierite. The rock comprises alternate quartzofeldspathic rich and garnet, biotite cordierite rich layers demonstrating the nature of gneissic banding (Fig. 3.9.c). Though gneissic bandings are present, these are often laterally impersistent and fused (Fig. 3.9.d).

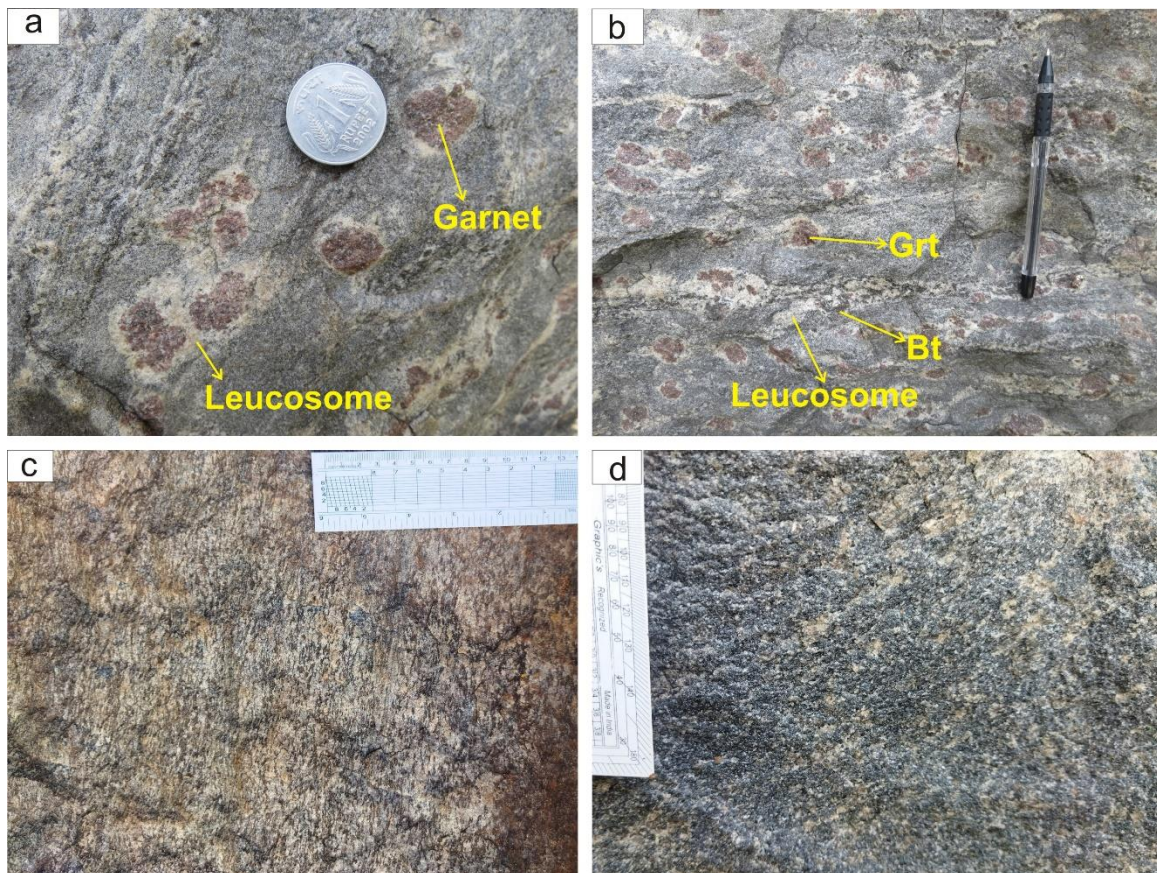


Figure 3.9: (a) The metapelitic enclave is fine-grained, and the fabric of the metapelite is defined by biotite; coarse-grained (~1-2 cm) garnet are rimmed by leucosomal segregation. (b) Stromatic leucosomal bands of variable thickness are present along the foliation and also cut the foliation at a low angle. The stromatic leucosomal bands often contain coarse grained garnets. A thin selvage of biotite rims the stromatic bands; biotite is also present within the leucosomes. (c) The metapelitic units exhibit relatively coarser grain sizes than the migmatite variety, and they comprise alternate quartzofeldspathic rich and garnet, biotite cordierite rich layers demonstrating the nature of gneissic banding. (d) The gneissic bandings are laterally impersistent and fused.

3.4 Intrusive metamafic dykes:

This is a fine-grained mafic rock that intrudes within the felsic litho units as dyke (Fig. 3.10.a). The thickness of these metamafic dykes varies from a few cm to tens of cm. It is also present as ground-level mounds. Metamafic dyke in the felsic orthogneisses is often folded and develops axial planar foliation (S3; Fig. 3.10.b). The metamafic dykes are deformed, stretched, and often pinch out, resulting in “pinch and swell” structure (Fig. 3.10.c-d).

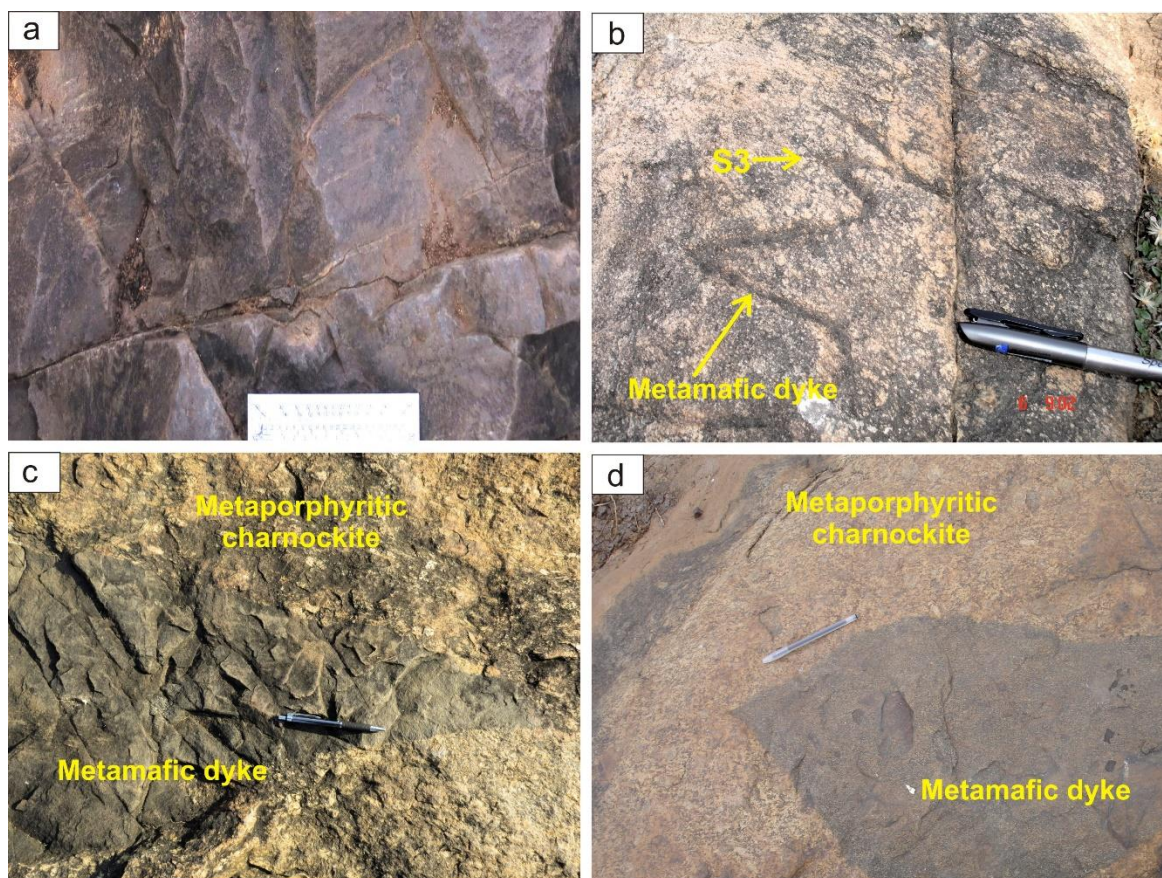


Figure 3.10: (a) The metamafic dyke is fine-grained mafic rock. (b) The metamafic dyke intrudes within the felsic litho units and is often folded and develops axial planar foliation S3. (c-d) The metamafic dykes are deformed, stretched, and often pinch out, resulting in “pinch and swell” structure. The intruding metamafic dykes cut the existing S2 fabric of the metaporphyrritic charnockite (c).

3.5 Structural relations:

Detailed field works suggest multiple deformational events suffered by the lithounits of the study area. A total of four major deformational events (D1-D4) are evident from field observations.

The mafic granulite enclaves preserve the earliest deformation fabric (S1; Fig.3.5.c). The S1 fabric is discordant with the foliation of the enclosing felsic orthogneiss, specially at the centre of the enclaves, while at the margin, it has been transposed along the host gneiss foliation (Fig.3.5.c). The foliation of the felsic orthogneiss swerves around the mafic granulite enclaves, indicating that the foliation within the mafic granulite is older (Fig.3.5.b).

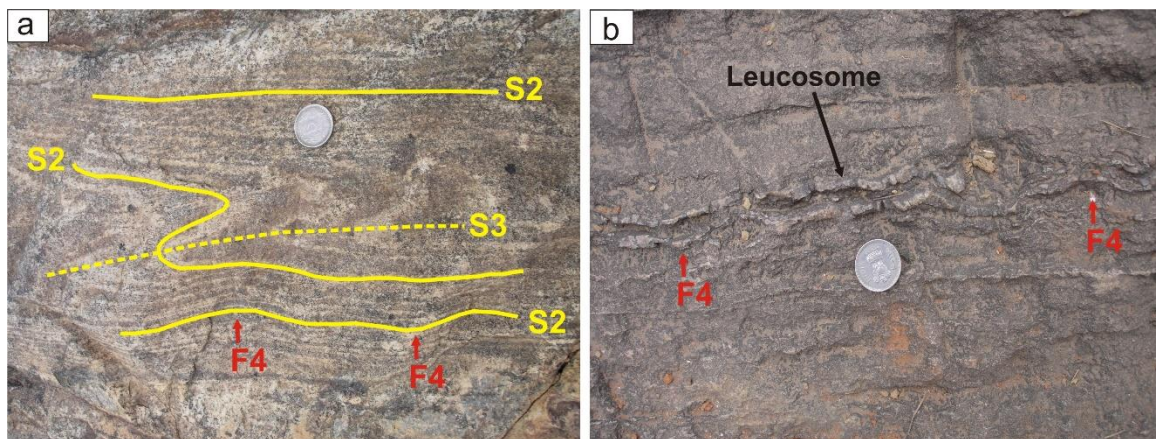


Figure 3.11: (a) The axial plane of S3 foliation is parallel to S2 gneissic banding and the last deformation (D4) is demarcated by open folds (F4) observed on the limbs of F3 folds. (b) F4 folds on the leucosomal segregations of the migmatitic felsic gneiss.

The foliation within the felsic orthogneisses formed subsequently during younger (D2) deformation. The fabric (S2) corresponding to D2 is persistent in all the felsic orthogneisses. In the migmatitic felsic gneiss, the S2 foliation is defined by gneissic banding and leucosomal segregations (Fig.3.2.a-c), while in the metaporphyrritic

charnockite, it is characterised by augen-shaped feldspar grains (Fig.3.3.c). In the biotite gneiss, it is manifested by alternate biotite-rich and quart-rich gneissic banding (Fig.3.3.e-f). The general strike of S2 is E-W (Fig. 3.1). However, the strike varies on the regional scale, from NE-SW to even almost N-S trends. S2 foliations are steeply dipping, with the dip amount varying between 75°-85°. In some regions, the foliations are almost vertical.

The folding of the S2 fabric (Fig. 3.2.b-c; 3.3.f; 3.11.a) marks the third deformational event (D3). It is the last major deformational event. The folding of S2 formed axial planar foliation S3 (Fig. 3.2.c; 3.3.f; 3.11.a). The axial plane of S3 foliation is parallel to S2 gneissic banding (Fig. 3.11.a). The metamafic dyke intrudes the felsic orthogneiss locally cross-cutting the S2 fabric, indicating its post-D2 emplacement (Fig. 3.10.c). The metamafic dykes are further folded along with the S2 fabric and also exhibit S3 axial planar fabric (Fig. 3.10.b). The S3 fold axis trends mostly eastward and are moderately plunging (37°→110°; 44°→100°).

The last deformation (D4) is demarcated by open folds (F4) observed on the limbs of F3 folds (Fig. 3.11.a-b). The F4 fold axis plunges towards the south (25°→180°; 65°→200°) and plunges moderately. F4 fold does not form any axial planar fabric.

Chapter 4

Magmatic petrogenesis and metamorphic evolution of the migmatitic felsic gneiss

Obtaining knowledge about the petrogenetic history of the felsic country rock is vital in understanding the crustal evolution of the study area. The migmatitic felsic gneiss (MFG) is deformed and metamorphosed and hosts other dominant felsic litho units in the area. This study aims to evaluate the metamorphic evolution and understand its protolith's petrogenetic history. Migmatitic felsic gneiss is geochemically characterised using bulk rock major and trace element data. With the help of detailed petrography, mineral chemistry and phase equilibria modelling, the metamorphic conditions of the studied rocks are evaluated.

4.1 Petrography:

The rock is fine to medium-grained, characterised by prominent gneissic banding, leucosomal patches, and bands. The phase assemblage of the studied rock unit mainly comprises quartz, K-feldspar, plagioclase, garnet, orthopyroxene, biotite and amphibole. Apart from these minor amount of ilmenite is present along with accessory phases like zircon, and apatite. The gneissic banding of the felsic orthogneiss is characterised by alternate quartz, feldspar-rich and ferromagnesian phase-rich bands (Fig. 4.1.a).

The quartzo-feldspathic layer comprising plagioclase, K-feldspar, and quartz forms a polygonal recrystallised matrix (Fig. 4.1.f). The abundance of plagioclase in the fine-grained quartzo-feldspathic band is comparatively less than K-feldspar. Plagioclase is often

deformed and exhibits wedge-shaped deformation twinning. Garnets present in the gneissic banding are fine-grained subhedral to anhedral (Fig. 4.1.a-c). Inclusions of biotite,

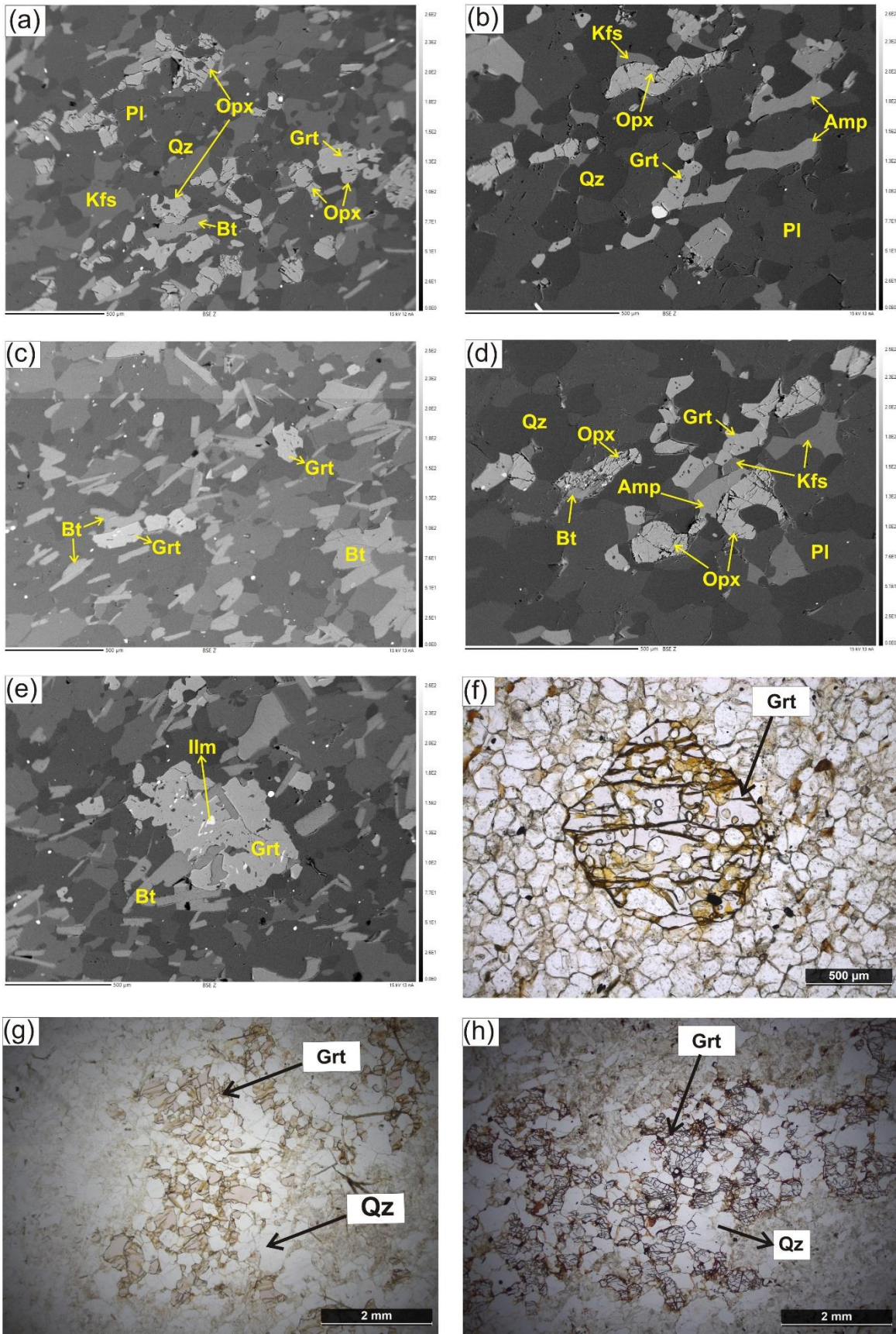


Figure 4.1: (a) The gneissic banding is characterised by alternate quartz, feldspar-rich and ferromagnesian phase-rich bands. (b) Orthopyroxene with garnet in the gneissic banding is deformed, elongated and oriented. Amphibole is also oriented and elongated. (c) Biotite flakes are highly oriented along the gneissic banding. Garnet contains very fine inclusion of Bt and Pl. (d) Both Amp and Bt are replacing Opx. (e) Biotite replaces garnet, and ilmenite inclusion is present in the garnet. (f) Ovoid-shaped coarse poikiloblastic garnets in quartzo-feldspathic recrystallised matrix contain quartz and alkali feldspar as inclusions. (g) Coarse-grained quartzo-feldspathic material surrounds skeletal garnet in leucosomal patches. (h) Leucosomal bands with coarse-grained skeletal garnet. Mineral abbreviations are after Whitney and Evans (2010).

plagioclase and ilmenite are present in garnet (Fig. 4.1.b; e). Orthopyroxene with garnet in the gneissic banding is deformed, elongated and oriented (Fig. 4.1.b).

Amphibole and biotite are present as hydrous phases in the rock matrix. Biotite flakes are highly oriented along the gneissic banding (Fig. 4.1.c). Amphibole is also oriented (Fig. 4.1.b). These hydrous phases are replacing both orthopyroxene and garnet (Fig. 4.1.d-e).

In the medium to fine-grained recrystallised matrix, comparatively coarse-grained quartzo-feldspathic patches and bands are often present (Fig. 4.1.f-g). These coarse-grained patches often contain garnet. Ovoid-shaped coarse poikiloblastic garnets in quartzo-feldspathic matrix contain quartz and alkali feldspar as inclusions (Fig. 4.1.f). Coarse grained quartzo-feldspathic material often surrounds these garnets. Skeletal garnet is also present along with quartz and k-feldspar within coarse-grained leucosomal patches and bands (Fig. 4.1.g-h).

4.2 Mineral chemistry:

Analytical procedure:

The CAMECA Sx Five Electron Probe Micro Analyser is used to obtain the phase composition of the studied felsic gneiss at the Geological Survey of India, Kolkata. All points were analysed with 15 kV acceleration voltage, 12 nA beam current and a beam size of 1 μm . Standards taken during analysis were natural minerals. Fe^{3+} is estimated using the cation recalculation scheme of Droop (1987). Amphibole cation recalculation is performed using the classification scheme of Leake et al. (1997). Mineral abbreviations

used in phase chemistry, and the following sections are after Whitney and Evans (2010). Phase chemistry data are presented in Table 4.1-7.

Garnet:

Representative garnet compositions are given in Table 4.1. Garnet composition ($\text{Alm}_{62-66}\text{Prp}_{6-8}\text{Grs}_{21-23}\text{Sps}_{6-8}$; $X_{\text{Mg}} = 0.09-0.11$) in the migmatitic felsic gneiss is mainly dominated by the almandine component. Garnet composition does not show any distinct core rim variation of composition.

Feldspar:

Both plagioclase and alkali feldspar are present in the rock. Table 4.2 (plagioclase) and 4.3 (K-feldspar) present the representative phase compositions. Plagioclase composition ($\text{An}_{24-30}\text{Ab}_{69-75}\text{Or}_{0-1}$) mainly concentrates

in the oligoclase field (Fig. 4.2.a). Alkali feldspar is dominated by the orthoclase component (88-95%). Mesoperthite exsolution lamellae has a 94-95% albite content, while in the host, albite content is 9-10%.

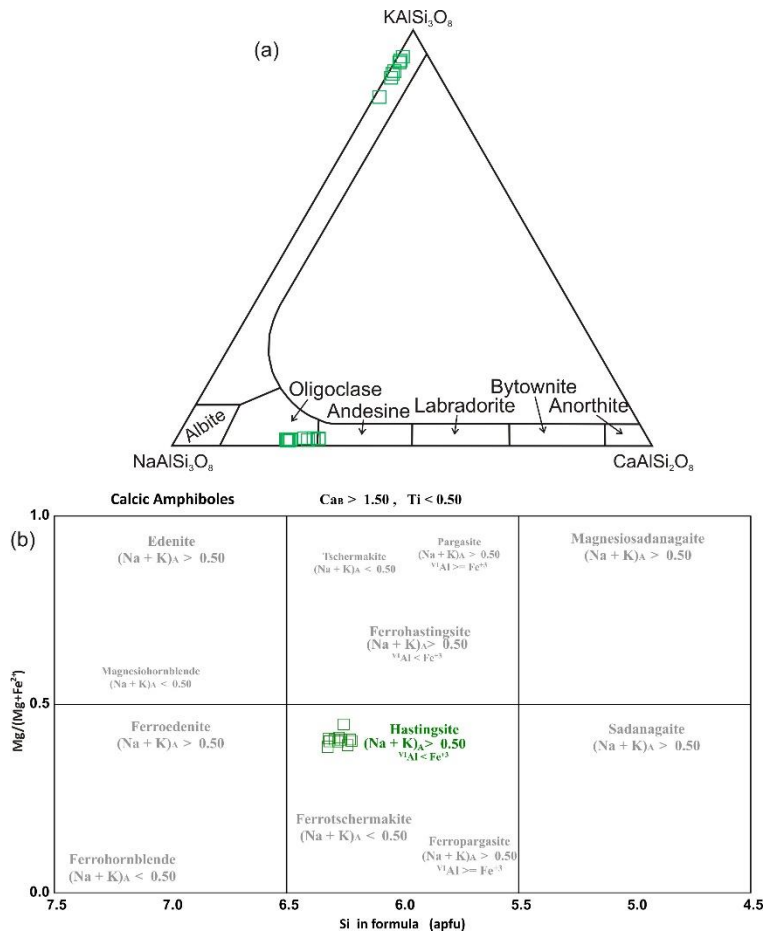


Figure 4.2: (a) Ternary feldspar diagram depicting feldspar composition of the migmatitic felsic gneiss. Plagioclase composition plots in the oligoclase field. (b) Amphibole compositions plot in hestingsite field in the amphibole classification diagram (Leake et al. 1997).

Table 4.1: Representative microprobe analyses of garnet and cation calculations based on 12 oxygens (oxide data given as wt%)

Point No.	1 / 1 .	2 / 1 .	11 / 1 .	34 / 1 .	39 / 1 .	43 / 1 .	56 / 1 .	53 / 1 .	65 / 1 .	71 / 1 .
Texture	rim	core	core	rim	core	rim	core	rim	core	rim
SiO ₂	35.94	35.81	36.46	36.79	36.22	36.05	35.60	36.08	35.68	36.32
TiO ₂	<d.l.	<d.l.	<d.l.	<d.l.	<d.l.	0.03	<d.l.	<d.l.	<d.l.	<d.l.
Al ₂ O ₃	20.69	20.20	20.77	20.70	20.93	20.45	20.56	21.31	20.53	20.33
Cr ₂ O ₃	0.03	<d.l.	0.01	<d.l.	<d.l.	<d.l.	<d.l.	<d.l.	<d.l.	<d.l.
FeO	30.83	30.87	30.37	30.11	29.67	30.44	30.74	30.77	30.76	30.41
MgO	1.65	1.61	1.65	1.74	1.78	1.80	1.83	1.82	1.82	1.62
CaO	7.14	7.17	7.53	7.73	7.73	7.33	7.17	7.12	7.33	7.33
MnO	2.46	3.20	2.61	2.95	2.63	2.82	2.81	2.94	2.54	2.77
Na ₂ O	<d.l.	0.02	<d.l.	0.05	0.01	0.06	0.01	<d.l.	<d.l.	0.00
K ₂ O	0.01	<d.l.	<d.l.	<d.l.	<d.l.	0.01	<d.l.	0.01	<d.l.	0.00
Total	98.8	99.0	99.6	100.1	99.0	99.0	98.7	100.18	98.77	98.91
Si	2.92	2.91	2.94	2.95	2.93	2.92	2.90	2.89	2.90	2.95
Ti	0.00	0.00	0.00	0.00	0.00	0.00	0.00	0.00	0.00	0.00
Al	1.98	1.94	1.97	1.95	1.99	1.95	1.97	2.01	1.97	1.95
Cr	0.00	0.00	0.00	0.00	0.00	0.00	0.00	0.00	0.00	0.00
Fe ⁺³	0.16	0.22	0.13	0.15	0.14	0.20	0.24	0.20	0.22	0.12
Fe ⁺²	1.94	1.88	1.92	1.87	1.87	1.86	1.85	1.86	1.87	1.94
Mg	0.20	0.20	0.20	0.21	0.21	0.22	0.22	0.22	0.22	0.20
Ca	0.62	0.62	0.65	0.66	0.67	0.64	0.62	0.61	0.64	0.64
Mn	0.17	0.22	0.18	0.20	0.18	0.19	0.19	0.20	0.17	0.19
Na	0.00	0.00	0.00	0.01	0.00	0.01	0.00	0.00	0.00	0.00
K	0.00	0.00	0.00	0.00	0.00	0.00	0.00	0.00	0.00	0.00
Total	8.00	8.00	8.00	8.00	8.00	8.00	8.00	8.00	8.00	8.00
X _{Alm}	0.66	0.64	0.65	0.63	0.63	0.64	0.64	0.64	0.64	0.65
X _{Py}	0.07	0.07	0.07	0.07	0.07	0.07	0.08	0.08	0.08	0.07
X _{Grs}	0.21	0.21	0.22	0.23	0.23	0.22	0.22	0.21	0.22	0.22
X _{Sps}	0.06	0.08	0.06	0.07	0.06	0.07	0.07	0.07	0.06	0.06
X _{Mg}	0.09	0.09	0.09	0.10	0.10	0.10	0.11	0.10	0.11	0.09

<d.l.: Below detection limit; not included in total

* Fe³⁺ recalculated according to the scheme of Droop (1987)**Orthopyroxene:**

The representative Opx compositions are presented in Table 4.4. Orthopyroxene shows an X_{Mg} value of 0.44-0.46. Opx does no distinct compositional variation between the core and rim.

Amphibole:

According to the classification scheme of Leake et al. (1997), amphibole belongs to the calcic group and plots in the hestingsite domain (Table 4.5; Fig. 4.2.b). Amp has an X_{Mg} between 0.38-0.44. Amphibole has TiO₂ content ranging between 4.19-4.95 wt%.

Biotite:

Representative biotite compositions are presented in Table 4.6. Biotite has an X_{Mg} value ranging between 0.41 to 0.51. Biotite present as inclusion in garnet is more magnesian (X_{Mg} = 0.55-0.61) than matrix biotite. TiO_2 content of biotite is between 4.19-4.95 wt%.

Apart from these ilmenite composition is also presented (Table 4.7).

Table 4.2: Representative microprobe analyses of plagioclase and cation calculations based on 8 oxygens (oxide data given as wt%)

Point No.	9 / 1.	17 / 1.	29 / 1.	73 / 1.	107 / 1.	8 / 1.	22 / 1.	37 / 1.	75 / 1.	102 / 1.
Texture	core					rim				
SiO ₂	59.99	61.40	60.14	58.95	61.25	60.11	59.29	60.61	60.45	62.12
TiO ₂	0.02	<d.l.	<d.l.	<d.l.	0.02	<d.l.	<d.l.	<d.l.	<d.l.	<d.l.
Al ₂ O ₃	23.91	23.99	24.39	23.91	22.31	23.95	24.30	23.70	24.22	22.66
Cr ₂ O ₃	<d.l.	<d.l.	<d.l.	0.01	<d.l.	0.01	<d.l.	<d.l.	<d.l.	<d.l.
FeO	0.07	0.11	0.16	0.22	0.16	0.28	0.35	0.15	0.22	0.25
MgO	<d.l.	<d.l.	<d.l.	<d.l.	<d.l.	<d.l.	<d.l.	0.01	0.01	<d.l.
CaO	5.68	5.78	6.28	6.02	5.17	6.14	6.28	5.56	5.77	5.24
MnO	<d.l.	<d.l.	<d.l.	0.06	0.05	<d.l.	<d.l.	<d.l.	<d.l.	<d.l.
Na ₂ O	8.43	8.38	8.05	8.29	8.94	8.17	8.21	8.69	8.30	8.84
K ₂ O	0.24	0.26	0.19	0.12	0.11	0.21	0.17	0.23	0.21	0.10
Total	98.51	100.04	99.33	97.72	98.08	99.05	98.74	99.03	99.36	99.21
Si	2.71	2.73	2.70	2.69	2.78	2.71	2.68	2.73	2.71	2.78
Ti	0.00	0.00	0.00	0.00	0.00	0.00	0.00	0.00	0.00	0.00
Al	1.27	1.26	1.29	1.29	1.19	1.27	1.30	1.26	1.28	1.20
Cr	0.00	0.00	0.00	0.00	0.00	0.00	0.00	0.00	0.00	0.00
Fe ⁺²	0.00	0.00	0.01	0.01	0.01	0.01	0.01	0.01	0.01	0.01
Mg	0.00	0.00	0.00	0.00	0.00	0.00	0.00	0.00	0.00	0.00
Ca	0.00	0.00	0.00	0.00	0.00	0.00	0.00	0.00	0.00	0.00
Mn	0.28	0.28	0.30	0.29	0.25	0.30	0.30	0.27	0.28	0.25
Na	0.74	0.72	0.70	0.73	0.79	0.71	0.72	0.76	0.72	0.77
K	0.01	0.01	0.01	0.01	0.01	0.01	0.01	0.01	0.01	0.01
Total	5.02	5.01	5.01	5.03	5.02	5.01	5.03	5.03	5.01	5.01
X _{An}	0.27	0.27	0.30	0.28	0.24	0.29	0.29	0.26	0.27	0.25
X _{Ab}	0.72	0.71	0.69	0.71	0.75	0.70	0.70	0.73	0.71	0.75
X _{Or}	0.01	0.01	0.01	0.01	0.01	0.01	0.01	0.01	0.01	0.01

<d.l.: Below detection limit; not included in total

Table 4.3: Representative microprobe analyses of alkali feldspar and cation calculations based on 8 oxygens (oxide data given as wt%)

Point No.	98 / 1 .	99 / 1 .	core	host	lamellae
Texture	rim				
SiO ₂	63.56	63.81	64.17	67.43	
TiO ₂	<d.l.	<d.l.	<d.l.	0.01	
Al ₂ O ₃	17.42	17.69	18.29	19.51	
Cr ₂ O ₃	<d.l.	<d.l.	0.06	<d.l.	
FeO	0.03	0.02	0.01	0.13	
MgO	0.01	0.04	<d.l.	<d.l.	
CaO	0.03	<d.l.	<d.l.	0.23	
MnO	0.03	0.07	0.06	0.06	
Na ₂ O	1.17	1.02	1.09	10.95	
K ₂ O	14.70	15.13	15.01	0.76	
Total	97.43	98.30	99.18	99.10	
Si	3.01	3.01	2.99	2.98	
Ti	0.00	0.00	0.00	0.00	
Al	0.97	0.98	1.00	1.02	
Cr	0.00	0.00	0.00	0.00	
Fe ⁺²	0.00	0.00	0.00	0.00	
Mg	0.00	0.00	0.00	0.00	
Ca	0.00	0.00	0.00	0.00	
Mn	0.00	0.00	0.00	0.01	
Na	0.11	0.09	0.10	0.94	
K	0.89	0.91	0.89	0.04	
Total	5.00	5.01	5.00	5.00	
X _{An}	0.00	0.00	0.00	0.01	
X _{Ab}	0.11	0.09	0.10	0.95	
X _{Or}	0.89	0.91	0.90	0.04	

<d.l.: Below detection limit; not included in total

Table 4.4: Representative microprobe analyses of orthopyroxene and cation calculations based on 6 oxygens (oxide data given as wt%)

Point No.	101 / 1 .	103 / 1 .	104 / 1 .	105 / 1 .	106 / 1 .	110 / 1 .
Texture	core	core	rim	core	rim	rim
SiO ₂	49.59	46.94	47.98	47.08	46.75	48.17
TiO ₂	0.09	0.04	0.04	0.04	0.05	0.00
Al ₂ O ₃	0.79	0.95	0.80	0.78	0.83	0.84
Cr ₂ O ₃	<d.l.	0.02	0.01	<d.l.	<d.l.	<d.l.
FeO	35.52	36.38	35.72	36.03	36.40	36.14
MgO	14.15	13.74	14.16	13.89	13.73	14.19
CaO	0.31	0.32	0.30	0.31	0.32	0.33
MnO	1.14	1.41	1.18	1.43	1.43	1.17
Na ₂ O	0.04	<d.l.	0.05	<d.l.	0.06	0.01
K ₂ O	<d.l.	<d.l.	<d.l.	<d.l.	0.02	<d.l.
Total	101.63	99.81	100.30	99.63	99.60	100.87
Si	1.93	1.87	1.89	1.87	1.86	1.89
Ti	0.00	0.00	0.00	0.00	0.00	0.00
Al	0.04	0.04	0.04	0.04	0.04	0.04
Cr	0.00	0.00	0.00	0.00	0.00	0.00
Fe ^{+3*}	0.10	0.22	0.18	0.21	0.24	0.18
Fe ⁺²	1.06	0.99	1.00	0.99	0.98	1.01
Mg	0.82	0.81	0.83	0.82	0.82	0.83
Ca	0.01	0.01	0.01	0.01	0.01	0.01
Mn	0.04	0.05	0.04	0.05	0.05	0.04
Na	0.00	0.00	0.00	0.00	0.00	0.00
K	0.00	0.00	0.00	0.00	0.00	0.00
Total	4.00	4.00	4.00	4.00	4.00	4.00
X _{Mg}	0.44	0.45	0.45	0.45	0.46	0.45

<d.l.: Below detection limit; not included in total

* Fe³⁺ recalculated according to the scheme of Droop (1987)

Table 4.5: Representative microprobe analyses of amphibole and cation calculations based (after Leake et al., 1997) on 23 oxygens (oxide data given as wt%)

Point No.	6 / 1 .	14 / 1 .	15 / 1 .	27 / 1 .	49 / 1 .	51 / 1 .	58 / 1 .	74 / 1 .
Texture	core	[^] Pl	[^] Pl	core	core	[^] Pl	[^] Grt	core
SiO ₂	40.58	40.29	40.91	40.63	39.82	40.23	40.18	39.59
TiO ₂	1.88	1.91	1.77	1.44	1.79	1.86	1.65	1.75
Al ₂ O ₃	10.57	10.66	10.70	10.51	10.69	10.46	10.60	10.48
Cr ₂ O ₃	0.02	<d.l.	<d.l.	<d.l.	<d.l.	<d.l.	0.04	0.04
FeO	22.53	22.34	22.78	22.92	22.64	22.29	21.36	22.84
MgO	7.19	7.09	6.95	7.11	7.12	7.29	7.84	6.93
CaO	11.07	11.25	11.26	11.22	11.25	11.17	11.49	11.16
MnO	0.32	0.28	0.30	0.18	0.20	0.32	0.32	0.16
Na ₂ O	1.31	1.33	1.36	1.33	1.45	1.51	1.37	1.60
K ₂ O	1.66	1.59	1.66	1.64	1.55	1.49	1.57	1.60
Total	97.46	96.92	97.98	97.19	96.66	96.84	96.62	96.36
Si	6.29	6.28	6.32	6.32	6.23	6.28	6.25	6.24
Al (IV)	1.71	1.72	1.68	1.68	1.77	1.72	1.75	1.76
Ti	0.00	0.00	0.00	0.00	0.00	0.00	0.00	0.00
Sum T	8.00	8.00	8.00	8.00	8.00	8.00	8.00	8.00
Al (VI)	0.23	0.24	0.27	0.24	0.20	0.20	0.20	0.18
Ti	0.22	0.22	0.21	0.17	0.21	0.22	0.19	0.21
Cr ⁺³	0.00	0.00	0.00	0.00	0.00	0.00	0.00	0.00
Fe ⁺³	0.49	0.45	0.40	0.52	0.53	0.48	0.52	0.47
Mg	1.66	1.65	1.60	1.65	1.66	1.69	1.82	1.63
Fe ⁺²	2.40	2.44	2.52	2.42	2.40	2.41	2.26	2.50
Mn	0.00	0.00	0.00	0.00	0.00	0.00	0.00	0.00
Li	0.00	0.00	0.00	0.00	0.00	0.00	0.00	0.00
Sum C	5.00	5.00	5.00	5.00	5.00	5.00	5.00	5.00
Mg	0.00	0.00	0.00	0.00	0.00	0.00	0.00	0.00
Fe ⁺²	0.03	0.02	0.02	0.04	0.03	0.02	0.00	0.03
Mn	0.04	0.04	0.04	0.02	0.03	0.04	0.04	0.02
Li	0.00	0.00	0.00	0.00	0.00	0.00	0.00	0.00
Ca	1.84	1.88	1.86	1.87	1.88	1.87	1.92	1.88
Na	0.09	0.06	0.07	0.07	0.06	0.07	0.04	0.06
Sum B	2.00	2.00	2.00	2.00	2.00	2.00	2.00	2.00
Ca	0.00	0.00	0.00	0.00	0.00	0.00	0.00	0.00
Na	0.31	0.34	0.34	0.33	0.38	0.39	0.37	0.43
K	0.33	0.32	0.33	0.33	0.31	0.30	0.31	0.32
Sum A	0.64	0.65	0.66	0.66	0.69	0.68	0.68	0.75
Total	15.64	15.65	15.66	15.66	15.69	15.68	15.68	15.75
X _{Mg}	0.41	0.40	0.39	0.40	0.41	0.41	0.45	0.39

<d.l.: Below detection limit; not included in total

Table 4.6: Representative microprobe analyses of biotite and cation calculations based on 22 oxygens (oxide data given as wt%)

Point No.	38 / 1.	78 / 1.	81 / 1.	82 / 1.	87 / 1.	92 / 1.	96 / 1.	100 / 1.	84 / 1.	112 / 1.
Texture		[^] Grt	[^] Grt	[^] Grt	[^] Grt	[^] Grt	[^] Grt	[^] Grt	incl in Grt	incl in Grt
SiO ₂	35.15	36.18	35.10	35.45	36.65	36.61	35.26	36.95	35.55	37.31
TiO ₂	4.95	4.78	4.84	4.76	4.37	4.87	4.87	4.19	4.72	4.37
Al ₂ O ₃	13.47	13.91	13.53	13.82	14.19	14.09	13.68	14.32	13	13.1
Cr ₂ O ₃	<d.l.	<d.l.	<d.l.	<d.l.	<d.l.	<d.l.	0.06	0.03	<d.l.	0.07
FeO	0.00	0.03	0.05	0.04	<d.l.	0.04	0.03	0.37	0.03	0.03
MgO	22.51	21.42	21.50	21.23	20.96	21.36	20.77	18.98	18.05	16.8
CaO	9.14	10.75	10.28	10.65	11.06	10.86	10.94	11.19	12.48	14.78
MnO	0.08	0.11	0.17	0.05	0.06	0.1	0.04	0.08	0.1	0.09
Na ₂ O	0.03	0.08	0.12	0.09	0.06	0.14	0.13	0.45	0.2	0.11
K ₂ O	8.66	9.32	9.31	9.42	9.29	9.39	9.33	8.66	9.26	9.68
Total	95.97	96.81	95.04	95.78	96.91	97.65	95.29	95.35	93.57	96.55
Si	5.5	5.5	5.5	5.5	5.6	5.5	5.5	5.6	5.5	5.6
Ti	0.6	0.5	0.6	0.6	0.5	0.6	0.6	0.5	0.6	0.5
Al	2.5	2.5	2.5	2.5	2.5	2.5	2.5	2.6	2.4	2.3
Cr	0.0	0.0	0.0	0.0	0.0	0.0	0.0	0.0	0.0	0.0
Fe ⁺²	2.9	2.7	2.8	2.7	2.7	2.7	2.7	2.4	2.4	2.1
Mg	2.1	2.4	2.4	2.5	2.5	2.4	2.5	2.5	2.9	3.3
Ca	0.0	0.0	0.0	0.0	0.0	0.0	0.0	0.1	0.0	0.0
Mn	0.0	0.0	0.0	0.0	0.0	0.0	0.0	0.0	0.0	0.0
Na	0.0	0.0	0.0	0.0	0.0	0.0	0.0	0.1	0.1	0.0
K	1.7	1.8	1.9	1.9	1.8	1.8	1.8	1.7	1.8	1.8
Total	15.5	15.6	15.7	15.7	15.6	15.6	15.7	15.5	15.7	15.7
X _{Mg}	0.42	0.47	0.46	0.47	0.48	0.48	0.48	0.51	0.55	0.61

<d.l.: Below detection limit; not included in total

Table 4.7: Representative microprobe analyses of ilmenite and cation calculations based on 3 oxygens (oxide data given as wt%)

Point No.	44 / 1 .	54 / 1 .	76 / 1 .	93 / 1 .
Texture	Incl in Grt			
SiO ₂	49.59	46.94	47.98	47.08
TiO ₂	0.09	0.04	0.04	0.04
Al ₂ O ₃	0.79	0.95	0.80	0.78
Cr ₂ O ₃	<d.l.	0.02	0.01	<d.l.
FeO	35.52	36.38	35.72	36.03
MgO	14.15	13.74	14.16	13.89
CaO	0.31	0.32	0.30	0.31
MnO	1.14	1.41	1.18	1.43
Na ₂ O	0.04	<d.l.	0.05	<d.l.
K ₂ O	<d.l.	<d.l.	<d.l.	<d.l.
Total	101.63	99.81	100.30	99.63
Si	1.93	1.87	1.89	1.87
Ti	0.00	0.00	0.00	0.00
Al	0.04	0.04	0.04	0.04
Cr	0.00	0.00	0.00	0.00
Fe ^{+3*}	0.10	0.22	0.18	0.21
Fe ⁺²	1.06	0.99	1.00	0.99
Mg	0.82	0.81	0.83	0.82
Ca	0.01	0.01	0.01	0.01
Mn	0.04	0.05	0.04	0.05
Na	0.00	0.00	0.00	0.00
K	0.00	0.00	0.00	0.00
Total	4.00	4.00	4.00	4.00

<d.l.: Below detection limit; not included in total

* Fe³⁺ recalculated according to the scheme of Droop (1987)

4.3 Geochemistry:

Based on the major and trace element analysis (analytical techniques in Appendix), the geochemical characteristics of the migmatitic felsic gneiss are depicted here (Table 4.8). Geochemical characters of the felsic country rock of the area are compared with equivalent felsic orthogneisses (Saikia et al. 2017; Mukherjee et al. 2019) that exhibit similar lithological relations.

Table 4.8: Whole rock major (wt%) and trace element (ppm) composition of representative samples of the migmatitic felsic gneiss

Sample	SD18	SD29B	SD30	SD10B	SD10A	SD29A	SD57
Location	24°05.584' N; 24°4.842' N; 24°4.854' N; 24°06.290' N; 24°06.297' N; 24°4.840' N; 24°11.675' N; 87°19.100' E 87°20.105' E 87°20.096' E 87°18.544' E 87°18.494' E 87°20.106' E 87°21.418' E						
SiO ₂	72.48	71.45	75.11	66.91	67.34	73.74	73.86
TiO ₂	0.29	0.51	0.26	0.77	0.55	0.49	0.31
Al ₂ O ₃	15.33	14.68	13.78	16.42	16.60	13.83	15.16
MnO	0.04	0.10	0.05	0.12	0.18	0.07	0.02
FeO _T	1.40	2.70	1.42	3.66	3.60	2.54	1.07
CaO	1.12	1.57	1.05	2.67	5.37	2.42	0.89
MgO	0.50	0.79	0.58	0.30	0.45	0.59	0.29
Na ₂ O	4.27	4.01	3.79	5.88	4.98	4.76	2.92
K ₂ O	4.22	3.64	3.31	1.81	0.22	1.03	5.26
P ₂ O ₅	0.10	0.13	0.04	0.25	0.16	0.13	0.05
Cs	0.2	3.4	1.4	0.0	0.1	2.1	0.3
Rb	51.0	69.2	89.2	19.7	5.8	37.6	106.4
Ba	292.7	1117.4	775.3	582.2	946.1	438.1	1084.7
Th	5.8	5.3	11.4	0.6	5.7	5.8	20.5
U	0.7	0.9	1.1	0.2	1.3	0.9	1.4
Nb	3.0	3.7	3.1	5.0	4.4	4.7	3.9
Ta	0.4	1.8	0.5	2.1	0.7	2.3	BDL
La	32.0	23.6	39.8	23.0	23.5	34.1	52.6
Ce	56.2	43.5	71.5	43.2	50.2	62.9	110.0
Pr	6.9	5.6	9.0	6.0	7.0	8.2	13.1
Nd	25.9	22.7	33.8	26.4	30.7	33.0	53.7
Sm	4.6	4.3	5.8	5.5	6.6	5.9	10.3
Eu	1.0	1.4	1.0	1.8	1.7	1.2	1.6
Gd	4.4	4.0	5.5	5.1	6.2	5.3	8.9
Dy	5.2	4.4	4.9	4.9	7.0	5.0	3.9
Er	4.0	3.3	3.6	3.0	4.7	3.2	1.4
Yb	4.5	3.6	3.7	2.7	4.8	3.0	1.1
Lu	0.7	0.5	0.6	0.4	0.7	0.5	0.2
Sr	245.7	181.1	198.4	335.0	265.9	187.9	78.6
Y	31.1	24.8	29.8	27.4	39.2	26.2	14.7
Zr	136.9	191.4	159.7	129.0	223.0	200.0	143.4
Hf	4.4	5.7	4.7	3.2	5.9	5.6	3.5
Pb	6.3	22.1	20.3	11.9	10.3	15.5	30.2
Ga	13.1	13.3	14.0	18.7	17.2	15.3	16.8
XFe	0.74	0.77	0.71	0.92	0.89	0.81	0.79
A/CNK	1.12	1.09	1.17	1.00	0.91	1.04	1.25
K ₂ O+Na ₂ O	8.49	7.65	7.10	7.69	5.20	5.79	8.18
K ₂ O/Na ₂ O	0.99	0.91	0.87	0.31	0.04	0.22	1.80
La _N /Lu _N	4.84	4.57	7.37	6.24	3.31	7.84	32.30
La _N /Yb _N	4.85	4.47	7.38	5.85	3.32	7.68	32.80
Gd _N /Yb _N	0.80	0.92	1.22	1.64	1.03	1.46	6.51
Eu/Eu*	0.70	1.01	0.56	1.05	0.79	0.64	0.50
Pb _N /Nb _N	4.51	5.61	4.78	7.67	6.67	7.07	5.86
TZr (°C)[1]	778.10	804.30	800.20	752.70	789.40	805.80	794.50
TZr (°C)[2]	732.60	761.90	762.30	694.70	732.60	762.60	757.10

Table 4.8: continued

Sample	SD56B	SD38	SD59B	SD52B	SD37	SD8B	SD55
Location	24°12.483' N; 24°05.582' N; 24°09.925' N; 24°06.665' N; 24°04.930' N; 24°04.091' N; 24°12.463' N; 87°22.016' E 87°19.099' E 87°20.422' E 87°18.932' E 87°20.139' E 87°22.230' E 87°21.968' E						
SiO ₂	74.45	73.70	64.53	68.03	59.42	73.10	74.54
TiO ₂	0.18	0.56	0.60	0.64	0.72	0.10	0.13
Al ₂ O ₃	15.32	13.27	14.97	14.49	20.04	14.95	13.60
MnO	0.04	0.06	0.12	0.07	0.13	0.01	0.04
FeO _T	1.62	2.36	5.35	4.10	3.65	0.64	1.52
CaO	0.49	1.60	2.12	2.83	5.82	2.36	0.44
MgO	0.54	0.83	2.17	1.61	1.29	0.04	0.39
Na ₂ O	3.45	3.10	2.23	4.14	5.66	7.07	3.60
K ₂ O	3.31	3.90	6.66	2.71	0.76	0.85	4.45
P ₂ O ₅	0.02	0.06	0.08	0.19	0.47	0.02	0.01
Cs	0.3	1.1	2.4	0.4	0.1	0.0	0.1
Rb	49.0	80.0	187.7	55.3	3.9	4.8	62.2
Ba	1211.5	791.4	1462.7	480.4	426.6	71.5	1125.2
Th	14.1	10.8	19.5	0.9	7.2	29.5	15.8
U	1.7	1.2	0.6	0.1	2.0	1.5	2.1
Nb	4.5	4.0	5.1	5.7	6.1	2.0	6.2
Ta	BDL	BDL	0.6	0.1	0.2	0.2	BDL
La	60.9	27.0	51.6	33.6	20.3	30.9	53.8
Ce	131.3	55.4	104.8	71.2	46.6	63.3	119.3
Pr	12.7	6.1	10.8	7.7	5.9	6.9	8.5
Nd	45.9	22.2	37.2	29.0	24.5	25.5	27.1
Sm	8.0	4.0	6.2	5.6	5.7	5.0	3.7
Eu	1.4	1.1	1.9	1.1	1.5	1.0	1.9
Gd	7.5	3.6	5.0	4.9	5.7	5.1	4.7
Dy	7.0	3.3	3.2	4.0	5.8	4.6	9.5
Er	5.1	2.3	1.9	2.3	3.9	2.5	8.0
Yb	5.0	2.3	2.1	2.1	4.0	1.9	8.4
Lu	0.8	0.4	0.3	0.3	0.6	0.3	1.2
Sr	41.7	193.8	198.9	166.7	370.1	69.3	22.8
Y	46.8	20.0	16.6	22.7	35.6	22.4	66.9
Zr	188.8	217.2	193.1	130.5	147.0	132.8	291.1
Hf	6.2	5.3	5.1	3.4	3.9	3.6	11.2
Pb	19.0	20.6	27.7	8.2	11.5	9.3	17.1
Ga	15.7	13.7	20.1	14.4	20.8	21.5	23.7
XFe	0.75	0.74	0.71	0.72	0.74	0.94	0.80
A/CNK	1.51	1.08	1.01	0.97	0.97	0.89	1.18
K ₂ O+Na ₂ O	6.76	7.00	8.89	6.85	6.42	7.92	8.05
K ₂ O/Na ₂ O	0.96	1.26	2.99	0.65	0.13	0.12	1.24
La _N /Lu _N	8.12	7.94	16.11	11.28	3.46	11.09	4.52
La _N /Yb _N	8.19	7.96	17.06	10.87	3.45	10.79	4.36
Gd _N /Yb _N	1.19	1.25	1.85	1.97	1.16	2.19	0.47
Eu/Eu*	0.54	0.87	1.06	0.66	0.79	0.61	1.35
Pb _N /Nb _N	6.87	6.12	7.81	8.59	9.27	2.97	9.39
TZr (°C)[1]	836.00	819.00	786.50	754.00	745.50	750.40	856.80
TZr (°C)[2]	814.40	780.70	733.40	696.30	679.40	690.20	830.40

N represents normlisation after McDonough and Sun (1995); XFe = FeOT/[FeOT+MgO]; [1] Watson and Harrison (1983); [2] Boehnke et al. (2013)

In the total alkali-silica (TAS) diagram (Fig. 4.3.a) (Middlemost 1994), migmatitic felsic gneiss are predominantly concentrated in the granite field, while few samples extend into granodiorite, quartz monzonite and diorite fields. The X_{Fe} ($=FeO_T/[FeO_T+MgO]$) of the migmatitic felsic gneiss ranges from 0.94 to 0.71. In the geochemical classification diagrams of Frost et al. (2001), the bulk of the migmatitic felsic gneiss samples is concentrated in the magnesian field, with only three samples in the ferroan field (Fig. 4.3.c). The migmatitic felsic gneisses are predominantly calc-alkalic to calcic, with only two samples in the alkali-calcic to alkali fields (Fig. 4.3.d). The migmatitic felsic gneiss straddles the boundary of metaluminous to peraluminous. ASI ($=\text{molar } Al_2O_3/(CaO+Na_2O+K_2O)$) value for the bulk of the samples ranges from 0.9 to 1.1, with only a few samples having $ASI > 1.1$ (Fig. 4.3.e). In the AFM diagram (Fig. 4.3.b), migmatitic felsic gneiss shows affinity towards the calc-alkaline series.

The primitive mantle normalised (McDonough and Sun 1995) trace element spider diagram (Fig. 4.4.a) gives an overall negative slope. Rb, Ba, and Pb in the studied rock samples show positive anomalies, whereas Nb, Sr, P, and Ti give prominent negative anomalies. The chondrite normalised (McDonough and Sun 1995) REE patterns (Fig. 4.4.b) of the

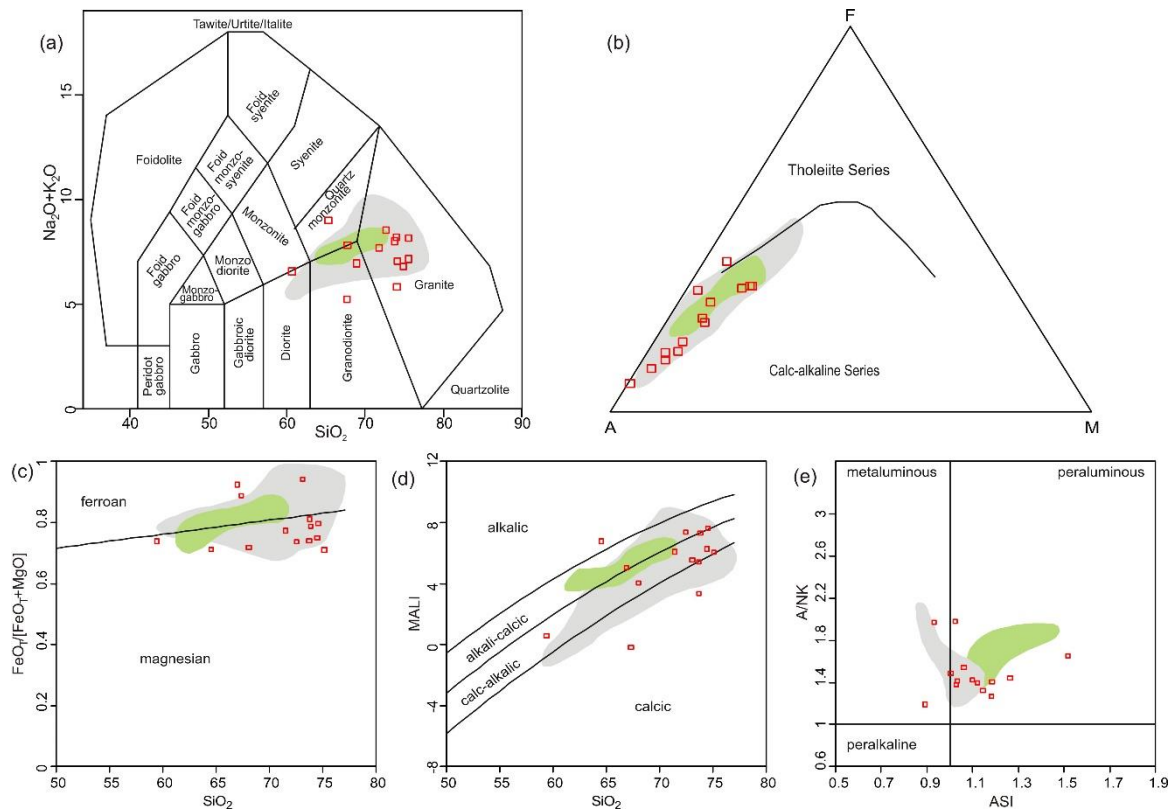
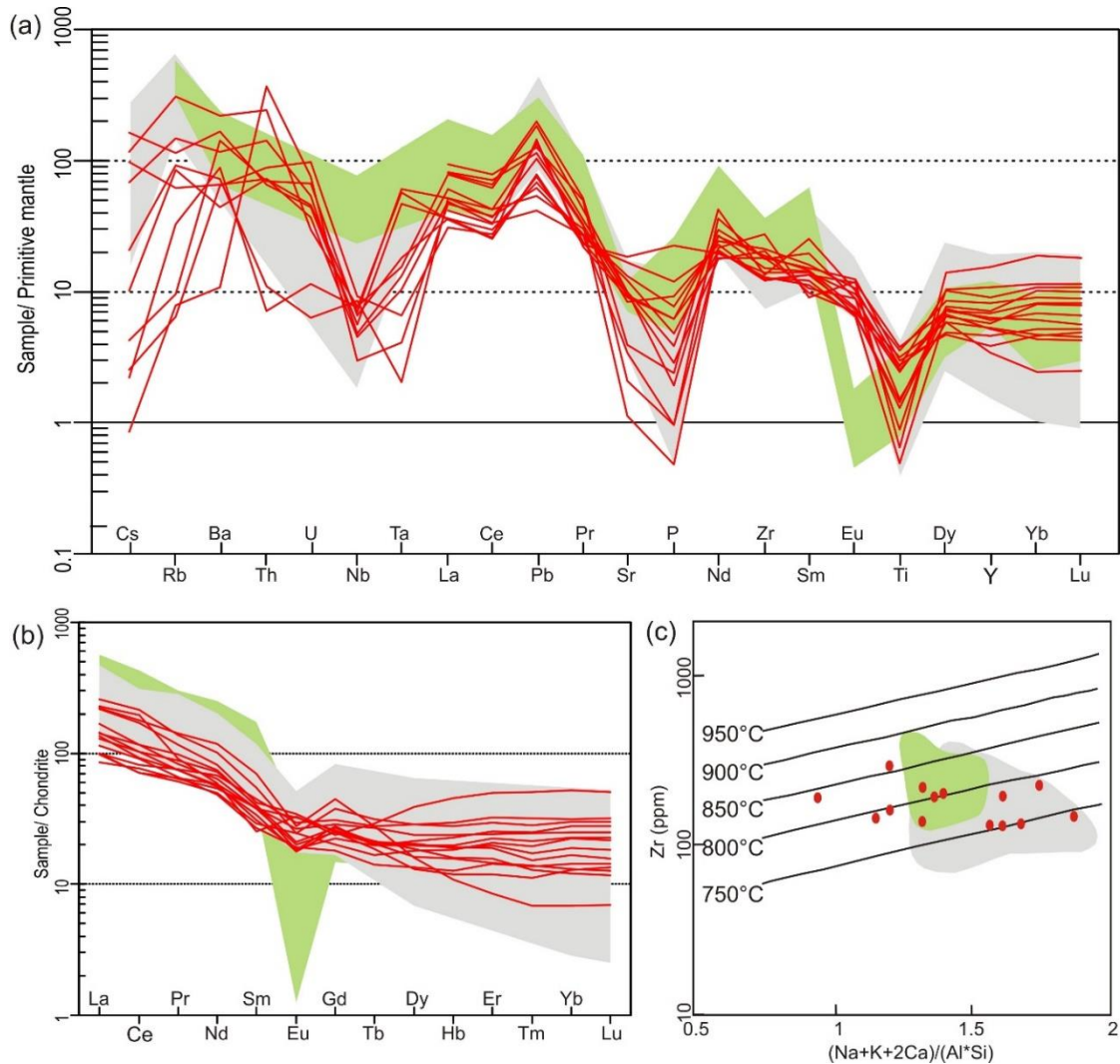


Figure 4.3: Migmatitic felsic gneiss is compared with felsic orthogneisses from the Dumka-Deoghar (grey) and Bathani (light green) area. (a) In the total alkali-silica (TAS) diagram (Middlemost 1994), migmatitic felsic gneiss are predominantly concentrated in the granite field, while few samples extend into granodiorite, quartz monzonite and diorite fields. (b) In the AFM diagram (Fig. 4.3.b), migmatitic felsic gneiss shows affinity towards the calc-alkaline series. (c-e) The geochemical classification diagrams of Frost et al. (2001) MFG major element compositions are plotted. $X_{Fe} = FeO_T / [FeO_T + MgO]$; MALI = Modified alkali lime index ($Na_2O + K_2O - CaO$); ASI = molar $Al_2O_3 / (Na_2O + K_2O + CaO - 1.67 P_2O_5)$; A/NK = molar $Al_2O_3 / (Na_2O + K_2O)$;

migmatitic felsic gneiss show LREE enrichment over HREE ($La_N/Lu_N = 3.3-32.3$), with a relatively flat HREE pattern ($Gd_N/Lu_N = 0.47-6.51$). The studied rock samples depict moderate negative europium anomaly ($Eu/Eu^* = 0.5-0.9$), with only a few samples showing slight positive EU anomaly ($Eu/Eu^* = \sim 1.1$).



*Figure 4.4: Migmatitic felsic gneiss is compared with felsic orthogneisses from the Dumka-Deoghar (grey) and Bathani (light green) area. (a) The primitive mantle normalised (McDonough and Sun 1995) trace element spider diagram. (b) The chondrite normalised (McDonough and Sun 1995) REE diagram. (c) Zircon saturation temperature (T_{Zr}) plotted in the Zr (ppm) vs $M = (K+Na+2Ca)/(Al*Si)$ diagram.*

4.4 Magmatic temperature:

Estimating the magmatic temperature is a useful tool for understanding the petrogenesis of the igneous rock. Due to the absence of suitable mineral pairings and low-temperature re-equilibration, determining the magmatic temperature is challenging (Miller et al. 2003). Given that zircon solubility is very temperature-sensitive, and that zircon is frequently found in felsic and intermediate rocks as an accessory phase (Miller et al. 2003), zircon saturation temperature (Fig. 4.4.c) (T_{Zr}) (Watson and Harrison 1983; Boehnke et al. 2013) offers a straightforward and reliable proxy for the magmatic temperature. Despite the widespread use of zircon saturation thermometry, zircon saturation is essentially bulk composition (on the value of $M = (K+Na+2Ca)/(Al*Si)$) dependent (Watson and Harrison 1983). The inheritance of older zircon and the changing nature of the zircon saturation temperature during fractional crystallisation complicate zircon saturation even more (King et al. 2001). Zircon saturation temperature rises as fractional crystallisation progresses, although the actual magmatic temperature falls (Siégl et al. 2018). Using the calibration of Boehnke et al. (2013), the studied granitoids yield magmatic temperature in the range of 680-830°C (Avg. ~745 °C). The bulk of the samples yields a low magmatic temperature, while two samples have a magmatic temperature >800°C. Variations in magmatic temperature can be influenced by (a) the inheritance of older zircon or (b) the compositional variation of the granitoids, which control Zr saturation during different stages of magmatic crystallisation.

4.5 Mineral evolution and physical condition of metamorphism:

To comprehend the metamorphic evolution, an extensive understanding of the textural relations among various phases plays a crucial role. Textural relations, combined with phase chemistry, are used to understand the different stages of metamorphism by binding the prograde, peak, and retrogressive metamorphic history.

In the high grade of metamorphism, the prograde assemblage is usually obscured during the peak metamorphism. Here, in the migmatitic felsic gneiss, the peak metamorphism is represented by the assemblage of garnet, orthopyroxene, K-feldspar, plagioclase, quartz and melt. Poikiloblastic garnets with blobs of residual melt and skeletal garnet in coarse-grained leucosomal patches and bands indicate peritectic garnet growth with simultaneous melting during the peak metamorphism. Biotite inclusions in the garnet grains give a glimpse of the prograde history. The breakdown of biotite during the prograde and peak metamorphic history can be a probable source behind the peak metamorphic assemblage. The peak metamorphic partial melting can be explained by the following reaction (Patiño Douce and Beard 1995):



The presence of garnet and orthopyroxene in the peak metamorphic assemblage indicates a high grade of metamorphism. The presence of mesoperthitic feldspar, orthopyroxene, garnet and ilmenite (absence of rutile) indicates a high temperature and moderate pressure during the peak metamorphic event.

The retrogressive metamorphic history of the migmatitic felsic gneiss is defined by a hydration event that resulted in the formation of hydrous minerals (biotite, amphibole) replacing peak metamorphic phases such as garnet and orthopyroxene.

4.5.1 Conventional thermobarometry:

Understanding metamorphic evolution is incomplete without having a comprehensive idea about the physical conditions of metamorphism. The P-T condition is estimated using conventional thermobarometry to understand the physical conditions of metamorphism (Table 4.9). The physical condition of peak metamorphism is estimated using the compositions of garnet and adjacent orthopyroxene and plagioclase. The geothermometers (Lee and Ganguly, 1988) and barometers (Bhattacharya et al., 1991) estimate P-T conditions of 655-700°C and 7.5-7.9 kbar in the peak assemblage. Garnet-amphibole (Graham and Powell 1984) and Ti in biotite (Henry et al. 2005) ion exchange thermometry (Bhattacharya et al. 1992) are calculated using the compositions of biotite and garnet with adjacent amphibole. During retrogression, garnet-biotite and adjacent plagioclase compositions constrain the pressure (Hoisch 1990) along with Al in amphibole

barometry (Hammarstrom and Zen 1986; Schmidt 1992). The thermobarometry yields a P-T estimate of biotite formation that converges at ~600°C and ~6 kbar.

Table 4.9: P-T estimates through conventional thermobarometric calculations

Assemblge		Thermometry		Barometry		
		P (kbar, ref)	T (°C)	T (°C, ref)		P (kbar)
Grt-Opx-Pl-Qz	GO	7	655-700	GOPS	700	7.5-7.9
Grt-Amp-Bt	Ti in Bt		610-650	GBPQ		6.1-6.5
	GA		577 ± 13	Al in Amp1		6.2 ± 0.17
Al in Amp2					5.8 ± 0.19	

GO: Garnet - orthopyroxene geothermometer (Bhattacharya et al., 1991).

GOPS: Garnet - orthopyroxene - plagioclase - quartz barometer (Eckert et al., 1991).

GA: Garnet - Amphibole thermometer (Graham and Powell, 1984).

Al in Amp1: Al in amphibole barometer (Schmidt, 1992)

Al in Amp2: Al in amphibole barometer (Hammarstrom and Zen, 1986)

Ti in Biotite thermometry (Henry et al. 2005)

GBPQ: Garnet - biotite - plagioclase - quartz barometer (Höisch, 1990).

4.5.2 Phase equilibria modelling:

Numerically simulated phase equilibria modelling (pseudosection approach) is calculated in NCFMASHT (Na₂O-CaO-FeO-MgO-Al₂O₃-SiO₂-H₂O-TiO₂) components system to understand the metamorphic evolution of the studied migmatitic felsic gneiss. The bulk composition relevant for the pseudosection construction depends on the volume of the rock that reacts to be in chemical equilibrium at the intended P-T condition (Stuwe 1997). Under high-grade metamorphic conditions, fluid-mediated element transfer is restricted, often resulting in localised bulk compositions representing equilibrium. However, mesoscopic leucosomal patches and bands suggest a comparatively more extensive equilibrium area. Phase equilibrium modelling is done using major oxide bulk compositions of sample no SD-52 to model. As in deep crustal conditions, H₂O is generally present within mineral structures or in the melt phase; the migmatitic felsic gneiss's water content is estimated so that free fluid is absent in the presence of melt. For the phase equilibrium modelling (pseudosection), computation of the phase diagram is done using the program PerpleX (ver. 7.0.11; Connolly 2005) with the internally consistent thermodynamic dataset of Holland and Powell (2011) (TC-DS633). The a-X relationships of the minerals chosen for the numerical calculations of the phase diagram are the

following: clinopyroxene (Holland and Powell 1996), clino-amphibole (Diener and Powell 2012), melt (White et al. 2014), garnet (White et al. 2014), orthopyroxene (White et al. 2014), feldspars (Holland and Powell 2003). In addition to the phase diagram, compositional isopleth for garnet is calculated and plotted in the phase diagram in the appropriate assemblage fields to narrow down the estimated P-T conditions of the rock. Perple-X subordinate program WARAMI (Connolly 2005, 2009) is used for these computations.

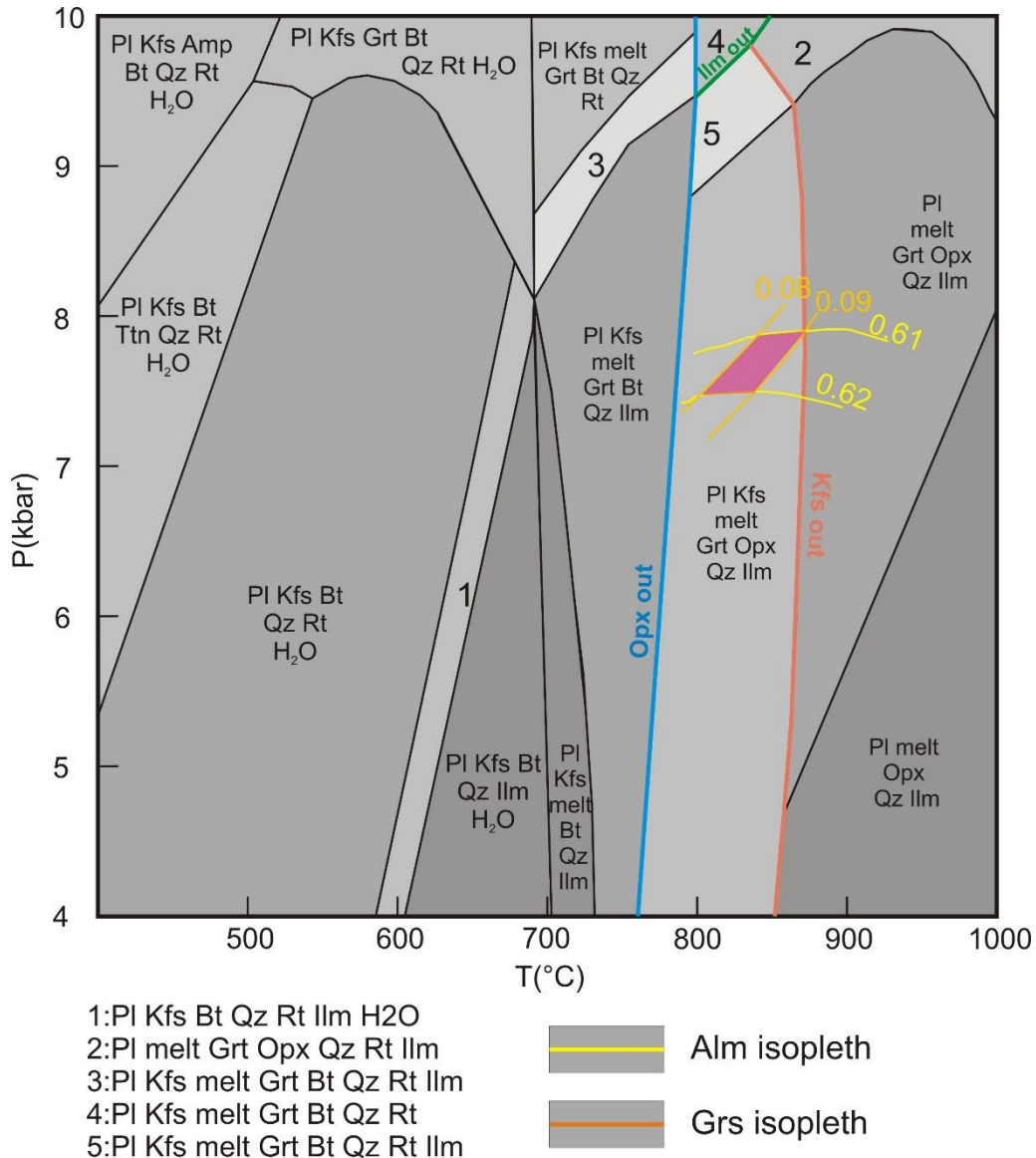


Figure 4.5: Numerically simulated phase equilibria modelling is calculated in NCFMASHT ($\text{Na}_2\text{O}-\text{CaO}-\text{FeO}-\text{MgO}-\text{Al}_2\text{O}_3-\text{SiO}_2-\text{H}_2\text{O}-\text{TiO}_2$) components system.

Result: In the constructed pseudosection (Fig. 4.5), the melt starts to form around 700 °C. The melt-in-line is highly temperature sensitive. With increasing temperature (around 750

°C), the melt-in line is followed by the biotite-out line. The segment between the Opx-out line and the Kfs-out line marks the peak metamorphic assemblage field of Grt-Opx-Pl-Kfs-Qz-melt in the pseudosection. The peak metamorphic field is between 750-850 °C. Almandine and grossular isopleths further constrain the peak metamorphic field between 750-850 °C and 7.5-8 Kbar pressure.

Reference

- Bhattacharya, A., Mohanty, L., Maji, A., Sen, S.K., and Raith, M. (1992) Non-ideal mixing in the phlogopite-annite binary: constraints from experimental data on Mg-Fe partitioning and a reformulation of the biotite-garnet geothermometer. *Contributions to Mineralogy and Petrology*, 111, 87–93.
- Boehnke, P., Watson, E.B., Trail, D., Harrison, T.M., and Schmitt, A.K. (2013) Zircon saturation re-revisited. *Chemical Geology*, 351, 324–334.
- Connolly, J.A.D. (2005) Computation of phase equilibria by linear programming: A tool for geodynamic modeling and its application to subduction zone decarbonation. *Earth and Planetary Science Letters*, 236, 524–541.
- (2009) The geodynamic equation of state: What and how. *Geochemistry, Geophysics, Geosystems*, 10.
- Diener, J.F.A., and Powell, R. (2012) Revised activity–composition models for clinopyroxene and amphibole. *Journal of Metamorphic Geology*, 30, 131–142.
- Droop, G.T.R. (1987) A general equation for estimating Fe 3+ concentrations in ferromagnesian silicates and oxides from microprobe analyses, using stoichiometric criteria. *Mineralogical Magazine*, 51, 431–435.
- Frost, B.R., Barnes, C.G., Collins, W.J., Arculus, R.J., Ellis, D.J., and Frost, C.D. (2001) A geochemical classification for granitic rocks. *Journal of Petrology*, 42, 2033–2048.
- Graham, C.M., and Powell, R. (1984) A garnet–hornblende geothermometer: calibration, testing, and application to the Pelona Schist, Southern California. *Journal of Metamorphic Geology*, 2, 13–31.
- Hammarstrom, J.M., and Zen, E. (1986) Aluminum in hornblende: an empirical igneous

- geobarometer. *American Mineralogist*, 71, 1297–1313.
- Henry, D.J., Guidotti, C. V, and Thomson, J.A. (2005) The Ti-saturation surface for low-to-medium pressure metapelitic biotites: Implications for geothermometry and Ti-substitution mechanisms, 90, 316–328.
- Hoisch, T.D. (1990) Empirical calibration of six geobarometers for the mineral assemblage quartz+muscovite+biotite+plagioclase+garnet. *Contributions to Mineralogy and Petrology*, 104, 225–234.
- Holland, T., and Powell, R. (1996) Thermodynamics of order-disorder in minerals; II, Symmetric formalism applied to solid solutions. *American Mineralogist*, 81, 1425–1437.
- (2003) Activity-compositions relations for phases in petrological calculations: An asymmetric multicomponent formulation. *Contributions to Mineralogy and Petrology*, 145, 492–501.
- Holland, T.J.B., and Powell, R. (2011) An improved and extended internally consistent thermodynamic dataset for phases of petrological interest, involving a new equation of state for solids. *Journal of Metamorphic Geology*, 29, 333–383.
- King, P.L., Chappell, B.W., Allen, C.M., and White, A.J.R. (2001) Are A-type granites the high-temperature felsic granites ? Evidence from fractionated granites of the Wangrah Suite. *Australian Journal of Earth Sciences*, 501–514.
- Leake, B.E., Woolley, A.R., Arps, C.E.S., Birch, W.D., Gilbert, M.C., Grice, J.D., Hawthorne, F.C., Kato, A., Kisch, H.J., Krivovichev, V.G., and others (1997) Nomenclature of amphiboles: Report of the subcommittee on amphiboles of the international mineralogical association, commission on new minerals and mineral names. *Canadian Mineralogist*, 35, 219–246.
- McDonough, W.F., and Sun, S. s. (1995) The composition of the Earth. *Chemical Geology*, 120, 223–253.
- Middlemost, E.A.K. (1994) Naming materials in the magma/igneous rock system. *Earth Science Reviews*, 37, 215–224.

- Miller, C.F., McDowell, S.M., and Mapes, R.W. (2003) Hot and cold granites: Implications of zircon saturation temperatures and preservation of inheritance. *Geology*, 31, 529–532.
- Mukherjee, S., Dey, A., Sanyal, S., Ibanez, M., and Pulak, M. (2019) Bulk rock and zircon geochemistry of granitoids from the Chotanagpur Granite Gneissic Complex (CGGC): implications for the late Paleoproterozoic continental arc magmatism in the East Indian Shield. *Contributions to Mineralogy and Petrology*, 174, 1–17.
- Patiño Douce, A.E., and Beard, J.S. (1995) Dehydration-melting of biotite gneiss and quartz amphibolite from 3 to 15 kbar. *Journal of Petrology*, 36, 707–738.
- Saikia, A., Bibhuti, G., Tatiana, K., Liudmila, L., Tamara, B., and Mansoor, A. (2017) Geochemical and U–Pb zircon age characterisation of granites of the Bathani Volcano Sedimentary sequence, Chotanagpur Granite Gneiss Complex, eastern India: vestiges of the Nuna supercontinent in the Central Indian Tectonic Zone. *Geological Society, London, Special Publications*, 457, 233–252.
- Schmidt, M.W. (1992) Amphibole composition in tonalite as a function of pressure: an experimental calibration of the Al-in-hornblende barometer. *Contributions to Mineralogy and Petrology*, 110, 304–310.
- Siégel, C., Bryan, S.E., Allen, C.M., and Gust, D.A. (2018) Use and abuse of zircon-based thermometers: A critical review and a recommended approach to identify antecrystic zircons. *Earth-Science Reviews*, 176, 87–116.
- Watson, E.B., and Harrison, T.M. (1983) Zircon saturation revisited: temperature and composition effects in a variety of crustal magma types. *Earth and Planetary Science Letters*, 64, 295–304.
- White, R.W., Powell, R., Holland, T.J.B., Johnson, T.E., and Green, E.C.R. (2014) New mineral activity–composition relations for thermodynamic calculations in metapelitic systems. *Journal of Metamorphic Geology*, 32, 261–286.
- Whitney, D.L., and Evans, B.W. (2010) Abbreviations for Names of Rock-Forming Minerals. *American Mineralogist*, 95, 185–187.

Chapter 5

Magmatic and metamorphic evolution of the metaporphyrritic charnockite and biotite gneiss

Apart from the migmatitic felsic gneiss country rock (MFG), the lithology of the area is dominated by the intrusive metaporphyrritic charnockite and the associated biotite gneiss. This chapter aims to evaluate the magmatic petrogenesis and metamorphic evolution of the two associated rock types sharing gradational contact with each other (detailed in Chapter 3) and establish a relation between them. Detailed petrography, whole rock geochemistry, phase chemistry and phase equilibria modelling are utilised for the study.

5.1 Petrography:

This section describes, in detail, the petrography of the metaporphyrritic charnockite (PC) and biotite gneiss (BG). From here on, abbreviations of PC and BG are used for metaporphyrritic charnockite and biotite gneiss, respectively. As mentioned in Chapter 3, these two granitoids are adjacent and share a gradational contact. At the same time, these rock types exhibit similar relations with the country rock. Also, both the rock types are deformed and metamorphosed; as a result, the petrographic description is broadly divided into two aspects: (i) relict magmatic textures and (ii) metamorphic and deformational overprint. It is difficult to identify the relict magmatic textures as, in most cases, these are entirely obliterated due to deformation and metamorphism. Despite metamorphism in the coarse-grained metaporphyrritic charnockite, magmatic textures are still preserved.

5.1.1 Metaporphyritic charnockite (PC):

This coarse-grained rock exhibits a bimodal grain size distribution representing a typical porphyritic texture. The major phases comprise the rock type include plagioclase (~35%), K-feldspar (~15%), quartz (~30%), orthopyroxene (~8%), along with garnet (~5%) and amphibole (~4%) and modal abundance of PC plots in the granodiorite field in the QAP diagram (Fig. 5.1) (Le Maitre et al. 2005). Apart from these phases, PC contains ilmenite (~2%), magnetite (~1%), zircon, and apatite as accessory phases. Plagioclase, K-feldspar, quartz and orthopyroxene define the coarse-grained porphyritic nature of the rock type. The matrix consists of finer grains of plagioclase, quartz, K-feldspar, orthopyroxene, magnetite and ilmenite.

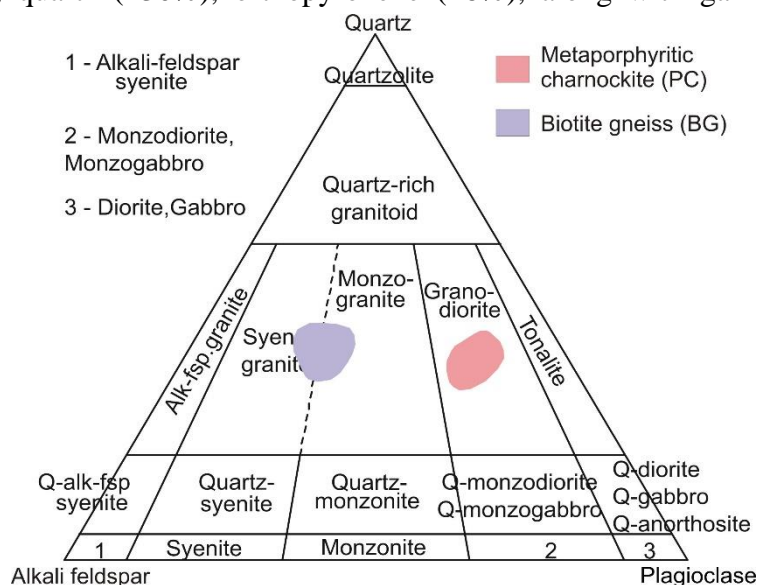


Figure 5.1: QAP diagram based on modal proportions, PC plots in the granodiorite field and BG plots in the granite field.

In hand specimens (2-6 cm) as well as under microscope, megacrysts of plagioclase often exhibit perfect tabular euhedral shape (Fig. 5.2.d). The megacrystic “lath-shaped” plagioclase also demonstrates simple twin often in combination with lamellar twin (Fig. 5.2.d; 5.3.a-b). Apart from plagioclase, K-feldspar megacryst is also present (Fig. 5.2.h), but its abundance is much less than plagioclase. In few instances, these feldspar grains contain inclusions of orthopyroxene (Fig. 5.3.a). Antiperthite feldspar grains are present in the rock matrix (Fig. 5.3.e).

Orthopyroxene is present in two distinct modes: (a) large (1-3 mm) megacrysts (Fig. 5.2.a-b) and (b) fine-grained (<250 μm) orthopyroxene (Fig. 5.2.e-g). The orthopyroxene megacrysts often preserve their euhedral tabular shape and short prismatic habit in low-strain zones (Fig. 5.2.a-b). Cluster of these tabular euhedral orthopyroxene grains often exhibit relict cumulus texture (Fig. 5.2.c). The other mode of orthopyroxene is fine-grained

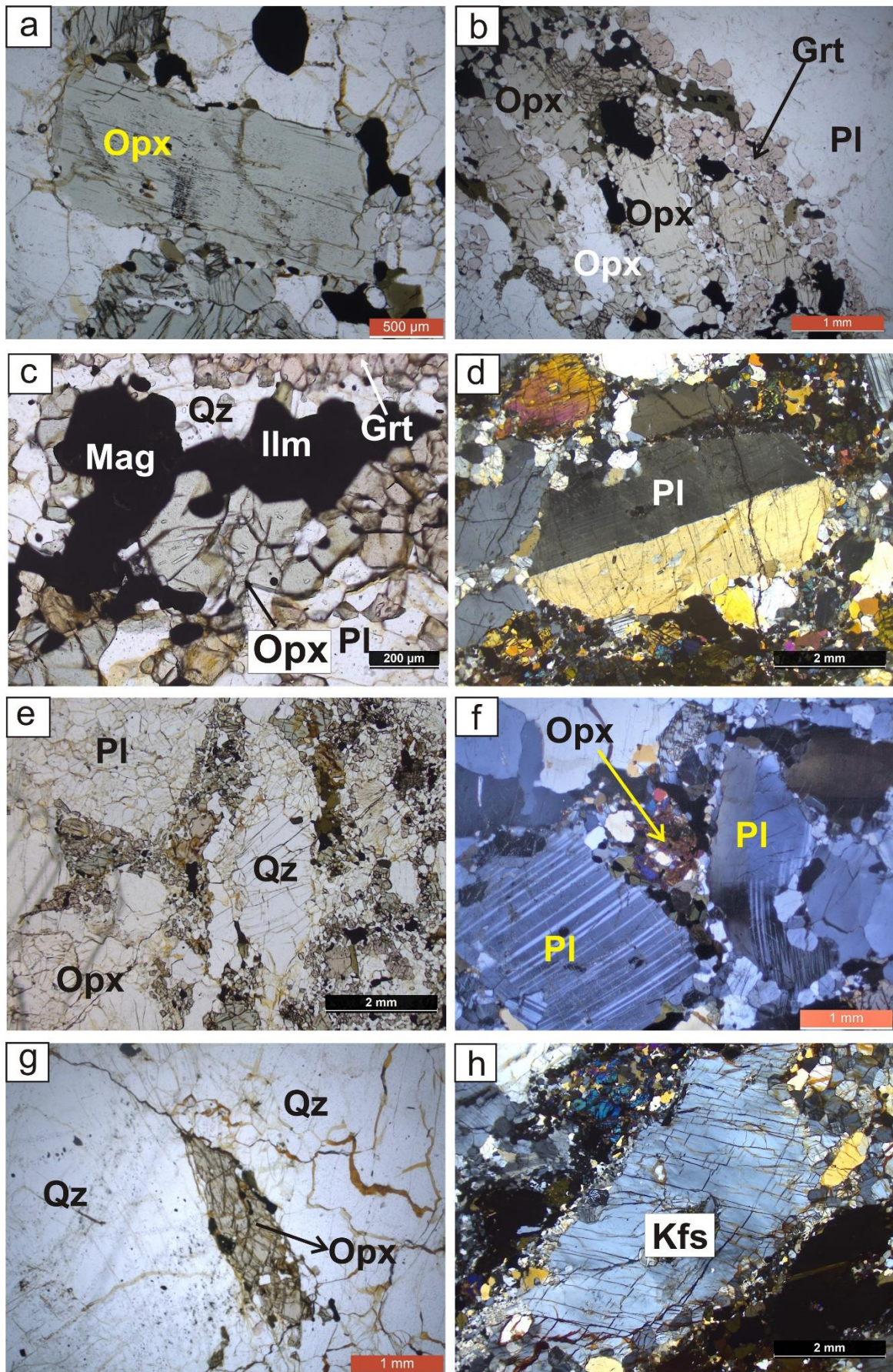


Figure 5.2: (a) The orthopyroxene megacrysts often preserve their euhedral tabular shape and short prismatic habit in low-strain zones. (b) Clusters of these tabular euhedral orthopyroxene grains often exhibit relict cumulus texture. (c) Ilm and Mgt exhibit a relict interlocking texture with orthopyroxene. (d) Megacrysts of plagioclase often exhibit perfect tabular euhedral shape. (e-g) Fine-grained “lace-like” Opx are present in between coarse-grained plagioclase and quartz. These fine grained orthopyroxene often show a low (30-40°) angle with Pl and Qz, less than 60°. (h) Megacrystic Kfs is partially recrystallised along the boundary.

“lace-like”, and present in between coarse-grained plagioclase, quartz (Fig. 5.2.e-g). These fine grained orthopyroxene often show a low dihedral (30-40°) angle with Pl, Qz, much less than 60° (Fig. 5.2.f-g). Often, Ilm and Mgt exhibit a relict interlocking texture with orthopyroxene (Fig. 5.2.c). Ilmenite and magnetite grains are euhedral to subhedral (Fig. 5.4.a, e). In many cases, ilmenite and magnetite are in contact with each other, sharing an almost straight grain boundary (Fig. 5.4.a). The modal proportion of ilmenite is higher than magnetite.

As mentioned above, the rock is deformed, and its manifestation is quite evident in the rock petrography. The megacrystic plagioclase grains are often partially to completely recrystallised (Fig. 5.3.a-d). Coarse plagioclase grains are often recrystallised to fine grains along their boundary, forming a typical core-mantle structure (Fig. 5.3.d). Even when these plagioclase grains are partially to fully recrystallised into polygonal grains, the faint outline of euhedral faces can still be identified (Fig. 5.3.c). Deformation results in the folding of lamellar twins in plagioclase (Fig. 5.3.a). Similar to plagioclase, orthopyroxene is often bent and recrystallised along the boundary. Coarse quartz grains in the rock exhibit deformational signatures, such as undulose extinction, sub-grain formation, quartz ribbons, and recrystallisation. K-feldspar grains have broken down in a few cases to form myrmakitic intergrowths (Fig. 5.3.f).

Garnet is present as a double corona along with quartz, separating adjacent grains of plagioclase and orthopyroxene (Fig. 5.4.a-b). While quartz forms in the vicinity of orthopyroxene, garnet formation is strictly restricted along the margin of plagioclase. The garnet grains are bead-shaped and assume the shape of recrystallised plagioclase present along the margins of plagioclase megacrysts (Fig. 5.3.c-d). This garnet formation is present along both fine (Fig. 5.4.b) and coarse-grained (Fig. 5.4.a) orthopyroxene. In rare instances, fine-grained clinopyroxene is present with garnet in the double corona and shares a non-

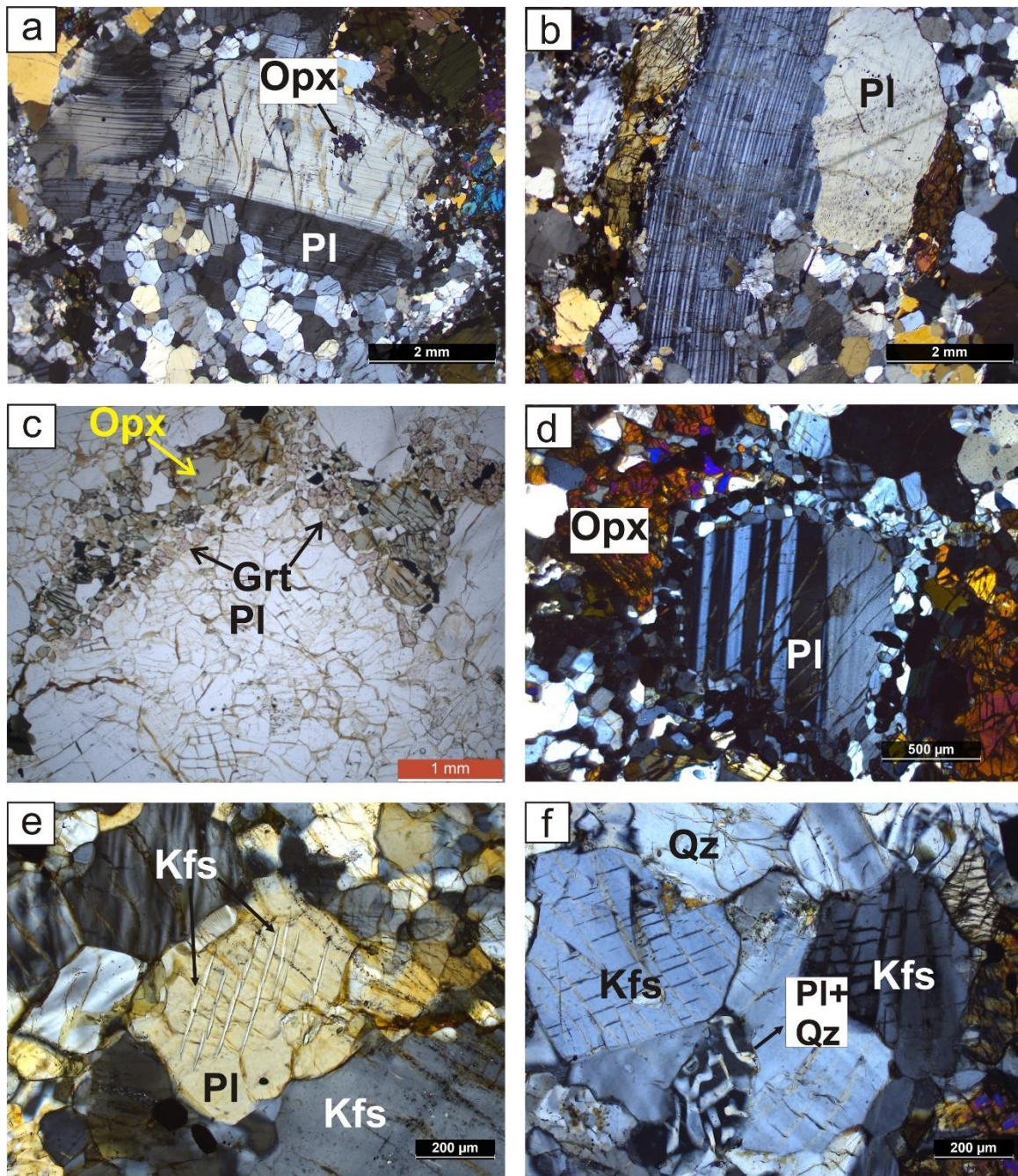


Figure 5.3: (a-b) The megacrystic “lath-shaped” plagioclase often exhibits simple twins often in combination with lamellar twins. The feldspar grain contains inclusions of orthopyroxene. They are partially recrystallised. Lamellar twins are also folded as a result of deformation. (c) The megacrystic plagioclase grains are completely recrystallised into polygonal grains, and the faint outline of euhedral faces can still be identified. Fine grained garnet is present between Pl and Opx. The garnet grains are bead-shaped and assume the shape of recrystallised plagioclase present along the margins of plagioclase megacrysts. (d) Coarse plagioclase grains are recrystallised along their boundary, forming a typical core-mantle structure. (e) Antiperthitic exsolution lamellae of K-feldspar within a plagioclase host. (f) K-feldspar forms myrmakitic intergrowth along the margin.

reactive straight boundary with garnet (Fig. 5.4.c). Amphibole occurs as the rock's sole hydrous phase, replacing grains of Opx and garnet (Fig. 5.4.d-f).

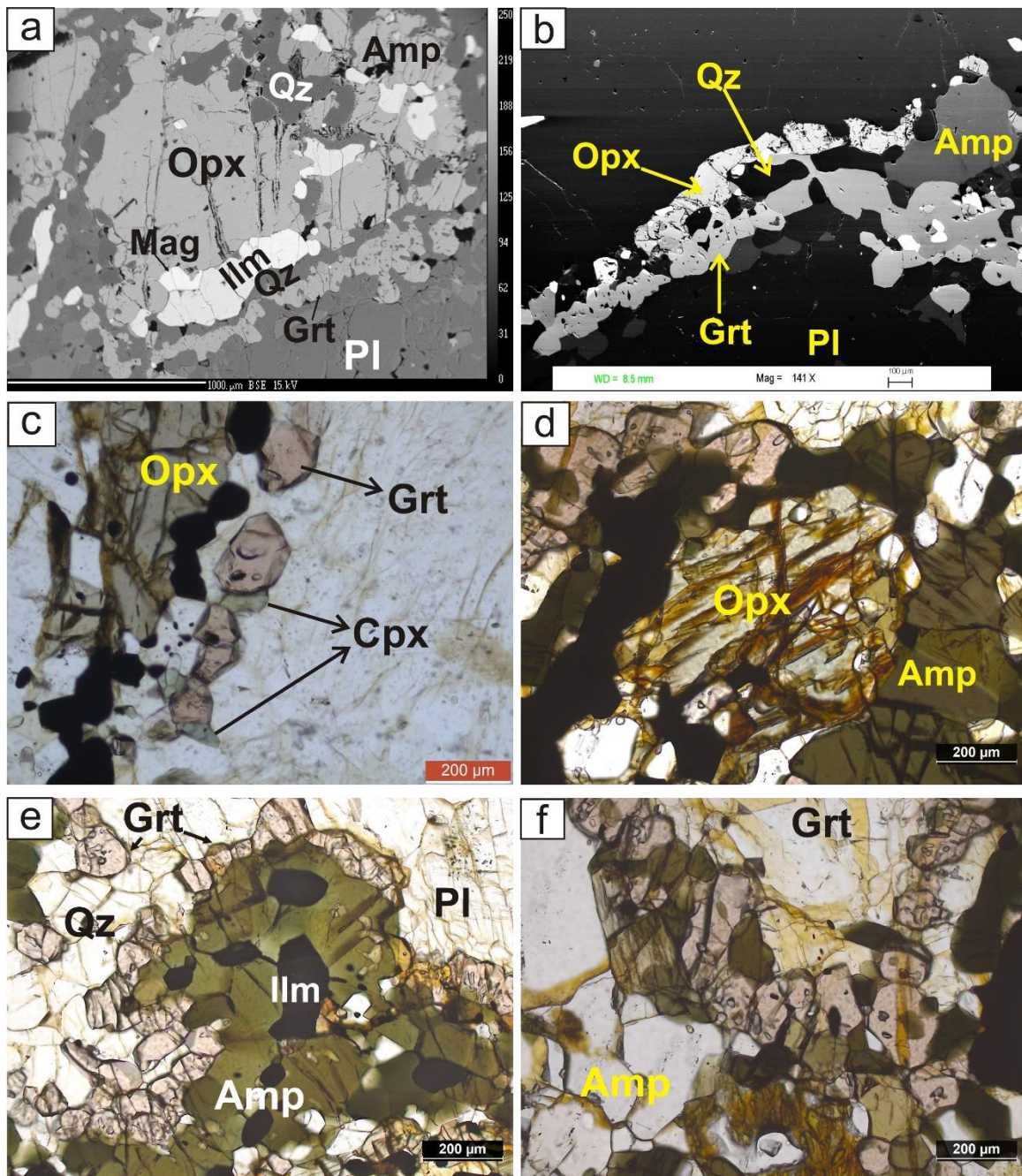


Figure 5.4: (a-b) Garnet quartz double corona separates megacrystic and “lace-like” Opx from plagioclase. Garnet formation is strictly restricted along the margin of plagioclase. The garnet grains are bead-shaped. (c) Clinopyroxene is present in the coronal garnet and shares a non-reactive boundary with the garnet. (d-e) Amphibole partially (d) to fully (e) replaces Opx. (f) Amphibole replaces garnet.

5.1.2 Biotite gneiss (BG):

The major mineral assemblage of this rock type consists of quartz (~35%), plagioclase (~15%), K-feldspar (~35%), biotite (~10%) and garnet (~3%). Minor amounts of oxide phases include ilmenite and magnetite. Unlike charnockite, the modal abundance of K-feldspar dominates plagioclase, and in the QAP diagram (Le Maitre et al. 2005), BG plots in the field of granite (Fig. 5.1). Alternate bands of biotite-rich and quartz-rich layers define the gneissic banding of the rock (Fig. 5.5.a-b).

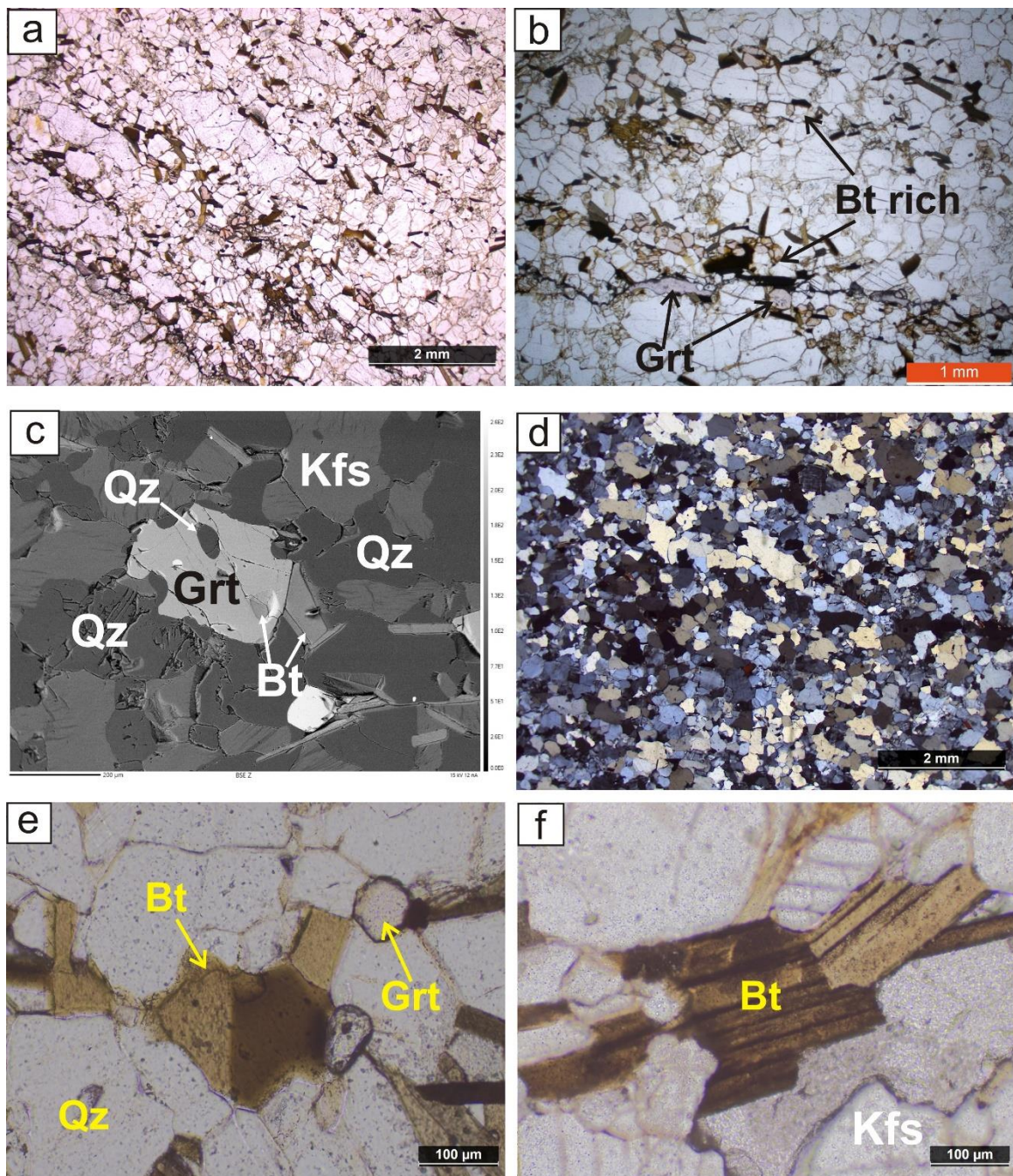


Figure 5.5: (a-b) Biotite gneiss exhibits alternate bands that are rich and poor with biotite. (c) Biotite is present as inclusion in garnet. (d) Fine recrystallised grains of quartz and feldspar in the matrix. (e-f) Biotite present in the recrystallised matrix are also deformed. (f) Fine grain biotite in the rock matrix is bent due to deformation.

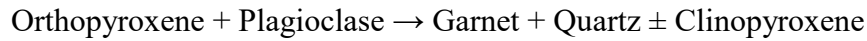
The major hydrous phase in the rock is biotite; it is present as medium-sized grains in the rock matrix (Fig. 5.5.b). Garnet grains are small to medium-sized, subhedral to anhedral (Fig. 5.5.a-c). Biotite is also present as inclusion within garnet (Fig. 5.5.c). Texturally, garnet grains are present in association with biotite. Feldspar (both plagioclase and K-feldspar) and quartz is fine grained and recrystallised (Fig. 5.5.d). The biotites in the fine grained recrystallised matrix are predominantly oriented (Fig. 5.5.a-b) and are often deformed by kinking (Fig. 5.5.e) and bending (Fig. 5.5.f).

5.1.3 Textural evolution:

The textural study suggests that relict magmatic textures are mainly preserved in the coarse-grained feldspar grains. Tabular, euhedral, and 'lath-shaped' plagioclase that exhibit simple and combination twins generally indicate a magmatic origin (Vernon 2004). Inclusions of orthopyroxene in plagioclase indicate its probable magmatic origin. This view is further strengthened by large euhedral orthopyroxene grains that preserve tabular and short prismatic habit, as such morphology is reported in orthopyroxene that crystallises from a melt phase (Smith et al. 2004; Bédard et al. 2007). The fine-grained orthopyroxene that makes a low ($<60^\circ$) dihedral angle (Holness 2006, 2010) with euhedral plagioclase or plagioclase-quartz grain boundaries can be best explained by in-situ crystallisation from an interstitial melt phase (Holness 2006, 2010; Mahapatro et al. 2013). Further, orthopyroxene forms a relict interlocking texture with ilmenite and magnetite, which also vouches for the magmatic origin of the oxide phases. So, the coarse-grained cumulus texture comprising phenocrysts of plagioclase, K-feldspar, quartz, and orthopyroxene, along with oxide phases and fine-grained inter cumulus orthopyroxene, quartz define the magmatic assemblage of the metaporphyratic charnockite.

This magmatic assemblage is further deformed and metamorphosed. Deformation affected the magmatic assemblage of feldspar, orthopyroxene and quartz, resulting in recrystallisation, bending, and sub-grain formation. Even when these plagioclase grains are partially recrystallized into polygonal grains, the faint outline of euhedral faces can still be

identified. These features are consistent with the view that plagioclase phenocrysts were variably deformed. Usually, metamorphism goes hand in hand with deformation. The formation of garnet marks one significant metamorphic overprint of PC. The textural disposition of the garnet quartz double corona between orthopyroxene and plagioclase indicates the following reaction,



The formation of thin coronae of quartz and garnet and strict confinement of garnet along the plagioclase margin indicate that element mobility is significantly limited during the reaction. Possible elemental mobility of Fe, Mg and Si during the reaction is restricted up to the thickness of the double corona. The garnets adjacent to the plagioclase are bead-shaped and assume the shape of adjoining recrystallised plagioclase, which suggests Al is almost immobile. The garnet formation is followed by hydration that forms amphibole, replacing both orthopyroxene and garnet.

Similar to charnockite, garnet formation indicates a significant metamorphic overprint in the biotite gneiss. Biotite formation in the rock matrix presents two possibilities for their formation: (a) primary magmatic biotites or (b) metamorphic biotites by hydration. These biotites present in the matrix define the gneissic banding and can form by replacing garnet during hydration. However, the abundance of garnet is far less (less than three times) compared to biotite to account for biotite formation by garnet replacement during retrogression. Furthermore, the biotites in the rock matrix are highly oriented and deformed, favouring biotite formation before deformation and metamorphism over post metamorphic hydration. The possibility of primary biotite formation is further strengthened by the presence of biotite in the rock matrix prior to garnet is evidenced by biotite inclusions in garnet.

5.2 Phase chemistry:

5.2.1 Analytical techniques:

Major elemental analyses of the metaporphyritic charnockite were carried out at the Department of Geology and Geophysics, Indian Institute of Technology, Kharagpur, using a Cameca SX100 Electron Probe Micro Analyser. It is equipped with four wavelength-dispersive spectrometers (WDS). All points were analysed with 20 nA beam current, 15

kV acceleration voltage, and a beam size of 1 μm . For the analyses, natural minerals and synthetic compounds were used as standards.

Major elemental analyses of the biotite gneiss were carried out at the Geological Survey of India, Kolkata. Analyses were performed using the CAMECA Sx Five Electron Probe Micro Analyser. All points were analysed with 15 kV acceleration voltage, 12 nA beam current and a beam size of 1 μm . For the analyses, natural minerals were used as standards.

Mineral name abbreviations are based on Whitney and Evans (2010). For the calculation of Fe^{3+} , the cation recalculation scheme of Droop (1987) is used. Phase chemistry data of pyroxene (Table 5.1), garnet (Table 5.2), feldspar (Table 5.3), amphibole (Table 5.4), biotite (Table 5.5) and oxides (Table 5.6) are presented.

5.2.2 Metaporphyritic charnockite:

Pyroxene:

The two modes of Opx suggested by the petrographic study do not show any compositional variation. Orthopyroxene is dominantly ferroan ($X_{\text{Mg}} = 0.30\text{-}0.35$) and shows no distinct compositional variation between core and rim. The Al/Ca vs. X_{Mg} diagram (Zhao et al. 2023) plots the orthopyroxene in the metaluminous systems field (Fig. 5.6.a). $X_{\text{Al}} (= \text{Si} + \text{Al} - 2; \text{Kelsey et al. 2003})$ value of orthopyroxene is quite low (≤ 0.02). In the X_{Mg} vs. X_{Al} plot (Fig. 5.6.b) (Rajesh et al. 2011; Zhao et al. 2023), the studied orthopyroxene samples plot in the field resembling orthopyroxenes of ubiquitous igneous origin. The few rare Cpx present with coronal garnet have X_{Mg} of 0.44-0.45.

Feldspar:

Plagioclase composition ($\text{An}_{30\text{-}35}\text{Ab}_{64\text{-}69}\text{Or}_{0\text{-}2}$) is stringently confined in the andesine field close to the oligoclase boundary (Fig. 5.6.c). Plagioclase does not depict any characteristic compositional variation. Albite content of K-feldspar varies between 7-19%. Variation in the albite content of K-feldspar grains does not match any textural trend, e.g. core-rim variation. Feldspar exsolutions are typically antiperthitic in nature. The host plagioclase has an anorthite content of 28-30%, and the lamellae are almost pure orthoclase ($\text{Ab} = \sim 4\%$).

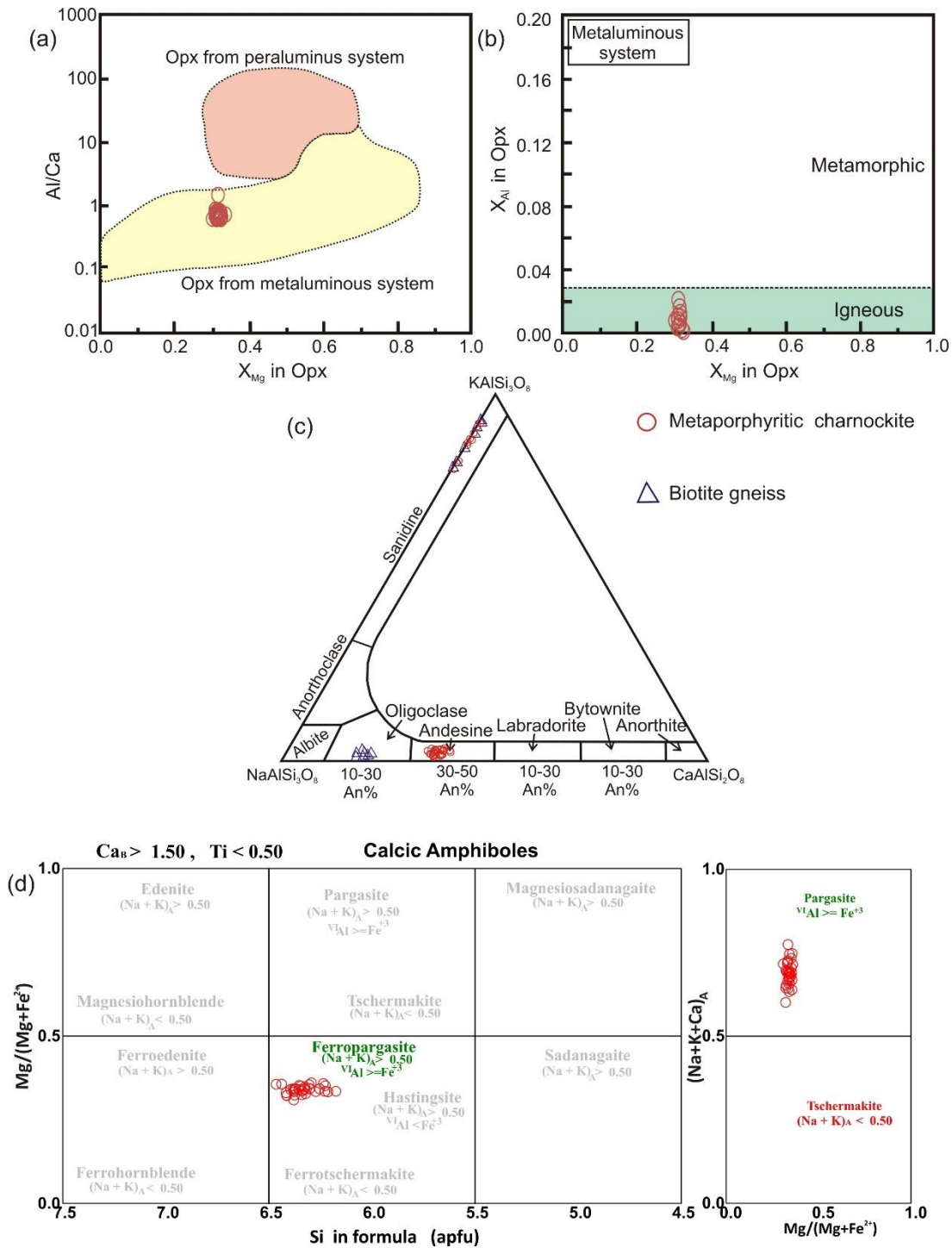


Figure 5.6: (a) In the Al/Ca vs X_{Mg} ($=Mg/(Mg+Fe)$) in Opx diagram (Zhao et al., 2023) Opx composition of PC plots in the metaluminous system. (b) X_{Al} ($=2-(Si+Al)$; Kelsey et al., 2003) vs. X_{Mg} in Opx diagram, (metaluminous system; Zhao et al., 2023 modified after Rajesh et al., 2011) Opx compositions plot (in the field of igneous Opx). (c) Ab-An-Or ternary feldspar classification diagram. Plagioclase composition of metaporphyritic charnockite plots in the andesine field while the plagioclase composition of biotite gneiss plots in the oligoclase field. (d) In the Amphibole classification diagram (Leake et al., 1997), Amp compositions plot in the field of ferropargasite.

Garnet:

The Garnet composition ($\text{Alm}_{65-69}\text{Prp}_{5-8}\text{Grs}_{20-23}\text{Spss}_{3-4}$; $X_{\text{Mg}} = 0.08-0.11$) is dominated by a high almandine component with a considerable amount of grossular. Garnet does not show any core-rim compositional variation.

Amphibole:

According to the classification scheme of Leake et al. (1997), amphibole is classified as ferropargasite (Fig. 5.6.d). It does not have any significant compositional variation. Al content of amphibole is between 1.961-2.083 a.p.f.u. Amphibole has a X_{Mg} of 0.309-0.361.

Oxides:

Ilmenite and magnetite are the two oxides present in the rock. Fe_2O_3 content of ilmenite varies between 3-5wt%.

5.2.3 Biotite gneiss:**Biotite:**

Matrix biotite has a X_{Mg} content of 0.5-0.55. Biotite inclusions in garnet are slightly more magnesian ($X_{\text{Mg}} = \sim 0.6$) than matrix biotite. TiO_2 content of both matrix and inclusion biotite ranges between 3-4 wt%. Matrix biotite does not show any core-rim compositional variation.

Garnet:

Garnet composition ($\text{Alm}_{79-83}\text{Prp}_{7-9}\text{Grs}_{2-3}\text{Spss}_{6-7}$; $X_{\text{Mg}} = 0.08 - 0.11$) is predominantly richer in almandine and significantly depleted in grossular compared to charnockite. Garnet does not show any distinct compositional variation.

Feldspar:

Plagioclase is more albitic ($\text{An}_{13-15}\text{Ab}_{84-86}\text{Or}_{<1}$; oligoclase) (Fig. 5.6.c) than PC. Orthoclase content of plagioclase is almost negligible (<1%). On the other hand, alkali feldspars are chiefly orthoclase rich ($\text{Ab}_{7-20}\text{Or}_{80-93}$). Neither type of feldspars shows any compositional variation.

Table 5.1: Representative microprobe analyses and calculated cations of orthopyroxene based on 6 oxygens

Rock type	Metaporphyrritic charnockite														Clinopyroxene	
	Orthopyroxene														73 / 1.	85 / 1.
Phase	1 / 1.	9 / 1.	13 / 1.	40 / 1.	49 / 07	47 / 1.	49 / 08	49 / 23	49 / 36	10 / 1.	13 / 1.	49 / 37	49 / 46			
Point	48.59	47.97	48.99	49.07	49.07	49.08	49.23	49.36	48.70	49.37	49.46	51.10	50.49			
SiO ₂	0.07	0.06	0.07	0.06	0.06	0.07	0.05	0.06	0.04	0.03	0.05	0.14	0.13			
TiO ₂	1.11	1.09	0.47	0.46	0.46	0.50	0.50	0.52	0.47	0.38	0.51	1.19	1.38			
Al ₂ O ₃	0.81	0.82	0.00	0.19	0.19	0.29	0.00	0.05	0.11	0.00	0.27	0.11	0.44			
Fe ₂ O ₃ *	37.46	38.10	38.94	39.02	39.02	39.05	39.02	39.56	39.17	39.09	38.32	17.39	17.34			
FeO	10.68	9.94	10.18	10.15	10.15	10.15	10.10	10.00	9.95	9.96	9.35	8.02	7.66			
MgO	0.82	0.80	0.73	0.71	0.71	0.64	0.68	0.65	0.63	0.63	0.87	21.38	21.24			
CaO	0.54	0.45	0.45	0.68	0.68	0.65	0.61	0.67	0.55	0.59	0.53	0.27	0.38			
MnO	0.01	0.02	0.01	0.00	0.00	0.02	0.02	0.03	0.00	0.02	0.03	0.40	0.41			
Na ₂ O	0.01	0.01	0.00	0.01	0.01	0.00	0.00	0.01	0.00	0.00	0.00	0.01	0.00			
K ₂ O	100.13	99.26	99.93	100.34	100.34	100.50	100.21	100.98	99.62	100.09	99.41	100.00	99.48			
Total	1.96	1.96	1.99	1.98	1.98	1.98	1.99	1.99	1.99	2.00	1.98	1.98	1.97			
Si	0.00	0.00	0.00	0.00	0.00	0.00	0.00	0.00	0.00	0.00	0.00	0.00	0.00			
Ti	0.06	0.05	0.02	0.02	0.02	0.02	0.02	0.02	0.02	0.02	0.02	0.05	0.06			
Al	0.04	0.03	0.03	0.03	0.03	0.03	0.03	0.03	0.03	0.03	0.04	0.00	0.01			
Ca	0.05	0.03	0.00	0.01	0.01	0.01	0.00	0.00	0.00	0.00	0.01	0.56	0.57			
Fe ⁺³ *	1.26	1.30	1.32	1.32	1.32	1.32	1.32	1.33	1.34	1.33	1.34	0.46	0.45			
Fe ⁺² *	0.64	0.61	0.62	0.61	0.61	0.61	0.61	0.60	0.60	0.60	0.58	0.89	0.89			
Mg	0.02	0.02	0.02	0.02	0.02	0.02	0.02	0.02	0.02	0.02	0.02	0.01	0.01			
Mn	0.00	0.00	0.00	0.00	0.00	0.00	0.00	0.00	0.00	0.00	0.00	0.03	0.03			
Na	0.00	0.00	0.00	0.00	0.00	0.00	0.00	0.00	0.00	0.00	0.00	0.00	0.00			
K	0.34	0.32	0.32	0.32	0.32	0.32	0.32	0.31	0.31	0.31	0.30	0.66	0.67			
X _{Mg}	0.01	0.01	0.01	0.01	0.01	0.01	0.02	0.01	0.01	0.02	0.01	0.04	0.04			
X _{Al}																

*Fe₂O₃ and Fe⁺³ is recalculated after the scheme of Droop (1987)

Table 5.2: Representative microprobe analyses and calculated cations of garnet based on 12 oxygens

Rock type	Metaporphyrictic charnockite										Biotite gneiss		
	Point	26 / 1 .	32 / 1 .	51 / 1 .	69 / 1 .	8 / 1 .	11 / 1 .	53 / 1 .	133 / 1 .	141 / 1 .	154 / 1 .		
SiO ₂		37.44	37.41	37.49	37.23	37.61	37.51	35.88	36.09	35.70	35.97		
TiO ₂		0.00	0.00	0.03	0.03	0.02	0.02	0.02	0.00	0.02	0.01		
Al ₂ O ₃		20.47	20.22	20.31	20.52	19.94	19.97	20.03	20.33	19.82	19.70		
Fe ₂ O ₃ *		1.65	1.46	1.04	1.48	1.28	1.61	3.79	3.30	4.11	3.82		
FeO		30.16	29.87	30.46	29.86	30.17	30.08	27.96	35.50	35.26	34.25		
MgO		1.86	1.67	1.83	1.96	1.56	1.53	1.92	1.88	1.74	1.85		
CaO		7.46	7.78	7.52	7.52	7.86	7.88	7.63	0.96	1.01	1.01		
MnO		1.71	1.69	1.47	1.49	1.80	1.78	1.69	2.66	2.94	3.98		
Na ₂ O		0.00	0.04	0.00	0.00	0.03	0.04	0.01	0.06	0.03	0.03		
K ₂ O		0.00	0.00	0.01	0.02	0.00	0.00	0.00	0.03	0.00	0.00		
Total		100.81	100.24	100.15	100.16	100.31	100.41	98.93	100.82	100.65	100.64		
Si		2.99	3.00	3.01	2.98	3.02	3.01	2.92	2.93	2.92	2.94		
Ti		0.00	0.00	0.00	0.00	0.00	0.00	0.00	0.00	0.00	0.00		
Al		1.92	1.91	1.92	1.94	1.89	1.89	1.92	1.95	1.91	1.90		
Ca		0.10	0.09	0.06	0.09	0.08	0.10	0.23	0.20	0.25	0.23		
Fe ⁺³ *		2.01	2.00	2.04	2.00	2.03	2.02	1.90	2.41	2.41	2.34		
Fe ⁺² *		0.22	0.20	0.22	0.23	0.19	0.18	0.23	0.23	0.21	0.23		
Mg		0.64	0.67	0.65	0.65	0.68	0.68	0.67	0.08	0.09	0.09		
Mn		0.12	0.11	0.10	0.10	0.12	0.12	0.12	0.18	0.20	0.28		
Na		0.00	0.01	0.00	0.00	0.00	0.01	0.00	0.01	0.00	0.00		
K		0.00	0.00	0.00	0.00	0.00	0.00	0.00	0.00	0.00	0.00		
X _{ALM}		0.67	0.67	0.68	0.67	0.67	0.67	0.65	0.83	0.83	0.80		
X _{GRS}		0.07	0.07	0.07	0.08	0.06	0.06	0.08	0.08	0.07	0.08		
X _{PRP}		0.04	0.04	0.03	0.03	0.04	0.04	0.04	0.03	0.03	0.03		
X _{SPSS}		0.21	0.22	0.21	0.22	0.22	0.23	0.23	0.06	0.07	0.09		
X _{Mg}		0.10	0.09	0.10	0.10	0.08	0.08	0.11	0.09	0.08	0.09		

*Fe₂O₃ and Fe⁺³ is recalculated after the scheme of Droop (1987)

Table 5.3: Representative microprobe analyses and calculated cations of feldspar based on 8 oxygens

Rock type	Metaporphyrific charnockite						Biotite gneiss					
	2 / 1 .	15 / 1 .	50 / 2 .	50 / 3 .	4 / 1 .		121 / 1 .	127 / 1 .	131 / 1 .	117 / 1 .	122 / 1 .	
Phase	Pl	Pl	Pl	Pl	Kfs		Pl	Pl	Pl	Kfs	Kfs	
SiO ₂	61.41	59.85	60.16	60.41	64.15		64.77	64.87	64.70	64.85	64.39	
Al ₂ O ₃	24.52	23.95	24.64	24.93	18.41		21.12	21.34	21.09	18.05	17.91	
FeO	0.34	0.22	0.00	0.01	0.04		0.07	0.09	0.10	0.02	0.00	
MgO	0.00	0.00	0.02	0.00	0.01		0.01	0.00	0.00	0.00	0.01	
CaO	6.54	6.75	7.10	7.03	0.02		3.07	3.16	2.90	0.01	0.05	
Na ₂ O	7.86	7.37	7.24	7.23	1.29		10.09	9.94	10.02	0.89	2.22	
K ₂ O	0.21	0.31	0.26	0.32	14.30		0.14	0.10	0.09	15.61	13.70	
Total	100.96	98.46	99.47	99.99	99.17		99.51	99.55	98.97	99.75	98.54	
Si	2.71	2.71	2.69	2.69	2.99		2.87	2.87	2.88	3.01	3.00	
Al	1.28	1.28	1.30	1.31	1.01		1.10	1.11	1.11	0.99	0.98	
Fe ⁺²	0.31	0.33	0.34	0.34	0.00		0.15	0.15	0.14	0.00	0.00	
Mg	0.01	0.01	0.00	0.00	0.00		0.00	0.00	0.00	0.00	0.00	
Ca	0.00	0.00	0.00	0.00	0.00		0.00	0.00	0.00	0.00	0.00	
Na	0.67	0.65	0.63	0.62	0.12		0.87	0.85	0.86	0.08	0.20	
K	0.01	0.02	0.01	0.02	0.85		0.01	0.01	0.01	0.92	0.82	
XOr	0.01	0.02	0.01	0.02	0.88		0.01	0.01	0.01	0.92	0.80	
XAb	0.68	0.65	0.64	0.64	0.12		0.85	0.85	0.86	0.08	0.20	
XAn	0.31	0.33	0.35	0.34	0.00		0.14	0.15	0.14	0.00	0.00	

Table 5.4: Representative microprobe analyses and calculated cations of amphibole based on 23 oxygens

Rock type	Metaporphyrritic charnockite									
Point	12 / 1 .	17 / 1 .	19 / 1 .	24 / 1 .	30 / 1 .	20 / 1 .	21 / 1 .	22 / 1 .	60 / 1 .	61 / 1 .
SiO ₂	40.39	40.96	40.84	41.01	40.51	40.82	41.28	39.96	39.20	39.27
TiO ₂	2.03	1.84	1.84	2.08	1.96	1.70	2.04	2.05	2.03	2.08
Al ₂ O ₃	10.73	11.05	11.11	10.79	10.91	11.02	10.79	10.59	10.68	10.90
Cr ₂ O ₃	0.00	0.05	0.07	0.05	0.00	0.02	0.00	1.30	0.00	0.00
FeO	22.90	23.99	23.76	23.26	23.89	22.66	23.46	23.17	23.57	24.34
MgO	5.89	6.25	5.88	6.10	5.96	6.15	6.34	5.94	5.95	5.89
CaO	11.26	11.26	11.28	11.06	11.03	11.06	11.06	10.75	11.23	11.29
MnO	0.11	0.17	0.12	0.11	0.08	0.14	0.01	0.08	0.21	0.17
Na ₂ O	1.40	1.49	1.34	1.49	1.47	1.36	1.52	1.52	1.52	1.44
K ₂ O	1.62	1.66	1.60	1.60	1.65	1.76	1.72	1.72	1.74	1.70
Total	96.40	98.96	97.89	97.54	97.50	96.68	98.25	97.08	96.16	97.07
Si	6.38	6.30	6.34	6.38	6.32	6.39	6.37	6.27	6.23	6.18
Al ^(IV)	1.62	1.70	1.66	1.62	1.68	1.61	1.63	1.73	1.77	1.82
Ti	0.00	0.00	0.00	0.00	0.00	0.00	0.00	0.00	0.00	0.00
Sum T	8.00	8.00	8.00	8.00	8.00	8.00	8.00	8.00	8.00	8.00
Al ^(VI)	0.37	0.31	0.37	0.36	0.33	0.43	0.34	0.23	0.23	0.20
Ti	0.24	0.21	0.21	0.24	0.23	0.20	0.24	0.24	0.24	0.25
Cr ⁺³	0.00	0.01	0.01	0.01	0.00	0.00	0.00	0.16	0.00	0.00
Fe ⁺³	0.13	0.35	0.26	0.20	0.28	0.19	0.23	0.27	0.33	0.46
Mg	1.39	1.43	1.36	1.41	1.38	1.44	1.46	1.39	1.41	1.38
Fe ⁺²	2.87	2.70	2.78	2.78	2.78	2.74	2.74	2.70	2.79	2.72
Mn	0.00	0.00	0.00	0.00	0.00	0.00	0.00	0.00	0.00	0.00
Sum C	5.00	5.00	5.00	5.00	5.00	5.00	5.00	5.00	5.00	5.00
Mg	0.00	0.00	0.00	0.00	0.00	0.00	0.00	0.00	0.00	0.00
Fe ⁺²	0.02	0.04	0.04	0.04	0.06	0.04	0.06	0.07	0.01	0.02
Mn	0.02	0.02	0.02	0.01	0.01	0.02	0.00	0.01	0.03	0.02
Ca	1.90	1.86	1.88	1.84	1.84	1.86	1.83	1.81	1.91	1.90
Na	0.06	0.08	0.07	0.10	0.08	0.09	0.10	0.11	0.05	0.05
Sum B	2.00	2.00	2.00	2.00	2.00	2.00	2.00	2.00	2.00	2.00
Ca	0.00	0.00	0.00	0.00	0.00	0.00	0.00	0.00	0.00	0.00
Na	0.37	0.37	0.34	0.35	0.36	0.32	0.35	0.35	0.42	0.39
K	0.33	0.33	0.32	0.32	0.33	0.35	0.34	0.35	0.35	0.34
Sum A	0.70	0.69	0.65	0.67	0.69	0.68	0.69	0.69	0.77	0.73
TOTAL	15.70	15.69	15.65	15.67	15.69	15.68	15.69	15.69	15.77	15.73
X _{Mg}	0.32	0.34	0.33	0.33	0.33	0.34	0.34	0.33	0.33	0.34
Sub-Group	Ferropar gasite	Hasting site	Ferropa rgasite	Ferropa rgasite	Ferropar gasite	Ferropa rgasite	Ferropa rgasite	Hasting site	Hastin gsite	Hastin gsite

Table 5.5: Representative microprobe analyses and calculated cations of biotite based on 11 oxygens

Rock type	Biotite gneiss										
	Point	115 / 1.	126 / 1.	129 / 1.	130 / 1.	137 / 1.	142 / 1.	146 / 1.	134 / 1.	135 / 1.	136 / 1.
Texture		Maxtrix									
		Inclusion in garnet									
SiO ₂		36.23	36.44	37.24	36.84	35.86	35.77	36.95	36.64	36.37	37.28
TiO ₂		3.74	3.23	3.27	3.14	2.72	3.46	3.64	3.38	3.27	3.42
Al ₂ O ₃		14.80	14.47	15.00	14.54	14.80	13.63	14.05	13.49	13.72	14.41
FeO		19.69	19.47	19.91	19.34	18.98	19.34	18.79	16.55	16.54	15.43
MgO		11.26	12.26	12.85	12.18	12.11	11.74	12.91	14.19	14.75	15.96
CaO		0.00	0.00	0.00	0.00	0.35	0.06	0.00	0.04	0.01	0.03
MnO		0.00	0.13	0.00	0.12	0.68	0.11	0.14	0.00	0.09	0.14
Na ₂ O		0.10	0.10	0.09	0.08	0.43	0.09	0.13	0.51	0.10	0.26
K ₂ O		9.45	9.55	9.63	9.40	7.42	9.29	9.47	9.08	9.49	9.08
Total		95.37	95.77	98.21	95.84	93.56	93.63	96.20	94.11	94.38	96.20
Si		2.77	2.78	2.77	2.80	2.78	2.79	2.79	2.81	2.78	2.77
Ti		0.22	0.19	0.18	0.18	0.16	0.20	0.21	0.19	0.19	0.19
Al		1.34	1.30	1.31	1.30	1.35	1.25	1.25	1.22	1.24	1.26
Fe ⁺²		1.26	1.24	1.24	1.23	1.23	1.26	1.19	1.06	1.06	0.96
Mg		1.28	1.39	1.42	1.38	1.40	1.37	1.45	1.62	1.68	1.77
Ca		0.00	0.00	0.00	0.00	0.03	0.01	0.00	0.00	0.00	0.00
Mn		0.00	0.01	0.00	0.01	0.04	0.01	0.01	0.00	0.01	0.01
Na		0.01	0.01	0.01	0.01	0.06	0.01	0.02	0.08	0.01	0.04
K		0.92	0.93	0.91	0.91	0.73	0.93	0.91	0.89	0.92	0.86
X _{Mg}		0.50	0.53	0.53	0.53	0.53	0.52	0.55	0.60	0.61	0.65

Table 5.6: Representative microprobe analyses and calculated cations of ilmenite and magnetite at 3 and 4 oxygen basis

Point	38 / 1 .	39 / 1 .	64 / 1 .	23 / 1 .	24 / 1 .	38 / 1 .	39 / 1 .	51 / 1 .	57 / 1 .	58 / 1 .
Phase	Ilm	Ilm	Ilm	Ilm	Ilm	Ilm	Ilm	Mag	Mag	Mag
SiO ₂	0.01	0.03	0.03	0.04	0.02	0.01	0.00	0.08	0.04	0.18
TiO ₂	49.96	50.01	49.46	50.30	50.06	52.92	51.06	0.72	0.09	0.50
Al ₂ O ₃	0.15	0.14	0.11	0.17	0.15	0.14	0.13	1.38	0.30	0.40
Fe ₂ O ₃ *	5.37	5.30	5.16	3.75	3.27	0.00	3.71	65.93	67.86	66.69
FeO*	43.81	43.70	43.20	44.16	43.91	45.58	44.89	31.81	30.94	31.21
MgO	0.25	0.22	0.19	0.27	0.21	0.18	0.18	0.10	0.04	0.19
CaO	0.00	0.03	0.01	0.01	0.04	0.00	0.00	0.05	0.02	0.07
MnO	0.31	0.33	0.36	0.26	0.29	0.20	0.31	0.00	0.03	0.04
Na ₂ O	0.01	0.02	0.01	0.01	0.01	0.01	0.01	0.02	0.00	0.02
Total	100.56	100.57	99.52	99.66	98.78	99.87	101.07	100.26	99.48	99.60
Oxygen	3.00	3.00	3.00	3.00	3.00	3.00	3.00	4.00	4.00	4.00
Si	0.00	0.00	0.00	0.00	0.00	0.00	0.00	0.00	0.00	0.01
Ti	0.95	0.95	0.95	0.96	0.97	1.01	0.96	0.02	0.00	0.01
Al	0.00	0.00	0.00	0.00	0.00	0.00	0.00	0.06	0.01	0.02
Fe ⁺³ *	0.10	0.10	0.10	0.07	0.06	0.00	0.07	1.89	1.97	1.93
Fe ⁺² *	0.92	0.92	0.92	0.94	0.94	0.97	0.94	1.01	1.00	1.00
Mg	0.01	0.01	0.01	0.01	0.01	0.01	0.01	0.01	0.00	0.01
Ca	0.00	0.00	0.00	0.00	0.00	0.00	0.00	0.00	0.00	0.00
Mn	0.01	0.01	0.01	0.01	0.01	0.00	0.01	0.00	0.00	0.00
Na	0.00	0.00	0.00	0.00	0.00	0.00	0.00	0.00	0.00	0.00

*Fe₂O₃ and Fe⁺³ is recalculated after the scheme of Droop (1987)

5.3 Whole rock Geochemistry:

To geochemically characterise the studied granitoids, the whole rock major and trace element composition has been obtained from 29 selected samples. Among them, 14 samples are from the metaporphyritic charnockite, and 15 are from biotite gneiss. Both major and trace element composition is determined from the selected samples. Detailed analytical technique is given in the Appendix.

Major and trace element characteristics of the metaporphyritic charnockite (Table 5.7) and biotite gneiss (Table 5.8) are distinct. The whole rock SiO_2 content of the biotite gneiss ($\text{SiO}_2 = \sim 71\text{--}77\%$) is higher compared to the charnockitic suite ($\text{SiO}_2 = 61\text{--}70\%$).

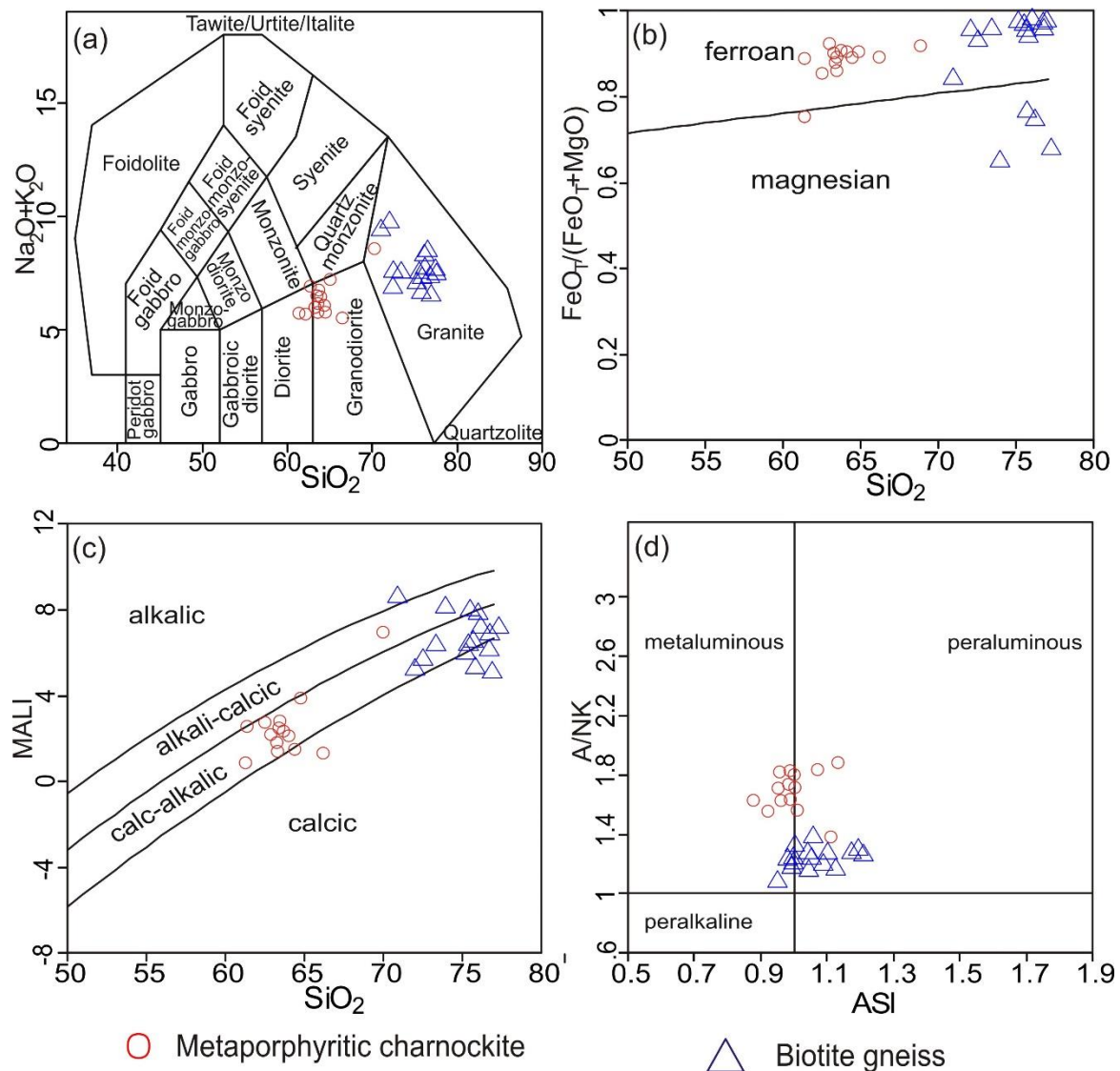


Figure 5.7: Geochemical classification diagrams where metaporphyrific charnockite and biotite gneiss are represented by red circle and blue triangle respectively. (a) In the total alkali silica (TAS) diagram of Middlemost, (1994) metaporphyrific charnockite plots in the field of granodiorite, while biotite gneiss concentrates mainly in the field of granite. (b-d) Granite classification diagrams (Frost et al., 2001) showing ferroan, calc-alkalic, meta- to peraluminous nature for both rock types. MALI = Modified alkali lime index ($\text{Na}_2\text{O} + \text{K}_2\text{O} - \text{CaO}$); ASI= molar $\text{Al}_2\text{O}_3/(\text{Na}_2\text{O} + \text{K}_2\text{O} + \text{CaO} - 1.67 \text{ P}_2\text{O}_5)$; A/NK= molar $\text{Al}_2\text{O}_3/(\text{Na}_2\text{O} + \text{K}_2\text{O})$;

Alkali content ($\text{Na}_2\text{O} + \text{K}_2\text{O}$) of the biotite gneiss (~7.51%) is also higher than charnockite (~6.35%) which characterises biotite gneiss (BG) as granite and metaporphyrific charnockite (PC) as granodiorite in the total alkali-silica (TAS) diagram (Fig. 5.7.a) of Middlemost (1994). On the contrary to these dissimilarities, both these rock types are strictly ferroan ($X_{\text{Fe}}^{\text{PC}} = \sim 0.89$; $X_{\text{Fe}}^{\text{BG}} = \sim 0.90$) (Fig. 5.7.b) and calc alkalic (Fig. 5.7.c) in nature (Frost et al. 2001). Both the rock types straddle the boundary of peraluminous and metaluminous (Frost et al. 2001) (Fig. 5.7.d), with biotite gneiss ($\text{A/CNK} = \sim 1.05$) being slightly peraluminous and metaporphyrific charnockite ($\text{A/CNK} = \sim 0.95$) being slightly metaluminous. K_2O content of the two rock types is moderately high, with $\text{K}_2\text{O}/\text{Na}_2\text{O}$ ranging from 0.6 to 3.

Primitive mantle normalised (after McDonough & Sun, 1995) trace element plot (Fig. 5.7.e) manifests a gradually decreasing trend in abundance from LILE to HFSE. The overall pattern for the two rock types is quite similar, with both showing negative anomalies (Fig. 5.7.e) for Cs, Nb, Ta, Sr, P and Ti. However, the magnitude of the negative anomaly is more significant for biotite gneiss than for metaporphyrific charnockite. Also, in contrast to biotite gneiss, metaporphyrific charnockite shows a pronounced depletion of Th. Chondrite normalised (McDonough and Sun 1995) REE patterns of the two rock types also overlap (Fig. 5.7.f). LREE is slightly enriched compared to HREE ($\text{La}_\text{N}/\text{Yb}_\text{N} = 2.6-17.0$ for BG; $\text{La}_\text{N}/\text{Yb}_\text{N} = 2.4-11.7$ for PC). HREE pattern for both rock types is essentially flat ($\text{Gd}_\text{N}/\text{Yb}_\text{N} = \sim 1.3$ for BG; $\text{Gd}_\text{N}/\text{Yb}_\text{N} = \sim 1.6$ for PC). Negative Eu anomaly ($\text{Eu}/\text{Eu}^* = 0.1-0.7$ for BG; $\text{Eu}/\text{Eu}^* = 0.4-1.0$ for PC) is discerned for both the rock types, but it is slightly more enhanced for BG. The overall REE content of biotite gneiss is higher than in the metaporphyrific charnockite. The primitive mantle normalised trace element plot and the chondrite normalised REE pattern of the charnockites and biotite gneiss are compared with ferroan granitoids from other parts of CGGC (Mukherjee et al. 2018, 2022; Sequeira et al. 2022) and the overall pattern is quite similar (Fig. 5.7.e-f). Distinctly high values of the

HFSEs (Ce, Nb, Zr, Y) and high value of Ga/Al designates both of these two ferroan granitoids as A-type granites according to the discrimination diagram (Fig. 5.7.g-j) of Whalen et al., (1987).

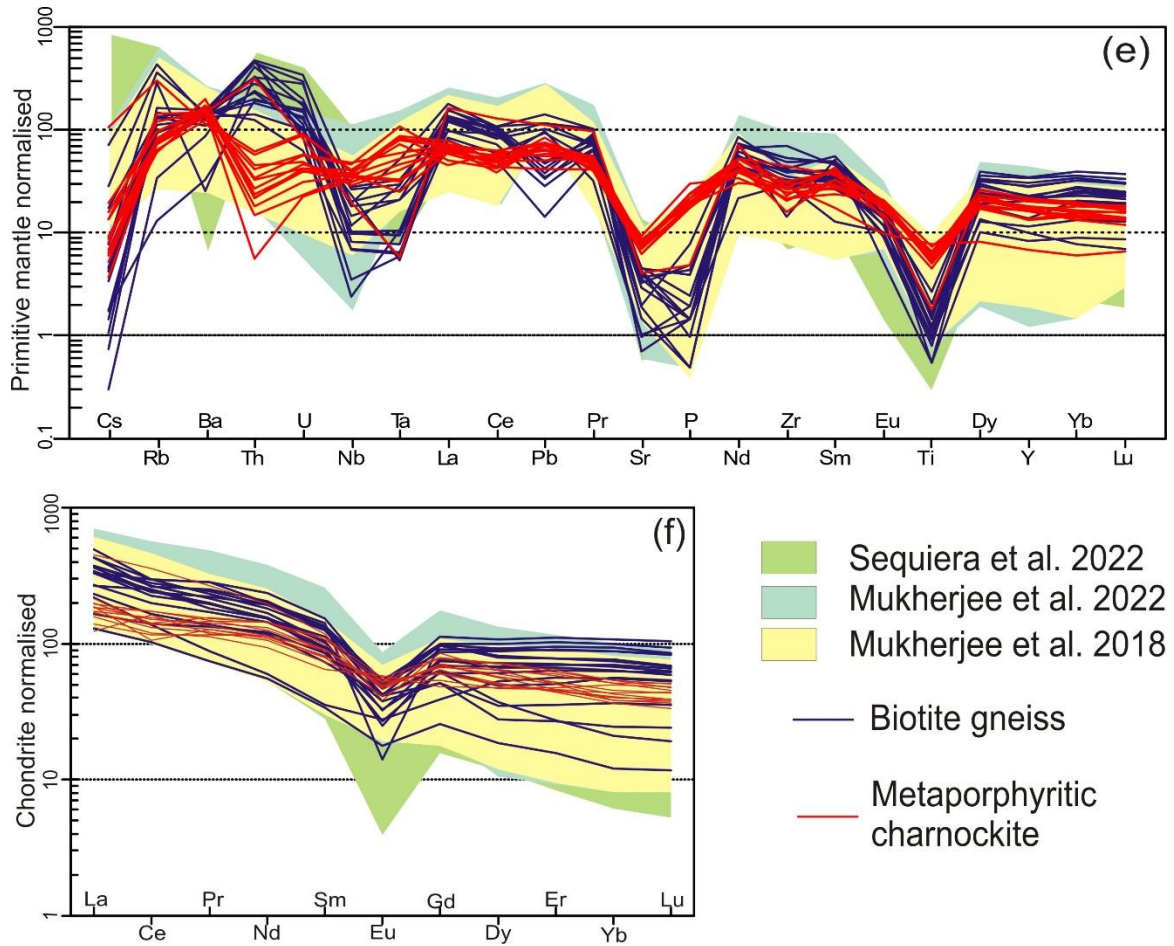


Figure 5.7 (continued): (e) Primitive mantle normalised (after McDonough & Sun, 1995) trace element plot is showing negative anomalies for Cs, Nb, Ta, Sr, P and Ti. The trace element plot of metaporphyritic charnockite and biotite gneiss are compared with ferroan granitoids from CGGC (Mukherjee et al., 2018a, 2022; Sequeira et al., 2022). (f) Chondrite normalised (McDonough and Sun, 1995) Chondrite normalised REE patterns of the two rock types. The REE plot of metaporphyritic charnockite and biotite gneiss are compared with published ferroan granitoids from CGGC (Mukherjee et al., 2018a, 2022; Sequeira et al., 2022).

Major (FeO_T , MgO , TiO_2 , A/CNK, CaO and P_2O_5) and trace elements (Nb, Sr) forms distinct, coherent trend in the variation diagrams with SiO_2 (Fig. 5.8.a-h). In the bivariate plots, FeO_T , MgO , TiO_2 , CaO , P_2O_5 , Sr and Nb exhibit negative correlation while A/CNK show positive correlation with SiO_2 . However, in the bivariate plots versus maficity ($=\text{FeO}_T + \text{MgO}$), TiO_2 , CaO , P_2O_5 , Nb and Eu show a strong positive correlation (Fig. 5.8.j, l, n, o, p). SiO_2 , A/CNK and $(\text{Na}_2\text{O} + \text{K}_2\text{O})$ demonstrate a negative correlation

with increasing maficity (Fig. 5.8.i, k, m). The major oxide and trace element trends in the variation diagrams are quite consistent with the overall trend of CGGC ferroan granitoids (Mukherjee et al. 2018, 2022; Sequeira et al. 2022) (Fig. 5.8).

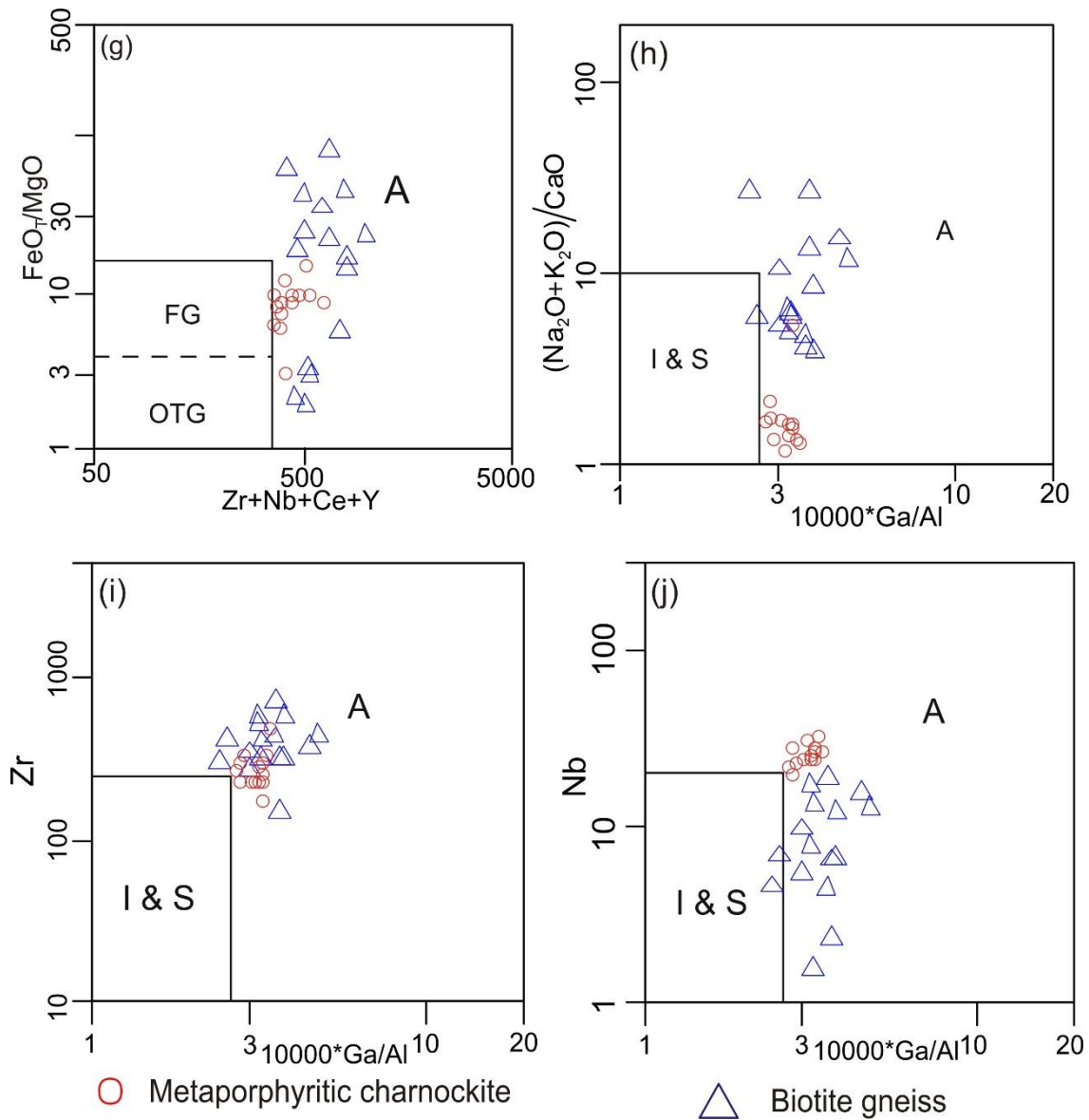


Figure 5.7 (continued): (g-j) Granite classification diagrams (Whalen et al., 1987) classify both metaporphyritic charnockite and biotite gneiss as A-type granites.

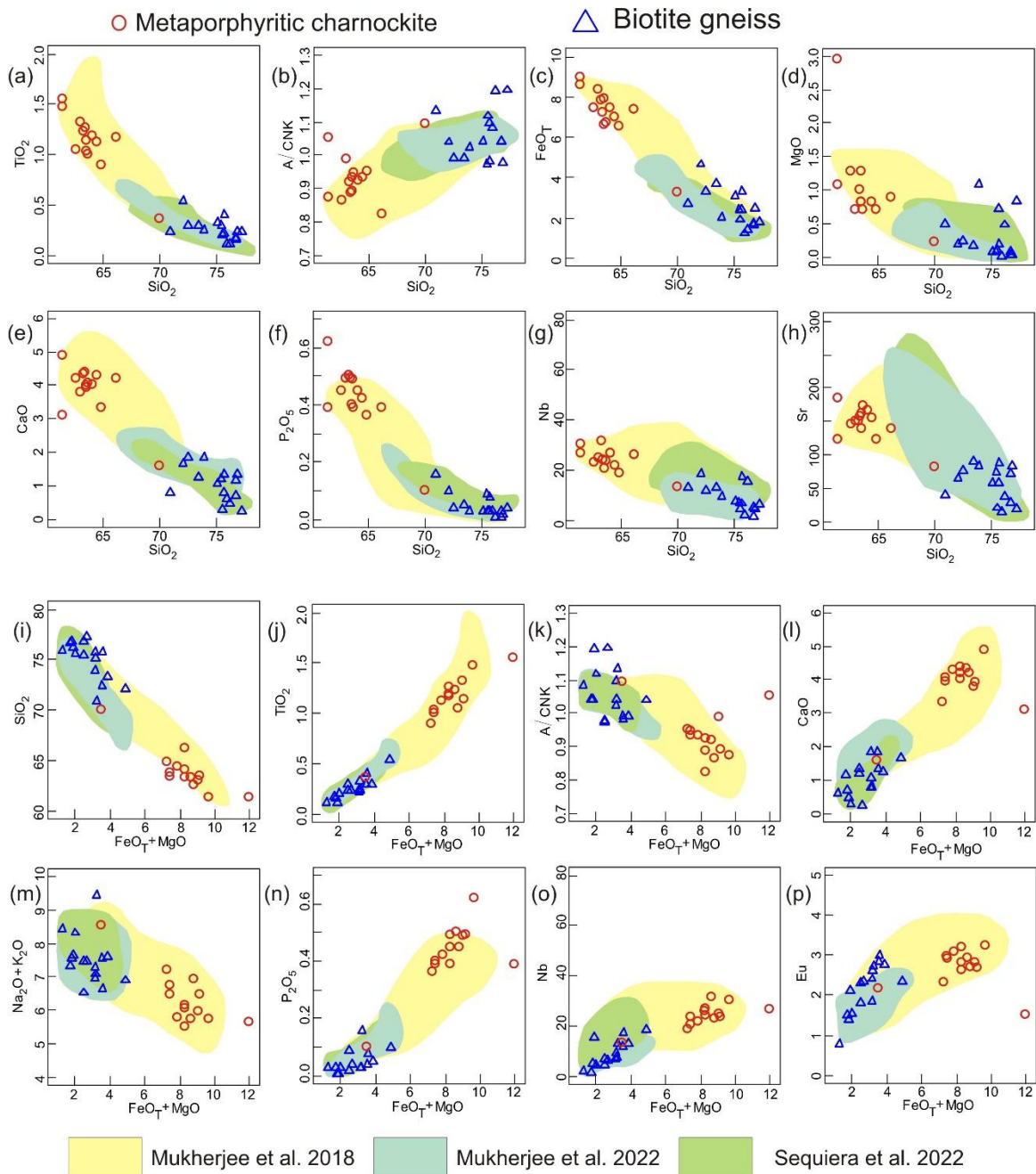


Figure 5.8: Metaporphyritic charnockite and biotite gneiss, bulk rock compositions are plotted in the variation diagram of SiO_2 vs TiO_2 (a), A/CNK (b), FeO_T (c), MgO (d), CaO (e), P_2O_5 (f), Nb (g), Sr (h) and $(\text{FeO}_T + \text{MgO})$ vs SiO_2 (i), TiO_2 (j), A/CNK (k), CaO (l), $\text{Na}_2\text{O} + \text{K}_2\text{O}$ (m), P_2O_5 (n), Nb (o), Eu (p) (Major oxides in wt% and trace element in ppm). Further compositions are compared with CGGC ferroan granitoids (Mukherjee et al., 2018a, 2022; Sequeira et al., 2022).

Table 5.7: Major (wt%) and trace element (ppm) composition of representative samples of metaporphyritic charnockite

Sample	SD1	SD2	SD9A	SD11	SD12	SD13	SD14
Location on Map	C1	C14	C8	C7	C6	C5	C4
SiO ₂	66.22	61.39	64.09	64.43	63.73	63.48	62.97
TiO ₂	1.17	1.47	1.18	1.12	1.01	1.14	1.33
Al ₂ O ₃	12.83	15.02	14.48	15.08	15.63	14.19	14.82
MnO	0.13	0.17	0.15	0.15	0.14	0.12	0.17
FeO _T	7.42	8.61	7.48	7.03	6.72	7.89	8.34
CaO	4.22	4.90	4.01	4.29	4.08	3.93	3.80
MgO	0.89	1.07	0.79	0.82	0.70	1.27	0.70
Na ₂ O	3.42	3.62	3.26	3.72	3.80	3.08	2.89
K ₂ O	2.09	2.13	2.81	2.05	2.65	3.4	3.07
P ₂ O ₅	0.39	0.62	0.45	0.42	0.39	0.49	0.49
FeO _T /[Fe O _T +MgO]	0.89	0.89	0.90	0.90	0.91	0.86	0.92
FeO _T +Mg O	8.31	9.68	8.27	7.85	7.42	9.16	9.04
A/CNK	0.82	0.87	0.92	0.93	0.95	0.89	0.99
K ₂ O+Na ₂ O	5.51	5.75	6.07	5.77	6.45	6.48	5.96
K ₂ O/Na ₂ O	0.61	0.59	0.86	0.55	0.70	1.10	1.06
Cs	0.13	0.41	0.28	0.18	0.18	0.08	0.33
Rb	38.24	58.09	47.38	36.67	50.07	46.53	57.02
Ba	824.20	1010.13	1156.60	1029.28	1093.11	975.62	1106.91
Th	4.99	2.73	1.73	0.45	2.15	1.19	1.78
U	1.85	1.14	0.84	0.45	0.93	0.47	0.79
Nb	26.09	30.36	26.94	21.71	23.56	23.58	25.03
Ta	3.24	4.05	3.08	3.21	0.92	1.22	2.68
La	50.94	37.71	47.20	32.87	39.54	43.97	29.32
Ce	83.89	73.56	87.30	71.40	85.97	106.18	99.79
Pr	13.52	10.52	14.49	10.78	11.83	13.70	11.02
Nd	65.41	42.53	66.27	51.95	51.24	57.14	51.88
Sm	14.84	9.59	16.31	11.86	12.06	13.44	13.15
Eu	2.61	3.25	3.19	3.08	2.91	2.69	2.82
Gd	14.03	9.67	15.75	11.91	12.01	13.99	13.35
Dy	15.77	11.75	17.74	12.29	12.45	14.09	15.79
Er	9.62	7.64	10.22	7.16	7.26	8.05	9.23
Yb	8.31	7.97	8.69	6.43	6.51	6.88	8.23
Lu	1.26	1.18	1.17	0.96	0.92	0.95	1.12
Sr	139.50	184.79	166.30	154.44	173.02	138.20	150.73
Y	87.76	70.79	93.68	57.76	69.85	76.77	86.63
Zr	472.67	226.85	293.08	322.03	279.96	168.35	217.65
Hf	11.29	5.47	7.00	8.71	6.75	4.24	5.56
Pb	7.67	6.29	8.85	10.61	9.87	11.41	9.67
Ga	23.63	25.17	25.25	23.16	26.62	24.63	25.88
TZr(°C)(1)	845.8	775.7	812.3	822.3	809.4	758.0	793.1
TZr(°C)(2)	792.1	710.7	758.2	770.3	755.3	693.9	739.2
TAp(°C)(3)	1022.2	1033.8	1018.5	1012.8	995	1023.5	1017.8
La _N /Lu _N	11.51	9.10	11.45	9.74	12.18	13.18	7.46
La _N /Yb _N	4.17	3.21	3.69	3.47	4.13	4.34	2.42
Gd _N /Yb _N	1.37	0.98	1.47	1.50	1.49	1.65	1.31
Eu/Eu*	0.55	1.03	0.61	0.79	0.74	0.60	0.65

Table 5.7 continued

Sample	SD15	SD16	SD17	SD47	SD52A	SD53N	SD59A
Location on Map	C2	C3	C9	C13	C10	C11	C12
SiO ₂	63.50	63.36	63.30	69.99	62.55	64.83	61.4
TiO ₂	1.04	1.26	1.23	0.36	1.05	0.9	1.56
Al ₂ O ₃	15.60	14.68	14.71	15.1	14.85	14.92	13.55
MnO	0.14	0.15	0.16	0.05	0.12	0.11	0.13
FeO _T	6.65	7.24	7.82	3.26	7.49	6.53	9.01
CaO	3.97	4.38	4.33	1.58	4.19	3.35	3.12
MgO	0.81	1.01	0.85	0.22	1.28	0.7	2.94
Na ₂ O	3.94	3.52	3.41	3.04	3.67	3.18	1.99
K ₂ O	2.81	2.61	2.31	5.49	3.25	4	3.63
P ₂ O ₅	0.40	0.49	0.50	0.1	0.45	0.36	0.39
FeO _T /[Fe O _T +MgO]	0.89	0.88	0.90	0.94	0.85	0.90	0.75
FeO _T +Mg O	7.46	8.25	8.67	3.48	8.77	7.23	11.95
A/CNK	0.93	0.89	0.92	1.09	0.86	0.95	1.05
K ₂ O+Na ₂ O	6.75	6.13	5.72	8.53	6.92	7.18	5.62
K ₂ O/Na ₂ O	0.71	0.74	0.68	1.81	0.89	1.26	1.82
Cs	0.13	0.11	0.20	0.17	0.14	0.29	2.25
Rb	44.28	44.44	43.71	86.68	44.99	72.18	182.07
Ba	1326.60	974.83	903.38	973.42	1013.99	1004.62	750.68
Th	1.89	1.45	3.32	25.35	2.63	3.63	4.64
U	0.80	0.63	1.16	1.64	0.85	0.99	1.77
Nb	20.59	24.11	31.89	13.10	22.98	19.07	26.80
Ta	1.71	1.95	2.22	0.21	1.18	1.51	2.97
La	40.25	43.73	46.35	106.12	41.29	44.22	44.70
Ce	80.18	92.07	105.53	217.71	95.19	65.20	74.73
Pr	11.31	13.20	14.14	24.75	12.52	11.90	10.29
Nd	48.19	60.19	66.04	90.07	51.85	49.81	38.59
Sm	10.87	13.40	15.80	17.56	13.40	11.66	7.04
Eu	2.99	2.81	2.93	2.15	2.72	2.32	1.52
Gd	10.68	13.41	15.57	16.96	13.88	12.61	6.86
Dy	11.57	14.71	17.39	15.62	13.94	12.68	5.52
Er	7.40	8.39	9.88	8.07	7.39	7.05	3.13
Yb	6.97	7.32	8.64	6.16	6.21	5.87	2.65
Lu	1.09	1.06	1.24	0.91	0.92	0.82	0.45
Sr	162.17	156.66	150.24	80.85	146.36	123.83	123.91
Y	58.27	78.17	94.09	73.96	72.56	69.88	29.55
Zr	260.47	216.89	332.46	242.25	221.80	223.25	298.46
Hf	6.98	5.40	7.81	6.27	5.37	5.46	9.54
Pb	12.56	9.43	8.38	16.93	11.12	11.31	11.13
Ga	22.68	24.75	26.28	26.11	23.93	22.27	20.31
TZr(°C)(1)	800.2	778.0	821.9	824.4	773.9	792.8	827.5
TZr(°C)(2)	743.7	715.9	768.4	785.0	708.9	737.9	781.6
TAp(°C)(3)	995.8	1022.2	1024.4	904	1001.1	996.7	968
La _N /Lu _N	10.56	11.76	10.62	33.36	12.77	15.41	28.51
La _N /Yb _N	3.92	4.06	3.65	11.70	4.52	5.11	11.47
Gd _N /Yb _N	1.24	1.48	1.46	2.23	1.81	1.74	2.10
Eu/Eu*	0.84	0.64	0.57	0.38	0.61	0.58	0.67

N represents normalisation after McDonough and Sun (1995) (1)Watson and Harrison (1983); (2) Boehnke et al. (2013); (3)Harrison and Watson (1984)

Table 5.8: Major (wt%) and trace element (ppm) composition of representative samples of biotite gneiss

Sample	SD4A	SD5A	SD5B	SD6	SD7	SD22	SD23	SD24
Location on Map	B4	B2	B12	B14	B13	B3	B5	B6
SiO ₂	73.41	75.76	75.48	75.12	72.49	76.22	70.94	77.26
TiO ₂	0.30	0.41	0.30	0.33	0.29	0.11	0.23	0.24
Al ₂ O ₃	13.06	11.70	12.55	12.54	13.76	13.49	14.70	11.65
MnO	0.06	0.05	0.03	0.02	0.07	ND	0.08	0.02
FeO _T	3.69	3.35	2.42	3.07	3.30	1.40	2.72	1.79
CaO	1.24	1.35	1.23	1.07	1.86	0.49	0.78	0.27
MgO	0.17	0.20	0.07	0.07	0.23	0.48	0.49	0.83
Na ₂ O	4.87	4.06	4.60	4.31	4.11	3.82	2.37	2.14
K ₂ O	2.71	2.59	2.88	2.76	3.43	3.82	7.07	5.30
P ₂ O ₅	0.05	0.08	0.09	0.03	0.04	0.01	0.16	0.04
FeO _T /[FeO _T +MgO]	0.96	0.94	0.97	0.98	0.93	0.74	0.85	0.68
FeO _T +MgO	3.86	3.55	2.49	3.14	3.53	1.88	3.21	2.62
A/CNK	0.99	0.98	0.97	1.04	0.99	1.19	1.13	1.20
K ₂ O+Na ₂ O	7.58	6.65	7.48	7.07	7.54	7.64	9.44	7.44
K ₂ O/Na ₂ O	0.56	0.64	0.63	0.64	0.83	1.00	2.98	2.48
Cs	0.07	0.10	0.09	0.10	0.09	0.37	0.60	1.50
Rb	56.59	58.14	48.24	43.63	79.08	78.07	217.52	263.78
Ba	940.10	968.07	921.52	885.33	723.63	886.88	970.72	901.96
Th	16.16	22.50	14.62	25.95	19.26	11.47	37.89	18.60
U	3.01	3.66	2.67	5.68	2.54	2.04	4.05	2.10
Nb	13.20	17.33	6.78	7.79	11.87	15.39	12.84	6.44
Ta	0.97	1.10	0.35	1.08	0.78	0.20	1.93	0.35
La	63.36	89.09	64.18	102.58	81.07	78.60	116.60	54.71
Ce	154.65	172.09	121.75	162.13	147.36	137.50	180.98	100.83
Pr	16.73	22.50	15.90	23.38	20.63	18.10	26.18	12.83
Nd	70.07	88.82	65.73	93.58	87.56	69.86	107.77	53.99
Sm	16.69	20.11	14.09	19.49	19.13	12.53	22.65	10.82
Eu	2.78	3.01	2.32	2.62	2.84	2.13	2.71	2.34
Gd	17.23	19.88	13.66	19.16	19.36	10.21	22.36	10.18
Dy	21.54	24.48	16.66	20.19	22.71	6.80	26.38	8.61
Er	14.42	16.52	11.18	12.52	15.22	4.28	17.78	5.65
Yb	14.15	16.00	11.30	12.34	14.95	3.93	17.30	5.88
Lu	2.05	2.29	1.62	1.70	2.09	0.59	2.56	0.88
Sr	91.16	88.88	74.10	58.52	76.13	37.81	38.91	19.35
Y	122.06	147.16	87.27	94.45	130.70	35.92	149.56	49.58
Zr	408.03	514.77	420.67	566.98	566.96	373.12	442.32	317.00
Hf	11.61	13.67	12.71	18.20	15.92	16.16	15.33	9.99
Pb	5.19	6.37	4.26	5.72	7.41	15.50	21.43	14.20
Ga	22.44	19.57	16.99	21.00	27.65	32.22	37.37	22.52
TZr(°C)(1)	868	896	872.3	912.9	901.2	884.3	889.3	870.8
TZr(°C)(2)	834	869.7	839.7	893.4	873.8	865.2	865.6	850
TAp(°C)(3)	871.6	937.3	946.2	843.7	843	769.6	963.1	887.6
La _N /Lu _N	8.82	11.09	11.27	17.20	11.02	37.79	12.98	17.80
La _N /Yb _N	3.04	3.78	3.86	5.65	3.68	13.58	4.58	6.32
Gd _N /Yb _N	0.99	1.00	0.98	1.26	1.05	2.10	1.05	1.40
Eu/Eu*	0.50	0.46	0.51	0.41	0.45	0.57	0.37	0.68

Table 5.8: continued

Sample	SD25	SD26	SD27A	SD28	SD42	SD48	SD54A
Location on Map	B7	B8	B9	B10	B15	B11	B1
SiO ₂	75.73	76.79	76.92	72.07	76.72	76	75.6
TiO ₂	0.22	0.16	0.23	0.54	0.18	0.11	0.2
Al ₂ O ₃	12.45	12.05	12.16	12.77	12.61	12.9	12.61
MnO	0.06	0.01	0.02	0.06	0.03	0.03	0.06
FeO _T	2.39	1.73	2.45	4.65	1.64	1.22	1.90
CaO	0.82	0.70	1.37	1.67	1.15	0.6	0.3
MgO	0.73	0.07	0.03	0.20	0.04	0.02	0.1
Na ₂ O	3.51	3.81	5.15	3.19	3.67	3.07	3.11
K ₂ O	3.78	3.73	1.37	3.70	3.67	5.35	5.2
P ₂ O ₅	0.03	0.01	0.02	0.10	0.03	0.03	0.03
FeO _T /[Fe O _T +MgO]	0.77	0.96	0.99	0.96	0.98	0.98	0.95
FeO _T +Mg O	3.12	1.80	2.48	4.85	1.68	1.24	2.00
A/CNK	1.10	1.04	0.98	1.04	1.04	1.08	1.12
K ₂ O+Na ₂ O	7.29	7.54	6.52	6.89	7.34	8.42	8.31
K ₂ O/Na ₂ O	1.08	0.98	0.27	1.16	1.00	1.74	1.67
Cs	0.04	0.02	0.01	0.02	0.16	0.16	0.03
Rb	56.57	88.58	20.32	98.82	67.13	171.55	81.16
Ba	1024.06	862.72	581.54	1020.15	846.78	169.74	1011.00
Th	26.22	36.13	33.05	38.50	38.30	26.60	9.96
U	1.98	5.98	3.47	6.91	1.72	2.29	1.26
Nb	6.65	5.35	4.51	18.40	1.56	2.28	4.56
Ta	0.39	0.29	0.23	1.23	0.39	0.22	0.24
La	78.55	80.47	89.39	78.41	85.44	101.13	51.63
Ce	153.52	149.19	162.32	182.87	149.56	182.62	83.84
Pr	18.12	18.10	19.96	21.53	18.45	26.12	8.17
Nd	70.45	70.69	77.12	83.40	70.21	91.08	27.33
Sm	13.91	15.21	15.50	18.63	13.52	21.13	5.22
Eu	2.41	1.40	1.81	2.35	1.50	0.80	1.55
Gd	12.58	14.79	15.24	18.15	12.22	19.36	7.73
Dy	12.14	17.70	16.41	22.33	9.19	19.32	12.97
Er	8.06	11.31	10.62	14.24	4.38	12.37	8.95
Yb	8.99	10.93	10.30	14.16	3.41	11.94	8.96
Lu	1.33	1.55	1.44	2.08	0.47	1.67	1.30
Sr	58.12	29.44	83.37	64.88	71.02	13.96	20.39
Y	59.44	89.60	95.80	120.17	43.29	98.57	88.89
Zr	325.25	277.37	428.68	733.08	324.46	151.62	307.94
Hf	10.99	10.30	12.90	21.09	10.22	5.62	8.66
Pb	7.18	7.46	4.99	7.07	17.48	17.56	14.51
Ga	24.90	18.89	22.68	24.02	21.36	24.76	16.21
TZr(°C)(1)	861.3	842.3	877.2	937.3	857	789.4	858.5
TZr(°C)(2)	833.1	808.5	846.9	921.7	825.9	746.8	830.8
TAp(°C)(3)	849.3	774.8	827.6	924.7	858.4	851.8	848.1
La _N /Lu _N	16.87	14.77	17.67	10.76	51.35	17.23	11.34
La _N /Yb _N	5.93	5.00	5.90	3.76	17.05	5.75	3.91
Gd _N /Yb _N	1.13	1.09	1.20	1.04	2.90	1.31	0.70
Eu/Eu*	0.55	0.28	0.36	0.39	0.36	0.12	0.75

N represents normalisation after McDonough and Sun (1995) (1)Watson and Harrison (1983); (2) Boehnke et al. (2013); (3)Harrison and Watson (1984)

5.4 Estimation of Magma temperature:

Estimating the temperature of magma that solidified into igneous rocks is a valuable tool in understanding the petrogenesis of the rock (Boehnke et al. 2013). A high magma temperature is a prerequisite for both A-type granitoids and charnockites (Clemens et al. 1986; King et al. 2001; Frost and Frost 2008b). Assessment of the magmatic temperature

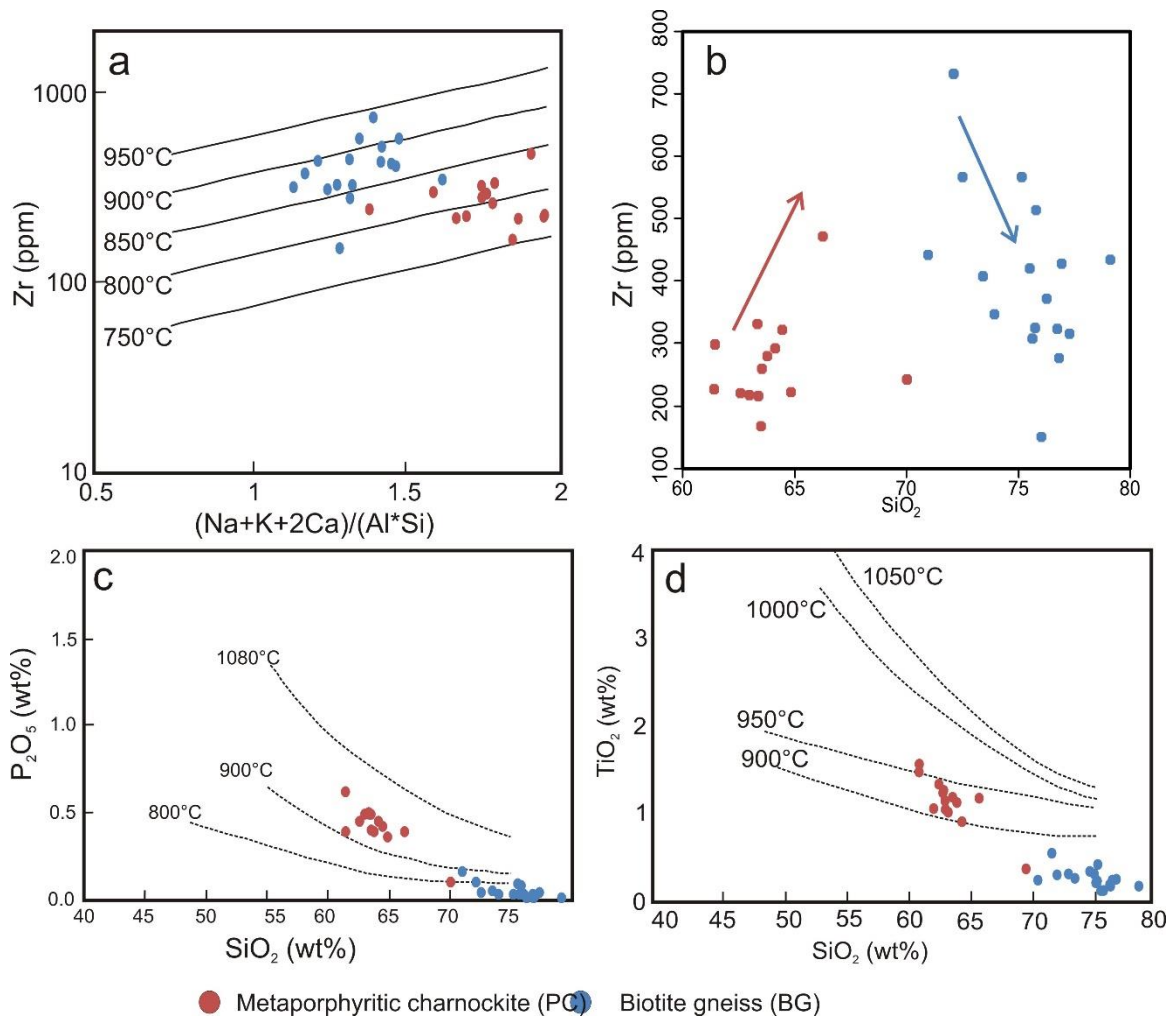


Figure 5.9: (a) Zircon saturation temperature (Watson and Harrison, 1983) of metaporphyritic charnockite and biotite gneiss are plotted in the Zr vs $M (=Na+K-2Ca)/(Al*Si)$. (b) Zr vs SiO_2 diagram demonstrates the opposite trend between PC and BG in Zr with increasing SiO_2 . (c) P_2O_5 vs SiO_2 plot constrain apatite saturation temperature (Harrison and Watson, 1984) for both rocks. (d) TiO_2 vs SiO_2 plot constrain magmatic temperature.

is difficult due to the lack of proper mineral pairs and low-temperature re-equilibration (Miller et al. 2003). Zircon saturation temperature (T_{Zr}) (Watson and Harrison 1983) often provides a simple and robust proxy for the magmatic temperature since zircon solubility is

extremely sensitive to temperature and zircon is prevalent in felsic and intermediate rocks as an accessory phase (Miller et al. 2003).

Although zircon saturation thermometry has been extensively used over the past few decades, zircon saturation is essentially dependent on the bulk composition (on the value of $M = (K+Na+2Ca)/(Al*Si)$) (Watson and Harrison 1983). Zircon saturation is further complicated by the inheritance of older zircon and the dynamic nature of the zircon saturation temperature during fractional crystallisation (King et al. 2001). As fractional crystallisation proceeds, zircon saturation temperature increases while the actual magmatic temperature decreases (Siégel et al. 2018). Based on all these, Siégel et al. 2018 argued that T_{Zr} estimates a 'theoretical' temperature, frequently deviating from the actual magma temperature. The authors further argued that the bulk rock zircon saturation thermometry applies to silicic rocks ($> 64\% SiO_2$) with $0.9 < M < 1.9$ in the absence of inherited zircon. For a robust estimation of magmatic temperature, several independent thermometers should be used along with a zircon saturation thermometer (Watson and Harrison 1983; Boehnke et al. 2013). Apart from the zircon saturation thermometer, apatite (Harrison and Watson 1984; Bea et al. 1992) and Fe-Ti oxide (Green and Pearson 1986) saturation thermometry are used.

All prior work (Mukherjee et al. 2018, 2022; Sequeira et al. 2022) on the Mesoproterozoic ferroan granites from various parts of the CGGC suggests that they do not contain any inherited zircons. All samples of the biotite gneiss fall within the recommended bulk composition range of $0.9 < M < 1.9$ with $SiO_2 > 64\%$. The zircon saturation thermometry of Watson and Harrison (1983) (Fig. 5.9.a) provides a magmatic temperature range of $790 - 940^\circ C$ with an average of $875 \pm 30^\circ C$. However, among the charnockite samples, only five samples are present in the recommended range of Siégel et al. 2018 and are considered for estimating the magmatic temperature. This yields a magmatic temperature in the range of $790 - 850^\circ C$ with an average value approximately $50^\circ C$ less than biotite gneiss (average $820 \pm 15^\circ C$). The calibration of Boehnke et al. (2013) yields a magmatic temperature $25 - 50^\circ C$ less than the calculations of Watson and Harrison 1983 with an average value of $850 \pm 40^\circ C$ and $770 \pm 20^\circ C$ respectively for biotite gneiss and charnockite. In Zr vs SiO_2 diagram (Fig. 5.9.b), Charnockite succumbed to a positive slope while biotite gneiss gives a negative slope, suggesting that the magma was undersaturated initially while during the crystallisation of BG protolith, it was saturated by Zr. Zircon

saturation thermometry thus provides a minimum temperature for charnockites but a maximum temperature for biotite gneiss (Jung and Pfänder 2007). Such effects of zircon saturation thermometry are well documented during fractional crystallisation (Siégel et al. 2018).

Apart from zircon, apatite is another customary accessory phase in granitoids. It is the most common, if not only phosphorus-bearing phase that dominates the bulk rock P_2O_5 content. The solubility of apatite in magma depends on the temperature; thus, the apatite saturation thermometry is quite reliable in constraining the magma temperature (Harrison and Watson 1984; Bea et al. 1992). The apparent negative correlation between silica and P_2O_5 suggests apatite saturation for charnockite and biotite gneiss. Apatite saturation thermometry is calculated using the equations of Harrison & Watson, 1984 for the metaluminous and Bea et al., 1992 for the peraluminous granitoids (Fig. 5.9.c). Apatite saturation thermometry constrains a temperature range of 740 - 950°C for the biotite gneiss with an average of $830 \pm 60^\circ\text{C}$. Apatite saturation thermometry estimates a much higher temperature for metaporphyritic charnockite than biotite gneiss, averaging $995 \pm 50^\circ\text{C}$ (840 - 1040°C).

The SiO_2 vs TiO_2 plot also shows a negative correlation for both the rock types, indicating saturation of the Ti-rich phase (which here is ilmenite). The SiO_2 vs TiO_2 plot (Fig. 5.9.d) (Green and Pearson 1986) suggests a temperature range of 900 - 950°C for the charnockite and a temperature range of 800 - 850°C.

5.5 Petrogenetic modelling of the charnockite (PC)-granite (BG) association:

Despite distinct differences in lithology, petrography and whole rock geochemistry, the two granitoids (PC and BG) are strongly related to each other. As described in Chapter 3, in the lithological map of the study area, charnockite (PC) and granite (BG) are adjacent and share a gradational contact, where BG is present along the margin of PC. Again, both rock types bear similar intrusive relations with the country rock. Despite plotting in different fields (granite (BG) and granodiorite (PC)) in both TAS and QAP diagrams, both rock types are typical ferroan A-type granitoids. In trace element diagrams, both granitoids exhibit identical patterns, with BG indicating a slightly higher magnitude of positive and negative anomaly for LILE (e.g. Th, U, Pb) and HFSE, respectively. Similarly, for the REE

diagram, the magnitude of LREE enrichment and negative Eu anomaly is slightly higher in BG.

In variation diagrams (with both silica and maficity), both PC and BG follow a coherent trend demonstrated by the ferroan granitoids of CGGC. Such trends indicate possible (a) magma mixing (Chappell 1996; Baxter and Feely 2003), (b) crustal assimilation (Castro 2014; Guo and Zou 2023), (c) fractional crystallisation (Garcia-Arias and Stevens 2017b; Farina et al. 2020; Mukherjee et al. 2022) or (d) restite entrainment (Garcia-Arias and Stevens 2017a). The lack of petrographic features (Baxter and Feely 2002) such as mafic micro enclaves or felsic to mafic hybrid zones rules out magma mixing as a viable process. Also, since the granitoids do not form a subhorizontal trend crossing boundaries in the MALI diagram (Frost and Frost 2008a; Moreno et al. 2017) (restricted within calc-alkaline field) (Fig. 5.7.c), crustal assimilation seems like an unlikely process. Though restite entrainment can cause such a trend (Garcia-Arias and Stevens 2017a), the absence of any such restitic phase in the detailed petrographic study of both granitoids makes the process improbable. Nevertheless, a few rare enclaves of the felsic orthogneiss country rock are present in the metaporphyritic charnockite; the amount is far less to create such a coherent compositional trend throughout the vast region. This leaves fractionation as the only probable process that can support the geochemically coherent trend as well as other geochemical and field relations described above. Previous geochemical studies also reveal that crystal fractionation played a pivotal role in shaping the geochemistry of the ferroan granitoids of CGGC (Mukherjee et al. 2018, 2022; Sequeira et al. 2022). Thus, open system phase equilibria modelling is evaluated to understand further the role of crystal fractionation in the petrogenesis of ferroan charnockite-granite association in CGGC. Apart from understanding the fractionation process, the phase equilibria modelling helps to comprehend the role of physical and chemical parameters (P-T condition, H₂O content, and oxygen fugacity (fO₂) in stabilising orthopyroxene in the felsic magma.

5.5.1 Conditions of modelling:

The phase equilibrium modelling of the melt-crystal separation process during magma crystallisation is carried out in the NCKFMASHTO (Na₂O-CaO-K₂O-FeO-MgO-Al₂O₃-SiO₂-H₂O-TiO₂-O₂) system using the software Rcrust (version 22-09-03) (Mayne et al. 2016). The software Rcrust uses the “meemum” program of PerpleX (v. 6.8.6) suit of programs (Connolly 2009) along with the thermodynamic dataset of Holland & Powell

(2011) (hp11ver.dat). Considering the negligible MnO content in both metaporphyratic charnockite (0.05-0.17 wt%) and biotite gneiss (0.01-0.08 wt%), Mn is excluded from the phase equilibrium modelling system. For the phase equilibrium modelling, the following activity composition (a-X) relationships are used: biotite, orthopyroxene, ilmenite, muscovite, melt, staurolite and cordierite from White et al. (2014); clinopyroxene and clino-amphibole from Green et al., (2016); epidote from Holland & Powell, (2011); spinel-magnetite from White et al., (2002) and binary feldspars from Newton et al. (1981)(plagioclase) and Waldbaum & Thompson Jr., (1968) (alkali feldspar). End member phases 'ab' and 'mic' were excluded.

Ferroan granites are commonly considered to form at high temperatures (~900°C) and low pressure (<8 kbar) conditions (Patiño Douce 1997; Dall'Agnol et al. 2012; Frost and Frost 2013). A flat HREE pattern, Sr depletion and negative Eu anomaly in the studied granitoids assert the dominance of plagioclase over garnet as the residual phase in the source, advocating for a low-pressure condition of formation. Therefore, we modelled the isobaric melt-crystal fractionation over a pressure range of 3-5 kbar with an interval of 1 kbar. This pressure range is within the common pressure conditions of igneous charnockites (Zhao et al. 2023). Along each isobaric cooling path, a temperature range of 1000-650 °C is considered with an interval of 5°C.

Melt crystal separation is broadly governed by crystal settling and compaction (Bachmann and Huber, 2019 and the references therein) depending on melt viscosity, density, and average density of crystal phases. Compaction-driven melt extraction is generally considered as the predominant process of crystal fractionation in silicic magma (Holness et al. 2017; Bachmann and Huber 2019), due to its high viscosity and slight density variation with crystallising phases (Deering and Bachmann 2010; Castro 2013). Compaction-driven melt extraction can be facilitated after a significant proportion of crystallisation has occurred, generating a crystal matrix of finite rigidity (crystal mush) in the magma system (Bachmann and Huber 2019). Stress accommodation in the crystal mush is crucial in extracting interstitial melt during compaction (Bachmann and Huber 2019). Microstructural studies on magmatic charnockite also suggest compaction as a vital mechanism of melt extraction (Zhao et al. 2018). Studies (Lee and Morton 2015; Zhao et al. 2018) have shown that, though efficient, compaction can not extract all the remaining interstitial melt, and the remaining melt is trapped within the crystal mush. In the current

study, the process of fractional crystallisation is modelled in such a way that once the crystal volume reaches a threshold of 60%, 80% of the remaining melt will separate from the crystals. Each episode of crystal separation would create a crystal-dominated system (CS) and a residual melt-dominated system (MS). This melt-dominated system will continue to evolve along its designated P-T path (as described above), with the residual melt system passed on after each episode of crystal fractionation. Previous (Garcia-Arias and Stevens 2017b; Farina et al. 2020; Mayne et al. 2020; Mukherjee et al. 2022; Chakrabarty et al. 2023) workers also considered similar approaches.

Voluminous ferroan (A-type) granitoids are characterised by low H₂O content (Clemens et al. 1986; Klimm et al. 2003). To investigate the stability of orthopyroxene and the magmatic charnockite generation from the felsic (A-type) magma, the fractional crystallisation process is modelled at various H₂O dissolved content (1-2.5 wt% H₂O) in the initial magma. Further, to investigate the role of oxygen fugacity in the genesis of magmatic charnockite, fractional crystallisation is conducted at fayalite-magnetite-quartz (FMQ) buffer and FMQ+2. Due to the oxidised nature (magnetite present) of the charnockite, oxygen fugacity lower than FMQ+0 is not considered. The oxygen buffer conditions are transformed to Fe³⁺/Fe_{total} of the initial magma composition using the program Rhyolite-MELTS (Gualda and Ghiorso 2015).

5.5.2 Choice of initial magma composition:

Estimating a precise composition of the initial magma for an open system phase equilibria modelling is very crucial and often challenging. While evaluating the initial magma composition, it is noteworthy to consider the possible alteration of bulk composition as both rocks are metamorphosed. Detailed mesoscopic and microscopic studies of both rock types do not show any evidence of partial melting during metamorphism. Studies have shown that it is practically impossible to purge out all the melt after partially melting during a metamorphic regime owing to surface energy (Sawyer 1999, 2008). The complete absence of leucosome and preservation of the tabular shape of the coarse orthopyroxene and plagioclase grains do not support the view that the rock underwent partial melting and that the melt moved out of the system. Geochemical features such as high LREE/HREE (average (La/Lu)_N = 5.14; 6.58; respectively for charnockite and biotite gneiss) and a gradual decreasing trend from LILE to HFSE in the trace element spider diagram further provide evidence against melt loss during metamorphism. So, it is

safe to say that melt loss during metamorphism has not altered bulk composition. Textual study indicates that during garnet formation, limited mass transport occurred in the scale of the coronitic phases. Even late-stage hydration by the external fluid is also restricted, as manifested by the low abundance of hydrous phases in the granitoids (especially in PC).

Table 5.9: The starting magma composition of fractionation modelling, estimated based on the average composition of both metaporphyritic charnockite (n=15) and biotite gneiss (n=16) in a 3:2 ratio

Rock type	Metaporphyritic charnockite		Biotite gneiss		Starting composition ferroan granitoid	
	Average (n=14) (wt%)	± (wt%)	Average (n=15) (wt%)	± (wt%)	(wt%)	± (wt%)
SiO ₂	63.95	2.07	75.10	1.88	68.41	1.99
TiO ₂	1.13	0.27	0.26	0.11	0.78	0.21
Al ₂ O ₃	14.68	0.72	12.73	0.77	13.90	0.74
MnO	0.14	0.03	0.04	0.02	0.10	0.03
FeO _T	7.25	1.31	2.51	0.93	5.36	1.16
CaO	3.87	0.76	0.99	0.46	2.72	0.64
MgO	1.00	0.59	0.25	0.25	0.70	0.46
Na ₂ O	3.32	0.47	3.72	0.83	3.48	0.62
K ₂ O	3.02	0.89	3.82	1.37	3.34	1.08
P ₂ O ₅	0.42	0.11	0.05	0.04	0.27	0.08
FeO _T /[FeO _T + MgO]	0.88		0.91		0.88	
FeO _T +MgO	8.25		2.76		6.06	
A/CNK	0.93		1.05		0.97	
K ₂ O+Na ₂ O	6.35		7.54		6.82	
K ₂ O/Na ₂ O	0.91		1.03		0.96	

The average bulk composition of PC and BG are considered for the petrogenetic modelling of the charnockite-granite association through fractionation. Assessing the proportion in which both rock types contributed to forging the initial magma is crucial for accurately estimating bulk composition. The exposed areal extent of both rocks is considered for this. The study area's lithological map (Chapter-3; Fig. 3.1) shows the metaporphyritic charnockite has a larger extent than the biotite gneiss. The starting magma composition (Table 5.9) is estimated based on the average composition of both

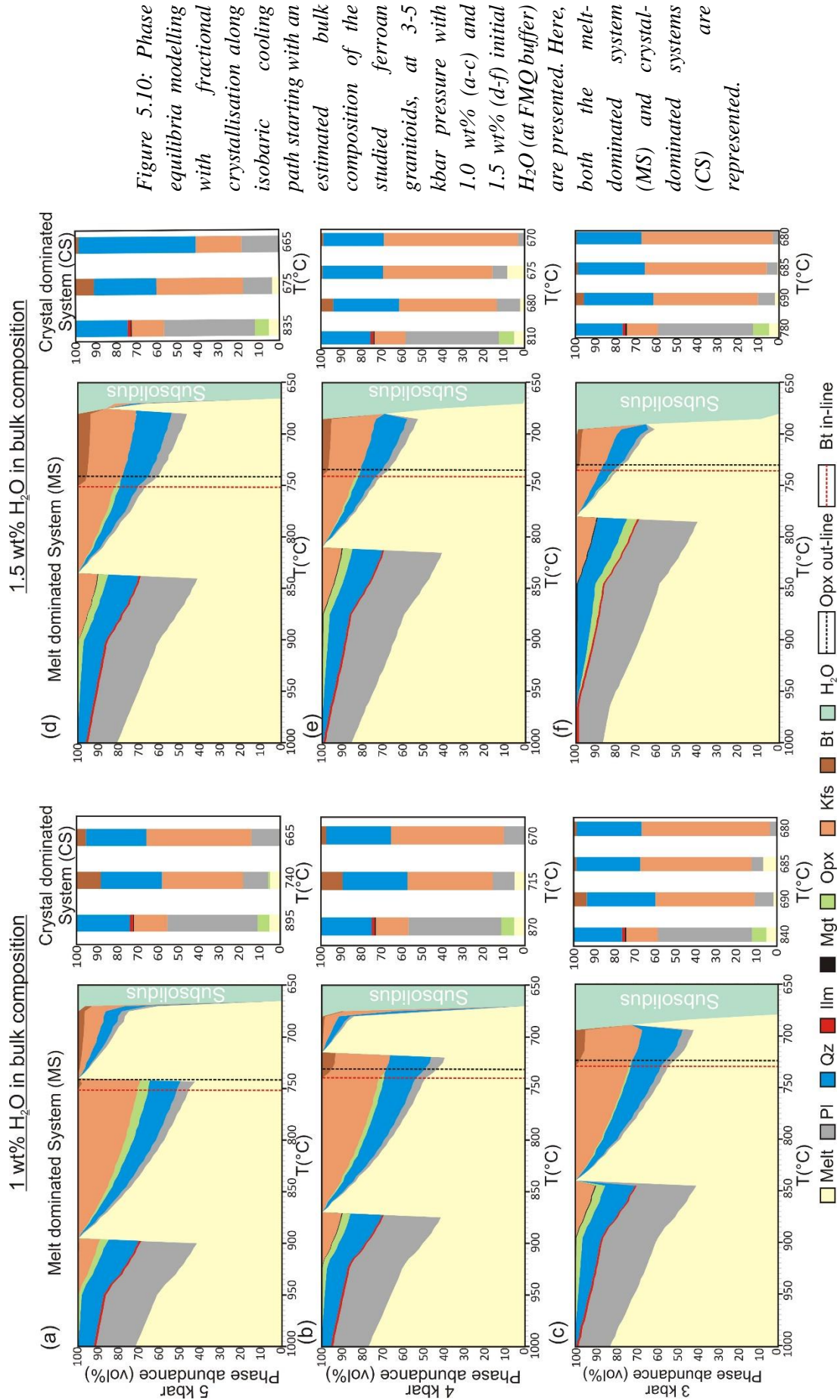
metamorphic charnockite (n=14) and biotite gneiss (n=15) in a 3:2 ratio based on the exposed ferroan granitoids of the study area (Table 5.9).

Notably, while assessing the initial magma composition, a few assumptions are taken into account; These include,

- (a) The deeper, unexposed parts of granitoids are not considered, and it is assumed they do not bear any significant difference with the measured composition;
- (b) Though minor, parts of the studied ferroan granitoids are beyond the detailed lithologically mapped study area. It is assumed that PC and BG exhibit similar (3:2) proportions even in those areas.
- (c) Also, based on the detailed petrographic study (as described above), it is assumed that the influence of subsolidus metamorphism on bulk composition is not significant to consider.

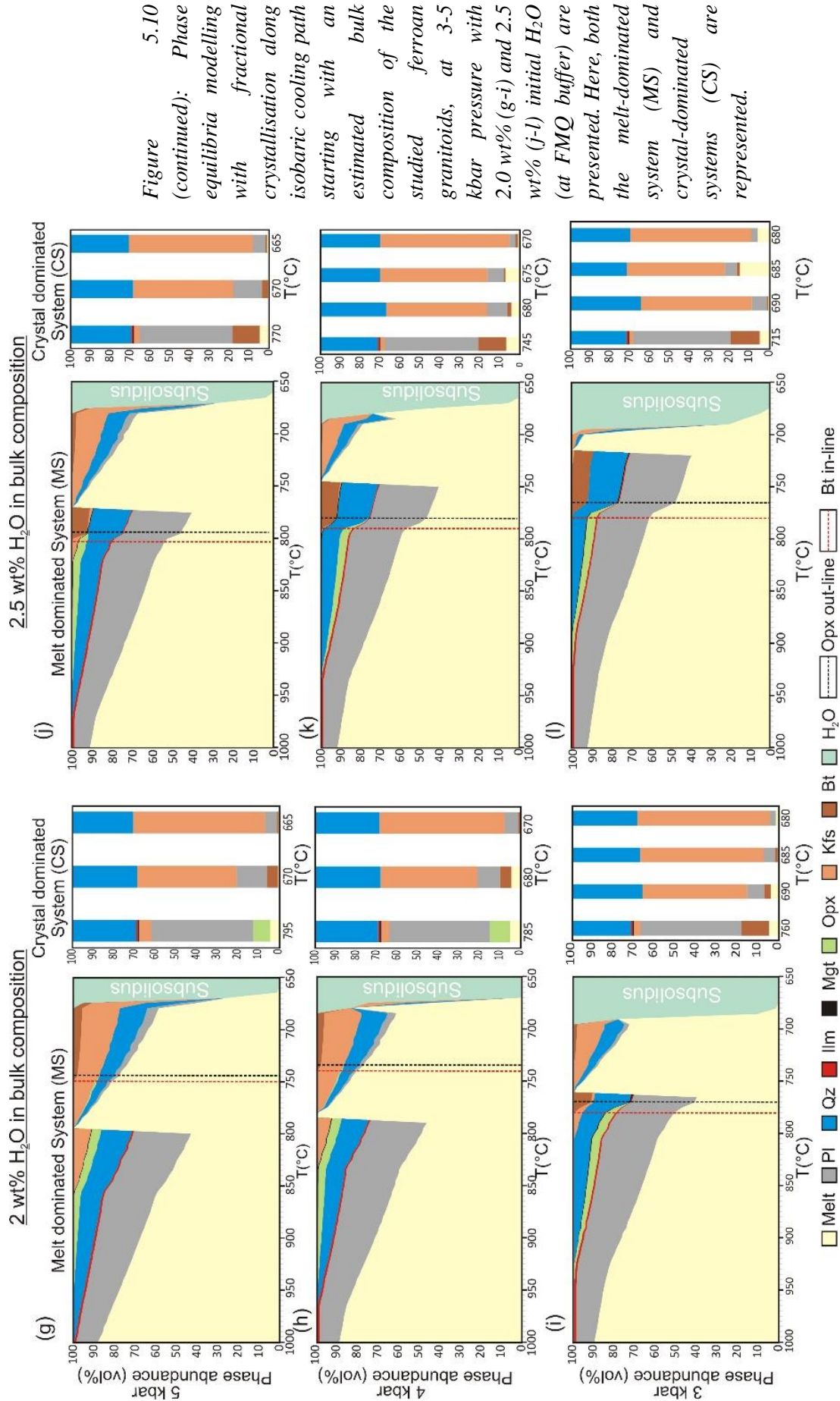
5.5.3 Results:

- (a) **1.0% H₂O at FMQ+0:** Under these conditions, plagioclase, ilmenite and quartz are the earliest crystallising phases in the melt system in all three (3 kbar, 4 kbar, 5 kbar) isobaric modelling systems (Fig. 5.10.a-c). Orthopyroxene crystallisation begins at high temperatures (between 995 – 980°C). K-feldspar crystallisation commences at 945°C at 5kbar, while at 3kbar pressure, it begins at 890°C. Magnetite starts crystallising between 970 and 940 °C at 3 and 5 kbar pressures, respectively. The first batch of fractionation, which occurs between 895°C and 845°C depending on the pressure, contains orthopyroxene, plagioclase, K-feldspar, quartz and ilmenite. Opx modal abundance in the solid system increases slightly from 6% at 5kbar to 8% at 3 kbar. X_{Mg} of the orthopyroxenes varies between 0.30 to 0.28. Biotite begins to crystallise between 745 and 725°C, at which point orthopyroxene volume decreases drastically. Therefore, the subsequent crystal system contains biotite as the dominant ferromagnesian phase, while orthopyroxene is absent (except at 5 kbar, where minor Opx is present in the second batch). The plagioclase from the first batch ($X_{An} = 0.37-0.35$) is more anorthitic than the second ($X_{An} = 0.23-0.18$) and later ones.



- (b) **1.5% H₂O at FMQ+0:** The crystallisation sequence at 1.5% H₂O is the same as 1% H₂O (Fig. 5.10.d-f). Opx crystallisation starts between 975-960°C. Biotite starts to crystallise after the first batch of crystal fractionation between 745-730°C. Orthopyroxene abundance in the first fractionated crystal system varies between 7.5-8.5%. Like at 1% H₂O, the second batch of extracted crystals is completely devoid of orthopyroxene. Fractionated Opx ($X_{Mg} = 0.27-0.28$) and Pl (First batch $X_{An} = 0.37-0.35$; Second batch $X_{An} = 0.17-0.18$) composition is similar to at 1% H₂O.
- (c) **2.0% H₂O at FMQ+0:** Under these conditions, the early crystallisation process is quite similar to 1 and 1.5% H₂O, with orthopyroxene starting to crystallise between 955-940°C (Fig. 5.10.g-i). At 5 and 4 kbar pressure, the first extracted batch of crystals contain 8 and 9% Opx respectively, and biotite crystallisation begins after the first fractionation, at 745 and 740°C respectively. However, for 2% H₂O, at 3 kbar, biotite crystallisation begins at 775°C before the first crystal fractionation and the first extracted crystal system is devoid of orthopyroxene. Ilm and Mgt abundance is similar to the earlier ones. Fractionated Opx ($X_{Mg} = 0.26-0.28$) and Pl (First batch $X_{An} = 0.34-0.35$; Second batch $X_{An} = 0.13-0.19$) composition is similar to that for 1% H₂O.
- (d) **2.5% H₂O at FMQ+0:** With a similar crystallisation sequence as described above, Opx starts crystallising between 940-925°C (Fig. 5.10.j-l). However, biotite crystallisation begins before the first crystal fractionation between 800-775°C, marking the consumption of the already crystallised Opx. All fractionated crystal batches are devoid of orthopyroxene.
- (e) **Model at FMQ+2 (Fig. 5.11):** Here, the overall crystallisation is almost the same as the condition at *FMQ+0*, with magnetite crystallisation starting earlier than at FMQ. The first fractionated batch of crystals contains 4-5% Opx up to 2 wt% magma H₂O. Unlike at 2.0 wt% H₂O at FMQ, the first batch of fractionated crystals is entirely devoid of Opx at 4 kbar. Also, the abundance of magnetite is more than that of ilmenite. Fractionated Opx composition is more magnesian ($X_{Mg} = 0.40-0.42$) than at FMQ with almost the same Pl composition. Only the first batch of extracted crystals (2 wt% H₂O) at 5kbar pressure contain 5% Opx. At 2 wt% H₂O, both at 4 and 3 kbar pressure, biotite crystallisation begins before the first extraction at 790 and 780°C, respectively.

The first batch of fractionated crystal-dominated bulks are less siliceous (64-67 wt.%), more aluminous (14-15 wt.%), more calcic (3-4 wt.%), more ferromagnesian



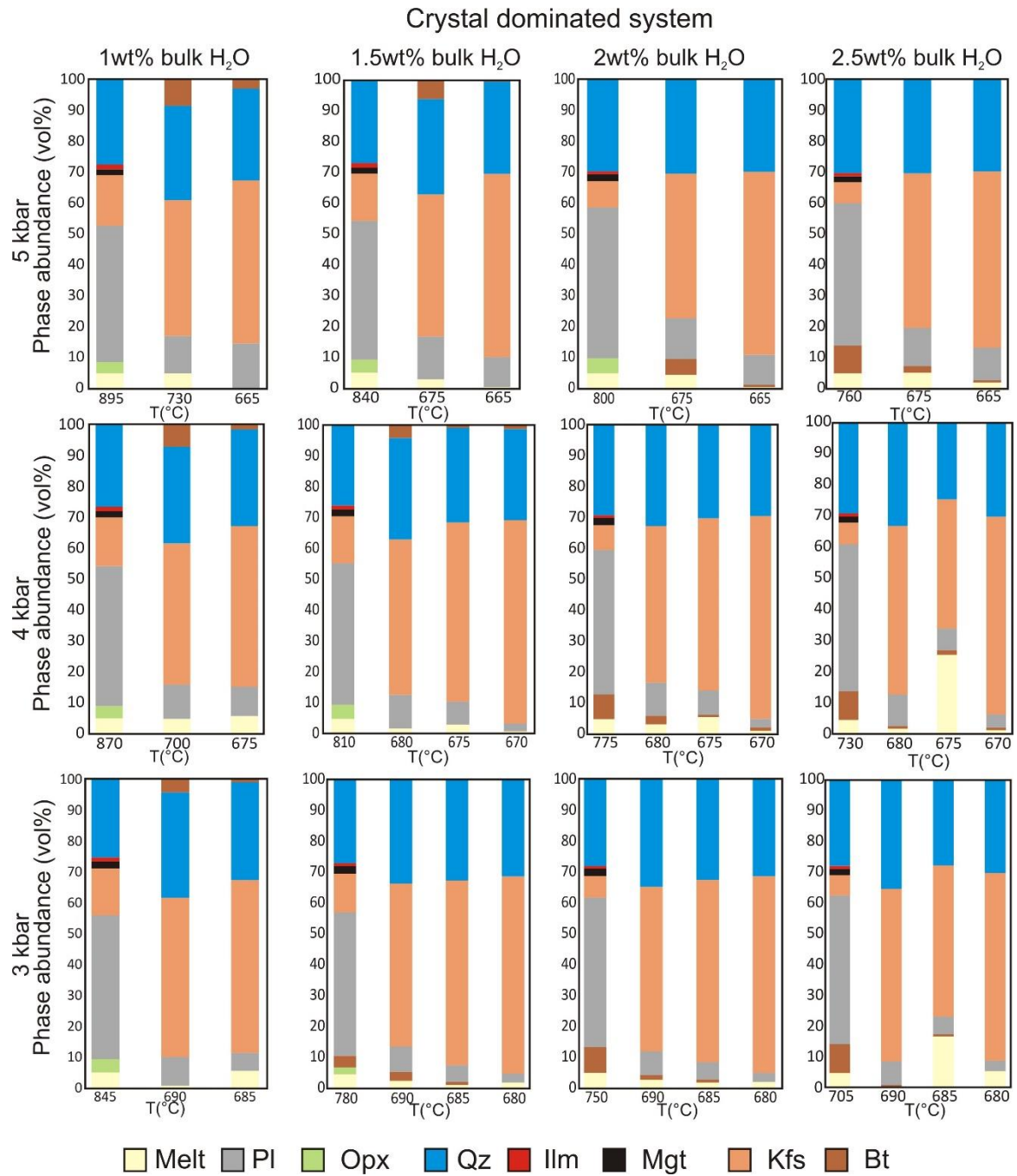


Figure 5.11: Phase equilibria modelling with fractional crystallisation along isobaric cooling path starting with an estimated bulk composition of the studied ferroan granitoids, at 3-5 kbar pressure with 1.0-2.5 wt% initial H₂O (at FMQ+2 fO₂) are presented. Here, only the crystal-dominated systems (CS) are represented.

(FeO+MgO= 6-9 wt%) and sodic ($K_2O/Na_2O = 0.5-0.6$) compared to the second and later batches of crystal-dominated bulks ($SiO_2=71-78$ wt%; $Al_2O_3=12-14$ wt%; $CaO<1$ wt%, FeO+MgO= 0.5-6 wt%; $K_2O/Na_2O = 0.8-2.5$). To test the modelled fractionation process with the natural system, the bulk chemical composition of each batch of fractionated crystal system is compared with the metaporphyritic charnockite and biotite gneiss (Fig. 5.12.a-d). While the first batch of fractionated crystals corroborates well with the metaporphyritic charnockite, the second and later batches of fractionations overlap with the biotite gneiss. Furthermore, orthopyroxene and plagioclase compositions are compared between the natural and modelled systems (Fig. 5.12.e-g). Compositionally, plagioclase from the first batches of fractionation is similar to the metaporphyritic charnockite and composition from the second batches is similar to the biotite gneiss (Fig. 5.12.g). Modelled orthopyroxene

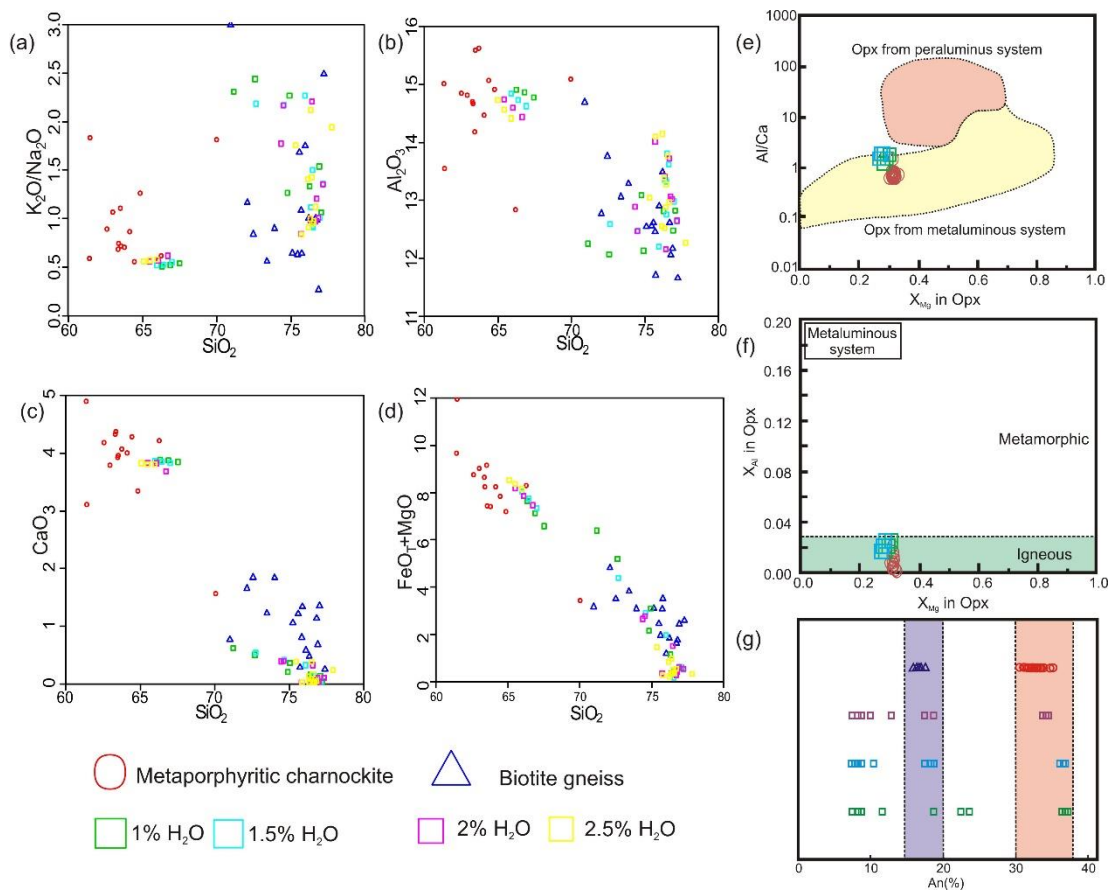


Figure 5.12: (a-d) Plots of SiO_2 vs. K_2O/Na_2O ; Al_2O_3 ; CaO ; (FeO_T+MgO) compares modelled bulk compositions with the studied ferroan granitoids. (e-f) Modelled Opx compositions are compared with natural Opx compositions from metaporphyritic charnockite in Al/Ca vs. X_{Mg} X_{Al} vs. X_{Mg} plot of orthopyroxene (Zhao et al., 2023). Modelled Opx compositions are compared with natural Opx compositions from metaporphyritic charnockite. (g) Modelled plagioclase composition (An%) is compared with plagioclase composition from the studied ferroan granitoids.

composition is also quite similar with the orthopyroxenes from metaporphyratic charnockite (Fig. 5.12.e-f).

5.6 Physical conditions of metamorphism:

A comprehensive understanding of the petrogenetic evolution of the ferroan granitoids is incomplete without a proper understanding of the post-magmatic metamorphic evolution. Determining the physical parameters of metamorphism is essential to interpreting a metamorphic occurrence. The physical conditions of metamorphism are constrained using conventional thermobarometry and phase equilibria modelling techniques. The compositional and textural characteristics of the metamorphic phases of the metaporphyratic charnockite constrain the P-T condition of metamorphism of the studied ferroan granitoids.

5.6.1 Conventional thermobarometry:

Several thermobarometers are utilised to estimate the P-T parameters, taking into account the metamorphic assemblage that developed in the examined rock. Table- 5.10 provides specifics on P-T estimates from conventional thermobarometry. The physical condition of metamorphism is estimated using the compositions of garnet and adjacent clinopyroxene and plagioclase. Garnet-clinopyroxene (GC) (Lee and Ganguly 1988) ion

Table 5.10: P-T estimates through conventional thermobarometric calculations

Assemblage	Thermometry			Barometry		
		P (kbar, ref)	T (°C)		T (°C, ref)	P (kbar)
Grt-Cpx-Pl-Qz	GC	8	780-820	GCPS	800	8-8.5
Amp-Pl-Qz	Pl-A		700-750	Al in Amp1		6.5 ± 0.12
				Al in Amp2		6.1 ± 0.13

GC: Garnet – clinopyroxene geothermometer (Ellis and Green, 1979).

GCPS: Garnet – clinopyroxene – plagioclase – quartz barometer (Eckert et al., 1991).

Pl-A: Plagioclase - hornblend thermometry (Holland and Blundy 1994)

Al in Amp1: Al in amphibole barometer (Schmidt, 1992)

Al in Amp2: Al in amphibole barometer (Hammarstrom and Zen, 1986)

exchange thermometers yield a temperature range of $\sim 800^{\circ}\text{C}$. Garnet-clinopyroxene-plagioclase-quartz (GCPQ) (Eckert et al. 1991) barometers estimate a pressure range of 8–8.5 kbar. P-T condition of amphibole formation is measured by the hornblende-plagioclase thermometry (Holland and Blundy 1994) and Al in amphibole barometry (Hammarstrom and Zen 1986; Schmidt 1992). Hornblende-plagioclase thermometry evaluates a temperature range of $700\text{--}750^{\circ}\text{C}$. Al in amphibole barometry yields an average pressure of ~ 6 kbar.

5.6.2 Phase equilibria modelling:

Numerically simulated phase equilibria modelling (pseudosection) of the studied metaporphyritic charnockite is calculated for a representative bulk composition to further constrain the P-T conditions during metamorphism. Pseudosection is constructed in NCFMAST ($\text{Na}_2\text{O-CaO-FeO-MgO-Al}_2\text{O}_3\text{-SiO}_2\text{-TiO}_2$) components system using major oxide bulk compositions of sample SD-11 (Table- 5.7). The porosity of rocks decreases to vanishingly small at upper amphibolite-granulite facies conditions (Clemens and Vielzeuf 1987), and structural water from the hydrous phases is the primary source of the H_2O

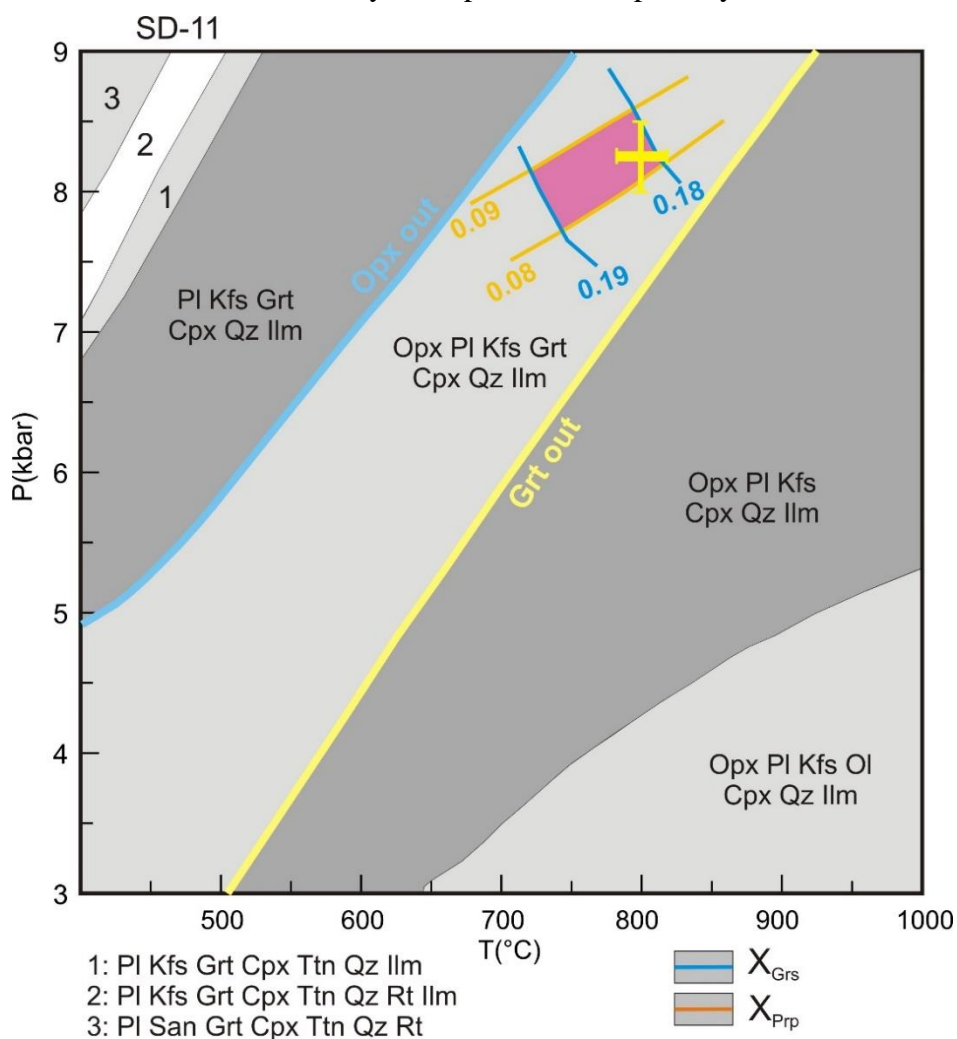


Figure 5.13: Numerically simulated phase equilibria modelling is calculated in NCFMASHT (Na_2O - CaO - FeO - MgO - Al_2O_3 - SiO_2 - TiO_2) components system.

present in the rock. Due to the lack of any primary hydrous phase in the protolith, H_2O is not considered in the bulk composition. Computation of the phase diagram is done using the program PerpleX (ver. 6.8.6; Connolly 2005) with the internally consistent thermodynamic dataset of Holland and Powell (2011) (TC-DS622). For the pseudosection construction, the solid solution activity composition (a-X) relationships of orthopyroxene (Powell and Holland 1999), clinopyroxene (Holland and Powell 1996), garnet, olivine (Holland and Powell 1998), plagioclase (Newton et al. 1981) and alkali feldspar (Waldbaum and Thompson Jr. 1968). To constrain the estimated P-T conditions of the rock, compositional isopleth for garnet is computed and plotted in the phase diagram in the relevant assemblage fields in addition to the phase diagram. These calculations are performed using the Perple-X subordinate programme WARAMI (Connolly, 2009, 2005).

Result: In the constructed pseudosection (Fig. 5.13), P-T conditions are estimated using the grossular and pyrope isopleths. Isopleths constrain a P-T condition range of 725-825°C and 7.5-8.5 kbar. P-T estimation from conventional thermobarometry correlates well with P-T estimation from pseudosection modelling.

References:

- Bachmann, O., and Huber, C. (2019) The Inner Workings of Crustal Distillation Columns; the Physical Mechanisms and Rates Controlling Phase Separation in Silicic Magma Reservoirs. *Journal of Petrology*, 60, 3–18.
- Baxter, S., and Feely, M. (2002) Magma mixing and mingling textures in granitoids: examples from the Galway Granite, Connemara, Ireland. *Mineralogy and Petrology*, 76, 63–74.
- Baxter, S., and Feely, M. (2003) Field and petrographic evidence for magma mixing and mingling in granitoids: examples from the Galway Granite, Connemara, Ireland. *Abstracts with Programmes, Geological Society of America, NE Section*, 35, 79.
- Bea, F., Fershtater, G., and Corretgé, L.G. (1992) The geochemistry of phosphorus in granite rocks and the effect of aluminium. *Lithos*, 29, 43–56.
- Bédard, J.H.J., Marsh, B.D., Hersum, T.G., Naslund, H.R., and Mukasa, S.B. (2007) Large-

- scale Mechanical Redistribution of Orthopyroxene and Plagioclase in the Basement Sill, Ferrar Dolerites, McMurdo Dry Valleys, Antarctica: Petrological, Mineral-chemical and Field Evidence for Channelized Movement of Crystals and Melt. *Journal of Petrology*, 48, 2289–2326.
- Boehnke, P., Watson, E.B., Trail, D., Harrison, T.M., and Schmitt, A.K. (2013) Zircon saturation re-revisited. *Chemical Geology*, 351, 324–334.
- Castro, A. (2013) Tonalite–granodiorite suites as cotectic systems: A review of experimental studies with applications to granitoid petrogenesis. *Earth-Science Reviews*, 124, 68–95.
- (2014) The off-crust origin of granite batholiths. *Geoscience Frontiers*, 5, 63–75.
- Chakrabarty, A., Mukherjee, S., Karmakar, S., Sanyal, S., and Sengupta, P. (2023) Petrogenesis and in situ U-Pb zircon dates of a suite of granitoid in the northern part of the Central Indian tectonic Zone: Implications for prolonged arc magmatism during the formation of the Columbia supercontinent. *Precambrian Research*, 387, 106990.
- Chappell, B.W. (1996) Magma Mixing and the Production of Compositional Variation within Granite Suites: Evidence from the Granites of Southeastern Australia. *Journal of Petrology*, 37, 449–470.
- Clemens, J.D., and Vielzeuf, D. (1987) Constraints on melting and magma production in the crust. *Earth and Planetary Science Letters*, 86, 287–306.
- Clemens, J.D., Holloway, J.R., and White, A.J.R. (1986) Origin of an A-type granite : Experimental constraints. *American Mineralogist*, 71, 317–324.
- Connolly, J.A.D. (2005) Computation of phase equilibria by linear programming: A tool for geodynamic modeling and its application to subduction zone decarbonation. *Earth and Planetary Science Letters*, 236, 524–541.
- (2009) The geodynamic equation of state: What and how. *Geochemistry, Geophysics, Geosystems*, 10.
- Dall’Agnol, R., Frost, C.D., and Rämö, O.T. (2012) IGCP Project 510 “A-type Granites and Related Rocks through Time”: Project vita, results, and contribution to granite research. *Lithos*, 151, 1–16.

- Deering, C.D., and Bachmann, O. (2010) Trace element indicators of crystal accumulation in silicic igneous rocks. *Earth and Planetary Science Letters*, 297, 324–331.
- Droop, G.T.R. (1987) A general equation for estimating Fe ³⁺ concentrations in ferromagnesian silicates and oxides from microprobe analyses, using stoichiometric criteria. *Mineralogical Magazine*, 51, 431–435.
- Eckert, J.O., Newton, R.C., and Kleppa, O.J. (1991) The ΔH of reaction and recalibration of garnet-pyroxene-plagioclase-quartz geobarometers in the CMAS system by solution calorimetry. *American Mineralogist*, 76, 148–160.
- Farina, Federico, Mayne, M.J., Stevens, G., Soorajlal, R., Frei, D., and Gerdes, A. (2020, April 21) Phase equilibria constraints on crystallization differentiation: insights into the petrogenesis of the normally zoned Buddusò Pluton in north-central Sardinia. (V. Janoušek, B. Bonin, W.J. Collins, F Farina, & P. Bowden, Eds.) *Post-Archean Granitic Rocks: Petrogenetic Processes and Tectonic Environments*. Geological Society of London.
- Frost, B.R., and Frost, C.D. (2008a) A Geochemical Classification for Feldspathic Igneous Rocks. *Journal of Petrology*, 49, 1955–1969.
- (2008b) On charnockites. *Gondwana Research*, 13, 30–44.
- Frost, B.R., Barnes, C.G., Collins, W.J., Arculus, R.J., Ellis, D.J., and Frost, C.D. (2001) A geochemical classification for granitic rocks. *Journal of Petrology*, 42, 2033–2048.
- Frost, C.D., and Frost, B.R. (2013) Proterozoic ferroan feldspathic magmatism. *Precambrian Research*, 228, 151–163.
- Garcia-Arias, M., and Stevens, G. (2017a) Phase equilibrium modelling of granite magma petrogenesis: A. An evaluation of the magma compositions produced by crystal entrainment in the source. *Lithos*, 277, 131–153.
- (2017b) Phase equilibrium modelling of granite magma petrogenesis: B. An evaluation of the magma compositions that result from fractional crystallization. *Lithos*, 277, 109–130.
- Green, E.C.R., White, R.W., Diener, J.F.A., Powell, R., Holland, T.J.B., and Palin, R.M. (2016) Activity–composition relations for the calculation of partial melting equilibria

- in metabasic rocks. *Journal of Metamorphic Geology*, 34, 845–869.
- Green, T.H., and Pearson, N.J. (1986) Ti-rich accessory phase saturation in hydrous mafic-felsic compositions at high P,T. *Chemical Geology*, 54, 185–201.
- Gualda, G.A.R., and Ghiorso, M.S. (2015) MELTS_Excel: A Microsoft Excel-based MELTS interface for research and teaching of magma properties and evolution. *Geochemistry, Geophysics, Geosystems*, 16, 315–324.
- Guo, Z., and Zou, H. (2023) Temperature and Hf-O isotope correlations of young erupted zircons from Tengchong (SE Tibet): Assimilation fractional crystallization during monotonic cooling. *Geoscience Frontiers*, 14, 101497.
- Hammarstrom, J.M., and Zen, E. (1986) Aluminum in hornblende: an empirical igneous geobarometer. *American Mineralogist*, 71, 1297–1313.
- Harrison, T.M., and Watson, E.B. (1984) The behavior of apatite during crustal anatexis: Equilibrium and kinetic considerations. *Geochimica et Cosmochimica Acta*, 48, 1467–1477.
- Holland, T., and Blundy, J. (1994) Non-ideal interactions in calcic amphiboles and their bearing on amphibole-plagioclase thermometry. *Contributions to Mineralogy and Petrology*, 116, 433–447.
- Holland, T., and Powell, R. (1996) Thermodynamics of order-disorder in minerals; II, Symmetric formalism applied to solid solutions. *American Mineralogist*, 81, 1425–1437.
- Holland, T., and Powell, R. (1998) An internally consistent thermodynamic data set for phases of petrological interest. *Journal of Metamorphic Geology*, 16, 309–343.
- Holland, T.J.B., and Powell, R. (2011) An improved and extended internally consistent thermodynamic dataset for phases of petrological interest, involving a new equation of state for solids. *Journal of Metamorphic Geology*, 29, 333–383.
- Holness, M.B. (2006) Melt–Solid Dihedral Angles of Common Minerals in Natural Rocks. *Journal of Petrology*, 47, 791–800.
- (2010) Decoding dihedral angles in melt-bearing and solidified rocks. In: (Ed.)

-
- M.A. Forster, and John D. Fitz Gerald, The Science of Microstructure - Part I. Journal of the Virtual Explorer, 35.
- Holness, M.B., Vukmanovic, Z., and Mariani, E. (2017) Assessing the Role of Compaction in the Formation of Adcumulates: a Microstructural Perspective. Journal of Petrology, 58, 643–673.
- Jung, S., and Pfänder, J.A. (2007) Source composition and melting temperatures of orogenic granitoids: constraints from CaO/Na₂O, Al₂O₃/TiO₂ and accessory mineral saturation thermometry. European Journal of Mineralogy, 19, 859–870.
- Kelsey, D.E., White, R.W., and Powell, R. (2003) Orthopyroxene–sillimanite–quartz assemblages: distribution, petrology, quantitative P–T–X constraints and P–T paths. Journal of Metamorphic Geology, 21, 439–453.
- King, P.L., Chappell, B.W., Allen, C.M., and White, A.J.R. (2001) Are A-type granites the high-temperature felsic granites ? Evidence from fractionated granites of the Wangrah Suite. Australian Journal of Earth Sciences, 501–514.
- Klimm, K., Holtz, F., Johannes, W., and King, P.L. (2003) Fractionation of metaluminous A-type granites: an experimental study of the Wangrah Suite, Lachlan Fold Belt, Australia. Precambrian Research, 124, 327–341.
- Le Maitre, R.W., Streckeisen, A., Zanettin, B., Le Bas, M.J., Bonin, B., and Bateman, P. (2005) Igneous rocks: a classification and glossary of terms: recommendations of the International Union of Geological Sciences Subcommittee on the Systematics of Igneous Rocks. Cambridge University Press.
- Leake, B.E., Woolley, A.R., Arps, C.E.S., Birch, W.D., Gilbert, M.C., Grice, J.D., Hawthorne, F.C., Kato, A., Kisch, H.J., Krivovichev, V.G., and others (1997) Nomenclature of amphiboles: Report of the subcommittee on amphiboles of the international mineralogical association, commission on new minerals and mineral names. Canadian Mineralogist, 35, 219–246.
- Lee, C.-T.A., and Morton, D.M. (2015) High silica granites: Terminal porosity and crystal settling in shallow magma chambers. Earth and Planetary Science Letters, 409, 23–31.

- Lee, H.A.N.Y., and Ganguly, J. (1988) Equilibrium Compositions of Coexisting Garnet and Orthopyroxene: Experimental Determinations in the System FeO-MgO-Al₂O₃-SiO₂, and Applications. *Journal of Petrology*, 29, 93–113.
- Mahapatro, S.N., Tripathy, A.K., Nanda, J.K., and Rath, S.C. (2013) Petrology of the Udayagiri anorthosite complex, Eastern Ghats Belt, India. *Journal of the Geological Society of India*, 82, 319–329.
- Mayne, M.J., Moyen, J.-F., Stevens, G., and Kaislaniemi, L. (2016) Rcrust: a tool for calculating path-dependent open system processes and application to melt loss. *Journal of Metamorphic Geology*, 34, 663–682.
- Mayne, M.J., Stevens, G., and Moyen, J.-F. (2020, April 21) A phase equilibrium investigation of selected source controls on the composition of melt batches generated by sequential melting of an average metapelite. (V. Janoušek, B. Bonin, W.J. Collins, F. Farina, & P. Bowden, Eds.) *Post-Archean Granitic Rocks: Petrogenetic Processes and Tectonic Environments*. Geological Society of London.
- McDonough, W.F., and Sun, S. s. (1995) The composition of the Earth. *Chemical Geology*, 120, 223–253.
- Middlemost, E.A.K. (1994) Naming materials in the magma/igneous rock system. *Earth Science Reviews*, 37, 215–224.
- Miller, C.F., McDowell, S.M., and Mapes, R.W. (2003) Hot and cold granites: Implications of zircon saturation temperatures and preservation of inheritance. *Geology*, 31, 529–532.
- Moreno, J.A., Baldim, M.R., Semprich, J., Oliveira, E.P., Verma, S.K., and Teixeira, W. (2017) Geochronological and geochemical evidences for extension-related Neoproterozoic granitoids in the southern São Francisco Craton, Brazil. *Precambrian Research*, 294, 322–343.
- Mukherjee, S., Dey, A., Ibanez-mejia, M., Sanyal, S., and Sengupta, P. (2018) Geochemistry, U-Pb geochronology and Lu-Hf isotope systematics of a suite of ferroan (A-type) granitoids from the CGGC: Evidence for Mesoproterozoic crustal extension in the east Indian shield. *Precambrian Research*, 305, 40–63.

- Mukherjee, S., Dey, A., Choudhury, S.R., and Mayne, M.J. (2022) Effect of source heterogeneity, melt extraction and crystal separation on the composition of a suite of ferroan (A-type) granites from parts of the Chotanagpur Granite Gneissic Complex (CGGC), India. *Lithos*, 430–431, 106875.
- Newton, R.C., Wood, B.J., and Kleppa, O.J. (1981) Thermochemistry of silicate solid solutions. *Bulletin de Mineralogie*, 104, 162–171.
- Patiño Douce, A.E. (1997) Generation of metaluminous A-type granites by low-pressure melting of calc-alkaline granitoids. *Geology*, 743–746.
- Powell, R., and Holland, T. (1999) Relating formulations of the thermodynamics of mineral solid solutions: Activity modeling of pyroxenes, amphiboles, and micas, 84, 1–14.
- Rajesh, H.M., Santosh, M., and Yoshikura, S. (2011) The Nagercoil Charnockite: a Magnesian, Calcic to Calc-alkalic Granitoid Dehydrated during a Granulite-facies Metamorphic Event. *Journal of Petrology*, 52, 375–400.
- Sawyer, E. (2008) Working with migmatites: nomenclature for the constituent parts. *Mineralogical Association of Canada Short Course Series*, 38, 1–28.
- Sawyer, E.W. (1999) Criteria for the recognition of partial melting. *Physics and Chemistry of the Earth, Part A: Solid Earth and Geodesy*, 24, 269–279.
- Schmidt, M.W. (1992) Amphibole composition in tonalite as a function of pressure: an experimental calibration of the Al-in-hornblende barometer. *Contributions to Mineralogy and Petrology*, 110, 304–310.
- Sequeira, N., Bhattacharya, A., and Bell, E. (2022) The ~1.4 Ga A-type granitoids in the “Chottanagpur crustal block” (India), and its relocation from Columbia to Rodinia? *Geoscience Frontiers*, 13, 1138.
- Siégel, C., Bryan, S.E., Allen, C.M., and Gust, D.A. (2018) Use and abuse of zircon-based thermometers: A critical review and a recommended approach to identify antecrystic zircons. *Earth-Science Reviews*, 176, 87–116.
- Smith, T.E., Thirlwall, M., Holm, P.E., and Harris, M.J. (2004) Petrogenesis of orthopyroxene- and amphibole-bearing andesites, Mustique, Grenadine Islands, Lesser Antilles Arc: Isotope, trace element and physical constraints. *Island Arc*, 13,

73–94.

- Vernon, R.H. (2004) A Practical Guide to Rock Microstructure. Cambridge University Press, Cambridge.
- Waldbaum, D.R., and Thompson Jr., J.B. (1968) Mixing properties of sanidine crystalline solutions: II. Calculations based on volume data¹. *American Mineralogist*, 53, 2000–2017.
- Watson, E.B., and Harrison, T.M. (1983) Zircon saturation revisited: temperature and composition effects in a variety of crustal magma types. *Earth and Planetary Science Letters*, 64, 295–304.
- Whalen, J.B., Currie, K.L., and Chappell, B.W. (1987) A-type granites: geochemical characteristics, discrimination and petrogenesis. *Contributions to Mineralogy and Petrology*, 95, 407–419.
- White, R.W., Powell, R., and Clarke, G.L. (2002) The interpretation of reaction textures in Fe-rich metapelitic granulites of the Musgrave Block, central Australia: constraints from mineral equilibria calculations in the system K₂O–FeO–MgO–Al₂O₃–SiO₂–H₂O–TiO₂–Fe₂O₃. *Journal of Metamorphic Geology*, 20, 41–55.
- White, R.W., Powell, R., Holland, T.J.B., Johnson, T.E., and Green, E.C.R. (2014) New mineral activity–composition relations for thermodynamic calculations in metapelitic systems. *Journal of Metamorphic Geology*, 32, 261–286.
- Whitney, D.L., and Evans, B.W. (2010) Abbreviations for Names of Rock-Forming Minerals. *American Mineralogist*, 95, 185–187.
- Zhao, K., Xu, X., and Erdmann, S. (2018) Thermodynamic modeling for an incrementally fractionated granite magma system: Implications for the origin of igneous charnockite. *Earth and Planetary Science Letters*, 499, 230–242.
- Zhao, K., Xu, X., Klemd, R., He, Z., and Zhang, X. (2023) A review of the genetic mechanisms generating igneous charnockite: CO₂ flushing and crystal-melt segregation in mushy reservoirs. *Earth-Science Reviews*, 237, 104295.

Chapter 6

High pressure metamorphism and partial melting of mafic granulite

The mafic granulite is present as enclave within the felsic orthogneiss litho-package, and structural relations suggest these rocks record an older metamorphic and deformational event corresponding to S1 foliation (Detailed in Chapter 3). These rocks are partially melted, resulting in leucosomal segregations of variable types (Type I-IV; Chapter 3). This chapter deals with the metamorphic evolution of the mafic granulite based on detailed petrographic study, phase chemistry and phase equilibria modelling.

6.1 Petrography:

This section describes mutual relations among minerals in the three petrological entities identified in the field studies. Three domains are (a) Melanosome that is dominated by dark minerals, namely garnet and clinopyroxene (Sawyer, 2008), (b) leucosome that is dominated by quartzofeldspathic materials with or without garnet (though the garnet-rich portion in a migmatite could be called neosome (Sawyer, 2008), we avoided this term as all leucosomes contain a variable amount of garnet), and (3) amphibole-rich selvage that separates melanosome and leucosome. The salient petrographical features of the three units are described below. Mineral abbreviations used are after Whitney and Evans (2010).

6.1.1 *Melanosome:*

In melanosome, coarse-grained garnet, plagioclase, clinopyroxene, amphibole, ilmenite, quartz, and orthopyroxene form the dominant mineralogy. Titanite, rutile, and apatite are accessory minerals dispersed throughout the melanosome. The predominant texture of the melanosome is a granoblastic mosaic defined by porphyroblastic garnet, clinopyroxene (Cpx₁) and plagioclase (Pl₁) (Fig.6.1.a). Small (1-2 mm) and discontinuous segregations of plagioclase ± quartz (~1-2 mm) separate the granoblastic phases (Fig. 6.1.b-c). The quartz and feldspar in the segregations form low dihedral angles with the

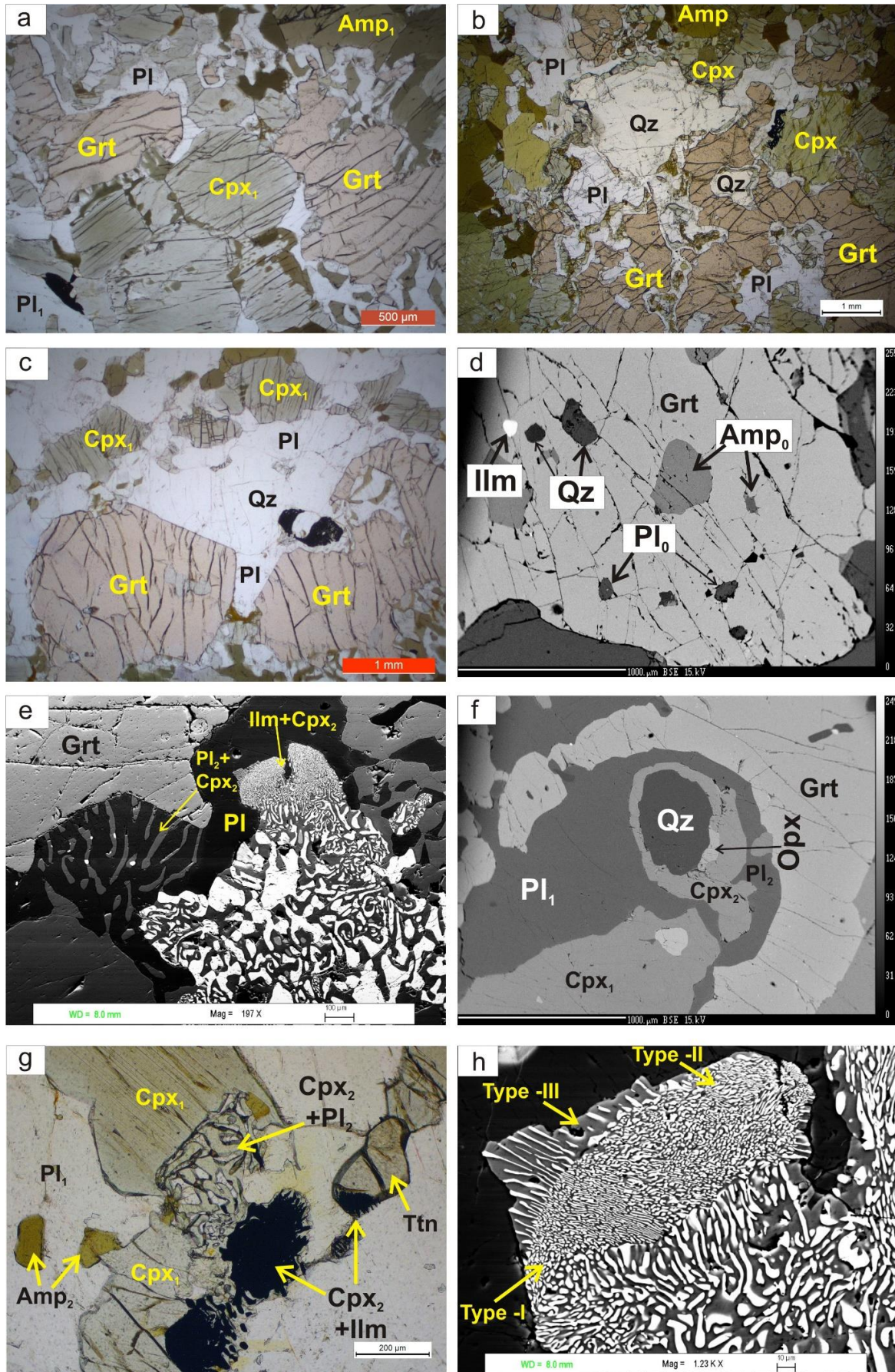


Figure 6.1: (a) Coarse grained garnet, plagioclase, clinopyroxene, amphibole, ilmenite, quartz, and orthopyroxene form the dominant mineralogy in the melanosome. (b-c) Granoblastic fabric is defined by coarse porphyroblasts of garnet, clinopyroxene (Cpx₁) and plagioclase (Pl₁) with small segregations of plagioclase \pm quartz. (b) The small quartzofeldspathic segregations follow the grain boundaries. (c) The small quartzofeldspathic segregations form low dihedral angles with the porphyroblastic phases. (d) The porphyroblastic garnet contains mineral inclusions of amphibole (Amp₀), ilmenite (Ilm), plagioclase (Pl₀) and quartz. (e) The porphyroblastic garnet develops an irregular rind of symplectic intergrowth of clinopyroxene (Cpx₂) and plagioclase (Pl₂) and the symplectic rind has a curved boundary that is convex towards the core of the garnet grain. Cpx₂-Ilm symplectite is separated from garnet by the Cpx₂-Pl₂ symplectite. (f) The contact between quartz and garnet grains is separated by a double corona of clinopyroxene (toward quartz) and plagioclase (towards garnet). Orthopyroxene is present with these coronal clinopyroxene. (g) Titanite occurs as elliptical grains and is variably replaced by a symplectic intergrowth of ilmenite and clinopyroxene. (h) The clinopyroxene-ilmenite symplectite completely replaces the titanite, retaining the original shape, and the size, shape and distance between two vermiculules vary widely in Cpx-Ilm symplectite.

porphyroblastic phases (Fig. 6.1.c). The porphyroblastic garnet contains one or more of the mineral inclusions amphibole (Amp₀), ilmenite (Ilm), plagioclase (Pl₀) and quartz (Fig. 6.1.d).

Commonly, the porphyroblastic garnet develops an irregular rind that is made up of symplectic intergrowth of clinopyroxene (Cpx₂) and plagioclase (Pl₂) that separate the garnet from Pl₁ (Fig. 6.1.e). The symplectic rind has a curved boundary that is convex towards the core of the garnet grain (Fig. 6.1.e). Rarely, at the contact, garnet is separated from quartz by a double corona of clinopyroxene (toward quartz) and plagioclase (towards garnet, Fig. 6.1.f). Locally, discontinuous orthopyroxene is present in the double corona, showing planar to curvilinear contact with secondary clinopyroxene (Cpx₂) (Fig. 6.1.f).

Titanite forms elliptical grains (Fig. 6.1.g) and is invariably separated from the porphyroblastic garnet by two layers of symplectites (Fig. 6.1.e). Symplectite of clinopyroxene (Cpx₂) and plagioclase (Pl₂) develop close to garnet, whereas vermicular intergrowth of ilmenite+clinopyroxene (Cpx₂) intergrowth forms on titanite (Fig. 6.1.e). In extreme cases, the

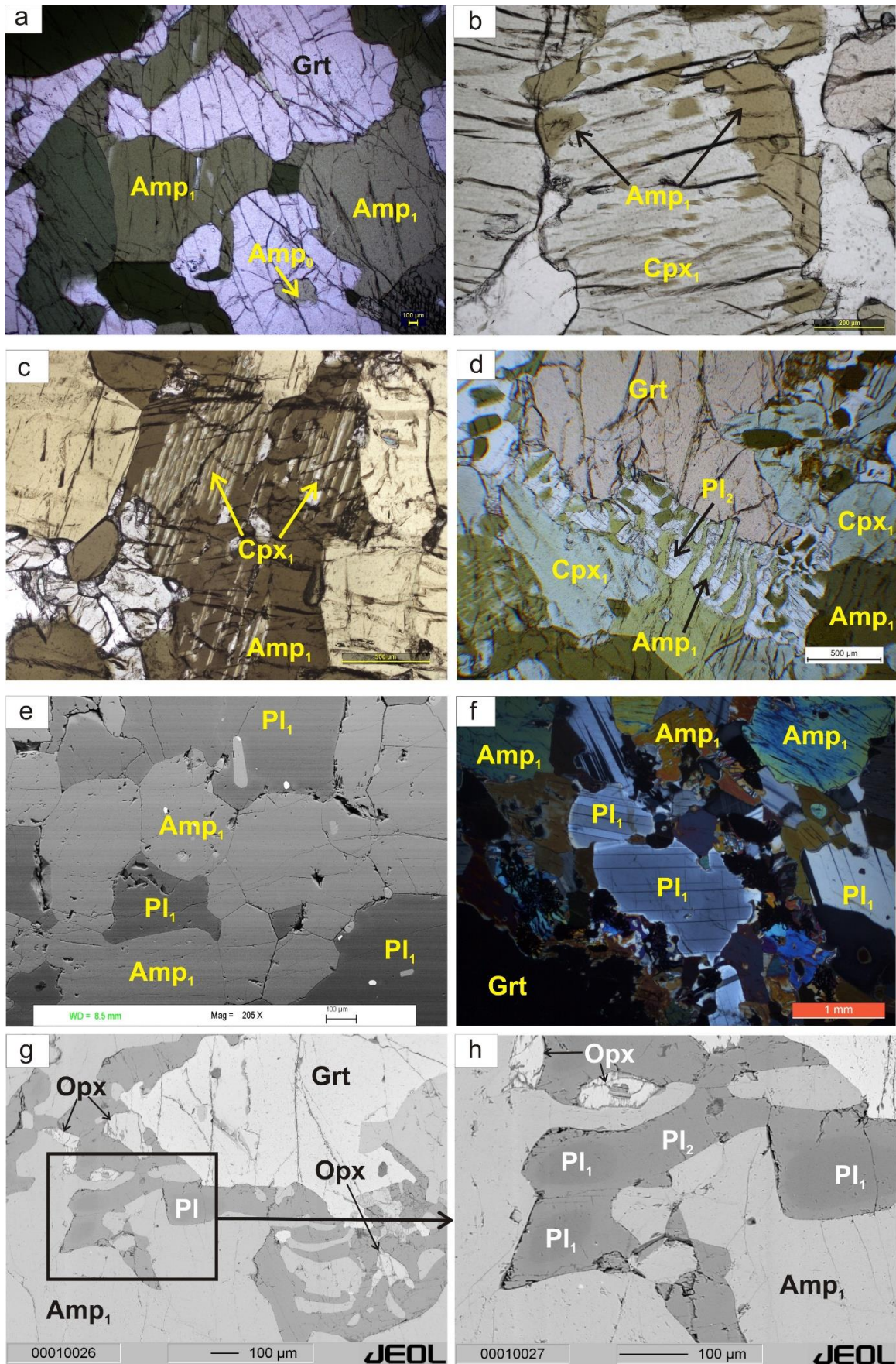


Figure 6.2: (a) The granoblastic garnet is replaced by amphibole. (b-c) The secondary amphibole preferentially replaces clinopyroxene pyroxene along the margin (b) and cleavage planes (c). (d) Amphibole replaces symplectic clinopyroxene. (e) Amphibole replaces plagioclase in the rock matrix. (f) At contact with secondary amphibole, plagioclase develops a thin rim (Pl₂) with different optical orientation. (g-h) Opx-Pl symplectite is replaced by Amp₁. Amp₁ replacement of Pl₁ results in Pl₂, marked by different shade in the BSE.

vermicular intergrowth of clinopyroxene-ilmenite completely replaces the titanite, retaining the original shape of the titanite (Fig. 6.1.e, h). The grain size and morphology of ilmenite and clinopyroxene vary widely in a vermicule population (Fig. 6.1.e, h). Three distinct morphologies of the vermicules are noted (Fig. 6.1.h). The finest (dimension) grains of ilmenite and clinopyroxene show almost planar contact (Type I) that grades into a coarse intergrowth with wavy interfaces (Type II). The two varieties define a ghost elliptical outline. In the third mode (Type III), ilmenite is distinctly coarser than the other two types. Proximal to the Type I and II aggregates, ilmenite and Cpx₂ show planar contact, and the former makes a high angle with the ghost outline (Fig. 6.1.h). The straight ilmenite blade of Type III appears to emanate from the finer ilmenite of Type I or II (Fig. 6.1.h). Away from the ghost outline, the ilmenite and Cpx₂ intergrowths in Type III become wormlike (Fig. 6.1.e-h). In places, the planar intergrowth of ilmenite and Cpx₂ in the Type III protrudes into the adjoining Pl₁. The approximate modal abundance ratio of Ilm and Cpx₂ in the symplectite varies from 1:1 in Type I and II to 2:1 in Type III.

The granoblastic garnet, plagioclase and clinopyroxene and the symplectites (both clinopyroxene-plagioclase (\pm orthopyroxene) and ilmenite-clinopyroxene) are variably replaced by amphibole (hereafter, Amp₁; Fig. 6.2). The Amp₁ preferentially and variably replaces clinopyroxene along the margin and cleavage planes (Fig. 6.2.b-c). In extreme cases, the Amp₁ completely replaces and retains the shape of the Cpx₁ it replaces (Fig. 6.2.c). At contact with secondary amphibole, plagioclase develops a thin rim (the thin rim is optically distinct in crossed polar image; Fig. 6.2.f and gives slightly different shade in BSE; Fig. 6.2.h; reverse zoning).

6.1.2 Leucosomes:

Due to its large grain size, the mutual relations among the minerals could not be studied under the microscope. Nevertheless, petrographic studies from a number of thin

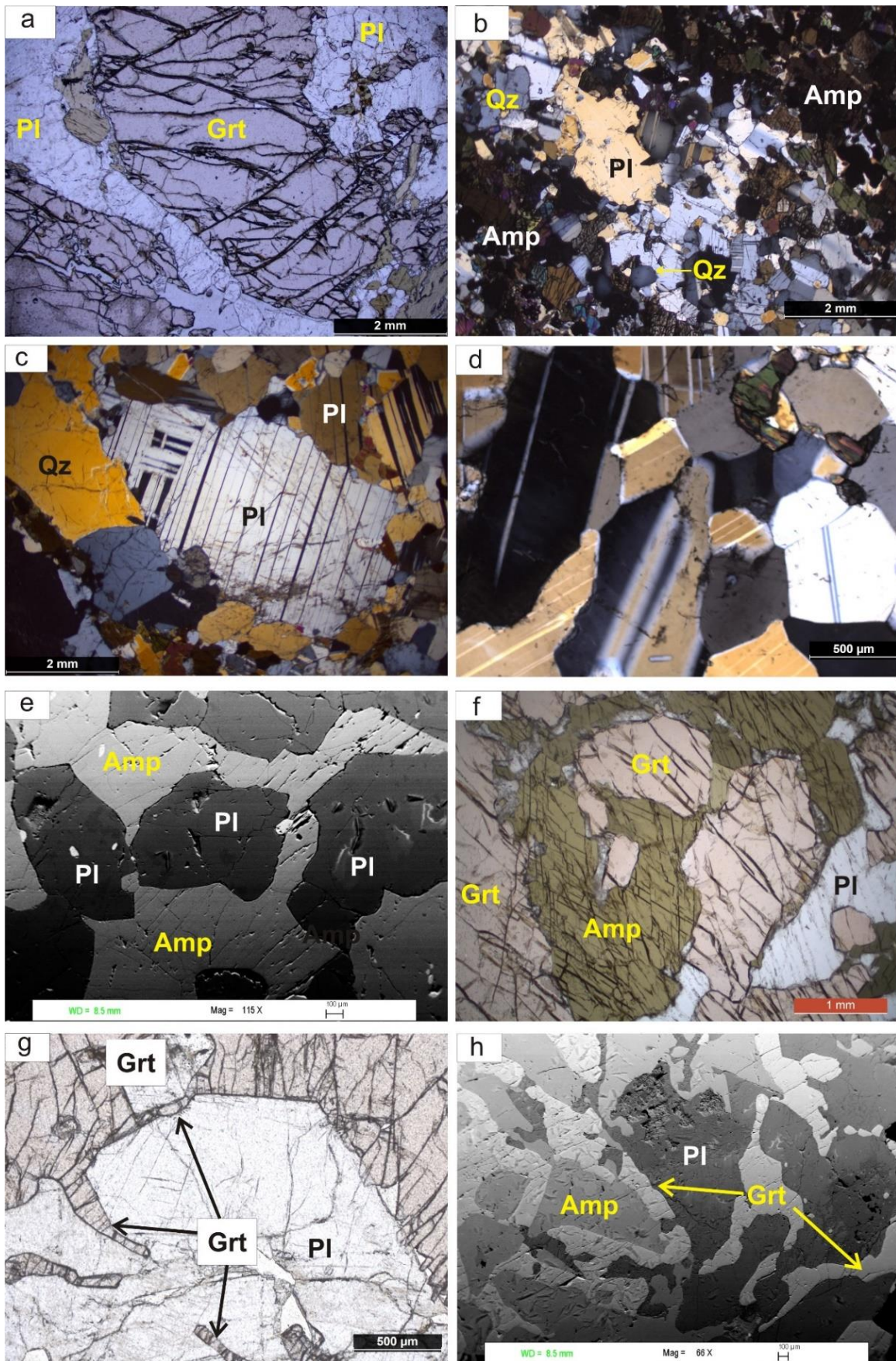


Figure 6.3: (a) Garnet the leucosome shows a euhedral outline against quartz and plagioclase. (b-d) The leucosome is chiefly constituted of quartz and plagioclase. Quartz and plagioclase show a relict interlocking texture (b) that is strongly overprinted by static recrystallisation and the formation of polygonal grain aggregates with well-developed triple points. Plagioclase grains often exhibit euhedral grains (c) and low dihedral angles (d). (e) Amphibole (Ampl) is secondary in nature and preferentially replaces polygonal plagioclase along its margin. (f) The boundary between the amphibole vein and garnet is highly corrugated, suggesting that amphibole did replace garnet. (g-h) Skeletal garnet is present in the leucosomes; These skeletal garnets usually originate from the margin of euhedral garnets as thin protruding arms in the micro-leucosomes.

sections reveal the following features. The earliest recognisable assemblage in the leucosome chiefly constituted quartz and plagioclase with a variable proportion of garnet (Fig. 6.3.a-d). The ratio of quartz and plagioclase varies from 1:5 to 2:3. Unlike the melanosome garnet the leucosome shows a euhedral outline against quartz and plagioclase (Pl_L) (Fig. 6.3.a). Quartz and plagioclase show a relict interlocking texture that is strongly overprinted by static recrystallisation and the formation of polygonal grain aggregates with well-developed triple points (Fig. 6.3.b-d). Plagioclase grains often exhibit euhedral ‘lath-shaped’ grains that are recrystallised along the boundary (Fig. 6.3.d). Amphibole (Ampl) is secondary in nature and preferentially replaces polygonal plagioclase along its margin (Fig. 6.3.e). However, garnet grains veined by amphibole are common. The boundary between the amphibole vein and garnet is highly corrugated, suggesting that amphibole replaces garnet (Fig. 6.3.f). Nowhere in the leucosome or the melanosome does amphibole show internal deformation; such a feature indicates that amphibole is post-kinematic. The leucosome is practically devoid of ilmenite, titanite and rutile. In some places, skeletal garnet is also observed in the leucosomes (Fig. 6.3.g-h). These skeletal garnets usually originate from the margin of euhedral garnets as thin protruding arms in the micro-leucosomes (Fig. 6.3.g).

6.1.3 Amphibolite rich selvage:

This domain is dominated by amphibole (>40 vol% amphibole; Amps). Proximal to the melanosome, patches of granoblastic aggregates of Grt and Cpx₁± Pl₁ occur within amphibole-rich aggregates (Fig. 6.4.a). Amphibole replaces the anhydrous minerals in different proportions and contains garnet and clinopyroxene relics. Amphibole in this zone

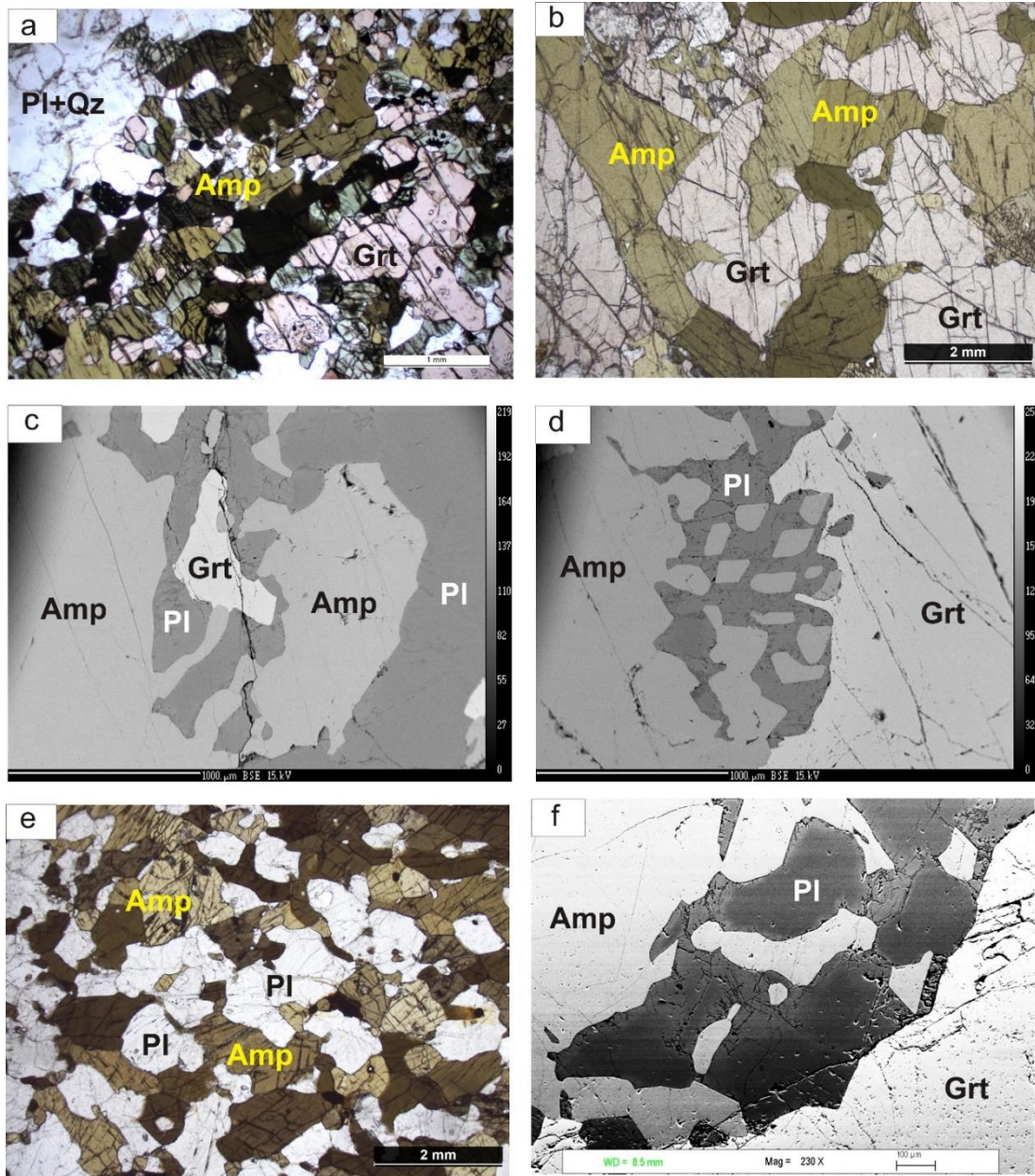


Figure 6.4: (a) Leucosomes are separated from the host mafic granulite by an amphibolite selvage. (b-c) Amphibole extensively replaces garnet. (d) Garnet breakdown resulted in the formation of comparatively coarse-grained symplectite of amphibole and plagioclase. (e-f) Amphibole is also replacing the polygonal plagioclase along its boundary, and Pl develops a rim along the boundary (visible in BSE image) along the contact with Amp, similar to melanosome and leucosome.

is practically devoid of internal deformation and preferentially replaces clinopyroxene, retaining its shape (Fig.6.4.a). Towards the leucosome, the grain size and the abundance of the amphibole increase. The amphibole commonly replaces coarse garnet in the leucosome (Fig. 6.4.b-d). In some places, garnet breakdown resulted in the formation of comparatively coarse-grained symplectite of amphiboles and plagioclases (Fig. 6.4.d).

Amphibole (Amps) forms a network along the polygonal boundaries of the plagioclase aggregates. Whenever in contact with amphiboles, plagioclase develops a thin rim that is more calcic than the core of the plagioclase (reverse zoning, confirmed by mineral chemistry, Fig. 6.4.e),

6.2 Mineral chemistry:

Analytical techniques:

Major elemental phase composition analyses of the mafic granulite were carried out at the Department of Geology and Geophysics, Indian Institute of Technology, Kharagpur, using a Cameca SX100 Electron Probe Micro Analyser. It is equipped with four wavelength-dispersive spectrometers (WDS). All points were analysed with 20 nA beam current, 15 kV acceleration voltage, and a beam size of 1 μm . For the analyses, natural minerals and synthetic compounds were used as standards.

The phase compositions of the leucosomal segregations were measured at the University of Cologne using JEOL JXA-8900RL electron microprobe (equipped with five-wavelength dispersive spectrometers). Points were analysed with 12 kV accelerating voltage, 6 nA beam current and 5-10 μm beam diameter. The machine was calibrated with the internal reference materials, both natural and synthetic.

Fe^{3+} is estimated using the cation recalculation scheme of Droop (1987). Amphibole cation recalculation is performed using the classification scheme of Leake et al. (1997). Mineral abbreviations used in phase chemistry, and the following sections are after Whitney and Evans (2010). In this section, the salient features of the minerals are presented according to the field and petrographic domains (melanosome, amphibole selvages, and leucosome). The representative mineral compositions are presented in Tables 6.1-5.

Garnet:

The garnet is dominated by almandine (43-64 mol%) with significant grossular (15-32 mol%) and pyrope (15-26 mol%) content. The spessartine component in garnet is always low (1-5 mol%) in content. The mineralogical domains control the compositional

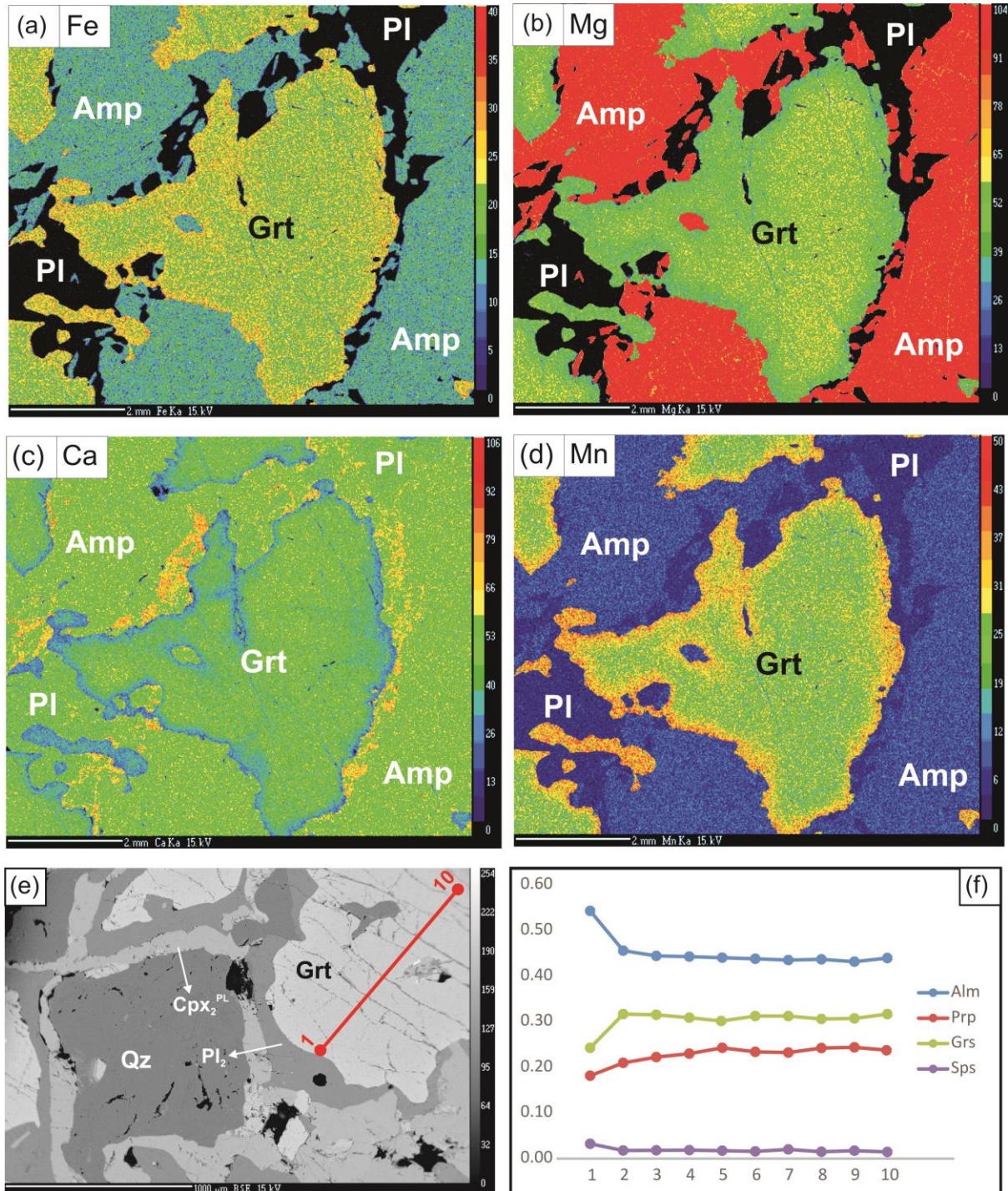


Figure 6.5: (a-d) X-ray intensity map of porphyroblastic garnets for elements Fe (a), Mg (b), Mn (b), Ca (d). X-ray intensity maps demonstrate compositional variation along the thin rim. (e-f) Core to rim compositional profile exhibits that the core of the garnet is distinctly richer in pyrope and grossular and impoverished in almandine relative to the rim.

variation of garnet as well as the nature of the coexisting phases. Garnet core composition (Table 6.1.a) in melanosome ($\text{Grt}_C = \text{Alm}_{43-50}\text{Prp}_{20-26}\text{Grs}_{24-32}\text{Spss}_{1-3}$, $X_{\text{Mg}} = \text{Mg}/(\text{Mg} + \text{Fe}^{2+}) = 0.30-0.38$) is more magnesian than its rim ($\text{Grt}_R = \text{Alm}_{50-56}\text{Prp}_{16-22}\text{Grs}_{19-29}\text{Spss}_{2-4}$, $X_{\text{Mg}} = 0.23-0.28$) adjacent to $\text{Cpx}_2\text{-Pl}_2$ symplectite or Amp_1 . Garnet composition in the amphibole-rich selvage zone (Table 6.1.b) is analogous to the melanosome showing similar compositional variation between core ($\text{Grt}_C^S = \text{Alm}_{43-50}\text{Prp}_{22-25}\text{Grs}_{28-31}\text{Spss}_{2-3}$, $X_{\text{Mg}} = 0.28-0.37$) and rim ($\text{Grt}_R^S = \text{Alm}_{52-59}\text{Prp}_{20-22}\text{Grs}_{16-27}\text{Spss}_{3-4}$, $X_{\text{Mg}} = 0.23-0.29$). In parity with the melanosome, the garnet core ($X_{\text{Mg}} = 0.32-0.37$) is more magnesian than the rim ($X_{\text{Mg}} = 0.27-0.32$). Leucosomal garnets (Table 6.1.c) exhibit similar core composition ($\text{Grt}_C^L = \text{Alm}_{47-51}\text{Prp}_{20-24}\text{Grs}_{23-27}\text{Spss}_{2-3}$, $X_{\text{Mg}} = 0.26-0.34$) as melanosome and selvage, but the rim composition ($\text{Grt}_R^L = \text{Alm}_{56-64}\text{Prp}_{15-22}\text{Grs}_{14-25}\text{Spss}_{3-5}$, $X_{\text{Mg}} = 0.21-0.27$) is distinctly more ferroan than the rim of garnet in melanosome and selvage. Overall, a notable compositional zoning is noted in the garnet (Fig. 6.5.a-d). The core of the garnet is distinctly richer in pyrope and grossular and impoverished in almandine relative to the rim of the garnet (Fig. 6.5.e-f). The core of the garnet is compositionally flat and covers most of the area, while the rim is thin (50-100 μm).

Plagioclase:

Depending on the textural association, the plagioclase in the melanosome matrix and the amphibole-rich portion show distinct compositional variation. The core of the melanosomal matrix plagioclase (Pl_1) is distinctly less calcic ($\text{An}_{45-56}\text{Ab}_{43-54}\text{Or}_{0-1}$) relative to the rim near amphibole and symplectic plagioclase (Pl_2) adjacent to garnet ($\text{An}_{73-85}\text{Ab}_{15-27}\text{Or}_{<1}$) (Table 6.2.a; Fig. 6.6.a). Compositionally, the rim of Pl_1 is roughly the same as Pl_2 . Plagioclase inclusions (Pl_0) in garnet are approximately similar to the core of Pl_1 ($\text{An}_{46-51}\text{Ab}_{49-53}\text{Or}_{0-1}$). The composition of plagioclase in the selvage (Pl_S) is quite similar to Pl_1 and exhibits a similar calcic rim adjacent to amphibole (Table 6.2.b). The plagioclase zoning near amphibole shows a flat core and a thin rim, showing an abrupt increase in anorthite content (Fig. 6.6.b-c). The composition of plagioclase in leucosome (Pl_L) is slightly less anorthitic relative to the melanosome matrix (Table 6.2.c). Similar to its counterpart in the latter, the core of the plagioclase ($\text{An}_{45-47}\text{Ab}_{55-53}\text{Or}_{0-1}$) in the leucosome is less anorthitic than its rim ($\text{An}_{75-85}\text{Ab}_{25-15}\text{Or}_{0-1}$), when in contact with secondary amphibole.

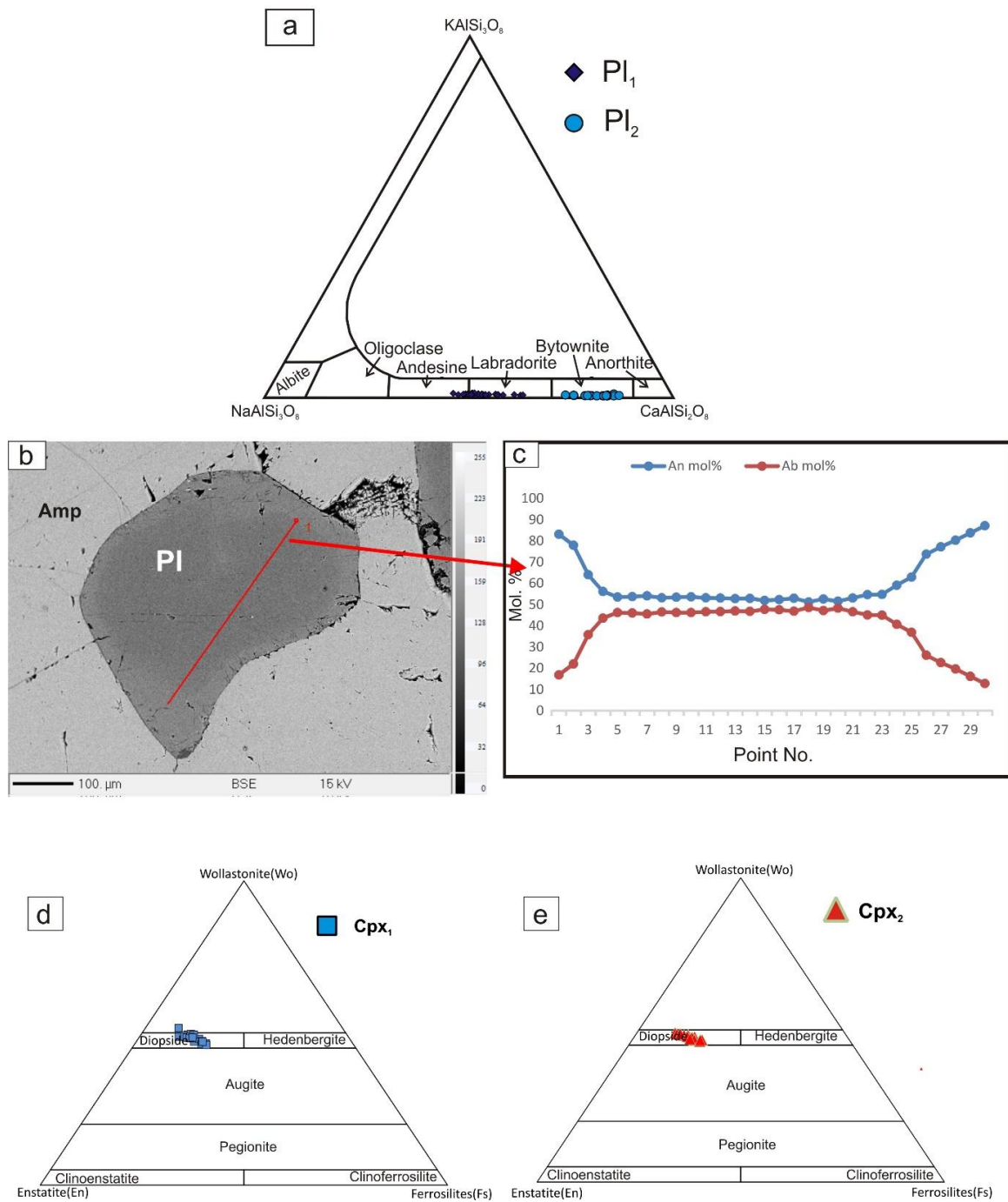


Figure 6.6: (a) The matrix plagioclase (Pl₁) is distinctly less calcic relative to secondary symplectic plagioclase (Pl₂). (b-c) Pl₁ exhibits distinct calcic rim in association with Amp₁. The variation of composition is abrupt across the flat core and thin rim. (d-e) Clinopyroxene (both Cpx₁ and Cpx₂) is mostly diopside in composition.

Pyroxene:

Clinopyroxene is diopsidic (Table 6.3.a) with insignificant variation from the core ($\text{Wo}_{46-52}\text{En}_{37-40}\text{Fs}_{8-16}$; $X_{\text{Mg}} = 0.69-0.83$) to the rim ($\text{Wo}_{46-49}\text{En}_{36-42}\text{Fs}_{10-18}$; $X_{\text{Mg}} = 0.67-0.81$). The Al_2O_3 content of the Cpx_1 core (3.3-4.4 wt%) is relatively more than the rim (1.23-2.55 wt%). There is a slight decrease in Na content from the core (**0.03-0.04 a.p.f.u**) to the rim (**0.02-0.03 a.p.f.u**) of Cpx_1 . The symplectic clinopyroxene (Cpx_2) is also diopsidic ($\text{Wo}_{46-49}\text{En}_{36-42}\text{Fs}_{9-17}$) and has a similar Mg /Fe ratio ($X_{\text{Mg}} = 0.68-0.82$) but lower Na content (**~0.02 a.p.f.u**) and Al_2O_3 content (0.91 -1.73 wt%) relative to the Cpx_1 . The orthopyroxenes (Table 6.3.b) in the melanosome yield X_{Mg} values ranging from 0.56 to 0.59 with Al_2O_3 content of **0.94-1.25wt%**. The minor orthopyroxenes present in the leucosomes are slightly less magnesian (X_{Mg} of 0.48-0.54) with similar Al_2O_3 content.

Amphibole:

According to the classification nomenclature of Leake et al.(1997), amphibole inclusions (Table 6.4.a; Amp_0) in garnet are pargasitic ($X_{\text{Mg}} = 0.56-0.67$; $(\text{Na} + \text{K})_{\text{A}} = 0.5-0.54$ a.p.f.u) (Fig. 6.7.b). The matrix amphibole in melanosome (Amp_1 ; $X_{\text{Mg}} = 0.59-0.72$) is compositionally magnesio-hornblende to tschermakite with an average TiO_2 content of ~1.56 wt% (Fig. 6.7.a). Amphibole composition in the selvage (Table 6.4.b; Amp_s ; $X_{\text{Mg}} = 0.62-0.71$) and leucosome (Table 6.4.c; Amp_L ; $X_{\text{Mg}} = 0.59-0.69$) also classify between magnesio-hornblende to tschermakite (Fig. 6.7.a) compositionally. TiO_2 content (avg. ~1.34 wt%) of Amp_s is similar to Amp_1 . However, the TiO_2 content of Amp_L (avg. ~0.91 wt%) is slightly less.

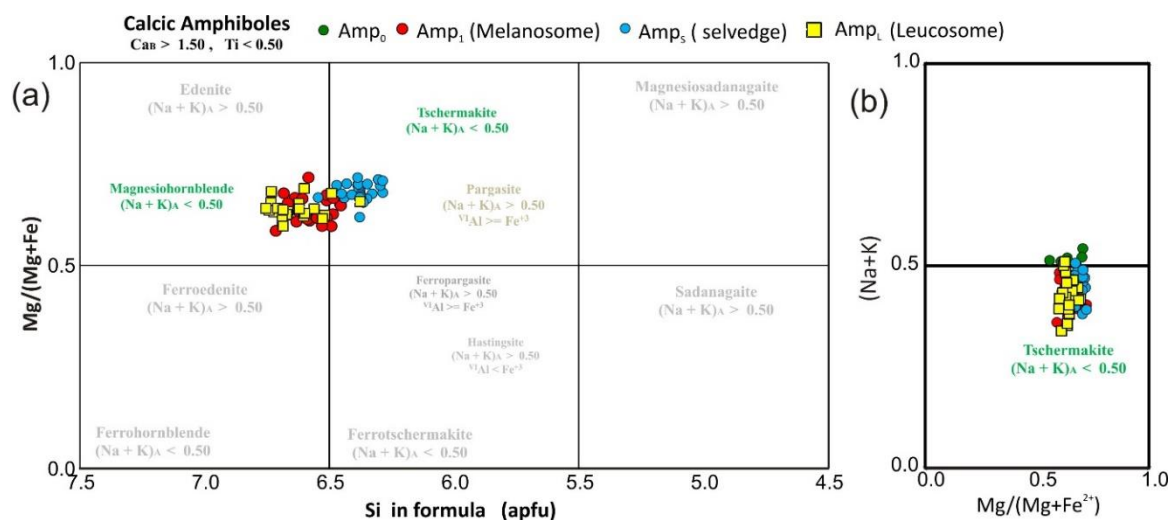


Figure 6.7: (a-b) Amphibole inclusions (Amp_0) in garnet are pargasitic, while the matrix amphibole (Amp_1) is magnesiohornblend. Amphibole in the selvage and leucosome (Amp_L) part is tschermakite compositionally.

Accessory phases:

Apatite contains 0.7-0.8 wt% F and ~0.25 wt% Cl. Titanite contains Al_2O_3 content of ~1 wt% and F, Cl content is negligible and exhibits no compositional variation (Table 6.5). Ilmenite contains Fe^{3+} 0.05-0.10.

Point No.	43 / 1.	61 / 1.	19 / 1.	119 / 1.	67 / 1.	20 / 1.	12 / 1.	108 / 1.	110 / 1.	111 / 1.
Texture	core					rim				
SiO_2	38.88	39.03	38.73	39.28	39.05	38.38	38.06	38.54	38.63	38.944
TiO_2	0.25	0.10	0.22	0.24	0.07	0.04	0.05	0.25	0.20	0.123
Al_2O_3	21.67	22.25	21.40	21.72	22.15	21.51	21.14	21.49	21.29	21.282
Cr_2O_3	0.11	0.00	0.03	0.00	0.00	0.02	0.13	0.04	0.06	0.057
FeO	22.38	23.06	23.80	22.98	24.75	26.64	25.61	24.82	26.17	26.882
MgO	5.99	6.61	5.23	5.61	5.42	4.93	4.20	4.68	4.16	4.342
CaO	11.75	10.42	11.40	10.71	9.93	8.99	10.37	10.60	9.97	8.847
MnO	0.88	0.91	0.81	0.88	1.30	1.23	1.45	1.00	1.29	1.321
Na_2O	0.02	0.03	0.03	0.06	0.01	0.01	0.04	0.00	0.03	0.031
K_2O	0.00	0.01	0.00	0.00	0.01	0.02	0.00	0.01	0.00	0
Total	102.0	102.7	101.7	101.5	102.7	101.8	101.05	101.44	101.79	101.83
Si	2.94	2.93	2.96	2.99	2.95	2.95	2.95	2.96	2.98	3.00
Ti	0.01	0.01	0.01	0.01	0.00	0.00	0.00	0.01	0.01	0.01
Al	1.93	1.97	1.92	1.95	1.97	1.95	1.93	1.95	1.93	1.93
Cr	0.01	0.00	0.00	0.00	0.00	0.00	0.01	0.00	0.00	0.00
Fe^{+3*}	0.15	0.16	0.15	0.06	0.10	0.15	0.17	0.10	0.09	0.05
Fe^{+2}	1.27	1.28	1.37	1.41	1.46	1.56	1.49	1.50	1.60	1.68
Mg	0.68	0.74	0.60	0.64	0.61	0.56	0.49	0.54	0.48	0.50
Ca	0.95	0.84	0.93	0.87	0.80	0.74	0.86	0.87	0.82	0.73
Mn	0.06	0.06	0.05	0.06	0.08	0.08	0.09	0.07	0.08	0.09
Na	0.00	0.00	0.00	0.01	0.00	0.00	0.01	0.00	0.00	0.00
K	0.00	0.00	0.00	0.00	0.00	0.00	0.00	0.00	0.00	0.00
Total	8.00	8.00	8.00	8.00	8.00	8.00	8.00	8.00	8.00	8.00
X_{Alm}	0.43	0.44	0.46	0.47	0.49	0.53	0.51	0.50	0.54	0.56
X_{Py}	0.23	0.25	0.20	0.21	0.21	0.19	0.17	0.18	0.16	0.17
X_{Grs}	0.32	0.29	0.32	0.29	0.27	0.25	0.29	0.29	0.28	0.24
X_{Sps}	0.02	0.02	0.02	0.02	0.03	0.03	0.03	0.02	0.03	0.03
X_{Mg}	0.35	0.37	0.30	0.31	0.30	0.27	0.25	0.26	0.23	0.23

* Fe^{3+} recalculated according to the scheme of Droop (1987)

Table 6.1.b: Representative microprobe analyses of garnet from selvedge and cation calculations based on 12 oxygens (oxide data given as wt%)

Point No.	16 / 1.	21 / 1.	33 / 1.	13 / 1.	21 / 1.	25 / 1.	29 / 1.	10 / 1.	12 / 1.	20 / 1.
Texture	core				rim					
SiO ₂	39.09	39.03	38.77	38.72	38.43	38.18	38.31	37.76	38.24	38.21
TiO ₂	0.18	0.15	0.15	0.17	0.12	0.02	0.03	0.07	0.03	0.08
Al ₂ O ₃	21.89	22.00	22.10	20.93	21.15	21.51	22.02	20.87	21.19	21.20
Cr ₂ O ₃	0.00	0.00	0.03	0.08	0.09	0.09	0.09	0.05	0.11	0.05
FeO	22.62	22.25	23.47	24.10	25.19	25.49	28.95	27.34	26.68	26.74
MgO	6.35	6.42	6.17	5.62	5.09	5.10	5.47	4.66	4.90	4.92
CaO	10.79	10.98	10.52	10.50	10.21	8.86	5.68	8.36	7.75	8.96
MnO	1.00	1.11	1.13	0.77	1.02	1.49	1.72	1.31	1.25	1.24
Na ₂ O	0.03	0.00	0.04	0.00	0.01	0.00	0.00	0.00	0.03	0.00
K ₂ O	0.00	0.00	0.03	0.00	0.00	0.00	0.01	0.03	0.06	0.00
Total	102.0	102.0	102.4	100.9	101.4	100.9	102.3	100.45	100.31	101.51
Si	2.95	2.95	2.92	2.98	2.95	2.95	2.94	2.95	2.98	2.95
Ti	0.01	0.01	0.01	0.01	0.01	0.00	0.00	0.00	0.00	0.00
Al	1.95	1.96	1.96	1.90	1.92	1.96	1.99	1.92	1.95	1.93
Cr	0.00	0.00	0.00	0.00	0.01	0.01	0.01	0.00	0.01	0.00
Fe ^{+3*}	0.12	0.13	0.18	0.12	0.15	0.12	0.12	0.17	0.08	0.15
Fe ⁺²	1.31	1.28	1.30	1.43	1.47	1.53	1.73	1.62	1.67	1.58
Mg	0.72	0.72	0.69	0.64	0.58	0.59	0.63	0.54	0.57	0.57
Ca	0.87	0.89	0.85	0.87	0.84	0.73	0.47	0.70	0.65	0.74
Mn	0.06	0.07	0.07	0.05	0.07	0.10	0.11	0.09	0.08	0.08
Na	0.00	0.00	0.01	0.00	0.00	0.00	0.00	0.00	0.00	0.00
K	0.00	0.00	0.00	0.00	0.00	0.00	0.00	0.00	0.01	0.00
Total	8.00	8.00	8.00	8.00	8.00	8.00	8.00	8.00	8.00	8.00
X _{Alm}	0.44	0.43	0.45	0.48	0.50	0.52	0.59	0.55	0.56	0.53
X _{Py}	0.24	0.24	0.24	0.22	0.20	0.20	0.21	0.18	0.19	0.19
X _{Grs}	0.29	0.30	0.29	0.29	0.28	0.25	0.16	0.24	0.22	0.25
X _{Sps}	0.02	0.02	0.02	0.02	0.02	0.03	0.04	0.03	0.03	0.03
X _{Mg}	0.35	0.36	0.35	0.31	0.28	0.28	0.27	0.25	0.26	0.26

* Fe³⁺ recalculated according to the scheme of Droop (1987)

Table 6.1.c: Representative microprobe analyses of garnet from leucosome and cation calculations based on 12 oxygens (oxide data given as wt%)

Point No.	123	147	163	175	183	104	112	116	146	186
Texture	core					rim				
SiO ₂	38.72	38.78	38.70	38.81	39.47	36.50	37.76	38.78	38.69	38.76
TiO ₂	0.04	0.15	0.09	0.10	0.09	0.00	0.04	0.00	0.16	0.03
Al ₂ O ₃	20.60	20.71	20.62	20.49	20.59	20.13	20.21	20.77	20.37	20.57
Cr ₂ O ₃	0.00	0.00	0.03	0.03	0.01	0.02	0.01	0.02	0.01	0.00
FeO	23.70	23.28	22.75	23.56	24.64	25.56	28.00	28.64	25.68	28.80
MgO	6.01	6.33	6.25	5.66	5.27	3.83	4.97	5.16	3.84	4.68
CaO	9.47	9.73	9.66	9.74	9.77	4.74	6.58	5.17	9.11	5.69
MnO	0.96	0.86	0.91	0.98	1.17	1.61	1.58	1.72	1.78	1.59
Na ₂ O	0.00	0.00	0.00	0.04	0.00	0.48	0.01	0.00	0.00	0.00
K ₂ O	0.02	0.00	0.01	0.00	0.01	0.08	0.02	0.01	0.00	0.00
Total	99.5	99.9	99.0	99.4	101.0	93.0	99.2	100.27	99.65	100.13
Si	3.01	3.00	3.02	3.03	3.04	3.08	2.99	3.04	3.06	3.05
Ti	0.00	0.01	0.01	0.01	0.01	0.00	0.00	0.00	0.01	0.00
Al	1.89	1.89	1.90	1.88	1.87	2.00	1.89	1.92	1.90	1.91
Cr	0.00	0.00	0.00	0.00	0.00	0.00	0.00	0.00	0.00	0.00
Fe ^{+3*}	0.70	0.73	0.73	0.66	0.61	0.48	0.59	0.60	0.45	0.55
Fe ⁺²	0.08	0.09	0.06	0.05	0.03	0.00	0.12	0.00	0.00	0.00
Mg	1.46	1.42	1.43	1.49	1.56	1.80	1.74	1.88	1.70	1.90
Ca	0.06	0.06	0.06	0.06	0.08	0.12	0.11	0.11	0.12	0.11
Mn	0.79	0.81	0.81	0.81	0.81	0.43	0.56	0.43	0.77	0.48
Na	0.00	0.00	0.00	0.01	0.00	0.08	0.00	0.00	0.00	0.00
K	0.00	0.00	0.00	0.00	0.00	0.01	0.00	0.00	0.00	0.00
Total	8.00	8.00	8.00	8.00	8.00	8.00	8.00	8.00	8.00	8.00
X _{Alm}	0.03	0.04	0.02	0.02	0.01	0.00	0.05	0.00	0.00	0.00
X _{Py}	0.61	0.60	0.61	0.61	0.63	0.77	0.69	0.77	0.66	0.76
X _{Grs}	0.03	0.02	0.03	0.03	0.03	0.05	0.04	0.05	0.05	0.04
X _{Sps}	0.33	0.34	0.34	0.34	0.33	0.18	0.22	0.18	0.30	0.19
X _{Mg}	0.95	0.94	0.96	0.97	0.98	1.00	0.94	1.00	1.00	1.00

* Fe³⁺ recalculated according to the scheme of Droop (1987)

Table 6.2.a: Representative microprobe analyses of plagioclase from the melanosome and cation calculations based on 8 oxygens (oxide data given as wt%)

Point No.	50 / 1.	47 / 1.	50 / 1.	63 / 1.	65 / 1.	18 / 1.	49 / 1.	4 / 1.	29 / 1.	41 / 1.	74 / 1.	80 / 1.
Texture	P11 core				P12 rim				P12 sym			
	56.61	55.01	55.05	56.47	50.21	46.60	48.48	48.37	49.72	47.85	55.89	57.36
SiO ₂	0.01	0.00	0.01	0.00	0.00	0.00	0.00	0.00	0.00	0.01	0.00	0.01
TiO ₂	27.93	28.03	29.13	27.36	32.21	33.94	32.92	33.25	32.85	33.99	28.65	27.68
Al ₂ O ₃	0.02	0.00	0.00	0.01	0.04	0.00	0.03	0.02	0.00	0.00	0.08	0.00
Cr ₂ O ₃	0.07	0.03	0.30	0.00	0.06	0.09	0.11	0.04	0.06	0.19	0.16	0.02
FeO	0.01	0.00	0.00	0.00	0.00	0.00	0.00	0.00	0.03	0.00	0.00	0.00
MgO	10.24	11.00	11.61	9.80	15.44	17.67	16.57	16.75	15.78	17.28	10.92	10.03
CaO	0.06	0.04	0.05	0.05	0.06	0.00	0.00	0.01	0.00	0.00	0.00	0.02
MnO	6.12	5.31	4.97	6.51	3.15	1.95	2.19	2.41	2.90	1.70	5.80	6.47
Na ₂ O	0.05	0.06	0.05	0.13	0.04	0.04	0.01	0.02	0.03	0.00	0.15	0.13
K ₂ O	101.20	99.51	101.18	100.43	101.29	100.31	100.33	100.91	101.48	101.01	101.90	101.85
Total	2.52	2.49	2.46	2.53	2.27	2.14	2.21	2.20	2.24	2.17	2.48	2.54
Si	0.00	0.00	0.00	0.00	0.00	0.00	0.00	0.00	0.00	0.00	0.00	0.00
Ti	1.46	1.50	1.53	1.45	1.71	1.84	1.77	1.78	1.75	1.82	1.50	1.44
Al	0.00	0.00	0.00	0.00	0.00	0.00	0.00	0.00	0.00	0.00	0.00	0.00
Cr	0.00	0.00	0.01	0.00	0.00	0.00	0.00	0.00	0.00	0.01	0.01	0.00
Fe ⁺²	0.00	0.00	0.00	0.00	0.00	0.00	0.00	0.00	0.00	0.00	0.00	0.00
Mg	0.49	0.53	0.56	0.47	0.75	0.87	0.81	0.82	0.76	0.84	0.52	0.48
Ca	0.00	0.00	0.00	0.00	0.00	0.00	0.00	0.00	0.00	0.00	0.00	0.00
Mn	0.53	0.47	0.43	0.57	0.28	0.17	0.19	0.21	0.25	0.15	0.50	0.55
Na	0.00	0.00	0.00	0.01	0.00	0.00	0.00	0.00	0.00	0.00	0.01	0.01
K	5.01	5.00	4.99	5.04	5.02	5.03	5.00	5.01	5.01	4.99	5.03	5.03
Total	0.48	0.53	0.56	0.45	0.73	0.83	0.81	0.79	0.75	0.85	0.51	0.46
X _{An}	0.52	0.46	0.44	0.54	0.27	0.17	0.19	0.21	0.25	0.15	0.49	0.53
X _{Ab}	0.00	0.00	0.00	0.01	0.00	0.00	0.00	0.00	0.00	0.00	0.01	0.01
X _{Or}												

Table 6.2.b: Representative microprobe analyses of plagioclase from the selvedge and cation calculations based on 8 oxygens (oxide data given as wt%)

Point No.	4 / 1 .	22 / 1 .	43 / 1 .	45 / 1 .	46 / 1 .	11 / 1 .	65 / 1 .	18 / 1 .	32 / 1 .	60 / 1 .
Texture	P11(S)					P12(S)				
SiO ₂	56.95	55.55	57.17	56.75	53.90	48.66	50.21	46.60	47.19	49.29
TiO ₂	0.00	0.02	0.00	0.00	0.02	0.07	0.00	0.00	0.00	0.00
Al ₂ O ₃	28.09	28.49	27.23	27.22	29.31	32.96	32.21	33.94	33.65	32.82
Cr ₂ O ₃	0.00	0.06	0.00	0.00	0.00	0.00	0.04	0.00	0.00	0.03
FeO	0.01	0.07	0.01	0.00	0.00	0.13	0.06	0.09	0.13	0.34
MgO	0.01	0.01	0.01	0.01	0.00	0.00	0.00	0.00	0.00	0.00
CaO	10.38	10.93	9.58	9.98	11.98	16.46	15.44	17.67	17.67	16.05
MnO	0.00	0.01	0.05	0.00	0.00	0.00	0.06	0.00	0.04	0.00
Na ₂ O	6.12	5.67	6.45	6.35	5.39	2.60	3.15	1.95	1.99	2.44
K ₂ O	0.16	0.10	0.12	0.15	0.11	0.01	0.04	0.04	0.03	0.02
Total	101.77	100.97	100.76	100.61	100.80	100.94	101.29	100.31	100.83	101.02
Si	2.52	2.48	2.55	2.54	2.42	2.21	2.27	2.14	2.16	2.23
Ti	0.00	0.00	0.00	0.00	0.00	0.00	0.00	0.00	0.00	0.00
Al	1.46	1.50	1.43	1.44	1.55	1.77	1.71	1.84	1.81	1.75
Cr	0.00	0.00	0.00	0.00	0.00	0.00	0.00	0.00	0.00	0.00
Fe ⁺²	0.00	0.00	0.00	0.00	0.00	0.00	0.00	0.00	0.01	0.01
Mg	0.00	0.00	0.00	0.00	0.00	0.00	0.00	0.00	0.00	0.00
Ca	0.49	0.52	0.46	0.48	0.58	0.80	0.75	0.87	0.86	0.78
Mn	0.00	0.00	0.00	0.00	0.00	0.00	0.00	0.00	0.00	0.00
Na	0.52	0.49	0.56	0.55	0.47	0.23	0.28	0.17	0.18	0.21
K	0.01	0.01	0.01	0.01	0.01	0.00	0.00	0.00	0.00	0.00
Total	5.01	5.01	5.02	5.02	5.04	5.02	5.02	5.03	5.02	5.00
X _{An}	0.48	0.51	0.45	0.46	0.55	0.78	0.73	0.83	0.83	0.78
X _{Ab}	0.51	0.48	0.55	0.53	0.45	0.22	0.27	0.17	0.17	0.22
X _{Or}	0.01	0.01	0.01	0.01	0.01	0.00	0.00	0.00	0.00	0.00

Table 6.2.c: Representative microprobe analyses of plagioclase from the leucosome and cation calculations based on 8 oxygens (oxide data given as wt%)

Point No.	167	139	145	150	168	31	107	114	121	176
Texture	P11(L)					P12(L)				
SiO ₂	55.86	53.54	53.57	53.61	55.29	45.37	45.71	47.58	47.63	47.22
TiO ₂	0.00	0.00	0.00	0.00	0.00	0.01	0.00	0.00	0.01	0.00
Al ₂ O ₃	27.55	26.62	26.89	26.69	27.58	33.59	32.51	31.22	31.86	32.61
Cr ₂ O ₃	0.02	0.01	0.00	0.00	0.00	0.00	0.00	0.00	0.01	0.00
FeO	0.09	0.19	0.23	0.11	0.08	0.17	0.18	0.11	0.13	0.10
MgO	0.00	0.01	0.00	0.00	0.00	0.00	0.01	0.00	0.00	0.00
CaO	10.26	10.23	10.15	9.97	10.34	17.12	16.99	15.49	15.77	16.36
MnO	0.00	0.02	0.02	0.00	0.01	0.01	0.01	0.00	0.02	0.00
Na ₂ O	6.54	6.41	6.30	6.51	6.59	1.67	1.88	2.87	2.83	2.18
K ₂ O	0.14	0.08	0.12	0.16	0.13	0.00	0.02	0.04	0.04	0.01
Total	97.85	97.12	97.28	97.04	100.01	97.94	97.31	97.32	98.31	98.49
Si	2.51	2.50	2.49	2.50	2.50	2.13	2.16	2.24	2.22	2.20
Ti	0.00	0.00	0.00	0.00	0.00	0.00	0.00	0.00	0.00	0.00
Al	1.46	1.46	1.47	1.47	1.47	1.86	1.81	1.73	1.75	1.79
Cr	0.00	0.00	0.00	0.00	0.00	0.00	0.00	0.00	0.00	0.00
Fe ⁺²	0.00	0.01	0.01	0.00	0.00	0.01	0.01	0.00	0.01	0.00
Mg	0.00	0.00	0.00	0.00	0.00	0.00	0.00	0.00	0.00	0.00
Ca	0.49	0.51	0.51	0.50	0.50	0.86	0.86	0.78	0.79	0.82
Mn	0.00	0.00	0.00	0.00	0.00	0.00	0.00	0.00	0.00	0.00
Na	0.57	0.58	0.57	0.59	0.58	0.15	0.17	0.26	0.26	0.20
K	0.01	0.01	0.01	0.01	0.01	0.00	0.00	0.00	0.00	0.00
Total	5.05	5.06	5.06	5.07	5.06	5.01	5.02	5.02	5.03	5.01
X _{An}	0.46	0.47	0.47	0.45	0.46	0.85	0.83	0.75	0.75	0.81
X _{Ab}	0.53	0.53	0.53	0.54	0.53	0.15	0.17	0.25	0.24	0.19
X _{Or}	0.01	0.00	0.01	0.01	0.01	0.00	0.00	0.00	0.00	0.00

Table 6.3.a: Representative microprobe analyses of clinopyroxene and cation calculations based on 6 oxygens (oxide data given as wt%)

Point No.	67 / 1.	55 / 1.	21 / 1.	5 / 1.	69 / 1.	7 / 1.	96 / 1.	97 / 1.	59 / 1.	72 / 1.	9 / 1.	21 / 1.
Texture	Cpx1 core				Cpx1 rim				Cpx2 sym			
SiO ₂	51.29	51.14	51.81	50.64	52.36	51.48	51.82	52.645	52.98	53.223	52.79	53.097
TiO ₂	0.31	0.31	0.31	0.42	0.17	0.34	0.159	0.205	0.203	0.189	0.271	0.069
Al ₂ O ₃	2.82	3.38	3.06	3.83	1.43	2.28	1.627	1.658	1.3	1.583	1.069	1.236
Cr ₂ O ₃	0.03	0.21	0.00	0.08	0.16	0.00	0.017	0	0.006	0.15	0.029	0
FeO	11.10	10.39	10.70	9.79	9.05	10.07	11.027	11.478	8.653	9.566	9.166	9.169
MgO	12.65	12.94	12.43	12.38	14.28	12.90	12.381	12.394	14.451	13.866	14.297	14.076
CaO	22.74	22.73	22.48	22.62	23.27	22.71	22.246	22.34	23.657	23.391	23.367	23.536
MnO	0.10	0.21	0.22	0.16	0.23	0.30	0.175	0.185	0.202	0.153	0.242	0.195
Na ₂ O	0.46	0.45	0.47	0.46	0.28	0.31	0.337	0.321	0.335	0.347	0.239	0.307
K ₂ O	0.00	0.02	0.00	0.00	0.03	0.00	0	0	0.014	0.008	0	0
Total	101.61	102.14	101.57	100.38	101.31	100.40	99.799	101.24	101.925	102.55	101.626	101.72
Si	1.89	1.87	1.91	1.89	1.92	1.92	1.95	1.96	1.93	1.94	1.93	1.94
Ti	0.01	0.01	0.01	0.01	0.00	0.01	0.00	0.01	0.01	0.01	0.01	0.00
Al	0.12	0.15	0.13	0.17	0.06	0.10	0.07	0.07	0.06	0.07	0.05	0.05
Cr	0.00	0.01	0.00	0.00	0.00	0.00	0.00	0.00	0.00	0.00	0.00	0.00
Fe ^{+3*}	0.10	0.11	0.06	0.07	0.10	0.07	0.04	0.03	0.09	0.06	0.09	0.07
Fe ⁺²	0.24	0.21	0.28	0.24	0.18	0.25	0.30	0.33	0.18	0.23	0.19	0.21
Mg	0.70	0.71	0.68	0.69	0.78	0.72	0.69	0.69	0.79	0.75	0.78	0.77
Ca	0.90	0.89	0.89	0.90	0.92	0.91	0.90	0.89	0.92	0.91	0.92	0.92
Mn	0.00	0.01	0.01	0.01	0.01	0.01	0.01	0.01	0.01	0.00	0.01	0.01
Na	0.03	0.03	0.03	0.03	0.02	0.02	0.02	0.02	0.02	0.02	0.02	0.02
K	0.00	0.00	0.00	0.00	0.00	0.00	0.00	0.00	0.00	0.00	0.00	0.00
Total	4.00	4.00	4.00	4.00	4.00	4.00	4.00	4.00	4.00	4.00	4.00	4.00
X _{Mg}	0.74	0.77	0.71	0.74	0.81	0.74	0.70	0.67	0.82	0.77	0.81	0.79

* Fe³⁺ recalculated according to the scheme of Droop (1987)

Table 6.3.b: Representative microprobe analyses of orthopyroxene and cation calculations based on 6 oxygens (oxide data given as wt%)

Point No.	17	32	33	133	134	143
Texture	Opx Sym			OpxL		
SiO ₂	51.17	50.58	50.80	51.26	51.88	52.14
TiO ₂	0.04	0.03	0.03	0.04	0.02	0.04
Al ₂ O ₃	1.04	1.01	0.94	0.78	0.86	0.78
Cr ₂ O ₃	0.03	0.09	0.03	0.00	0.00	0.00
FeO	28.90	28.91	28.46	30.26	30.01	29.86
MgO	18.87	18.84	18.75	15.89	16.21	16.42
CaO	0.41	0.43	0.43	0.83	0.67	0.51
MnO	0.51	0.43	0.34	0.80	0.74	0.64
Na ₂ O	0.00	0.05	0.03	0.04	0.06	0.00
K ₂ O	0.02	0.00	0.01	0.02	0.01	0.01
Total	101.00	100.37	99.81	99.92	100.46	100.40
Si	1.94	1.93	1.94	1.99	2.00	2.01
Ti	0.00	0.00	0.00	0.00	0.00	0.00
Al	0.05	0.05	0.04	0.04	0.04	0.04
Cr	0.00	0.00	0.00	0.00	0.00	0.00
Fe ^{+3*}	0.07	0.10	0.07	0.00	0.00	0.00
Fe ⁺²	0.84	0.82	0.84	0.98	0.97	0.96
Mg	1.06	1.07	1.07	0.92	0.93	0.94
Ca	0.02	0.02	0.02	0.03	0.03	0.02
Mn	0.02	0.01	0.01	0.03	0.02	0.02
Na	0.00	0.00	0.00	0.00	0.00	0.00
K	0.00	0.00	0.00	0.00	0.00	0.00
Total	0.00	0.00	0.00	4.00	4.00	4.00
X _{Mg}	4.00	4.00	4.00	0.48	0.49	0.49

* Fe³⁺ recalculated according to the scheme of Droop (1987)

Table 6.4.a: Representative microprobe analyses of amphibole from the melanosome and cation calculations based (after Leake et al., 1997) on 23 oxygens (oxide data given as wt%)

Point No.	16 / 1 .	26 / 1 .	61 / 1 .	42 / 1 .	63 / 1 .	5 / 1 .	26 / 1 .	30 / 1 .
Texture	Amp0		Amp1					
SiO ₂	44.76	42.45	45.69	45.26	45.15	46.00	45.09	45.10
TiO ₂	1.32	0.53	1.61	1.39	1.68	1.56	1.72	1.18
Al ₂ O ₃	11.96	14.69	10.02	10.86	10.42	10.55	10.78	11.53
Cr ₂ O ₃	0.00	0.05	0.00	0.23	0.08	0.03	0.13	0.09
FeO	14.66	18.87	13.60	15.29	14.94	13.72	16.05	14.75
MgO	12.75	9.55	13.90	12.61	12.96	12.99	11.82	12.67
CaO	11.84	12.21	11.72	11.75	11.89	11.81	11.64	11.86
MnO	0.09	0.00	0.00	0.08	0.11	0.15	0.06	0.12
Na ₂ O	2.02	1.55	1.62	1.79	1.70	1.57	1.88	1.85
K ₂ O	0.20	0.74	0.28	0.23	0.30	0.31	0.21	0.26
Total	99.68	101.10	98.56	99.56	99.67	98.88	99.55	99.54
Si	6.42	6.14	6.59	6.51	6.51	6.64	6.54	6.49
Al (IV)	1.58	1.86	1.41	1.49	1.49	1.36	1.46	1.51
Ti	0.00	0.00	0.00	0.00	0.00	0.00	0.00	0.00
Sum T	8.00	8.00	8.00	8.00	8.00	8.00	8.00	8.00
Al (VI)	0.45	0.65	0.29	0.36	0.28	0.44	0.38	0.44
Ti	0.14	0.06	0.17	0.15	0.18	0.17	0.19	0.13
Cr ⁺³	0.00	0.01	0.00	0.03	0.01	0.00	0.02	0.01
Fe ⁺³	0.44	0.64	0.47	0.46	0.47	0.27	0.33	0.43
Mg	2.73	2.06	2.99	2.71	2.78	2.80	2.55	2.71
Fe ⁺²	1.25	1.60	1.08	1.30	1.27	1.32	1.53	1.28
Mn	0.00	0.00	0.00	0.00	0.00	0.00	0.00	0.00
Li	0.00	0.00	0.00	0.00	0.00	0.00	0.00	0.00
Sum C	5.00	5.00	5.00	5.00	5.00	5.00	5.00	5.00
Mg	0.00	0.00	0.00	0.00	0.00	0.00	0.00	0.00
Fe ⁺²	0.07	0.05	0.09	0.08	0.06	0.06	0.08	0.07
Mn	0.01	0.00	0.00	0.01	0.01	0.02	0.01	0.01
Li	0.00	0.00	0.00	0.00	0.00	0.00	0.00	0.00
Ca	1.82	1.89	1.81	1.81	1.84	1.83	1.81	1.83
Na	0.10	0.06	0.10	0.10	0.09	0.10	0.10	0.09
Sum B	2.00	2.00	2.00	2.00	2.00	2.00	2.00	2.00
Ca	0.00	0.00	0.00	0.00	0.00	0.00	0.00	0.00
Na	0.47	0.38	0.35	0.40	0.39	0.34	0.43	0.42
K	0.04	0.14	0.05	0.04	0.06	0.06	0.04	0.05
Sum A	0.50	0.51	0.40	0.44	0.45	0.40	0.47	0.47
Total	15.50	15.51	15.40	15.44	15.45	15.40	15.47	15.47
X _{Mg}	0.67	0.56	0.72	0.66	0.68	0.67	0.61	0.67

Table 6.4.b: Representative microprobe analyses of amphibole from the selvedge and cation calculations based (after Leake et al., 1997) on 23 oxygens (oxide data given as wt%)

Point No.	66 / 1 .	71 / 1 .	83 / 1 .	11 / 1 .	30 / 1 .	17 / 1 .	23 / 1 .	44 / 1 .
Texture	AmpS							
SiO ₂	44.71	44.42	43.89	44.16	43.92	43.84	43.73	43.64
TiO ₂	1.11	1.16	1.14	1.06	1.31	1.33	1.23	1.83
Al ₂ O ₃	12.30	12.17	12.81	12.08	12.30	12.27	12.30	12.35
Cr ₂ O ₃	0.14	0.03	0.02	0.06	0.01	0.11	0.02	0.00
FeO	14.46	15.06	15.08	14.73	15.47	16.33	15.52	14.45
MgO	12.51	12.61	12.62	12.45	12.21	11.39	11.91	12.99
CaO	11.57	11.39	11.31	11.44	11.46	11.18	11.29	11.11
MnO	0.01	0.23	0.19	0.15	0.08	0.14	0.20	0.15
Na ₂ O	1.74	1.66	1.83	1.74	1.77	1.78	1.72	1.85
K ₂ O	0.53	0.52	0.58	0.60	0.54	0.65	0.58	0.57
Total	99.24	99.31	99.80	98.76	99.17	99.11	98.62	99.02
Si	6.44	6.38	6.30	6.41	6.35	6.38	6.37	6.29
Al (IV)	1.56	1.62	1.70	1.59	1.65	1.62	1.63	1.71
Ti	0.00	0.00	0.00	0.00	0.00	0.00	0.00	0.00
Sum T	8.00	8.00	8.00	8.00	8.00	8.00	8.00	8.00
Al (VI)	0.53	0.45	0.46	0.48	0.45	0.49	0.48	0.39
Ti	0.12	0.13	0.12	0.12	0.14	0.15	0.14	0.20
Cr ⁺³	0.02	0.00	0.00	0.01	0.00	0.01	0.00	0.00
Fe ⁺³	0.41	0.62	0.65	0.50	0.56	0.48	0.54	0.61
Mg	2.69	2.70	2.70	2.69	2.63	2.47	2.58	2.79
Fe ⁺²	1.23	1.11	1.06	1.20	1.22	1.40	1.26	1.02
Mn	0.00	0.00	0.00	0.00	0.00	0.00	0.00	0.00
Li	0.00	0.00	0.00	0.00	0.00	0.00	0.00	0.00
Sum C	5.00	5.00	5.00	5.00	5.00	5.00	5.00	5.00
Mg	0.00	0.00	0.00	0.00	0.00	0.00	0.00	0.00
Fe ⁺²	0.10	0.09	0.10	0.09	0.10	0.10	0.09	0.12
Mn	0.00	0.03	0.02	0.02	0.01	0.02	0.02	0.02
Li	0.00	0.00	0.00	0.00	0.00	0.00	0.00	0.00
Ca	1.79	1.75	1.74	1.78	1.78	1.74	1.76	1.71
Na	0.11	0.13	0.14	0.12	0.12	0.14	0.13	0.15
Sum B	2.00	2.00	2.00	2.00	2.00	2.00	2.00	2.00
Ca	0.00	0.00	0.00	0.00	0.00	0.00	0.00	0.00
Na	0.37	0.33	0.37	0.37	0.38	0.37	0.36	0.37
K	0.10	0.10	0.11	0.11	0.10	0.12	0.11	0.10
Sum A	0.47	0.43	0.48	0.48	0.48	0.49	0.47	0.47
Total	15.47	15.43	15.48	15.48	15.48	15.49	15.47	15.47
X _{Mg}	0.67	0.69	0.70	0.68	0.67	0.62	0.66	0.71

Table 6.4.c: Representative microprobe analyses of amphibole from the leucosome and cation calculations based (after Leake et al., 1997) on 23 oxygens (oxide data given as wt%)

Point No.	108	122	165	166	174	180	181	185
Texture	AmpL							
SiO ₂	43.78	44.15	45.19	45.41	45.70	44.80	44.98	44.98
TiO ₂	1.25	1.03	1.03	0.94	1.20	1.08	0.97	1.03
Al ₂ O ₃	11.36	10.83	10.24	9.93	10.83	10.75	11.81	11.34
Cr ₂ O ₃	0.03	0.03	0.07	0.04	0.01	0.03	0.00	0.01
FeO	15.05	14.86	14.69	14.48	14.46	15.12	14.39	14.55
MgO	11.35	11.55	11.90	12.00	11.97	11.04	11.65	11.80
CaO	10.98	10.84	10.69	10.86	10.91	10.95	11.00	10.83
MnO	0.16	0.13	0.17	0.17	0.12	0.15	0.11	0.11
Na ₂ O	1.95	2.03	1.70	1.66	1.79	1.72	1.92	1.74
K ₂ O	0.49	0.49	0.45	0.41	0.46	0.52	0.54	0.52
Total	96.41	95.95	96.14	95.90	97.46	96.18	97.40	96.91
Si	6.53	6.61	6.71	6.76	6.69	6.69	6.60	6.62
Al (IV)	1.47	1.39	1.29	1.24	1.31	1.31	1.40	1.38
Ti	0.00	0.00	0.00	0.00	0.00	0.00	0.00	0.00
Sum T	8.00	8.00	8.00	8.00	8.00	8.00	8.00	8.00
Al (VI)	0.53	0.52	0.50	0.50	0.56	0.58	0.64	0.59
Ti	0.14	0.12	0.11	0.11	0.13	0.12	0.11	0.11
Cr ⁺³	0.00	0.00	0.01	0.00	0.00	0.00	0.00	0.00
Fe ⁺³	0.31	0.31	0.36	0.32	0.30	0.25	0.27	0.35
Mg	2.52	2.57	2.63	2.66	2.61	2.46	2.55	2.59
Fe ⁺²	1.49	1.48	1.38	1.41	1.40	1.59	1.43	1.36
Mn	0.00	0.00	0.00	0.00	0.00	0.00	0.00	0.00
Li	0.00	0.00	0.00	0.00	0.00	0.00	0.00	0.00
Sum C	5.00	5.00	5.00	5.00	5.00	5.00	5.00	5.00
Mg	0.00	0.00	0.00	0.00	0.00	0.00	0.00	0.00
Fe ⁺²	0.07	0.07	0.08	0.07	0.07	0.05	0.06	0.09
Mn	0.02	0.02	0.02	0.02	0.01	0.02	0.01	0.01
Li	0.00	0.00	0.00	0.00	0.00	0.00	0.00	0.00
Ca	1.75	1.74	1.70	1.73	1.71	1.75	1.73	1.71
Na	0.16	0.17	0.19	0.18	0.20	0.18	0.19	0.19
Sum B	2.00	2.00	2.00	2.00	2.00	2.00	2.00	2.00
Ca	0.00	0.00	0.00	0.00	0.00	0.00	0.00	0.00
Na	0.41	0.42	0.29	0.30	0.31	0.32	0.36	0.30
K	0.09	0.09	0.09	0.08	0.09	0.10	0.10	0.10
Sum A	0.50	0.51	0.38	0.38	0.39	0.42	0.46	0.40
Total	15.50	15.51	15.38	15.38	15.39	15.42	15.46	15.40
X _{Mg}	0.62	0.62	0.64	0.64	0.64	0.60	0.63	0.64

Table 6.5: Representative microprobe analyses of ilmenite, titanite, rutile and apatite (oxide data given as wt%)

Point No.	31 / 1 .	32 / 1 .	33 / 1 .	121 / 1 .	39 / 1 .	Point No.	42	44
Phase	Ilm	Ilm	Ilm	Ttn	Rt	Phase	Apt	Apt
SiO ₂	0.00	0.06	0.01	30.03	0	SiO ₂	0.00	0.02
TiO ₂	50.87	51.06	51.09	39.00	98.109	TiO ₂	0.00	0.01
Al ₂ O ₃	0.17	0.15	0.15	1.22	0.351	Al ₂ O ₃	0.00	0.01
Cr ₂ O ₃	0.01	0.00	0.04	0.00	0.028	Cr ₂ O ₃	0.00	0.02
FeO	46.38	47.97	45.75	0.32	0.76	FeO	0.10	0.25
MgO	1.03	1.20	1.19	0.00	0.017	MgO	0.01	0.00
CaO	0.11	0.23	0.30	28.33	0.018	CaO	54.34	52.90
MnO	0.47	0.50	0.44	0.10	0	MnO	0.04	0.03
Na ₂ O	0.00	0.00	0.00	0.00	0	Na ₂ O	0.00	0.01
K ₂ O	0.00	0.00	0.00	0.00	0.006	K ₂ O	0.00	0.00
Total	99.06	101.16	98.96	99.02	101.5	P ₂ O ₅	40.60	40.14
Si	0.00	0.00	0.00	0.98	0	F	0.76	0.68
Ti	0.96	0.95	0.97	0.96	0.971945	Cl	0.23	0.27
Al	0.01	0.00	0.00	0.05	0.005448	Total	95.69	93.99
Cr	0.00	0.00	0.00	0.00	0.000292	O=F	0.32	0.29
Fe ^{+3*}	0.07	0.10	0.06	0.01	0.008513	O=Cl	0.05	0.06
Fe ⁺²	0.91	0.89	0.91	0.00	0	Revised SUM	95.69	93.99
Mg	0.04	0.04	0.04	0.00	0.000334	Si	0.00	0.00
Ca	0.00	0.01	0.01	0.99	0.000254	Ti	0.00	0.00
Mn	0.01	0.01	0.01	0.00	0	Al	0.00	0.00
Na	0.00	0.00	0.00	0.00	0	Cr	0.00	0.00
K	0.00	0.00	0.00	0.00	0.000101	Ca	4.80	4.75
Total	2	2	2	3	1	Fe ⁺²	0.01	0.02
* Fe ³⁺ recalculated according to the scheme of Droop (1987)						Mn	0.00	0.00
						Mg	0.00	0.00
						Na	0.00	0.00
						K	0.00	0.00
						P	2.83	2.85
						F	0.20	0.18
						Cl	0.03	0.04
						SUM	7.87	7.84
						OH	1.77	1.78

6.3 Metamorphic evolution:

Petrography and phase chemistry are crucial in understanding the metamorphic history. Several textural relations between constituent minerals assist in framing the metamorphic evolution of the mafic granulite at different stages of metamorphism. Due to the formation of leucosome and the garnet-clinopyroxene bearing the granoblastic fabric followed by the formation of secondary pyroxene, plagioclase and amphibole, tracing the mineralogical changes that occurred along the prograde P-T path is difficult. Nevertheless, the presence of mineral inclusions (amphibole, plagioclase, quartz and ilmenite) in porphyroblastic garnet and clinopyroxene (only amphibole) suggests that these minerals were present before the granoblastic assemblages. $\text{Ilm} + \text{Amp}_0 + \text{Pl}_0 + \text{Qz}$ assemblage is therefore considered **prograde assemblage (M_{PR})**. Several studies have argued that the leucosomes in high-grade rocks represent a quenched melt phase that formed in situ due to the partial melting of hydrous minerals (Hartel and Pattison 1996; Hansen et al. 2015; Yu et al. 2019; Cai et al. 2020). Despite intense solid-state deformation, certain textural features of the leucosomes, such as (a) the presence of relict interlocking texture between plagioclase and quartz, low dihedral angle (Fig. 6.1b-c; 6.3.b-d) and (b) stromatic to patchy to ramifying that cut across the foliation, are consistent with the view that the leucosomes in the studied area represent quenched melt (Chapter 3) (Sawyer 2008). The euhedral garnet in the leucosomes is therefore considered a peritectic phase (Brown, 2002; Cai et al., 2020; Hansen et al., 2015; Hartel & Pattison, 1996; Yu et al., 2019 and the references cited therein).

Based on textural features, it is presumed that the granoblastic assemblage (**Grt + Cpx₁ + Pl₁ + Rt + Ttn ± Qz**) developed in the melanosome at the culmination (peak) of metamorphism (**M_{PK}**). The assemblage of **M_{PK}** is typically developed in the high-pressure mafic granulite elsewhere in the world (Hartel and Pattison 1996; Zhao et al. 2001; O'Brien and Rötzler 2003; Pattison 2003). The intimate association of melanosome and leucosome suggest that **M_{PK}** coexisted with a melt phase (now represented as leucosome). The peritectic garnet in the leucosome presumably formed during the development of the melanosome. The small plagioclase and quartz-plagioclase segregations (micro leucosome) with curved grain boundaries occur along grain boundaries of the granoblastic assemblage (Fig. 6.1.b) are found in many migmatitic melanosomes as the intercumulous minerals

(Grant and Frost 1990; Harte et al. 1991; Hartel and Pattison 1996). The published studies posit that micro-leucosomes and small plagioclase grains making a low dihedral angle with the porphyroblastic phases are quenched melt (Grant and Frost 1990; Harte et al. 1991; Hartel and Pattison 1996). As observed in this study, micro granular texture is also found in the partial melting experiments (Wolf and Wyllie 1991). This follows that not all quartz and plagioclase grains in the melanosome may not form the granoblastic residue, and part of it represents the crystallised product of the trapped melt phase (Hartel and Pattison, 1996). Several studies (e.g. Clemens & Vielzeuf, 1987) have demonstrated that under most metamorphic conditions, rocks possess intrinsic porosity below 0.1. This observation and large solubility of H₂O in silicate melt support the view that significant melting under metamorphic conditions occurs under fluid-undersaturated conditions. Combining all the information following the amphibole melting reaction as suggested by several studies (Hartel and Pattison 1996; Pattison 2003; Cai et al. 2020) is inferred :



Some garnet could also have formed the reaction involving plagioclase and pyroxene during high-pressure metamorphism:



Berger et al. (2009) suggested that peritectic garnet formed in the mafic migmatite has a magmatic origin, i.e., these crystallised from the melt. Large euhedral garnet grains in leucosomes that are devoid of inclusions and have a Fe-rich composition could form insitu during crystallisation. Skeletal garnet represents the intermediary growth stage of garnet porphyroblast (Hartel and Pattison 1996; PADRÓN-NAVARTA et al. 2008). The formation of skeletal garnet within micro leucosomal patches, often connected with porphyroblastic garnets (Fig. 6.3.g-h), suggests garnet growth in the presence of melt. However, the large proportion of garnet in these leucosomes, almost garnetite in places, raises the possibility that leucosomes possibly represent the unfractionated restite plus the partial melts (Sawyer 1999; Brown 2002).

Subsequent to the stabilisation of the granoblastic assemblages, a number of retrograde reactions that consumed garnet occurred. These are described according to the sequence in which they appear. The **early retrograde assemblage (Mr₁)** comprises symplectic clinopyroxene + plagioclase that formed by the breakdown of the porphyroblastic garnet (Grt) through the following reaction:



This is a pressure-sensitive reaction, commonly used as a barometer that proceeds to the right with pressure lowering (Newton and Perkins 1982; Harley 1989; Mengel and Rivers 1991). Formation of this kind of symplectic intergrowth around garnet is widely reported from granulite facies terrains worldwide and commonly indicates near isothermal decompression (Zhao et al. 2000, 2001; Karmakar and Schenk 2015; Dey et al. 2019; Chatterjee et al. 2023; Roy Choudhury et al. 2023). Texturally adjacent occurrence of clinopyroxene-ilmenite symplectites to the $\text{Cpx}_2 + \text{Pl}_2$ symplectites indicates the possibility of synchronous formation of these two intergrowths and can be described by the following reaction (Chatterjee et al. 2023),



The formation of Cpx_2 -Ilm symplectite is described in detail in Chapter 7. The preferential growth of orthopyroxene on the secondary clinopyroxene and Opx - Pl_2 symplectite possibly formed due to the continued breakdown of porphyroblastic peak garnet (Grt) through the following reaction:

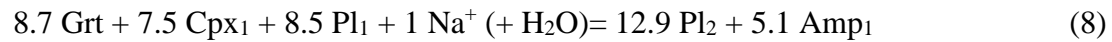
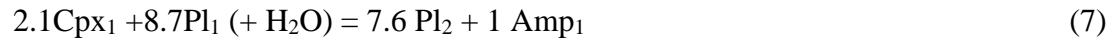
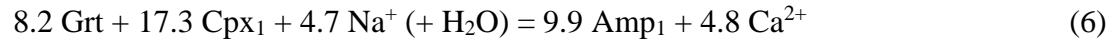


This also is a pressure-sensitive reaction (Newton and Perkins 1982; Bhattacharya et al. 1991; Eckert et al. 1991) and marks further lowering of pressure. The breakdown of garnet in both Cpx_2 - Pl_2 and Opx - Pl_2 symplectites form calcic plagioclase as garnet composition is devoid of Na. Similar anorthitic plagioclase formation has been documented by several workers (Zhao et al. 2001; Bhowmik and Roy 2003; Karmakar and Schenk 2015; Dey et al. 2019; Chatterjee et al. 2022). During garnet breakdown, as Ca is preferentially fractionated in the symplectic plagioclase and Mn remains in the garnet, the garnet margin becomes Mn rich, and Ca is depleted, resulting in the garnet rim.

The **late retrograde metamorphic stage (M_{R2})** represents amphibole (Amp_1) formation by partially to fully replacing garnet, clinopyroxene and plagioclase along fractures and grain boundaries. Pseudomorphic replacement of matrix (Cpx_1) and symplectic clinopyroxene (Cpx_2) during this hydration along with Pl_1 results in the formation of the Amp_1 and calcic plagioclase (Pl_2), possibly through the following reaction:



Similar to garnet breakdown reaction, this reaction also forms calcic plagioclase as a replacement of clinopyroxene (Cpx₁ and/or Cpx₂) and Pl₁ by Amp₁ results in excess Ca, which is likely accommodated in the Pl₁ rim forming Pl₂ as demonstrated by the following balanced reaction,



6.4 Physical conditions of metamorphism:

6.4.1 Conventional thermobarometry:

Conventional thermobarometry, using calibrated ion exchange and net-transfer reactions from the different stages of metamorphism, provides a thorough understanding of the physical conditions of metamorphism.

Peak assemblage (M_{PK}): The physical condition of peak metamorphism is estimated using the compositions of the porphyroblastic garnet core, along with the core compositions of adjacent primary clinopyroxenes (Cpx₁) and plagioclase (Pl₁). In the peak assemblage, using the geothermometers (Ellis and Green 1979) and barometers (Eckert et al. 1991), the P-T condition (800-900°C and 12.5-13 kbar) is determined.

Early retrograde assemblage (M_{R1}): Conventional geothermobarometry (Ellis and Green 1979; Eckert et al. 1991) of the early stage of retrogression is done using the rim compositions of porphyroblastic garnets, and composition of secondary plagioclase (Pl₂) + clinopyroxene (Cpx₂). This yields a P-T estimate that converges at 600-700°C and 6.5-8.5 kbar. Similarly, symplectic Opx yield P-T condition of ~700°C and ~7 kbar using garnet-orthopyroxene thermometry (Bhattacharya et al. 1991) and Grt-Opx-Pl-Qz barometry (Eckert et al. 1991).

Late retrograde assemblage (M_{R2}): For the conventional thermobarometry of the late stage of retrogression, garnet-hornblende thermometry (Graham and Powell 1984) and Al in amphibole barometry (Anderson and Smith 1995) considering rim compositions of garnet and the coexisting amphibole (Amp₂) is used. These record a temperature in the range of 550-650 °C and constrains the pressure at 6.5-7 kbar.

Table 6.6: P-T estimates through conventional thermobarometric calculations

Stages	Assemblage	Minerals in equilibrium	Thermometry			Barometry		
				P (ref)	T		T (ref)	P
M_{PK}	Peak	$Qz + Spn +$ $Grt_c +$ $Cpx_1 + Pl_1$	GC	13kbar	800-850 °C	GCPS	850°C	12.5-13 kbar
M_{R1}	Early retrogression	$Ilm + Cpx_2$ $+ Grt_r +$ $Opx + Pl_2$	GC	7kbar	650-700 °C	GCPS	700°C	6.5-8.5 kbar
			GO	7kbar	750-800 °C	GOPS	700°C	6.5-7.5 kbar
M_{R2}	Late retrogression	$Grt + Amp_1$	GA		550-650 °C	Al in Amp		6-7 kbar

GC: Garnet – clinopyroxene geothermometer (Ellis and Green 1979).

GCPS: Garnet – clinopyroxene – plagioclase – quartz barometer (Eckert et al. 1991).

GO: Garnet - orthopyroxene geothermometer (Bhattacharya et al. 1991).

GOPS: Garnet - orthopyroxene - plagioclase - quartz barometer (Eckert et al. 1991).

GA: Garnet - Amphibole thermometer (Graham and Powell, 1984).

Al in Amp: Al in amphibole barometer (Anderson and Smith 1995)

6.4.2 Pseudosection modelling:

Numerically simulated phase equilibria modelling (pseudosection) of the studied mafic granulite (SD-43) is evaluated in NCKFMASHT (Na₂O-K₂O-CaO-FeO-MgO-Al₂O₃-SiO₂-H₂O-TiO₂) components system. The pseudosections are computed using the program PerpleX (ver. 7.0.11; Connolly 2005) with the internally consistent thermodynamic dataset of Holland and Powell 2011 (TC-DS633). MnO is not considered for modelling as it is present in a negligible amount in the bulk composition. The phases associated with the modelling and their corresponding a-X models comprise clinopyroxene, melt, garnet and orthopyroxene (Holland et al. 2018), clino-amphibole (Diener and Powell 2012), feldspars (Holland and Powell 2003). Quartz, rutile, titanite and ilmenite are treated as pure end-member phases. In addition, compositional isopleths for garnet, clinopyroxene and amphibole are calculated and plotted in the phase diagram in the appropriate

assemblage fields to narrow down the estimated P-T conditions of the rock. PerpleX subordinate program WARMI (Connolly 2005, 2009) is used for these computations.

Rationale for choosing the bulk compositions for the pseudosection study

Determining the bulk composition for phase equilibria modelling of partially melted rock is fraught with problems associated with the alteration of bulk compositions during metamorphism. The measured bulk composition in a partially melted rock is not always accurate as it does not account for the melt loss during anatexis (Indares et al. 2008; Groppo et al. 2012). Migmatite morphology can provide a relative estimation of melt volume (Zhang et al. 2019). The leucosomal morphology (described in Chapter 3) is consistent with metatexite leucosomal segregations (Sawyer 2008) and a limited amount of partial melting with a maximum melt volume of <15%. Based on the migmatite morphology and leucosome volume, it is certain that though melt proportion crossed the melt connectivity threshold (MCT; melt volume 0-7%) (Rosenberg and Handy 2005; Soesoo and Bons 2015), melt volume was much below the solid-liquid transition (SLT; melt volume >40%) (Rosenberg and Handy 2005). According to the model of Zhang et al. (2019), the melt proportion is below framework-melting transition (FMT; melt volume ~21%;) (Chen et al. 2017). As with the arguments considered above, where partial melting is comparatively higher, probable melt loss is much more relevant in altering the measured bulk composition, but below FMT, melt loss is quite restricted (Zhang et al. 2019). As in the mafic granulites, lower melting fractions indicate melt loss (if any) is quite limited to significantly alter bulk composition.

Nevertheless, the bulk composition relevant for the pseudosection construction depends on the volume of the rock that reacts to be in chemical equilibrium at the intended P – T condition (Stuwe 1997). Also, under high-grade granulite facies conditions, fluid-mediated element transfer is restricted, often resulting in localised bulk compositions representing equilibrium (i.e., ‘effective bulk composition’) (Palin et al. 2016). Because of the disequilibrium reaction textures, pockets of melt and late-phase fluid influx retrogression observed in the studied rocks, “effective bulk” appears to be suitable for numerical modelling. The effective bulk composition is calculated by integrating the modal abundance of various phases with the corresponding phase compositions (Palin et al. 2016). The modal abundance is derived by the point count method in the petrographic study. The

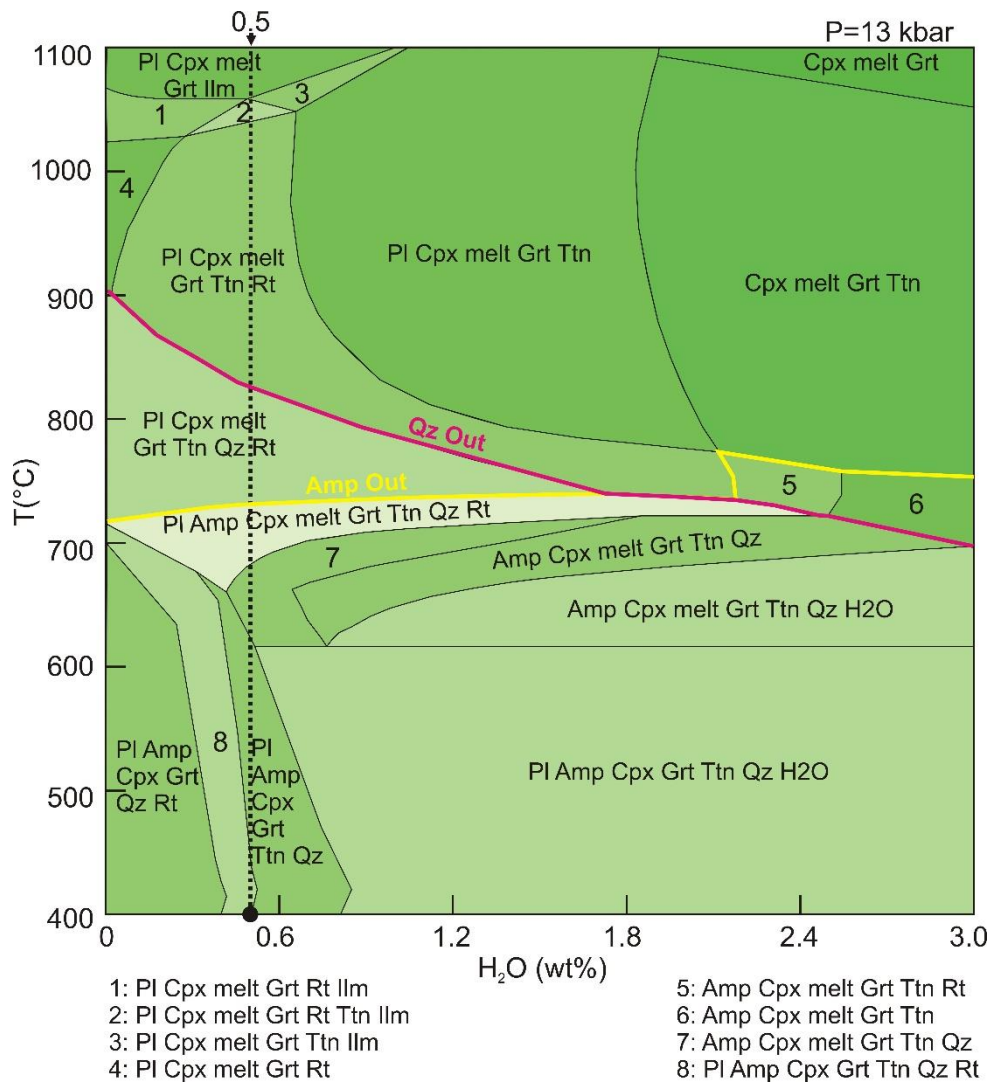


Figure 6.8: T - X_{H_2O} diagram is constructed at 13 kbar pressure in the phase equilibria modelling.

modeled bulk composition (in wt%) is $SiO_2 = 46.6$, $TiO_2 = 2.1$, $Al_2O_3 = 15.2$, $CaO = 14.2$, $MgO = 5.7$, $FeO = 13.7$, $Na_2O = 1.7$, $K_2O = 0.2$.

Rationale for the input fluid amount

In P-T pseudosection fluid is considered as pure phase H_2O . Careful evaluation of the H_2O content is necessary as it can significantly influence the degree of partial melting. The bulk H_2O content during the peak metamorphism is considered to model the partial melting of the metabasic rock. While considering meta-mafic rocks dominated by a hydrous phase (e.g. amphibole), H_2O content is considered in such a way that the rock is maximally hydrated, but free H_2O is minimal along prograde metamorphism (Stuck and Diener 2018). The amphiboles present in the selvage or as secondary amphiboles replacing Cpx and Grt

represent a probable fluid flux during retrogression and do not represent the H_2O amount during peak metamorphism or partial melting. Under deep crustal conditions, H_2O is generally present within mineral structures or in the melt phase, while free H_2O is generally minimal (Clemens and Vielzeuf 1987). Thus, the water content of the mafic granulite is estimated in such a way that free fluid is absent in the presence of a melt phase. Moreover, considering this, T- $X_{\text{H}_2\text{O}}$ diagram (Fig. 6.8) is constructed at 13 kbar pressure. The Amp-out and Qz-out lines constrain the peak metamorphic assemblage, and the H_2O amount is

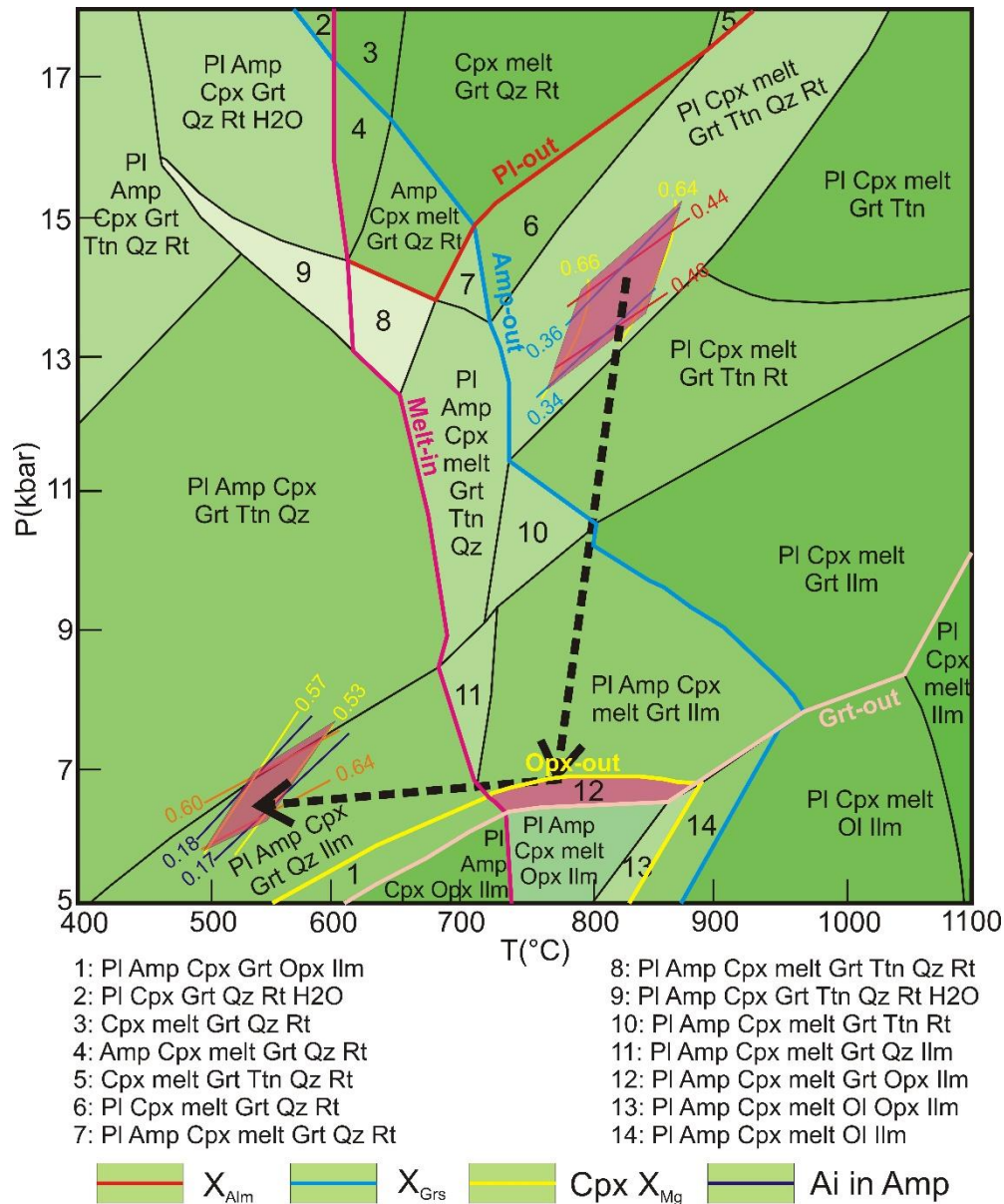


Figure 6.9: Numerically simulated phase equilibria modelling (pseudosection) of the studied mafic granulite is evaluated in NCKFMASHT (Na_2O - K_2O - CaO - FeO - MgO - Al_2O_3 - SiO_2 - H_2O - TiO_2) components system.

estimated based on this mineral assemblage and considering the absence of free fluid in the presence of melt. Based on these, the estimated H₂O amount is 0.5wt%.

Results:

In the constructed pseudosection (Fig. 6.9), partial melting starts between 650-750 °C, while amphibole reaches its stability limit at around 750 °C at 11 kbar, but around 8 kbar, amphibole is stable even at 900 °C. Opx is stable only upto 7 kbar pressure, while garnet destabilises at 6-6.5 kbar. Plagioclase destabilises at 14 kbar pressure, 700 °C. Here, the peak metamorphic assemblage is identified by the assemblage of garnet, clinopyroxene, plagioclase, quartz, titanite, rutile and melt. This phase assemblage extends from approximately 12-18 kbar and 750-1000 °C. The P-T condition of peak metamorphism is

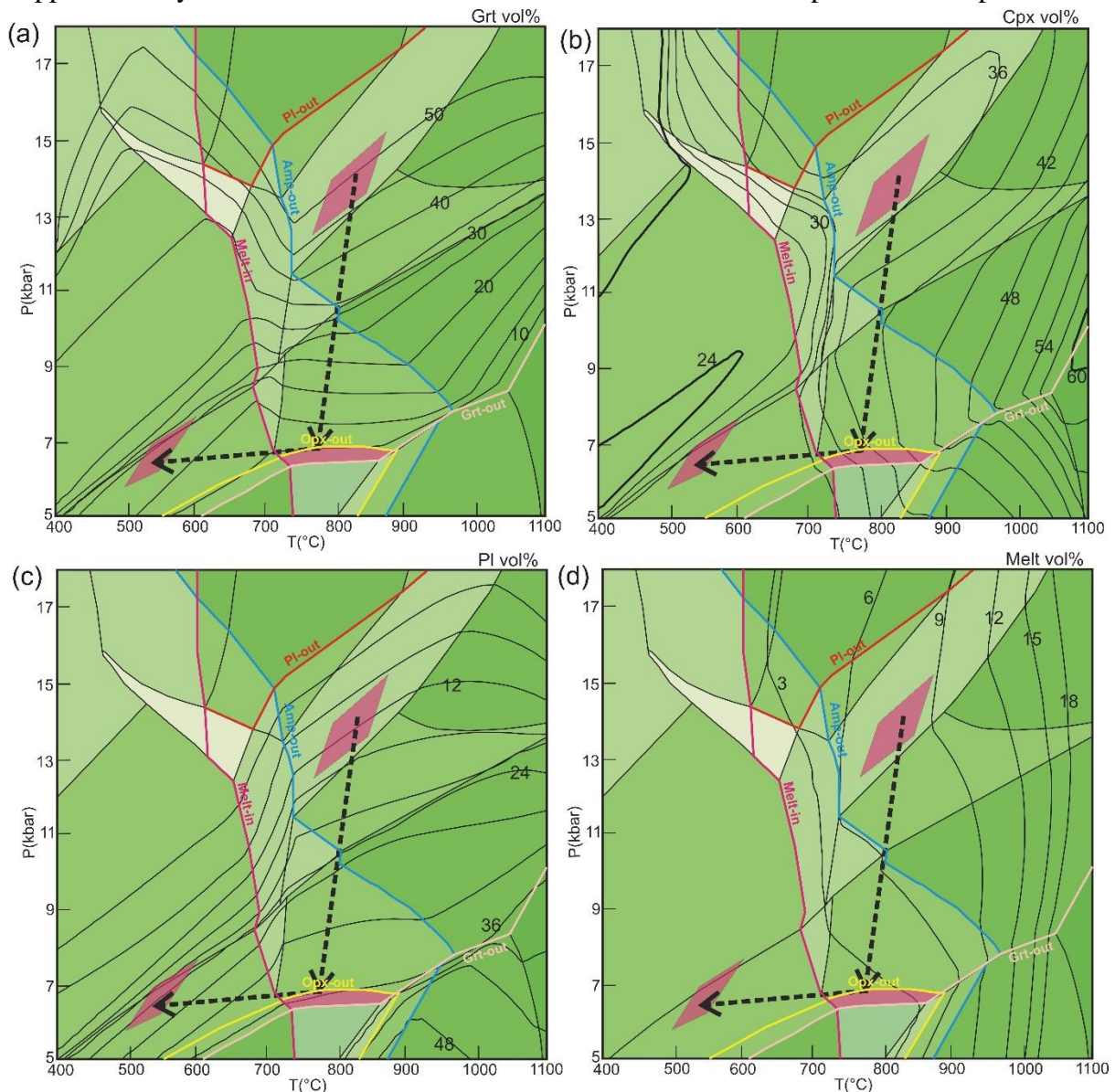


Figure 6.10: In the pseudosection, volume isopleths of Grt (a), Cpx (b), Pl (c), and melt (d) are calculated.

further constrained by compositional isopleths of garnet (almandine and grossular) and clinopyroxene [$X_{Mg} = \text{MgO}/(\text{MgO} + \text{FeO})$]. Isopleths estimate the P-T condition of peak metamorphism at 12–15 kbar and 800–900 °C. P-T condition of 6.5–7 kbar and 750–850 °C is constrained by the early retrogressive phase assemblage of garnet, clinopyroxene, amphibole, plagioclase, quartz, ilmenite, melt, and orthopyroxene. The compositional isopleths of amphibole (Al in amphibole), garnet (X_{Alm}) and Cpx (X_{Mg}) constrain P-T condition of late retrogression at 500–600 °C; 6.5–7 kbar.

In the calculated pseudosection, the decrease of pressure decreases garnet volume while there is an increase in plagioclase volume (Fig. 6.10). Both clinopyroxene and melt volume increase with the increase in temperature. The peak and early retrograde P-T conditions represent a steeply decompressive P-T path. Along this steeply decompressive

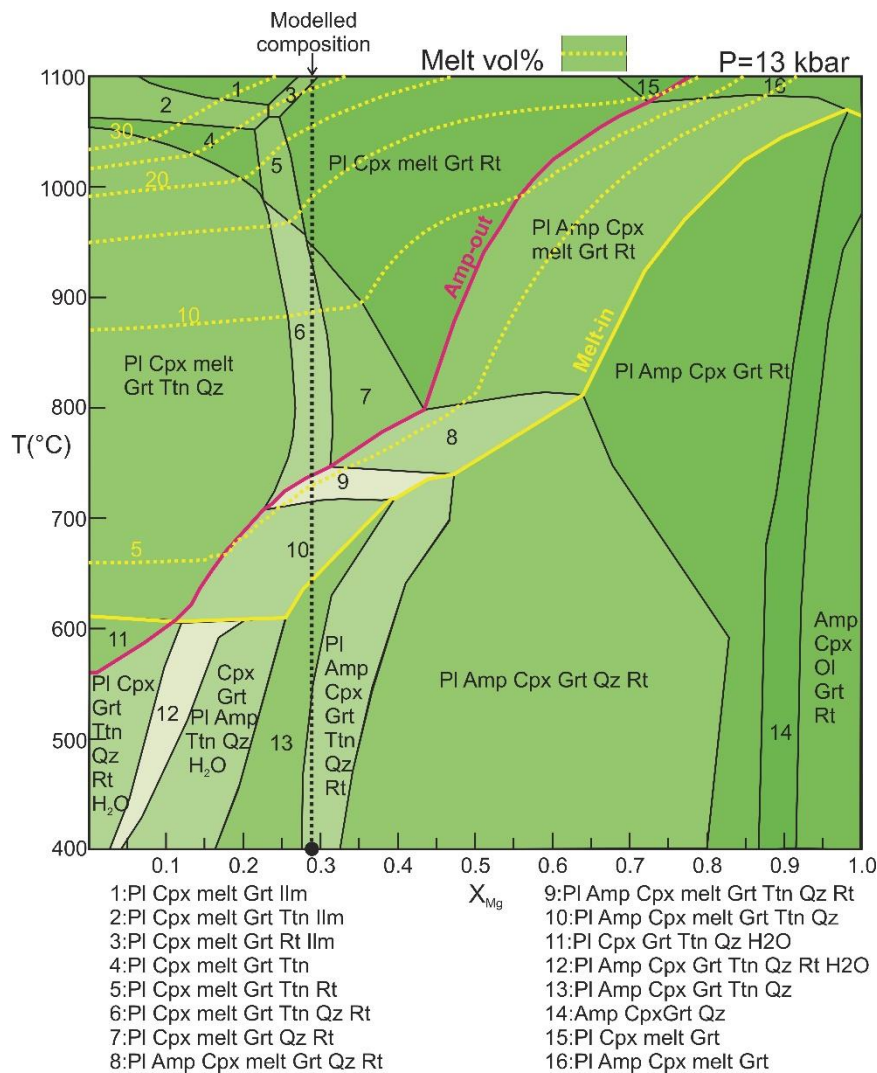


Figure 6.11: T- X_{Mg} (X_{Mg} varies along X-axis) diagram is constructed at 13 kbar pressure.

P-T path, there is a decrease in garnet volume from ~45% to ~10% (Fig. 6.10.a). This decrease in garnet

volume corresponds with an increase in plagioclase volume from ~12% to ~36% (Fig. 6.10.c). Clinopyroxene volume slightly increases from ~34% to ~37% along the P-T path (Fig. 6.10.b). Melt volume decreases along the decompressive P-T path (Fig. 6.10.d).

Control of bulk composition

Bulk rock composition plays a crucial role in phase equilibria modelling. Bulk rock geochemical study provides X_{Mg} range of 0.28-0.41. T- X_{Mg} (X_{Mg} varies along X-axis; Fig. 6.11) and T-X(Ca) [$=CaO/(CaO+Na_2O)$ (wt%)] (Fig. 6.12) diagram are constructed at 13 kbar pressure to understand the control of bulk rock composition in the peak metamorphism

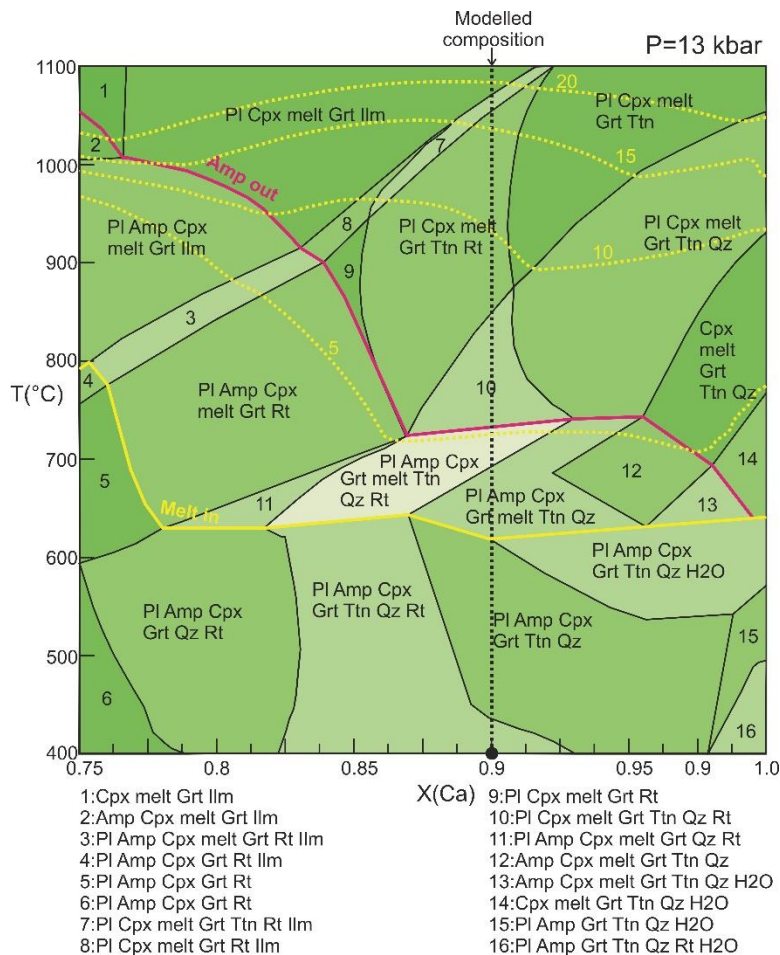


Figure 6.12: T-X(Ca) [$=CaO/(CaO+Na_2O)$ (wt%)] diagram is constructed at 13 kbar pressure.

of the mafic granulite. To understand the control of bulk rock X_{Mg} and X(Ca) on melting, melt volume isopleths are plotted in the T- X_{Mg} diagram. An increase in the bulk rock X_{Mg}

increases the stability limits of amphibole significantly, while the melt stability field is highly reduced to higher temperatures.

Similarly, the T-X(Ca) [$=\text{CaO}/(\text{CaO}+\text{Na}_2\text{O})$ (wt%)] diagram is constructed at 13 kbar. The melt in line is almost parallel with the X(Ca) axis, which suggests that the effect of bulk rock X(Ca) on melting is limited. The presence of titanite in the peak metamorphic assemblage is restricted to the comparatively higher value of X(Ca). In both diagrams, modelled composition plots are in the intended peak metamorphic field and provide an estimation of melt proportions. The T-X_{Mg} and T-X(Ca) estimate melt proportions of 5-15% and 5-10%, respectively, corresponding to the peak metamorphic assemblage. Such melt proportions correlate with the morphology of leucosomal segregations.

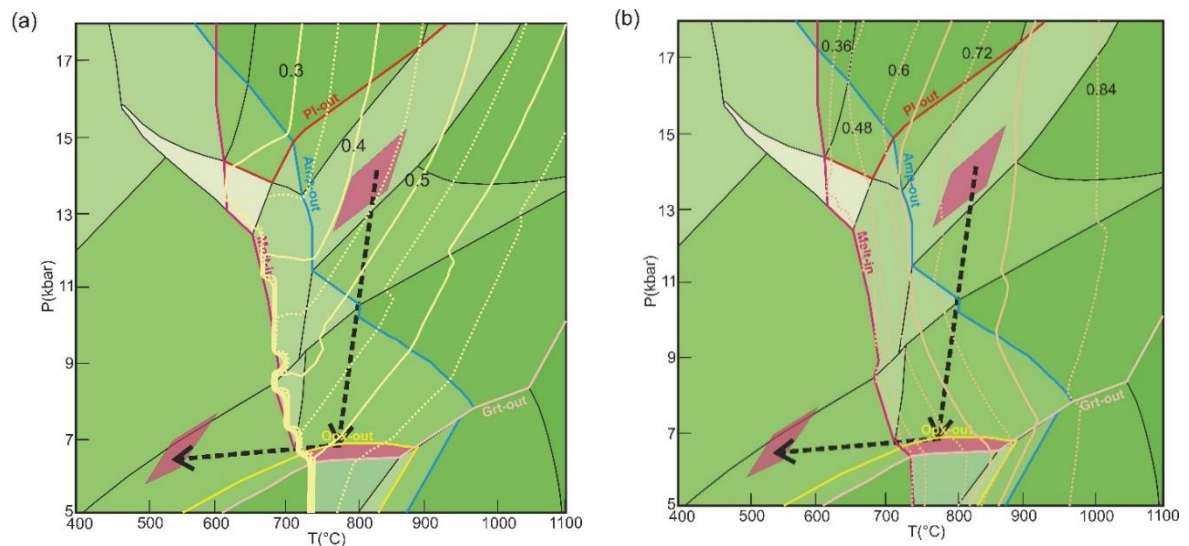


Figure 6.13: (a) The X(Fe) ($=\text{Fe}/(\text{Fe}+\text{Mg})$) melt isopleths are plotted in Along the decompressive P-T path, the melt becomes more ferroan. (b) In the X(Na) ($=\text{Na}/(\text{Na}+\text{K})$) melt isopleths diagram, melt composition becomes less sodic along the decompressive P-T path.

Melt composition:

To decipher the melt composition from phase equilibria, modelling X(Fe) ($=\text{Fe}/(\text{Fe}+\text{Mg})$) (Fig. 13.a) and X(Na) ($=\text{Na}/(\text{Na}+\text{K})$) (Fig. 13.b) melt isopleths are plotted in pseudosection. Along the decompressive P-T path, the melt becomes more ferroan with pressure drop; however, melt composition becomes less sodic. An increase in temperature increases melts X(Fe), which suggests an increase in melt volume makes the melt more ferroan. Similarly, the melt becomes more sodic with an increase in temperature.

References

- Anderson, J.L., and Smith, D.R. (1995) The effects of temperature and f_{O_2} on the Al-in-hornblende barometer. *American Mineralogist*, 80, 549–559.
- Berger, J., Caby, R., Liégeois, J.-P., Mercier, J.-C., and Demaiffe, D. (2009) Dehydration, melting and related garnet growth in the deep root of the Amalaoulaou Neoproterozoic magmatic arc (Gourma, NE Mali). *Geol. Mag.*, 146, 173–186.
- Bhattacharya, A., Krishnakumar, K.R., Raith, M., and Sen, S.K. (1991) An improved set of a -X parameters for Fe-Mg-Ca garnets and refinements of the orthopyroxene-garnet thermometer and the orthopyroxene-garnet-plagioclase-quartz barometer. *Journal of Petrology*, 32, 629–656.
- Bhowmik, S.K., and Roy, a (2003) Garnetiferous metabasites from the Sausar Mobile Belt: Petrology, P-T path and implications for the tectonothermal evolution of the Central Indian Tectonic Zone. *Journal of Petrology*, 44, 387–420.
- Brown, M. (2002) Retrograde processes in migmatites and granulites revisited. *Journal of Metamorphic Geology*, 20, 25–40.
- Cai, J., Liu, F., and Liu, C. (2020) A unique Paleoproterozoic HP–UHT metamorphic event recorded by the Bengbu mafic granulites in the southwestern Jiao–Liao–Ji Belt, North China Craton. *Gondwana Research*, 80, 244–274.
- Chatterjee, S., Karmakar, S., Mukherjee, S., Sanyal, S., and Sengupta, P. (2022) Origin of clinopyroxene-ilmenite symplectites in mafic granulites from eastern parts of the Chotanagpur granite gneissic complex, East Indian shield. *American Mineralogist*, In press.
- (2023) Origin of clinopyroxene-ilmenite symplectites in mafic granulites from eastern parts of the Chotanagpur granite gneissic complex, East Indian shield, 108, 2308–2322.
- Chen, Z., Liu, Y.-J., Chen, G.-N., and Peng, Z.-L. (2017) Rheological transitions in progressive melting of rock and their geological constraints from the Fuhu metatexite-diatexite profile in Guangdong Province, SE China. *Journal of Asian Earth Sciences*, 139, 192–201.
- Clemens, J.D., and Vielzeuf, D. (1987) Constraints on melting and magma production in the crust. *Earth and Planetary Science Letters*, 86, 287–306.

- Connolly, J.A.D. (2005) Computation of phase equilibria by linear programming: A tool for geodynamic modeling and its application to subduction zone decarbonation. *Earth and Planetary Science Letters*, 236, 524–541.
- (2009) The geodynamic equation of state: What and how. *Geochemistry, Geophysics, Geosystems*, 10.
- Dey, A., Karmakar, S., Mukherjee, S., Sanyal, S., Dutta, U., and Sengupta, P. (2019) High pressure metamorphism of mafic granulites from the Chotanagpur Granite Gneiss Complex, India: Evidence for collisional tectonics during assembly of Rodinia. *Journal of Geodynamics*, 129, 24–43.
- Diener, J.F.A., and Powell, R. (2012) Revised activity–composition models for clinopyroxene and amphibole. *Journal of Metamorphic Geology*, 30, 131–142.
- Droop, G.T.R. (1987) A general equation for estimating Fe 3+ concentrations in ferromagnesian silicates and oxides from microprobe analyses, using stoichiometric criteria. *Mineralogical Magazine*, 51, 431–435.
- Eckert, J.O., Newton, R.C., and Kleppa, O.J. (1991) The ΔH of reaction and recalibration of garnet-pyroxene- plagioclase-quartz geobarometers in the CMAS system by solution calorimetry. *American Mineralogist*, 76, 148–160.
- Ellis, D.J., and Green, D.H. (1979) An experimental study of the effect of Ca upon garnet-clinopyroxene Fe-Mg exchange equilibria. *Contributions to Mineralogy and Petrology*, 71, 13–22.
- Graham, C.M., and Powell, R. (1984) A garnet–hornblende geothermometer: calibration, testing, and application to the Pelona Schist, Southern California. *Journal of Metamorphic Geology*, 2, 13–31.
- Grant, J.A., and Frost, B.R. (1990) Contact metamorphism and partial melting of pelitic rocks in the aureole of the Laramie anorthosite complex, Morton Pass, Wyoming. *American journal of science*, 290, 425–475.
- Groppo, C., Rolfo, F., and Indares, A. (2012) Partial melting in the higher Himalayan crystallines of Eastern Nepal: The effect of decompression and implications for the “channel flow” model. *Journal of Petrology*, 53, 1057–1088.
- Hansen, E., Johansson, L., Andersson, J., LaBarge, L., Harlov, D., Möller, C., and Vincent, S. (2015) Partial melting in amphibolites in a deep section of the Sveconorwegian Orogen, SW Sweden. *Lithos*, 236–237, 27–45.
- Harley, S.L. (1989) The origins of granulites: A metamorphic perspective. *Geological Magazine*, 126, 215–247.

- Harte, B., Pattison, D.R.M., and Linklater, C.M. (1991) Field Relations and Petrography of Partially Melted Pelitic and Semi-Pelitic Rocks BT - Equilibrium and Kinetics in Contact Metamorphism: The Ballachulish Igneous Complex and Its Aureole. In G. Voll, J. Töpel, David R M Pattison, and F. Seifert, Eds., pp. 181–209. Springer Berlin Heidelberg, Berlin, Heidelberg.
- Hartel, T.H.D., and Pattison, D.R.M. (1996) Genesis of the Kapuskasing (Ontario) migmatitic mafic granulites by dehydration melting of amphibolite: The importance of quartz to reaction progress. *Journal of Metamorphic Geology*, 14, 591–611.
- Holland, T., and Powell, R. (2003) Activity-compositions relations for phases in petrological calculations: An asymmetric multicomponent formulation. *Contributions to Mineralogy and Petrology*, 145, 492–501.
- Holland, T., Green, E.C.R., and Powell, R. (2018) Melting of peridotites through to granites: A simple thermodynamic model in the system KNCFMASHTOCr. *Journal of Petrology*, 59, 881–900.
- Holland, T.J.B., and Powell, R. (2011) An improved and extended internally consistent thermodynamic dataset for phases of petrological interest, involving a new equation of state for solids. *Journal of Metamorphic Geology*, 29, 333–383.
- Indares, A., White, R.W., and Powell, R. (2008) Phase equilibria modelling of kyanite-bearing anatectic paragneisses from the central Grenville Province. *Journal of Metamorphic Geology*, 26, 815–836.
- Karmakar, S., and Schenk, V. (2015) Neoproterozoic UHT metamorphism and paleoproterozoic UHT reworking at Uweinat in the East Sahara Ghost Craton, SW Egypt: Evidence from petrology and texturally controlled in situ monazite dating. *Journal of Petrology*, 56, 1703–1742.
- Leake, B.E., Woolley, A.R., Arps, C.E.S., Birch, W.D., Gilbert, M.C., Grice, J.D., Hawthorne, F.C., Kato, A., Kisch, H.J., Krivovichev, V.G., and others (1997) Nomenclature of amphiboles: Report of the subcommittee on amphiboles of the international mineralogical association, commission on new minerals and mineral names. *Canadian Mineralogist*, 35, 219–246.
- Mengel, F., and Rivers, T. (1991) Decompression reactions and P - T conditions in high-grade rocks, northern Labrador: P - T - t paths from individual samples and implications for early proterozoic tectonic evolution. *Journal of Petrology*, 32, 139–167.
- Newton, R.C., and Perkins, D. (1982) Thermodynamic calibration of geobarometers based on the assemblages garnet - plagioclase - orthopyroxene (clinopyroxene) - quartz.

- American Mineralogist, 67, 203–222.
- O'Brien, P.J., and Rötzler, J. (2003) High-pressure granulites: Formation, recovery of peak conditions and implications for tectonics. *Journal of Metamorphic Geology*, 21, 3–20.
- PADRÓN-NAVARTA, J.A., GARRIDO, C.J., SÁNCHEZ-NAVAS, A., TOMMASI, A., LÓPEZ SÁNCHEZ-VIZCAÍNO, V., GÓMEZ-PUGNAIRE, M.T., and HUSSAIN, S.S. (2008) Oriented growth of garnet by topotactic reactions and epitaxy in high-pressure, mafic garnet granulite formed by dehydration melting of metastable hornblende-gabbro-norite (Jijal Complex, Kohistan Complex, north Pakistan). *Journal of Metamorphic Geology*, 26, 855–870.
- Palin, R.M., Weller, O.M., Waters, D.J., and Dyck, B. (2016) Quantifying geological uncertainty in metamorphic phase equilibria modelling; a Monte Carlo assessment and implications for tectonic interpretations. *Geoscience Frontiers*, 7, 591–607.
- Pattison, D.R.M. (2003) Petrogenetic significance of orthopyroxene-free garnet + clinopyroxene + plagioclase \pm quartz-bearing metabasites with respect to the amphibolite and granulite facies. *Journal of Metamorphic Geology*, 21, 21–34.
- Rosenberg, C.L., and Handy, M.R. (2005) Experimental deformation of partially melted granite revisited: implications for the continental crust. *Journal of Metamorphic Geology*, 23, 19–28.
- Roy Choudhury, S., Dey, A., Mukherjee, S., Sengupta, S., Sanyal, S., Karmakar, S., and Sengupta, P. (2023) Formation of aluminous clinopyroxene-ilmenite-spinel symplectic assemblage in a regionally metamorphosed calc-silicate granulite from the Chotanagpur Granite Gneiss Complex, East Indian shield. *Lithos*, 442–443, 107058.
- Sawyer, E. (2008) Working with migmatites: nomenclature for the constituent parts. *Mineralogical Association of Canada Short Course Series*, 38, 1–28.
- Sawyer, E.W. (1999) Criteria for the recognition of partial melting. *Physics and Chemistry of the Earth, Part A: Solid Earth and Geodesy*, 24, 269–279.
- Soesoo, A., and Bons, P.D. (2015) From Migmatites to Plutons: Power Law Relationships in the Evolution of Magmatic Bodies. *Pure and Applied Geophysics*, 172, 1787–1801.
- Stuck, T.J., and Diener, J.F.A. (2018) Mineral equilibria constraints on open-system melting in metamafic compositions. *Journal of Metamorphic Geology*, 36, 255–281.
- Stuwe, K. (1997) Effective bulk composition changes due to cooling: a model predicting complexities in retrograde reaction textures. *Contributions to Mineralogy and Petrology*, 129, 43–52.
- Whitney, D.L., and Evans, B.W. (2010) Abbreviations for Names of Rock-Forming

- Minerals. *American Mineralogist*, 95, 185–187.
- Wolf, M.B., and Wyllie, P.J. (1991) Dehydration-melting of solid amphibolite at 10 kbar: Textural development, liquid interconnectivity and applications to the segregation of magmas. *Mineralogy and Petrology*, 44, 151–179.
- Yu, S., Zhang, J., Li, S., Santosh, M., Li, Y., Liu, Y., Li, X., Peng, Y., Sun, D., Wang, Z., and others (2019) TTG-Adakitic-Like (Tonalitic-Trondhjemitic) Magmas Resulting From Partial Melting of Metagabbro Under High-Pressure Condition During Continental Collision in the North Qaidam UHP Terrane, Western China. *Tectonics*, 38, 791–822.
- Zhang, J., Liu, W., Yakymchuk, C., Sa, R., Zeng, Z., Ding, R., Tang, G., Liu, H., Xu, Q., and Wang, Y. (2019) Partial Melting and Crustal Deformation during the Early Paleozoic Wuyi–Yunkai Orogeny: Insights from Zircon U-Pb Geochronology and Structural Analysis of the Fuhuling Migmatites in the Yunkai Region, South China. *Minerals*.
- Zhao, G., Cawood, P.A., Wilde, S.A., and Lu, L. (2001) High-pressure granulites (Retrograded Eclogites) from the Hengshan Complex, North China Craton: Petrology and tectonic implications. *Journal of Petrology*, 42, 1141–1170.
- Zhao, G.C., Wilde, S.A., Cawood, P.A., and Lu, L.Z. (2000) Petrology and P – T path of the Fuping mafic granulites : implications for tectonic evolution of the central zone of the North China craton. *Journal of Metamorphic Geology*, 18, 375–391.

Chapter 7

Origin of clinopyroxene-ilmenite symplectites in mafic granulites

As described in Chapter 6, the enclave suite mafic granulite hosts a rare variety of symplectic intergrowth of ilmenite and clinopyroxene. This chapter deals in detail on those symplectic intergrowths.

Symplectic intergrowths of clinopyroxene and ilmenite are quite rare in metamorphic rocks. Clinopyroxene-ilmenite symplectites have been reported from mantle xenolith of deep origin, kimberlites, and other alkaline rocks (Nixon and Boyd 1979; Garrison and Taylor 1981; Litasov et al. 2003; Ashchepkov et al. 2014 and the references therein), where, their origin is explained either by exsolution from high pressure garnet (Ringwood and Lovering 1970) or clinopyroxene (Dawson and Reid 1970), or by cotectic or eutectic co-precipitation from a protokimberlite melt (Nixon and Boyd 1979; Garrison and Taylor 1981; Litasov et al. 2003). However, in metamorphic rocks formation of clinopyroxene-ilmenite symplectites is even rarer, and its occurrence is mainly restricted to high pressure metamorphic rocks such as HP basic granulites and retrogressed eclogites (O'Brien and Rötzler 2003; Zhang et al. 2003; Faryad et al. 2006; Marsh and Kelly 2017). Depending upon bulk rock compositions and the ambient physiochemical conditions, metabasic rocks contain one or more of the accessory phases, like titanite, rutile, and ilmenite, that chiefly contribute to the Ti-budget of the metabasic rocks. Experimental studies have shown that the solubility of Ti in pure H₂O is very low over a range of pressure and temperature (nominally soluble, Purtov and Kotel'nikova 1993; Ryzhenko et al. 2006; Antignano and Manning 2008; Rapp et al. 2010; Hayden and Manning 2011; Tanis et al. 2016; Karmakar 2021). However, the solubility of Ti is dramatically enhanced in the presence of halogen-rich, particularly F-rich fluid (Rapp et al. 2010). The experimental data suggest, therefore, different length scales of transport of Ti in crustal rocks depending on the physical conditions and the composition of the transporting media (Antignano and

Manning 2008; Rapp et al. 2010; Hayden and Manning 2011). Furthermore, rutile, titanite, and ilmenite are the main Ti-sink of metabasic rocks. An understanding of the relative stability of the three Ti-rich phases puts essential constraints on the behavior of Ti during the evolution of the metabasic rocks. Ti (and other HFSEs) is commonly used as a fixed reference frame for mass-balance calculations and geochemical interpretations in metamorphic and metasomatic processes (Ague 2011). This approach may be seriously affected if Ti becomes significantly mobile.

7.1 Petrography

The studied rocks display a plethora of textures, as described in Chapter 6. The following section discusses the textures that help understand the formation of the ilmenite-clinopyroxene intergrowth. Based on overprinting relations, textures and mineralogy of the studied rock can be divided into primary and secondary. The primary textures are defined by the granoblastic aggregates of garnet, clinopyroxene (Cpx₁), plagioclase (Pl₁), and rare quartz (Fig. 7.1.a-b). Titanite and rutile (Fig. 7.1.f-g; 7.2.a-b) that occur as accessory phases are scattered in the granoblastic mosaic. Garnet grains of variable size (1 mm to ≤ 10 mm) and shape contain one or more of the inclusions quartz, plagioclase (Pl₀), and amphibole (Amp₀) (Fig. 7.1.c), rutile, and ilmenite. Rarely does garnet contain ilmenite inclusion that is successively rimmed by rutile and plagioclase (Fig. 7.1.e). Although the inclusion of titanite is not seen in garnet, local inclusion of titanite is seen within the granoblastic clinopyroxene (Cpx₁), getting replaced by amphibole (Amp₂) (Fig. 7.1.g). This raises the possibility that titanite and rutile were stabilised during and/or prior to the stabilisation of the granoblastic assemblage. Locally, the inclusion of amphibole (Amp₀) and plagioclase (Pl₀) occurs within Cpx₁ (Fig. 7.1.d). The secondary textures are formed after the primary granoblastic assemblage. The most conspicuous secondary texture is a fine symplectic intergrowth of ilmenite and clinopyroxene (Cpx₂) (<2 μ m to 55 μ m lamellar width). The Ilm-Cpx₂ symplectite variably replaces titanite (Fig. 7.2.a-f, 7.3.d-h). The Ilm-Cpx₂ symplectite has a bulbous/wavy front that protrudes into the titanite (Fig. 7.2.a-b). Locally, the Ilm-Cpx₂ symplectite completely replaces titanite, preserving the original boundary of the titanite it replaces (Fig. 7.2.c-d). Ilmenite in the central part of the Ilm-Cpx₂ symplectite forms fine rod-shaped lamellae with small inter lamellar space (~ 2 μ m, Fig. 7.2.d). The marginal part of the symplectite shows distinctly coarse and irregular ilmenite lamellae in the matrix of clinopyroxene (Cpx₂) (Fig. 7.2.d). The Ilm-Cpx₂ symplectite contains fine

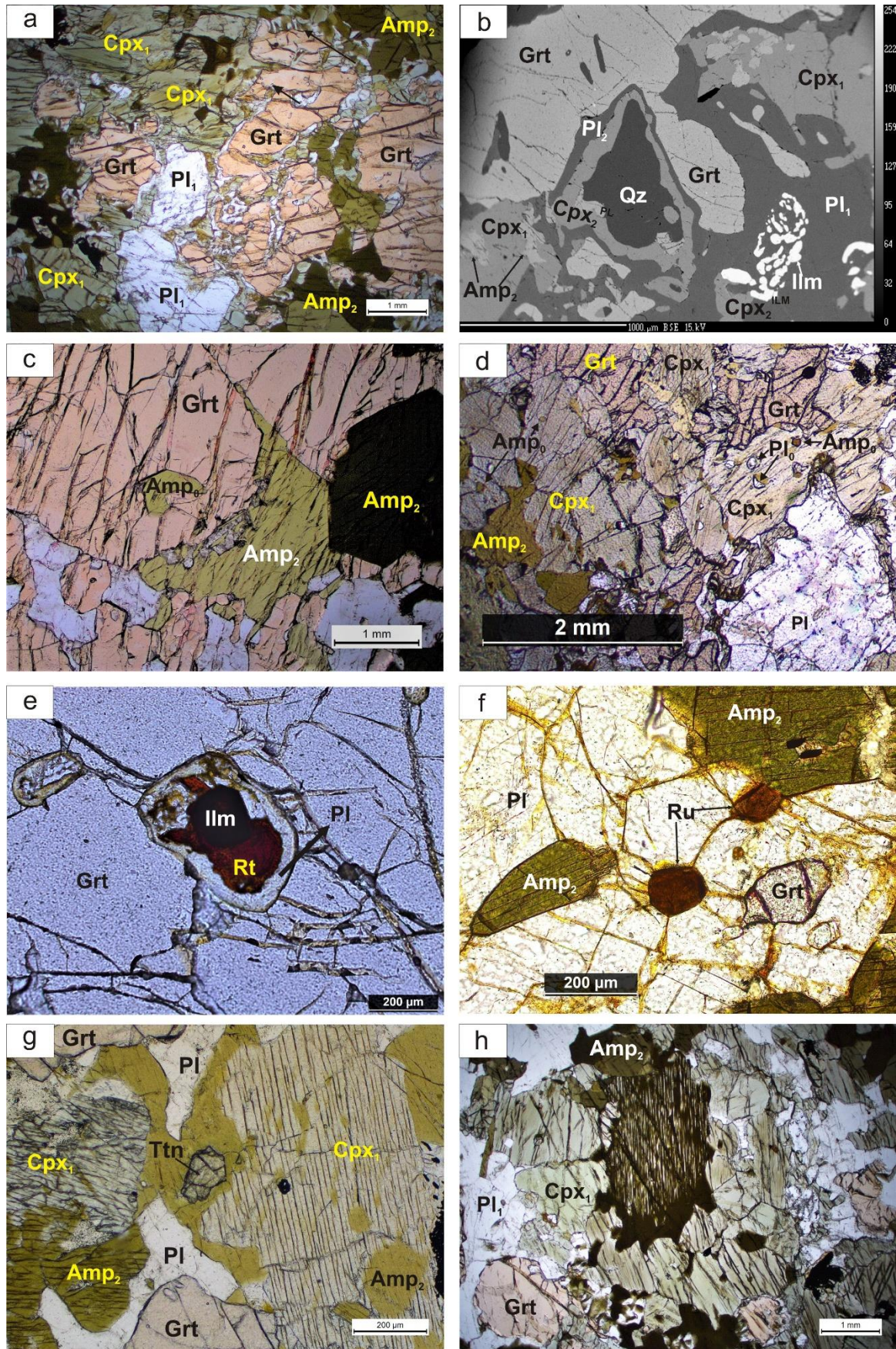


Figure 7.1: Photomicrographs and BSE images showing textural relations: (a) Garnet porphyroblasts of variable size and, medium-grained clinopyroxene (Cpx₁) and plagioclase (Pl₁) are forming the granoblastic mosaic matrix. Secondary amphibole (Amp₂) is replacing both Cpx₁ and garnet. (b) Quartz present in the matrix is reacting with garnet porphyroblasts to form a double corona of clinopyroxene (Cpx₂) and plagioclase (Pl₂). (c) Secondary amphibole (Amp₂) is replacing garnet porphyroblasts along its boundary, while primary amphibole (Amp₀) is present as inclusion within garnet. (d) Matrix clinopyroxene (Cpx₁) hosts inclusions of plagioclase (Pl₀) and amphibole (Amp₀). (e) Garnet contains ilmenite inclusion that is successively rimmed by rutile and plagioclase. (f) Rutile is present in the rock matrix and also in contact with Amp₂. (g) Titanite appears to be stranded within Amp₂ which is replacing Cpx₁. (h) Amphibole (Amp₂) is replacing matrix clinopyroxene (Cpx₁) along its boundary and cleavage planes. Abbreviations are after Whitney and Evans (2010).

grains of apatite (mostly visible in the Ca- X-ray intensity maps as the fine red dots within the symplectic domain) (Fig. 7.3.g; 7.5.g). Rarely, small volume of orthopyroxene lamellae are seen in ilmenite-clinopyroxene (Cpx₂) symplectite (Fig. 7.3.d). The Ilm-Cpx₂ symplectite is separated from garnet by a rind of plagioclase (Pl₂) (Fig. 7.2.c) or a symplectic intergrowth of plagioclase (Pl₂) and clinopyroxene (Cpx₂) that protrudes into garnet (Fig. 7.2.d-e). Proximal to titanite, Ilm-Cpx₂ symplectite (Fig. 7.2.a-b;e) develops that commonly replaces the titanite completely (Fig. 7.2.c-d). Nowhere in the rock does Ilm-Cpx₂ symplectite show physical contact with garnet. Plagioclase rind or Pl₂-Cpx₂ symplectite is always proximal to the garnet grain boundary. So, the secondary clinopyroxene (Cpx₂) is forming symplectic intergrowth with both plagioclase and ilmenite; from here on, they are denoted as Cpx₂^{PL} and Cpx₂^{ILM}, respectively. Secondary amphibole (Amp₂) variably replaces the primary granoblastic garnet, clinopyroxene (Fig. 7.1.c; g-h). Amp₂ also replaces the secondary clinopyroxene (Cpx₂) (Fig. 7.2.e). This feature suggests that Amp₂ formed after the development of the secondary clinopyroxene (Cpx₂). Secondary amphibole (Amp₂) preserves the initial shape of the clinopyroxene when replacing Cpx₁ and Cpx₂ (pseudomorphic replacement) (Fig. 7.1.i; 7.2.e-f). During this replacement of Cpx₁, titanite inclusion appears to be stranded within the secondary phase (Amp₂) (Fig. 7.1.g).

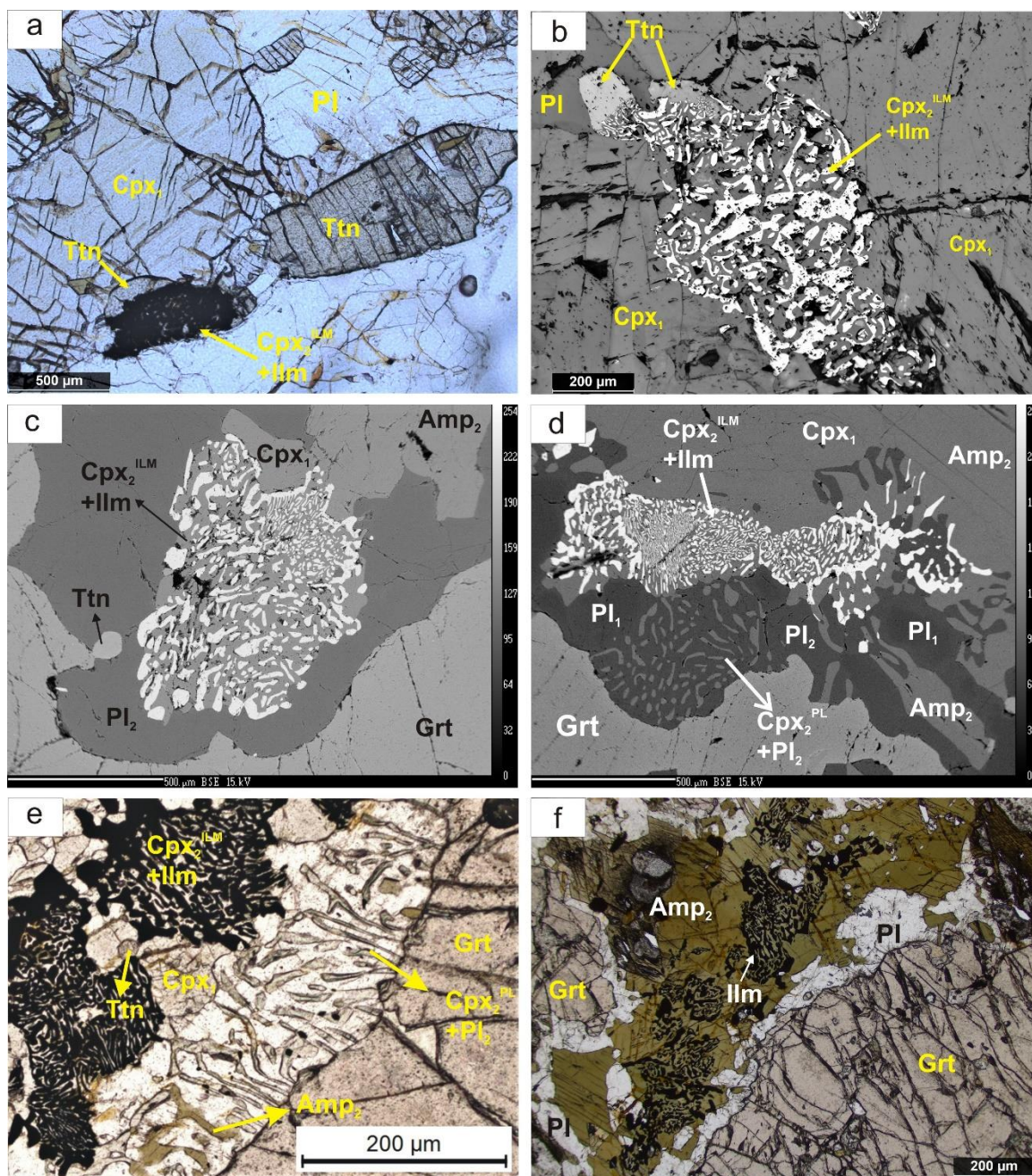


Figure 7.2: Photomicrographs and BSE images showing textural relations: (a) Titanite is present in the rock matrix in contact with Cpx₁ and is getting replaced by a symplectic intergrowth of Ilm and clinopyroxene (Cpx₂). (b) The symplectic intergrowth of Ilm and Cpx₂ almost completely replaces titanite. (c) Clinopyroxene (Cpx₂^{ILM})-ilmenite intergrowth is separated from porphyroblastic garnet by a rind of plagioclase (Pl₂). Small rounded grain of titanite (relict) is present within the plagioclase rind. (d) Cpx₂^{ILM}-Ilm symplectic intergrowth is set apart from porphyroblastic garnet by the symplectic intergrowth of clinopyroxene (Cpx₂^{PL}) and plagioclase (Pl₂). The Cpx₂^{ILM}-Ilm symplectite is extremely fine-grained (lamellar width <2 μm) towards the inside of the symplectic intergrowth.

Figure 7.2 continued (e) $\text{Cpx}_2^{\text{ILM}}$ -Ilm symplectite with relict titanite is separated from garnet by the Cpx_2^{PL} -Pl₂ symplectite. These two symplectites are adjacent, but the $\text{Cpx}_2^{\text{ILM}}$ -Ilm symplectite is proximal to titanite, and the Cpx_2^{PL} -Pl₂ symplectite is proximal to garnet. Amphibole (Amp_2) partially replaces clinopyroxene (Cpx_2^{PL}) in the symplectic intergrowth. (f) Symplectic clinopyroxene ($\text{Cpx}_2^{\text{ILM}}$) in association with ilmenite is replaced by amphibole, such that amphibole appears to form symplectic intergrowths with ilmenite.

7.2 Phase compositions:

Analytical techniques

Major elemental analyses were performed using a Cameca SX100 Electron Probe Micro Analyser equipped with four wavelength-dispersive spectrometers (WDS) from the Department of Geology and Geophysics, Indian Institute of Technology, Kharagpur. All points were analysed with 15 kV acceleration voltage, 20 nA beam current, and a beam size of 1 μm . The dwell time for the measured elements was set at 10 s for the peak and 5 s for the background. Natural minerals and synthetic compounds were used as standards. Representative mineral compositions are presented in Tables 7.1 to 7.4. Mineral abbreviations in figures and tables have been used after (Whitney and Evans 2010). Cation recalculation for the estimation of Fe^{3+} is done following the scheme of Droop (1987). In the following section, salient compositional features of the minerals are described.

Garnet

The garnets are dominantly solid solutions of almandine, pyrope, and grossular, with a minor amount of spessartine (Table- 7.1): almandine (43- 57mol %) contents are highest with a lesser amount of grossular (19- 33 mol%) and pyrope (16- 26%) and minor spessartine (1- 4 mol%). The porphyroblasts show internal core-rim zonation with the core compositions being less ferroan and grossular rich ($\text{Gr}_{\text{TC}}: \text{Alm}_{43-47}\text{Gr}_{\text{S}28-33}\text{Prp}_{21-26}\text{Sp}_{\text{S}1-2}$; $X_{\text{Mg}}=0.31-0.37$) than rims ($\text{Gr}_{\text{TR}}: \text{Alm}_{49-57}\text{Gr}_{\text{S}20-26}\text{Prp}_{16-20}\text{Sp}_{\text{S}2-4}$; $X_{\text{Mg}}=0.23-0.29$). TiO_2 content of garnet is negligible, below 0.25 wt%. Garnet core composition is flat, homogenous, and extended to the thin rim (Fig. 7.3.a-c).

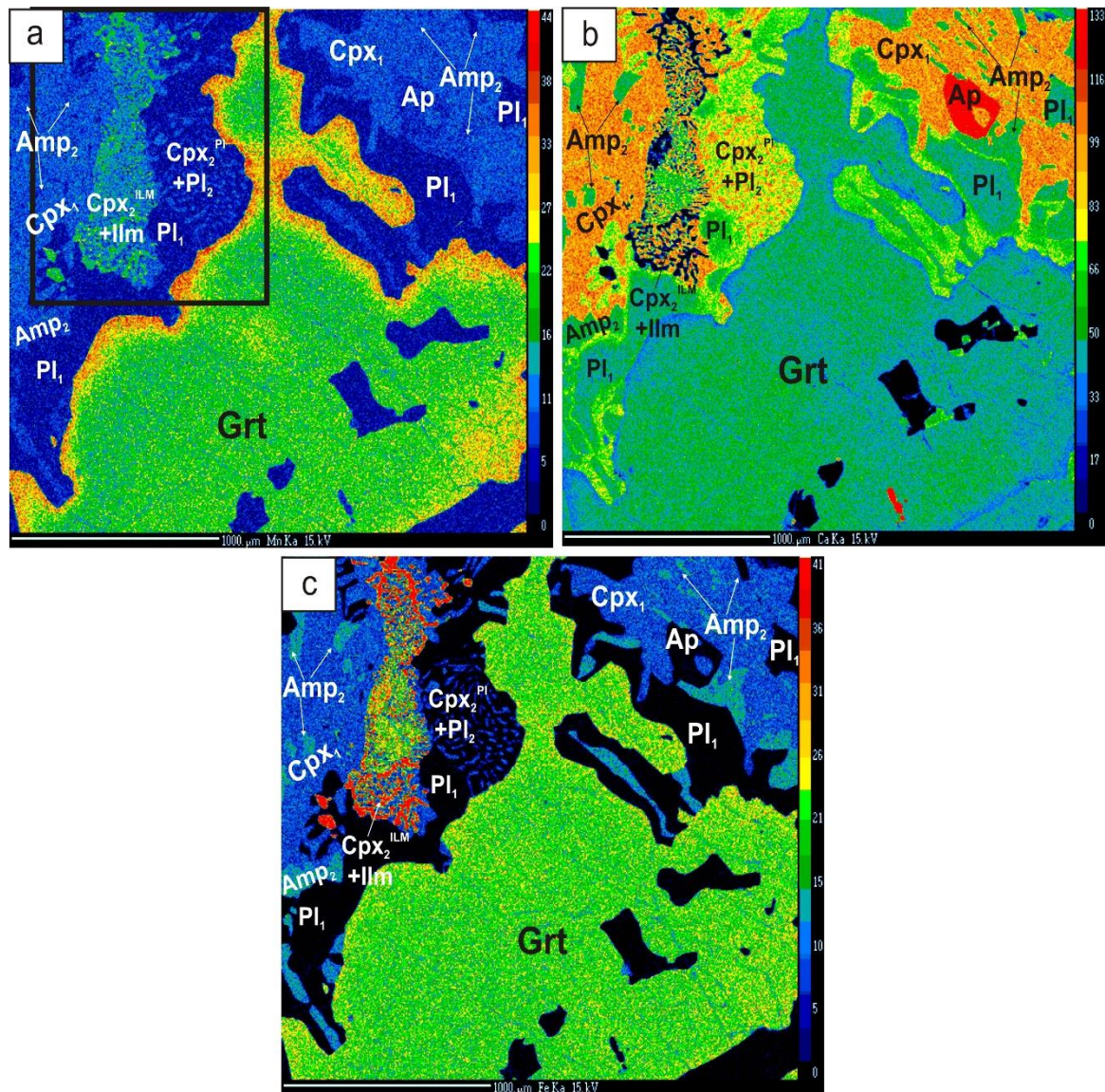


Figure 7.3: (a-c) X-ray intensity maps of Mn (a), Ca (b), and Fe (c) of a porphyroblastic garnet. All three maps show flat homogenous core composition extending up to the rim, which is thin. The X-ray intensity map of Mn shows a drastic increase in intensity in the thin rim, while the map of Fe shows a slight increase in intensity. The X-ray intensity map of Ca shows a dip in intensity in the rim. The area marked in the X-ray intensity map of Mn (a) is magnified in the X-ray intensity maps of figure d-h (same domains as Figure 3.d; Domain II).

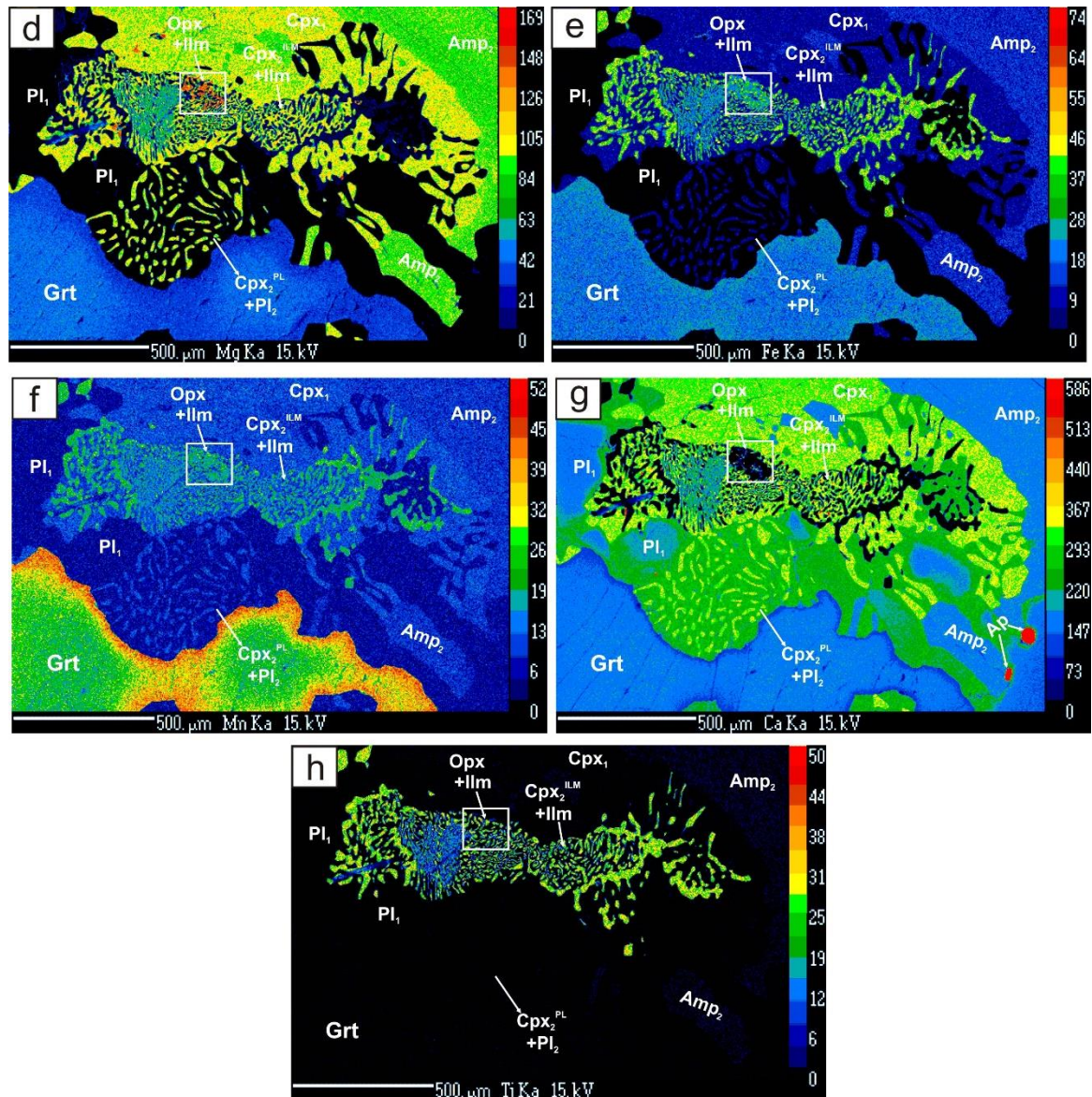


Figure 7.3 (continued): (d-h) These represent X-ray intensity maps of Mg, Fe, Mn, Ca, and Ti respectively. X-ray intensity elemental map of Mg (d) indicates restricted occurrences of orthopyroxene within this symplectic intergrowth of $\text{Cpx}_2^{\text{ILM}}$ -Ilm. The X-ray intensity map of Mg (d) also shows a dip in intensity in the rim of garnet porphyroblasts. Very fine grains of apatite are present in the $\text{Cpx}_2^{\text{ILM}}$ -Ilm symplectic intergrowth.

Pyroxene

Representative data of the pyroxenes are presented in Table 7.2. Both matrix clinopyroxenes (Cpx_1) and symplectic clinopyroxenes (Cpx_2^{PL} and $\text{Cpx}_2^{\text{ILM}}$) represent diopside-hedenbergite solid solutions with $X_{\text{Mg}}=0.72\text{-}0.83$ (Fig. 7.4). Cpx_1 has slightly higher Al (0.12-0.24 a.p.f.u) and Na (0.03-0.05 a.p.f.u) content than Cpx_2^{PL} and $\text{Cpx}_2^{\text{ILM}}$

(Al=0.05-0.10 a.p.f.u; Na=0.02-0.03 a.p.f.u). TiO₂ content of Cpx₁ (0.137-0.628 wt%) and Cpx₂ (0.069-0.536 wt%) is negligible. The orthopyroxenes in the symplectic intergrowths are magnesian with (X_{Mg}=0.55-0.58, Fig. 7.4).

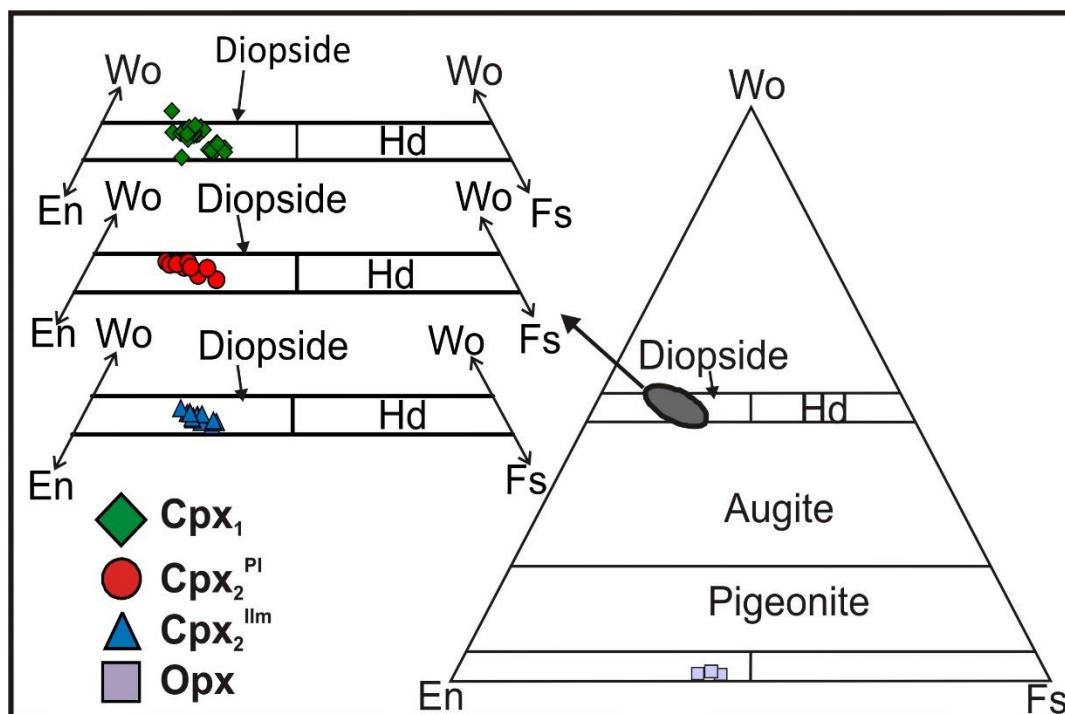


Figure 7.4: Plots showing compositional variation (or similarity) in clinopyroxene and orthopyroxene (Morimoto 1988) occurring in different textural settings.

Plagioclase.

Representative plagioclase compositions are given in Table 7.3. There is a considerable variation in plagioclase compositions depending on the textural types with $X_{OR} < 1$. The matrix plagioclase (Pl₁) shows a prominent increase in anorthite content from the core ($X_{An}=0.43-0.60$) to the rim ($X_{An}=0.75-0.86$) (Fig 7.3.g). Symplectic plagioclase (Pl₂) is similar to the rim of Pl₁ ($X_{An}=0.72-0.86$).

Amphibole.

Representative compositions of the amphiboles are presented in Table 7.4. According to the classification scheme of Leake et al. (1997) and Leake et al. (2004), all amphiboles are calcic. The amphibole inclusions in garnets (Amp₀) are mostly pargasitic in nature with $X_{Mg}=0.62-0.70$. The matrix amphibole (Amp₁) composition ranges between tschermakite and magnesio-hornblende with $X_{Mg}=0.59-0.72$.

Accessory minerals.

Representative chemical compositions of the accessory phases are in Table 7.5. Ilmenite present in the clinopyroxene + plagioclase symplectite is nearly pure FeTiO_3 . Rutile is present as a pure phase. Titanite is slightly aluminous (1.1-1.4 wt% Al_2O_3) with no F. Apatite has 1.657 wt% of F and 0.25 wt% of Cl.

Table 7.1: Representative microprobe analyses and calculated cations of garnet based on 12 oxygens

Sr. no.	G-1	G-2	G-3	G-4	G-5	G-6	G-7	G-8	G-9	G-10	G-11	G-12
Texture	Core	Rim	Core	Rim	Core	Rim	Core	Rim	Core	Rim	Core	Core
SiO_2	38.50	36.93	38.41	38.43	38.41	36.90	38.19	38.38	39.37	39.00	38.50	39.28
TiO_2	0.21	0.11	0.18	0.02	0.18	0.03	0.16	0.10	0.18	0.03	0.21	0.24
Al_2O_3	21.51	20.88	21.64	21.12	21.64	20.81	21.44	21.35	21.55	21.94	21.51	21.72
Cr_2O_3	0.01	0.07	bdl	0.08	bdl	0.04	0.06	0.14	0.04	0.10	0.01	bdl
Fe_2O_3^*	2.05	4.35	2.99	0.51	2.99	3.17	3.00	1.81	0.26	0.17	2.05	0.99
FeO^*	20.33	23.49	20.28	26.07	20.28	24.08	19.76	23.81	21.23	25.69	20.33	22.09
MgO	5.70	4.13	5.84	4.73	5.84	4.18	5.99	4.18	5.47	5.12	5.70	5.61
CaO	0.82	9.06	0.59	7.67	11.36	8.26	0.74	10.11	12.09	7.97	11.33	10.71
MnO	11.33	1.67	11.36	1.50	0.59	1.80	11.29	1.55	0.83	1.48	0.82	0.88
Na_2O	0.05	0.01	0.05	0.01	0.05	0.02	0.01	--	0.01	0.02	0.05	0.06
Total	100.50	100.71	101.34	100.13	101.34	99.29	100.65	101.43	101.03	101.52	100.50	101.57
Si	2.96	2.90	2.93	3.01	2.93	2.93	2.93	2.97	3.01	3.00	2.96	2.99
Ti	0.01	0.01	0.01	--	0.01	--	0.01	0.01	0.01	--	0.01	0.01
Al	1.95	1.93	1.95	1.95	1.95	1.95	1.94	1.95	1.94	1.99	1.95	1.95
Cr	--	--	--	--	--	--	--	0.01	--	0.01	--	--
Fe^{+3} *	0.12	0.26	0.17	0.03	0.17	0.19	0.17	0.11	0.01	0.01	0.12	0.06
Fe^{+2} *	1.31	1.54	1.30	1.71	1.30	1.60	1.27	1.54	1.36	1.65	1.31	1.41
Mg	0.65	0.48	0.67	0.55	0.67	0.50	0.69	0.48	0.62	0.59	0.65	0.64
Ca	0.93	0.76	0.93	0.64	0.93	0.70	0.93	0.84	0.99	0.66	0.93	0.87
Mn	0.05	0.11	0.04	0.10	0.04	0.12	0.05	0.10	0.05	0.10	0.05	0.06
Na	0.01	--	0.01	--	0.01	--	--	--	--	--	0.01	0.01
X_{Alm}	0.44	0.53	0.44	0.57	0.44	0.55	0.43	0.52	0.45	0.55	0.44	0.47
X_{Grs}	0.32	0.26	0.32	0.21	0.32	0.24	0.32	0.28	0.33	0.22	0.32	0.29
X_{Prp}	0.22	0.17	0.23	0.18	0.23	0.17	0.23	0.16	0.21	0.20	0.22	0.21
X_{Sps}	0.02	0.04	0.01	0.03	0.01	0.04	0.02	0.03	0.02	0.03	0.02	0.02
X_{Mg}	0.33	0.24	0.34	0.24	0.34	0.24	0.35	0.24	0.31	0.26	0.33	0.31

* Fe_2O_3 and Fe^{+3} is recalculated after the scheme of Droop (1987)

Table 7.2: Representative microprobe analyses and calculated cations of pyroxene based on 6 oxygens

Sr. No.	Px-1	Px-2	Px-3	Px-4	Px-5	Px-6	Px-7	Px-8	Px-9	Px-10	Px-11	Px-12	Px-13	Px-14	Px-15	Px-16
Texture	Cpx1	Cpx ₂ ^{PL}	Cpx1	Cpx ₂ ^{PL}	Cpx1	Cpx ₂ ^{PL}	Cpx1	Cpx ₂ ^{PL}	Cpx1	Cpx ₂ ^{PL}	Cpx ₂ ^{ILM}	Cpx ₂ ^{ILM}	Cpx ₂ ^{ILM}	Cpx ₂ ^{ILM}	Opx	Opx
SiO ₂	50.32	51.61	51.00	52.43	48.68	52.25	51.15	52.00	50.67	53.04	53.00	51.53	52.33	53.33	52.05	51.45
TiO ₂	0.56	0.13	0.40	0.19	0.63	0.12	0.34	0.25	0.54	0.14	0.38	0.46	0.22	0.32	0.58	0.08
Al ₂ O ₃	4.41	1.44	3.94	1.89	5.44	1.33	3.33	1.65	3.91	1.29	1.16	1.12	1.45	1.05	0.78	0.89
Cr ₂ O ₃	0.06	0.23	0.00	0.36	0.06	0.36	0.11	0.00	0.00	0.00	0.09	0.07	0.00	0.00	0.02	0.03
Fe ₂ O ₃ *	4.11	1.62	2.99	0.00	4.58	1.86	2.39	2.01	2.60	0.07	1.15	2.22	2.17	0.41	0.93	3.47
FeO*	7.15	7.31	7.31	9.68	6.71	7.78	7.16	8.09	7.89	9.56	8.66	7.17	8.75	10.43	25.53	26.95
MgO	13.49	13.15	12.82	12.96	12.48	13.36	13.04	13.26	12.30	13.23	13.65	13.49	13.04	12.79	20.21	18.54
CaO	20.20	22.93	22.27	22.07	20.71	22.97	22.63	22.66	22.42	22.38	23.01	22.89	22.67	22.85	0.42	0.54
MnO	0.07	0.12	0.27	0.21	0.17	0.24	0.26	0.11	0.29	0.23	0.18	0.23	0.13	0.04	0.49	0.51
Na ₂ O	0.72	0.34	0.54	0.30	0.70	0.29	0.41	0.31	0.50	0.31	0.23	0.26	0.33	0.31	0.03	0.01
Total	101.10	98.88	101.54	100.10	100.15	100.55	100.82	100.35	101.13	100.24	101.50	99.43	101.08	101.52	101.04	102.46
Si	1.86	1.95	1.88	1.96	1.82	1.95	1.89	1.94	1.88	1.98	1.96	1.94	1.94	1.97	1.95	1.93
Ti	0.02	0.00	0.01	0.01	0.02	0.00	0.01	0.01	0.02	0.00	0.01	0.01	0.01	0.01	0.02	0.00
Al	0.19	0.06	0.17	0.08	0.24	0.06	0.15	0.07	0.17	0.06	0.05	0.05	0.06	0.05	0.03	0.04
Cr	0.00	0.01	0.00	0.01	0.00	0.01	0.00	0.00	0.00	0.00	0.00	0.00	0.00	0.00	0.00	0.00
Fe ⁺³ *	0.11	0.05	0.08	0.00	0.13	0.05	0.07	0.06	0.07	0.00	0.03	0.06	0.06	0.01	0.03	0.10
Fe ⁺² *	0.22	0.23	0.22	0.30	0.21	0.24	0.22	0.25	0.24	0.30	0.27	0.23	0.27	0.32	0.80	0.85
Mg	0.74	0.74	0.70	0.72	0.69	0.74	0.72	0.74	0.68	0.74	0.75	0.76	0.72	0.71	1.13	1.04
Ca	0.80	0.93	0.88	0.88	0.83	0.92	0.90	0.91	0.89	0.89	0.91	0.92	0.90	0.91	0.02	0.02
Mn	0.00	0.00	0.01	0.01	0.01	0.01	0.01	0.00	0.01	0.01	0.01	0.01	0.00	0.00	0.02	0.02
Na	0.05	0.02	0.04	0.02	0.05	0.02	0.03	0.02	0.04	0.02	0.02	0.02	0.02	0.02	0.00	0.00
X _{Mg}	0.77	0.76	0.76	0.70	0.77	0.75	0.76	0.74	0.74	0.71	0.74	0.77	0.73	0.69	0.59	0.55

*Fe₂O₃ and Fe⁺³ is recalculated after the scheme of Droop (1987)

Table 7.3: Representative microprobe analyses and calculated cations of plagioclase based on 8 oxygens

Sr. no.	Pl-1	Pl-2	Pl-3	Pl-4	Pl-5	Pl-6	Pl-7	Pl-8	Pl-9	Pl-10	Pl-13
Texture	Pl ₁	Pl ₁	Pl ₁	Pl ₁	Pl ₁	Pl ₂	Pl ₁	Pl ₂	Pl ₁	Pl ₂	Pl ₂
	Core	Rim	Core	Rim	Core	Sym	Core	Sym	Core	Sym	rind
SiO ₂	56.96	47.66	56.74	47.28	57.07	47.43	56.41	48.05	57.90	47.78	50.81
Al ₂ O ₃	27.78	33.32	27.31	34.32	26.98	33.16	27.80	33.59	27.54	33.56	31.87
FeO	0.07	0.14	0.00	0.53	0.07	0.57	0.00	0.18	0.00	0.10	0.35
MgO	0.01	0.00	0.00	0.00	0.00	0.22	0.00	0.00	0.01	0.00	0.01
CaO	10.02	17.05	9.88	17.75	9.48	16.78	10.24	17.05	9.71	16.94	14.79
Na ₂ O	6.41	1.90	6.51	1.57	6.77	1.63	6.27	1.90	6.46	1.92	3.42
K ₂ O	0.05	0.01	0.07	0.02	0.10	0.09	0.04	0.01	0.10	0.01	0.02
Total	101.44	100.14	100.67	101.48	100.64	99.90	100.89	100.95	101.87	100.41	101.32
Si	2.53	2.18	2.54	2.15	2.55	2.18	2.52	2.19	2.55	2.18	2.29
Al	1.45	1.80	1.44	1.84	1.42	1.80	1.46	1.80	1.43	1.81	1.69
Fe ⁺²	0.00	0.01	0.00	0.02	0.00	0.02	0.00	0.01	0.00	0.00	0.01
Mg	0.00	0.00	0.00	0.00	0.00	0.02	0.00	0.00	0.00	0.00	0.00
Ca	0.48	0.84	0.47	0.86	0.45	0.83	0.49	0.83	0.46	0.83	0.71
Na	0.55	0.17	0.56	0.14	0.59	0.15	0.54	0.17	0.55	0.17	0.30
K	0.00	0.00	0.00	0.00	0.01	0.01	0.00	0.00	0.01	0.00	0.00
XOr	0.00	0.00	0.00	0.00	0.01	0.01	0.00	0.00	0.01	0.00	0.00
XAb	0.54	0.17	0.54	0.14	0.56	0.15	0.52	0.17	0.54	0.17	0.29
XAn	0.46	0.83	0.45	0.86	0.43	0.85	0.47	0.83	0.45	0.83	0.70

Table 7.4: Representative microprobe analyses and calculated cations of amphibole based on 23

Sr. no.	Am-1	Am-2	Am-3	Am-4	Am-5	Am-6	Am-7	Am-8
Phase	Amp ₂	Amp ₂	Amp ₂	Amp ₂	Amp ₂	Amp ₂	Amp ₀	Amp ₀
SiO ₂	45.11	46.02	45.78	45.28	45.26	46.03	44.76	43.83
TiO ₂	1.53	1.31	1.41	1.59	1.54	1.69	1.32	1.56
Al ₂ O ₃	11.09	10.65	10.26	10.65	10.65	9.88	11.96	11.92
Cr ₂ O ₃	0.31	0.23	0.17	0.01	0.07	0.04	0.00	0.30
FeO	15.14	13.90	14.68	15.90	16.30	16.34	14.66	15.34
MgO	11.55	12.64	12.10	11.76	11.86	11.28	12.75	11.85
CaO	11.47	11.65	11.41	11.32	11.49	11.38	11.84	11.65
MnO	0.17	0.00	0.14	0.16	0.13	0.17	0.09	0.02
Na ₂ O	1.82	1.66	1.61	1.82	1.78	1.61	2.02	1.99
K ₂ O	0.27	0.26	0.28	0.27	0.25	0.25	0.20	0.29
F	0.00	0.00	0.01	0.00	0.01	0.01	0.00	0.00
Cl	0.03	0.02	0.00	0.01	0.01	0.01	0.01	0.02
Total	98.49	98.33	97.83	98.78	99.34	98.68	99.68	98.86
Si	6.58	6.67	6.69	6.59	6.56	6.72	6.42	6.39
Al ^(IV)	1.42	1.33	1.31	1.41	1.44	1.28	1.58	1.61
Ti	0.00	0.00	0.00	0.00	0.00	0.00	0.00	0.00
Sum T	8.00	8.00	8.00	8.00	8.00	8.00	8.00	8.00
Al ^(VI)	0.49	0.49	0.46	0.42	0.38	0.42	0.45	0.43
Ti	0.17	0.14	0.15	0.17	0.17	0.19	0.14	0.17
Cr ⁺³	0.04	0.03	0.02	0.00	0.01	0.00	0.00	0.03
Fe ⁺³	0.26	0.25	0.28	0.35	0.41	0.27	0.44	0.38
Mg	2.51	2.73	2.63	2.55	2.56	2.45	2.73	2.57
Fe ⁺²	1.54	1.36	1.45	1.51	1.48	1.67	1.25	1.41
Mn	0.00	0.00	0.00	0.00	0.00	0.00	0.00	0.00
Sum C	5.00	5.00	5.00	5.00	5.00	5.00	5.00	5.00
Mg	0.00	0.00	0.00	0.00	0.00	0.00	0.00	0.00
Fe ⁺²	0.05	0.07	0.06	0.08	0.09	0.06	0.07	0.08
Mn	0.02	0.00	0.02	0.02	0.02	0.02	0.01	0.00
Ca	1.79	1.81	1.79	1.77	1.78	1.78	1.82	1.82
Na	0.13	0.12	0.13	0.14	0.12	0.14	0.10	0.10
Sum B	2.00	2.00	2.00	2.00	2.00	2.00	2.00	2.00
Ca	0.00	0.00	0.00	0.00	0.00	0.00	0.00	0.00
Na	0.38	0.35	0.32	0.38	0.38	0.31	0.47	0.47
K	0.05	0.05	0.05	0.05	0.05	0.05	0.04	0.05
Sum A	0.43	0.40	0.37	0.43	0.43	0.36	0.50	0.52
TOTAL	15.43	15.40	15.37	15.43	15.43	15.36	15.50	15.52
X _{Mg}	0.61	0.66	0.64	0.62	0.62	0.59	0.67	0.63
Group	Magnesian-hornblend	Magnesian-hornblend	Magnesian-hornblend	Magnesian-hornblend	Magnesian-hornblend	Magnesian-hornblend	Pargasite	Pargasite

Table 7.5: Representative microprobe analyses and calculated cations of Ti bearing phases and apatite

Sr. no.	Tn-1	Tn-2	Im-1	Im-2	Im-3	Im-4	Rt-1	Point	10
Phase	Ttn	Ttn	Ilm	Ilm	Ilm	Ilm	Rt	Phase	Ap
SiO ₂	29.84	30.35	0.05	0.000	0.00	0.04	0.00	SiO ₂	0.033
TiO ₂	38.67	39.35	51.03	52.134	52.39	51.18	98.14	TiO ₂	0.024
Al ₂ O ₃	1.41	1.09	0.16	0.165	0.19	0.15	0.35	Al ₂ O ₃	0
Cr ₂ O ₃	0.01	0.00	0.21	0.038	0.00	0.03	0.03	Cr ₂ O ₃	0
Fe ₂ O ₃ *	0.52	0.45	3.10	3.090	1.38	2.00	0.86	FeO	0.278
FeO*	0.00	0.00	42.74	44.063	42.67	43.53	0.00	MgO	0.026
MgO	0.04	0.00	1.20	1.134	1.57	0.74	0.02	CaO	56.038
CaO	28.98	28.64	0.11	0.050	0.17	0.20	0.02	MnO	0.048
MnO	0.09	0.05	0.53	0.569	0.49	0.42	0.00	Na ₂ O	0.05
Na ₂ O	0.02	0.01	0.00	0.000	0.02	0.02	0.00	K ₂ O	0
F	0.06	0.00	0.03	0.011	0.00	0.04	0.04	P ₂ O ₅	42.155
P ₂ O ₅	0.56	0.00	0.00	0.000	0.01	0.00	0.00	F	1.657
Total	100.20	99.94	99.16	101.25	98.88	98.36	99.46	Cl	0.24
Oxygen	5.00	5.00	3.00	3.000	3.00	3.00	2.00	Sum	100.55
Si	0.96	0.99	0.00	0.000	0.00	0.00	0.00	O=F	0.70
Ti	0.94	0.96	0.97	0.970	0.99	0.98	0.97	O=Cl	0.05
Al	0.05	0.04	0.00	0.005	0.01	0.00	0.01	Revised SUM	99.80
Cr	0.00	0.00	0.00	0.001	0.00	0.00	0.00	Si	0.00
Fe ⁺³ *	0.01	0.01	0.06	0.058	0.03	0.04	0.01	Ti	0.00
Fe ⁺² *	0.00	0.00	0.90	0.911	0.89	0.93	0.00	Al	0.00
Mg	0.00	0.00	0.05	0.042	0.06	0.03	0.00	Cr	0.00
Ca	1.00	1.00	0.00	0.001	0.00	0.01	0.00	Ca	4.72
Mn	0.00	0.00	0.01	0.012	0.01	0.01	0.00	Fe ⁺²	0.02
Na	0.00	0.00	0.00	0.000	0.00	0.00	0.00	Mn	0.00
F	0.01	0.00	0.00	0.001	0.00	0.00	0.00	Mg	0.00
P	0.02	0.00	0.00	0.000	0.00	0.00	0.00	Na	0.01
*Fe ₂ O ₃ and Fe ⁺³ is recalculated after the scheme of Droop (1987)								K	0.00
								P	2.81
								SUM	7.57
								F	0.41
								Cl	0.03
								OH	0.56

7.3 Modelling the formation of Cpx₂-Ilm symplectites using CSpace and XMapTools

Textural modeling of Ilm-Cpx₂(±Opx) symplectite: a mass balance approach

The textural features described above suggest that the symplectic intergrowth of Ilm-Cpx₂ (with rare Opx) develops preferentially over the titanite. Rutile was present prior to the formation of the symplectite. It is also possible that the rutile might have been involved in some symplectite forming process. However, textural features support the involvement of titanite in the formation of Ilm-Cpx₂ symplectite, while such features on account of rutile (e.g. presence of rutile in the vicinity of or in contact with Ilm-Cpx₂ symplectite) are absent. Accordingly, the textural modelling study used titanite as the only Ti-bearing reactant phase replaced by the Ilm-Cpx₂ (± Opx).

Mass balance calculations with the measured mineral compositions are a powerful technique to explain the observed mineralogy and the textural relations (Fisher 1989; Lang et al. 2004; Sengupta et al. 2004; Chowdhury et al. 2013). This approach returns stoichiometrically balanced chemical reactions involving the reactant and product phases and, hence, provides vital clues about the mobility of the different chemical species in a given compositional space (Lang and Rice 1985; Fisher 1989; Lang et al. 2004; Sengupta et al. 2004, 2009; Sengupta and Dasgupta 2009; Chowdhury et al. 2013; Karmakar et al. 2017). The computer program CSpace (Torres-Roldan et al. 2000) has been employed to identify stoichiometrically balanced chemical reaction(s) involving the measured compositions of the reactant and product phases. This algebraic analysis with Cspace involves the singular value decomposition (SVD) of a compositional matrix **M** of **m** mineral phases in terms of **n** components (**M**=**m** x **n**) (Lang et al. 2004). The chemical species that are suspected to show mobility (e.g FeO, MgO, CaO, Na₂O, TiO₂, etc in this study) are considered as ‘phases’ in the computational matrix (Sengupta and Dasgupta 2009). A detailed discussion on the SVD method is presented in several studies (Lang et al. 2004; Sengupta et al. 2004; Sengupta and Dasgupta 2009; Chowdhury et al. 2013). In the multi-component system with a number of mobile species, the CSpace programs can return several stoichiometrically balanced reactions for a set of reactant and product phases. Of these probable reactions, if the CSpace returns more than one reaction, the likely reaction will be chosen based on the following criteria:

1. The observed reactant and the product phases must lie on the opposite side of the reaction.
2. The calculated and observed volume ratio of the Ilm-Cpx₂ in the symplectite must match.

Calculation of volume ratio of Ilm-Cpx₂ symplectite obtained from reactions:

The coefficients in the obtained balanced reactions are the molar proportions of the phases and the volumes of the necessary solid phases are calculated by multiplying the molar proportions by the molar volume of that phase. The molar volume of the phase is obtained using the computer program PERPLE_X (ver. 6.9.1) (Connolly 2005, 2009) with the thermodynamic data of Holland and Powell (2011). For a particular solid solution phase, the molar volume of the different end-members are calculated, at an average P-T condition of 800°C, 9 kbar, based on the constrained physical conditions of metamorphism (presented in the following section). The molar volume of the solid-solution phases, (V_N^{SS}) is then calculated using the following relation:

$$V_N^{SS} = (X_A \times V_A) + (X_B \times V_B)$$

where A and B are the two end members of the solid-solution phase N, V is the molar volume of that end member, and X is the mole fraction of the corresponding end member.

Estimation of volume ratio of Ilm-Cpx₂ symplectite using XMapTools:

The volume proportion of Cpx and Ilm only from the Cpx₂-Ilm symplectic domain is estimated to check how well the modelled reaction product correlates with the observed textures. We have taken this as a parameter as other phases, such as Grt, Pl are formed or consumed in other concurrent reactions, and texturally they can't be attributed solely to the titanite breakdown reaction. Owing to the fine-grained nature of the Cpx₂-Ilm symplectites, estimation of observed volume proportion is difficult. For accurate estimation of the phase proportions of Cpx and Ilm in the symplectites, the software XMapTools (ver. 3.4.3) (Lanari et al. 2014, 2019) is used. In this process, X-ray intensity maps of the elements Si, Ti, Al, Fe^{TOTAL+2}, Mg, Na, Ca (Fig 7.5.a-g) of the selected microdomains, produced using EPMA are used to classify all the different phases accurately with the help of XMapTools and phase proportions of Cpx and Ilm are calculated only from the symplectic domain (Fig. 7.5.h), omitting all other phases present.

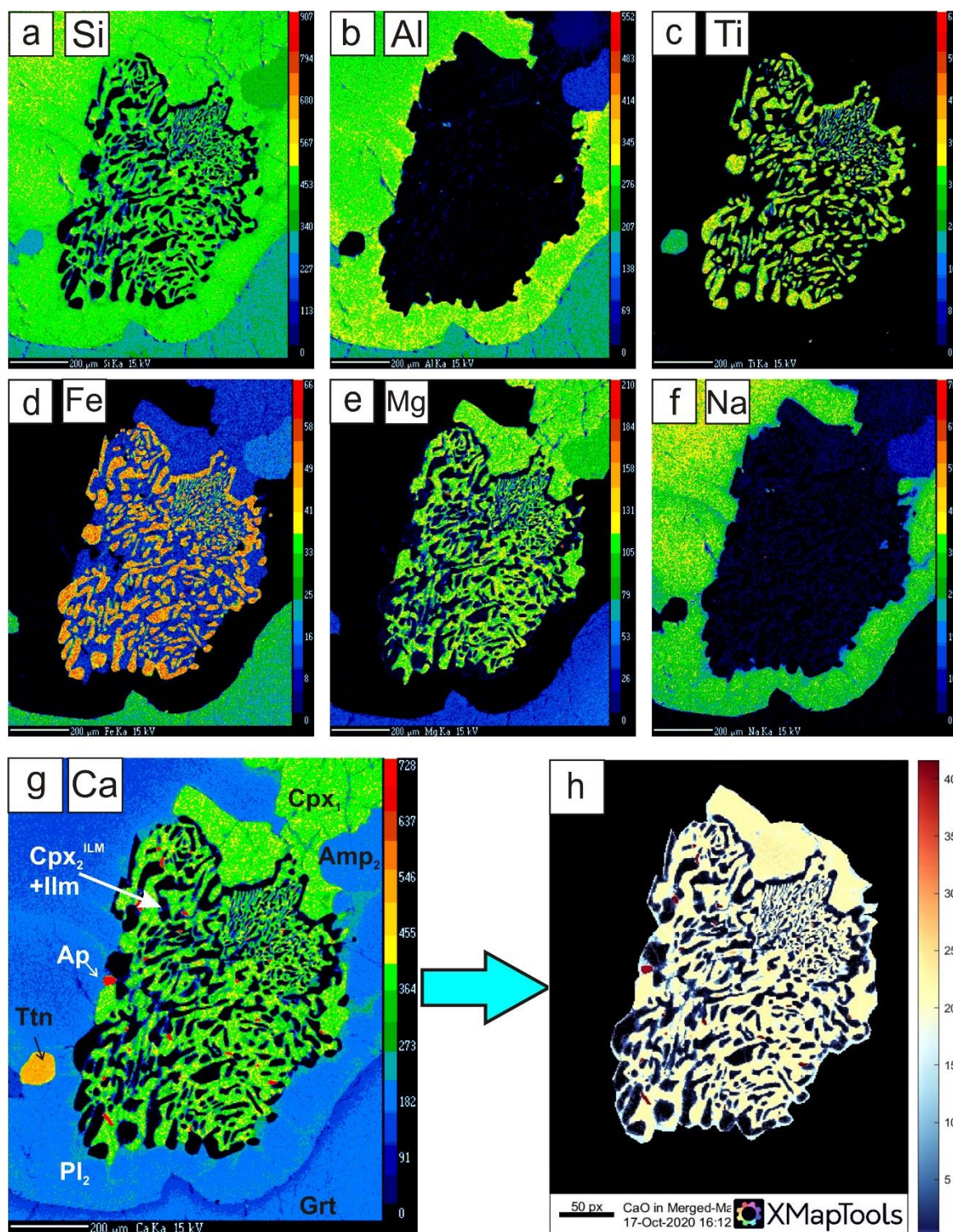


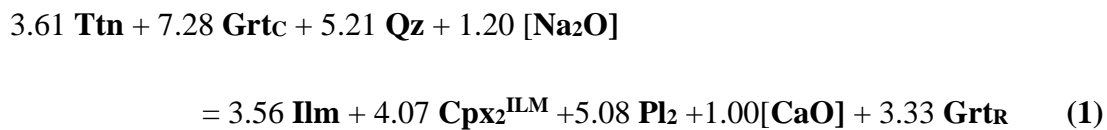
Figure 7.5: (a-g) Elemental X-ray intensity maps of Si, Al, Ti, Fe, Mg, Na, Ca from the same region of Fig. 7.2.c (Domain I). Fine-grained apatite is present within the Cpx₂-Ilm symplectites (red dots in the Ca map). (h) A Composite CaO map processed in the XMapTools software is used to calculate ilmenite and clinopyroxene phase proportions in the Cpx₂^{ILM}-Ilm symplectites in the textural modelling study.

The choice of domains for the textural modelling study

Two micro-domains viz. Domain I and Domain II are chosen for detailed textural analyses. In Domain I (Fig. 7.2.c), Ilm-Cpx₂ symplectite is separated from the porphyroblastic garnet by a rind of Pl₂. In Domain II, Ilm-Cpx₂ symplectite is separated from garnet by a symplectic intergrowth of Cpx₂-Pl₂ (Fig. 7.2.d). Proximal to garnet, the fine symplectite of clinopyroxene (Cpx₂^{PL}) and plagioclase (Pl₂^{CPX}) develops on and variably replaces the garnet. Away from garnet, lamellar intergrowth of Cpx₂-Ilm develops after titanite. In both domains, the core and rim of garnet are treated as reactant and product phases, respectively. The mineral compositions that are used for textural modelling from both of these micro-domains (Domain I and II), respectively.

Modelled reactions in Domain I:

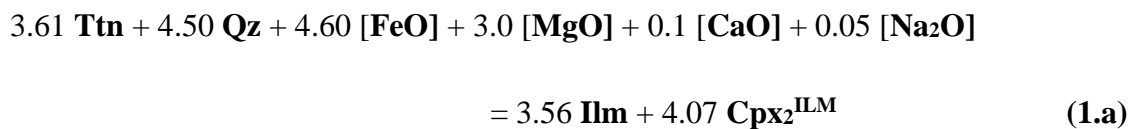
If all the product phases between titanite and garnet are considered, the CSpace program returns the net reaction:



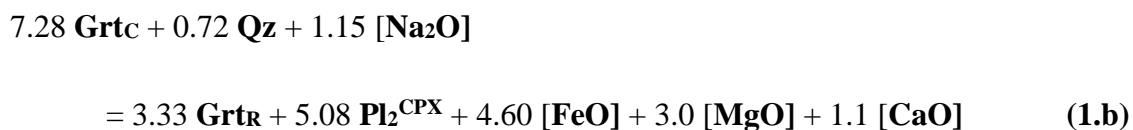
$$\Delta V_{\text{SOLID}} = V_{\text{PRODUCTS}} - V_{\text{REACTANTS}} = +7.5\%; \text{Cpx/Ilm} = 2.4 \text{ (observed Cpx/Ilm: 2.2)}$$

This net reaction has two parts.

At the titanite end, the likely reaction is,

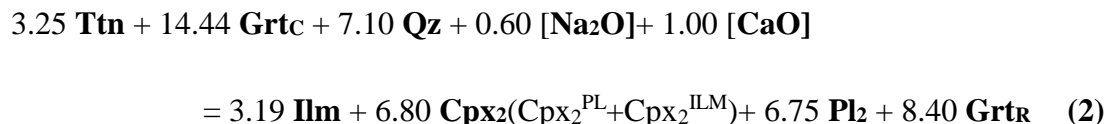


At the garnet end, the likely reaction is,



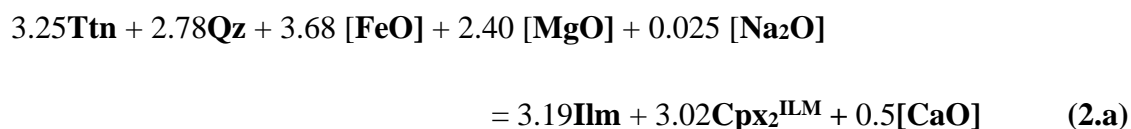
Modeled reactions in domain II:

If all the products are considered, the CSpace program produces the following net reaction,



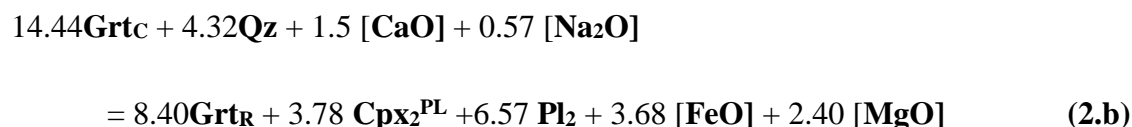
$$\Delta V_{\text{SOLID}} = V_{\text{PRODUCTS}} - V_{\text{REACTANTS}} = +6.6\%; \text{Cpx}(\text{Cpx}_2^{\text{PL}} + \text{Cpx}_2^{\text{ILM}})/\text{Ilm} = 4.5;$$

Similar to Domain I, the net reaction of Domain II can be divided into two sub-reactions. The following is the reaction at the titanite end,

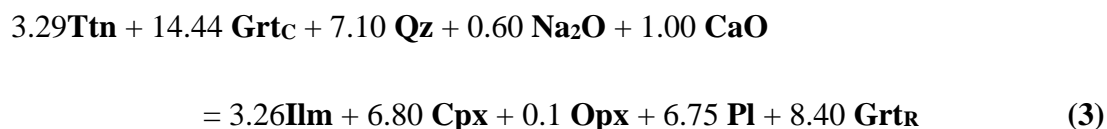


Calculated volume ratio of **Cpx₂/Ilm**, from reaction 2.a = **2.0**; (Observed Cpx/Ilm = 1.9)

The reaction at the garnet end,



From the calculated volume change and volume ratios, Domain II is very similar to Domain I, except for adding orthopyroxene as a product. The presence of minor amounts of orthopyroxene observed in the Cpx₂-Ilm symplectic domains may be accounted for by the following mass-balanced reaction:



7.4 Physical conditions of metamorphism

Detail study of the P-T evolution of the mafic rocks is beyond the purview of this study. In the following sections, the reconstruction of the change in the physical conditions of metamorphism led to the formation of the ilmenite-plagioclase-clinopyroxene intergrowth after the primary granoblastic assemblages.

7.4.1 Choice of phase compositions for the estimation of P-T condition of metamorphism

Ubiquitous presence of the assemblage garnet-clinopyroxene-plagioclase-quartz-titanite (\pm rutile) suggests that the studied mafic granulites witnessed high pressure metamorphism (O'Brien and Rötzler 2003; Pattison 2003). The high pressure assemblage was presumably in equilibrium with a melt phase (represented by the garnet-bearing leucosome) at the thermal maxima. A number of studies have shown that high pressure metamorphism of the rocks of diverse bulk compositions develop garnet on the prograde path. These garnet grains may serve as a substrate over which new garnet rims grow till the T_{\max} (maximum temperature) is reached (Saxena and Ganguly 1987; Spear 1993). This leads to prograde growth zoning (rim-ward decrease in Fe and Mn and increase in Mg) in garnet (Harte and Henley 1966; Hollister 1966; Lopez Ruiz 1976; Tuccillo et al. 1990; Ikeda 1993; Nyström and Kriegsman 2003; Kohn 2014; Dempster et al. 2020). Since garnet preferentially partitions Fe relative to the coexisting pyroxene, the highest temperature will be obtained with rim compositions of garnet and coexisting pyroxene if the former shows growth zoning. X-ray intensity maps and the measured composition of garnet show distinct enrichment of Fe and Mn in the thin rim (30-80 μ m) relative to the core of garnet (Fig. 4a;4c). The core part of garnet is compositionally homogeneous and is Mg-rich relative to the thin rim (Fig.4d). The thin rim of garnet, therefore, is interpreted to have formed during the partial exchange of elements with the coexisting ferromagnesian phases during retrogression (Spear 1993). Studies have demonstrated that at temperature $>750^{\circ}\text{C}$ and in presence of a melt phase, volume diffusion in garnet and pyroxene are sufficiently fast to homogenise large garnet porphyroblasts (>0.5 mm) over a range of cooling rates (Chakraborty and Ganguly 1991; Carlson and Schwarze 1997; Ganguly et al. 1998; Chakraborty 2008; Caddick et al. 2010). Several studies in high temperature granulite metamorphic belts record that equilibrium among the mineral assemblages that developed

during the T_{\max} occurs over a large area (several square km, Kelsey and Hand 2015). This explains the rare preservation of growth zoning in garnet in high to ultra-high-temperature metamorphism. Rapid and short-lived heating at a high temperature can only develop the rare prograde zoning in high to ultra-high-temperature granulites (Chen et al. 1998; Hollis et al. 2006). In view of all the observations, the compositionally homogeneous core compositions are chosen for the estimation of pressure and temperature during which the primary (granoblastic) assemblages are equilibrated. The compositions of the symplectic minerals and the rims of the porphyroblastic phases constrain the physical conditions during which the symplectic assemblage equilibrated during retrogression.

7.4.2 Conventional thermobarometry

For temperature estimation, Fe^{2+} -Mg exchange thermometer involving garnet and clinopyroxene is used (Ellis and Green 1979). Metamorphic pressure has been computed from the assemblage garnet-plagioclase-clinopyroxene-quartz (GCPS, Eckert et al. 1991). The core compositions of the granoblastic assemblage of $\text{Grt}_C + \text{Pl}_1 + \text{Cpx}_1 (\pm \text{Qz})$, yield a tight cluster of temperature of 800-850°C (Table-7.6). The Fe-Mg exchange thermometer has a very steep slope in the P-T field. This, together with the accuracy of the geothermometer ($\pm 50^\circ\text{C}$) suggests that the choice of reference pressure should not affect the estimated temperature values. At the reference temperature of 850°C, the GCPS barometer yields 12-13 kbar pressure for the core compositions of the granoblastic (primary) phases. The temperature of 850°C is, therefore, considered to be the maximum temperature recorded by the primary assemblages at the estimated pressure of 13 kbar. The rim compositions of garnet (Grt_R) coupled with symplectic $\text{Pl}_2 + \text{Cpx}_2^{\text{PL}}$ yield distinctly lower temperature (650-700°C) and pressure (6.5-8 kbar, Table-7.6). The estimated pressure and temperature is

Table 7.6: P-T estimates through conventional thermobarometric calculations

Minerals in equilibrium	Dataset		Thermometry (GC ¹)		Barometry (GCPS ²)	
	No.	Phases used	P (ref)	T (°C)	T (ref)	P (kbar)
$\text{Rt} + \text{Spn} + \text{Grt}_c + \text{Cpx}_1 + \text{Pl}_1$	1	G-1; Px-1; Pl-1;	13kbar	865	850°C	12.6
	2	G-3; Px-3; Pl-3;		825		12.7
	3	G-5; Px-5; Pl-5;		830		13
	4	G-7; Px-7; Pl-7;		844		13.1
	5	G-9; Px-9; Pl-9;		857		12.6
	6	G-2; Px-2; Pl-2;		654		7.4
$\text{Ilm} + \text{Cpx}_2 + \text{Grt}_r + \text{Opx} + \text{Pl}_2$	7	G-4; Px-4; Pl-4;	7kbar	693	700°C	6.4
	8	G-6; Px-6; Pl-6;		645		6.8
	9	G-8; Px-8; Pl-8;		690		7.9
	10	$\text{G-10; Px-10; Pl-10;}$		713		6.8

¹GC: Garnet – clinopyroxene geothermometer (Ellis and Green 1979).

²GCPS: Garnet – clinopyroxene – plagioclase – quartz barometer (Eckert et al. 1991).

considered as the recorded physical conditions when the symplectic intergrowth of $\text{Cpx}_2\text{-Pl}_2$ and Ilm-Cpx_2 were formed.

7.4.3 Isopleth intersection in pseudosection

Notwithstanding the following points:

1. The numerically computed phase diagram (pseudosection) is influenced by the input bulk rock composition. The chosen bulk rock composition may or may not represent the composition of the equilibrium.
2. Uncertainties associated with the internally consistent thermodynamic data and the activities of the solid solutions

The isopleth intersection methods yield reasonably well-constrained P-T estimates for metamorphism and are widely used by petrologists (Evans 2004; Palin et al. 2016).

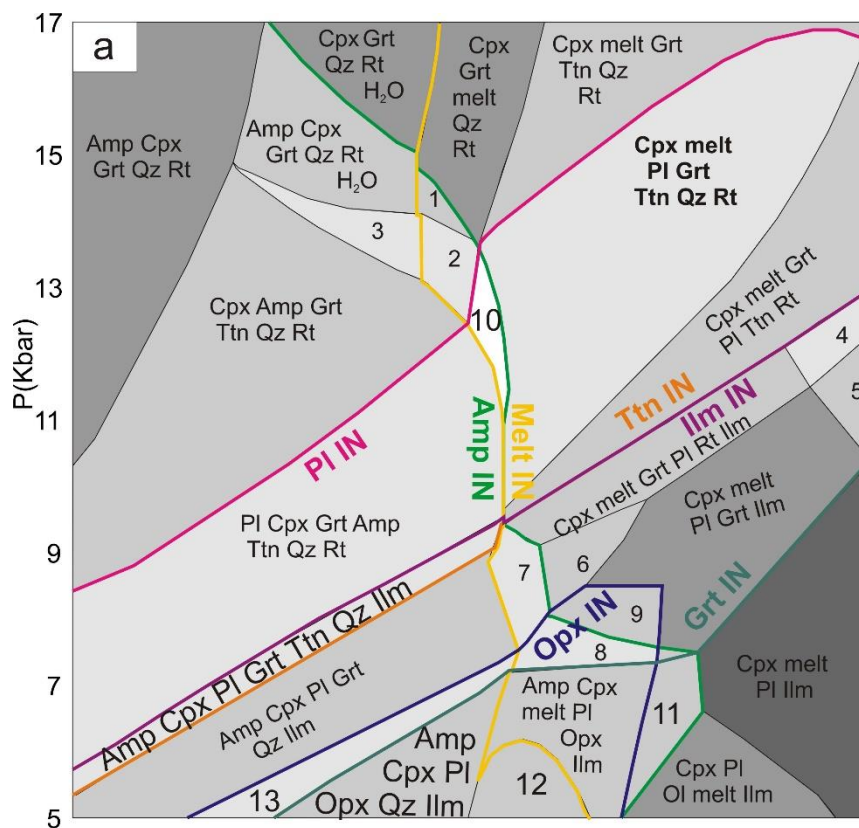


Figure 7.6: (a) P-T pseudosection corresponding to the EBC (obtained from Domain II (Fig. 7.2.d) by XMapTools) is calculated in the NCFMASHT ($\text{Na}_2\text{O-CaO-FeO-MgO-Al}_2\text{O}_3\text{-SiO}_2\text{-H}_2\text{O-TiO}_2$) system where amphibole, melt, plagioclase, garnet, sphene, ilmenite, clinopyroxene, orthopyroxene “IN” lines are marked.

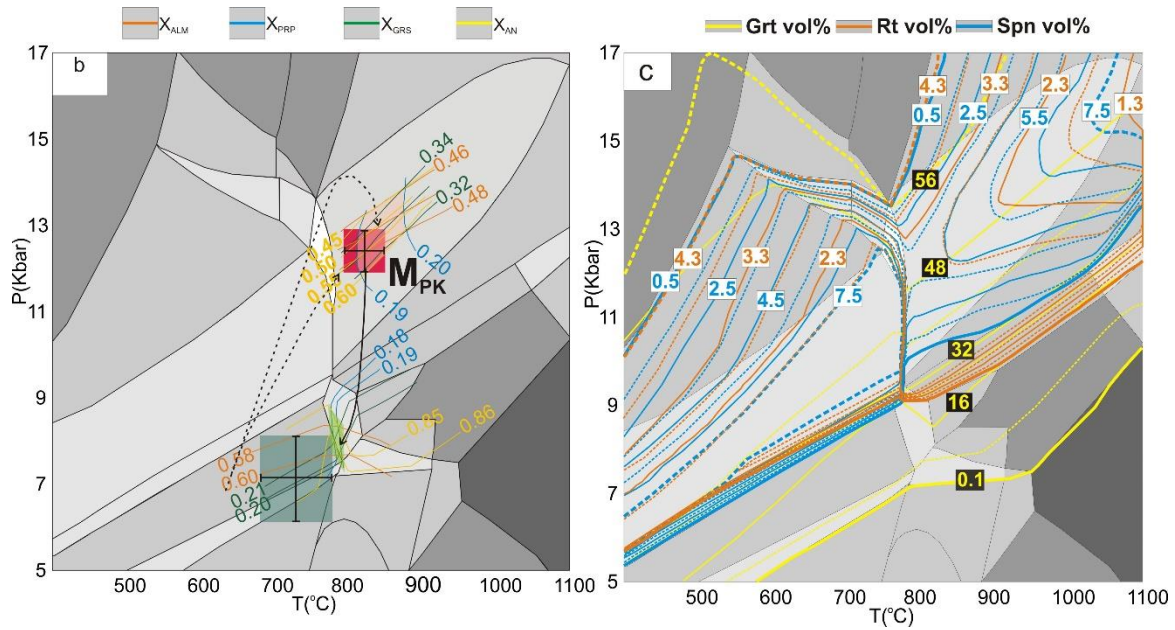


Figure 7.6 (continued): (b) Compositional isopleths for garnet (X_{ALM} , X_{PRP} , X_{GRS}) and plagioclase (X_{AN}) plotted on the pseudosection in the appropriate assemblage fields, constrain the P-T conditions of peak and retrogression. P-T conditions estimated using conventional thermobarometry are also plotted in the diagram with the “plus” signs with red (peak) and green (retrogression) squares. P-T conditions estimate a steeply positive P-T path (near isothermal). Dotted lines represent various possible prograde paths. (c) Volume isopleths of Grt, rutile and titanite are plotted on the pseudosection.

The P-T pseudosection has been computed using the program *Perple_X* (ver. 6.9.1; Connolly 2005) with the internally consistent thermodynamic dataset of Holland and Powell 2011 (TC-DS633). The a-X relationships of the minerals chosen for the numerical calculations of the phase diagram are the following: clinopyroxene (Holland et al. 2018), clino-amphibole (Green et al. 2016), melt (Holland et al. 2018), garnet (Holland et al. 2018), orthopyroxene (Holland et al. 2018), feldspars (Holland and Powell 2003). The numerically computed phase diagram is presented in Figure 7.6.a-c. In the computed P-T pseudosection, the primary granulitic assemblage (Grt-Cpx-Pl-Qz-Ttn-Rt) coexists with a melt phase at temperature >800°C between 9-13 kbar (Fig. 7.6.a-b). The intersection of the isopleths of the garnet core (X_{ALM} , X_{PRP} , X_{GRS}) and the plagioclase (X_{AN}) define a narrow P-T domain of 800-900°C and 11-13 kbar (Fig. 7.6.b). Several experimental studies on a range of basaltic compositions showed that dehydration melting of the basic rock produces high pressure assemblage (garnet+clinopyroxene+plagioclase+q) at >800°C between ~10-13 kbar (Rötzler and Romer 2001; Vielzeuf and Schmidt 2001; O’Brien and

Rötzler 2003; Pattison 2003). The presence of abundant garnet-bearing leucosome, presumed to be a melt phase, with the primary granoblastic assemblage and the results of

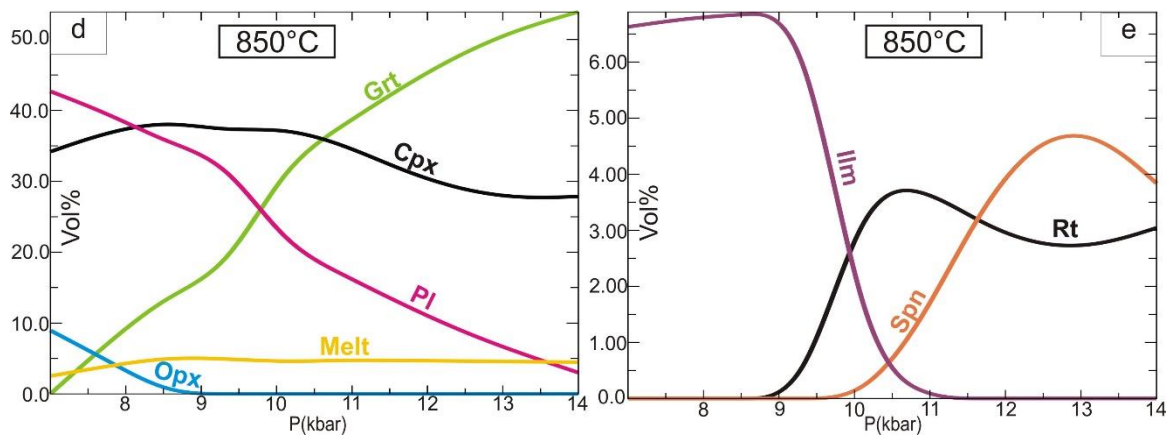


Figure 7.6 (continued): (d) Change in volume proportion of the major phases (Grt, Cpx, Opx, melt, Pl) and (e) Change in the volume proportions of the Ti-bearing phases (Ilm, Spn, Rt) during a pressure drop of 13 to 7 kbar at 850°C, i.e. along the estimated P-T path, is shown.

the melting experiment on mafic protolith corroborates the P-T values calculated of 800–900°C and 11–13 kbar from the isopleths intersection method. The computed P-T pseudosection has a small P-T field (7–9 kbar and ~750–800°C) in which the symplectic intergrowth of Ilm+Cpx₂(±Opx) and the plagioclase rind is stable with garnet. The isopleths of garnet rim (X_{ALM} , X_{PRP} , X_{GRS}) and the symplectic plagioclase (Pl_2 ; X_{AN}) converge within this field at ~7.5–8 kbar and 750–780°C (Fig. 7.6.b).

References:

- Ague, J.J. (2011) Extreme channelization of fluid and the problem of element mobility during Barrovian metamorphism. *American Mineralogist*, 96, 333–352.
- Antignano, A., and Manning, C.E. (2008) Rutile solubility in H₂O, H₂O–SiO₂, and H₂O–NaAlSi₃O₈ fluids at 0.7–2.0 GPa and 700–1000 °C: Implications for mobility of nominally insoluble elements. *Chemical Geology*, 255, 283–293.
- Ashchepkov, I. V., Alymova, N. V., Logvinova, A.M., Vladykin, N. V., Kuligin, S.S., Mityukhin, S.I., Downes, H., Stegnitsky, Y.B., Prokopiev, S.A., Salikhov, R.F., and others (2014) Picroilmnites in Yakutian kimberlites: Variations and genetic models. *Solid Earth*, 5, 915–938.
- Caddick, M.J., Konopásek, J., and Thompson, A.B. (2010) Preservation of garnet growth zoning and the duration of prograde metamorphism. *Journal of Petrology*, 51, 2327–2347.

- Carlson[†], W.D., and Schwarze, E. (1997) Petrological significance of prograde homogenization of growth zoning in garnet: an example from the Llano Uplift. *Journal of Metamorphic Geology*, 15, 631–644.
- Chakraborty, S. (2008) Diffusion in solid silicates: A tool to track timescales of processes comes of age. *Annual Review of Earth and Planetary Sciences*, 36, 153–190.
- Chakraborty, S., and Ganguly, J. (1991) Compositional Zoning and Cation Diffusion in Garnets. In J Ganguly, Ed., *Diffusion, Atomic Ordering, and Mass Transport: Selected Topics in Geochemistry* pp. 120–175. Springer US, New York, NY.
- CHEN, N., Sun, M., YOU, Z., and Malpas, J. (1998) Well-preserved garnet growth zoning in granulite from the Dabie Mountains, central China. *Journal of Metamorphic Geology*, 16, 213–222.
- Chowdhury, P., Talukdar, M., Sengupta, P., Sanyal, S., and Mukhopadhyay, D. (2013) Controls of P-T path and element mobility on the formation of corundum pseudomorphs in Paleoproterozoic high-pressure anorthosite from Sittampundi, Tamil Nadu, India. *American Mineralogist*, 98, 1725–1737.
- Connolly, J.A.D. (2005) Computation of phase equilibria by linear programming: A tool for geodynamic modeling and its application to subduction zone decarbonation. *Earth and Planetary Science Letters*, 236, 524–541.
- (2009) The geodynamic equation of state: What and how. *Geochemistry, Geophysics, Geosystems*, 10.
- Dawson, J.B., and Reid, A.M. (1970) A pyroxene-ilmenite intergrowth from the Monastery Mine, South Africa. *Contributions to Mineralogy and Petrology*, 26, 296–301.
- Dempster, T.J., Coleman, S., Kennedy, R., Chung, P., and Brown, R.W. (2020) Growth zoning of garnet porphyroblasts: Grain boundary and microtopographic controls. *Journal of Metamorphic Geology*, 38, 1011–1027.
- Droop, G.T.R. (1987) A general equation for estimating Fe 3+ concentrations in ferromagnesian silicates and oxides from microprobe analyses, using stoichiometric criteria. *Mineralogical Magazine*, 51, 431–435.
- Eckert, J.O., Newton, R.C., and Kleppa, O.J. (1991) The ΔH of reaction and recalibration of garnet-pyroxene-plagioclase-quartz geobarometers in the CMAS system by solution calorimetry. *American Mineralogist*, 76, 148–160.
- Ellis, D.J., and Green, D.H. (1979) An experimental study of the effect of Ca upon garnet-clinopyroxene Fe-Mg exchange equilibria. *Contributions to Mineralogy and Petrology*, 71, 13–22.
- Evans, T.P. (2004) A method for calculating effective bulk composition modification due to crystal fractionation in garnet-bearing schist: Implications for isopleth thermobarometry. *Journal of Metamorphic Geology*, 22, 547–557.
- Faryad, S.W., Perraki, M., and Vrána, S. (2006) P-T evolution and reaction textures in retrogressed eclogites from Svetlik, the Moldanubian Zone (Czech Republic). *Mineralogy and Petrology*, 88, 297–319.

- Fisher, G.W. (1989) Matrix analysis of metamorphic mineral assemblages and reactions. *Contributions to Mineralogy and Petrology*, 102, 69–77.
- Ganguly, J., Cheng, W., and Chakraborty, S. (1998) Cation diffusion in aluminosilicate garnets: Experimental determination in pyrope-almandine diffusion couples. *Contributions to Mineralogy and Petrology*, 131, 171–180.
- Garrison, J.R., and Taylor, L.A. (1981) Petrogenesis of pyroxene-oxide intergrowths from kimberlite and cumulate rocks: co-precipitation or exsolution? *American Mineralogist*, 66, 723–740.
- Green, E.C.R., White, R.W., Diener, J.F.A., Powell, R., Holland, T.J.B., and Palin, R.M. (2016) Activity–composition relations for the calculation of partial melting equilibria in metabasic rocks. *Journal of Metamorphic Geology*, 34, 845–869.
- Harte, B., and Henley, K.J. (1966) Occurrence of compositionally zoned almanditic garnets in regionally metamorphosed. *Nature*, 210, 689–692.
- Hayden, L.A., and Manning, C.E. (2011) Rutile solubility in supercritical NaAlSi₃O₈-H₂O fluids. *Chemical Geology*, 284, 74–81.
- Holland, T., and Powell, R. (2003) Activity-compositions relations for phases in petrological calculations: An asymmetric multicomponent formulation. *Contributions to Mineralogy and Petrology*, 145, 492–501.
- Holland, T., Green, E.C.R., and Powell, R. (2018) Melting of peridotites through to granites: A simple thermodynamic model in the system KNCFMASHTOCr. *Journal of Petrology*, 59, 881–900.
- Holland, T.J.B., and Powell, R. (2011) An improved and extended internally consistent thermodynamic dataset for phases of petrological interest, involving a new equation of state for solids. *Journal of Metamorphic Geology*, 29, 333–383.
- Hollis, J.A., Harley, S.L., White, R.W., and Clarke, G.L. (2006) Preservation of evidence for prograde metamorphism in ultrahigh-temperature, high-pressure kyanite-bearing granulites, South Harris, Scotland. *Journal of Metamorphic Geology*, 24, 263–279.
- Hollister, L.S. (1966) Garnet Zoning: An Interpretation Based on the Rayleigh Fractionation Model. *Science*, 154, 1647–1651.
- Ikeda, T. (1993) Compositional zoning patterns of garnet during prograde metamorphism from the Yanai district, Ryoke metamorphic belt, southwest Japan. *Lithos*, 30, 109–121.
- Karmakar, S. (2021) Formation of clinohumite ± spinel in dolomitic marbles from the Makrohar Granulite Belt, Central India: Evidence of Ti mobility during metamorphism. *American Mineralogist*, 106, 1818–1827.
- Karmakar, S., Mukherjee, S., Sanyal, S., and Sengupta, P. (2017) Origin of peraluminous minerals (corundum, spinel, and sapphirine) in a highly calcic anorthosite from the Sittampundi Layered Complex, Tamil Nadu, India. *Contributions to Mineralogy and Petrology*, 172, 67.
- Kelsey, D.E., and Hand, M. (2015) On ultrahigh temperature crustal metamorphism: Phase

- equilibria, trace element thermometry, bulk composition, heat sources, timescales and tectonic settings. *Geoscience Frontiers*, 6, 311–356.
- Kohn, M.J. (2014) *Geochemical Zoning in Metamorphic Minerals. Treatise on Geochemistry: Second Edition*, 4, 249–280.
- Lanari, P., Vidal, O., De Andrade, V., Dubacq, B., Lewin, E., Grosch, E.G., and Schwartz, S. (2014) XMapTools: A MATLAB©-based program for electron microprobe X-ray image processing and geothermobarometry. *Computers and Geosciences*, 62, 227–240.
- Lanari, P., Vho, A., Bovay, T., Airaghi, L., and Centrella, S. (2019) Quantitative compositional mapping of mineral phases by electron probe micro-analyser. *Geological Society Special Publication*, 478, 39–63.
- Lang, H.M., and Rice, J.M. (1985) Regression modelling of metamorphic reactions in metapelites, snow peak, Northern Idaho. *Journal of Petrology*, 26, 857–887.
- Lang, H.M., Watcher, A.J., Peterson, V.L., and Ryan, J.G. (2004) Coexisting clinopyroxene/spinel and amphibole/spinel symplectites in metatroctolites from the Buck Creek ultramafic body, North Carolina Blue Ridge. *American Mineralogist*, 89, 20–30.
- Litasov, K.D., Malkovets, V.G., Kostrovitsky, S.I., and Taylor, L.A. (2003) Petrogenesis of ilmenite-bearing symplectite xenoliths from vitim alkaline basalts and yakutian kimberlites, Russia. *International Geology Review*, 45, 976–997.
- Lopez Ruiz, J. (1976) The Zoning of Garnets As an Indicator of the P.T. history of their host-rocks. *Annales de la Société Géologique de Belgique*, 99, 337–346.
- Marsh, J.H., and Kelly, E.D. (2017) Petrogenetic relations among titanium-rich minerals in an anatectic high-P mafic granulite. *Journal of Metamorphic Geology*, 35, 717–738.
- Morimoto, N. (1988) Nomenclature of pyroxenes: subcommittee on pyroxenes Commission on New Minerals and Mineral Names (CNMMN) International Mineral Association (IMA). *Schweizerische Mineralogische und Petrographische Mitteilungen*, 68, 95–111.
- Nixon, P.H., and Boyd, F.R. (1979) Garnet bearing lherzolites and discrete nodule suites from the Malaita Alnoite, Solomon Islands, S.W. Pacific, and their bearing on oceanic mantle composition and geotherm. *The Mantle Sample: Inclusion in Kimberlites and Other Volcanics*, 16, 400–423.
- Nyström, A.I., and Kriegsman, L.M. (2003) Prograde and retrograde reactions, garnet zoning patterns, and accessory phase behaviour in SW Finland migmatites, with implications for geochronology. *Geological Society Special Publication*, 220, 213–230.
- O'Brien, P.J., and Rötzler, J. (2003) High-pressure granulites: Formation, recovery of peak conditions and implications for tectonics. *Journal of Metamorphic Geology*, 21, 3–20.
- Palin, R.M., Weller, O.M., Waters, D.J., and Dyck, B. (2016) Quantifying geological uncertainty in metamorphic phase equilibria modelling ; a Monte Carlo assessment and implications for tectonic interpretations. *Geoscience Frontiers*, 7, 591–607.

- Pattison, D.R.M. (2003) Petrogenetic significance of orthopyroxene-free garnet + clinopyroxene + plagioclase \pm quartz-bearing metabasites with respect to the amphibolite and granulite facies. *Journal of Metamorphic Geology*, 21, 21–34.
- Purtov, V.K., and Kotel'nikova, A.L. (1993) Solubility of titanium in chloride and fluoride hydrothermal solutions. *International Geology Review*, 35, 279–287.
- Rapp, J.F., Klemme, S., Butler, I.B., and Harley, S.L. (2010) Extremely high solubility of rutile in chloride and fluoride-bearing metamorphic fluids: An experimental investigation. *Geology*, 38, 323–326.
- Ringwood, A.E., and Lovering, J.F. (1970) Significance of pyroxene-ilmenite intergrowth among kimberlite xenoliths. *Earth and Planetary Science Letters*, 7, 371–375.
- Rötzler, J., and Romer, R.L. (2001) P-T-t evolution of ultrahigh-temperature granulites from the Saxon Granulite Massif, Germany. Part I: Petrology. *Journal of Petrology*, 42, 1995–2013.
- Ryzhenko, B.N., Kovalenko, N.I., and Prisyagina, N.I. (2006) Titanium complexation in hydrothermal systems. *Geochemistry International*, 44, 879–895.
- Saxena, S., and Ganguly, J. (1987) Mixtures and mineral reactions.
- Sengupta, P., and Dasgupta, S. (2009) Modelling of Metamorphic Textures with C-Space: Evidence of Pan-African High-grade Reworking in the Eastern Ghats Belt, India. In *Physics and Chemistry of the Earth's Interior* pp. 29–39.
- Sengupta, P., Raith, M.M., and Levitsky, V.I. (2004) Compositional characteristics and paragenetic relations of magnesiohögbohmite in aluminous amphibolites from the Belomorian complex, Baltic Shield, Russia. *American Mineralogist*, 89, 819–831.
- Sengupta, P., Dutta, U., Bhui, U.K., and Mukhopadhyay, D. (2009) Genesis of wollastonite- and grandite-rich skarns in a suite of marble-calc-silicate rocks from Sittampundi, Tamil Nadu: Constraints on the P-T-fluid regime in parts of the Pan-African mobile belt of South India. *Mineralogy and Petrology*, 95, 179–200.
- Spear, F.S. (1993) *Metamorphic Phase Equilibria and Pressure-temperature-time Paths*. Mineralogical Society of America.
- Tanis, E.A., Simon, A., Zhang, Y., Chow, P., Xiao, Y., Hanchar, J.M., Tschauner, O., and Shen, G. (2016) Rutile solubility in NaF-NaCl-KCl-bearing aqueous fluids at 0.5-2.79 GPa and 250-650 °C. *Geochimica et Cosmochimica Acta*, 177, 170–181.
- Torres-Roldan, R.L., Garcia-Casco, A., and Garcia-Sanchez, P.A. (2000) CSpace: An integrated workplace for the graphical and algebraic analysis of phase assemblages on 32-bit wintel platforms. *Computers and Geosciences*, 26, 779–793.
- Tuccillo, M.E., Essene, E.J., and Van Der Pluijm, B.A. (1990) Growth and retrograde zoning in garnets from high-grade metapelites: implications for pressure-temperature paths. *Geology*, 18, 839–842.
- Vielzeuf, D., and Schmidt, M.W. (2001) Melting relations in hydrous systems revisited: Application to metapelites, metagreywackes and metabasalts. *Contributions to Mineralogy and Petrology*, 141, 251–267.

- Whitney, D.L., and Evans, B.W. (2010) Abbreviations for Names of Rock-Forming Minerals. *American Mineralogist*, 95, 185–187.
- Zhang, R.Y., Zhai, S.M., Fei, Y.W., and Liou, J.G. (2003) Titanium solubility in coexisting garnet and clinopyroxene at very high pressure: The significance of exsolved rutile in garnet. *Earth and Planetary Science Letters*, 216, 591–601.

Chapter 8

Metamorphic evolution of the metamafic dykes

The emplacement of metamafic dykes and their metamorphism indicates a probable shift in tectonic conditions (Sengupta 1993; Bleeker and Ernst 2006; Bhui et al. 2007). Thus the study of metamafic dykes is often essential to understand the crustal evolution of the study area. Metamafic dykes in the study area are present as intrusive bodies in the porphyritic charnockite. These metamafic dykes are deformed and metamorphosed. In the current study, detailed petrography, phase chemistry and phase equilibria modelling are done to comprehend the metamorphic evolution of the metamafic dykes. The mineral name abbreviations used are after (Whitney and Evans 2010)

8.1 Petrography:

The studied rock is fine-grained, comprising a mineral assemblage of amphibole, plagioclase, quartz, garnet and pyroxenes (both ortho- and clino-). The major minerals that constitute the metamafic dyke include plagioclase (~35%), amphibole (~25%), clinopyroxene (~15%), orthopyroxene (~10%), garnet (~5%) and quartz (~5%). Apart from these, ilmenite (~3%), magnetite (~2%), and apatite (<1%) are present as accessory phases. The fine-grained matrix of metamafic dyke comprising pyroxene, plagioclase and amphibole exhibits prominent grain orientation (Fig. 4.1.a). The elongated and oriented pyroxene and amphibole primarily define the grain orientation. Apart from grain orientation, the metamafic dyke demonstrates crude banding of alternate plagioclase-rich and pyroxene-amphibole rich layers (Fig. 4.1.a-c). Though clinopyroxene, orthopyroxene

and amphibole predominantly govern the ferromagnesian phases of the metamafic dyke, their abundances vary significantly. Though overall, amphibole abundance is higher,

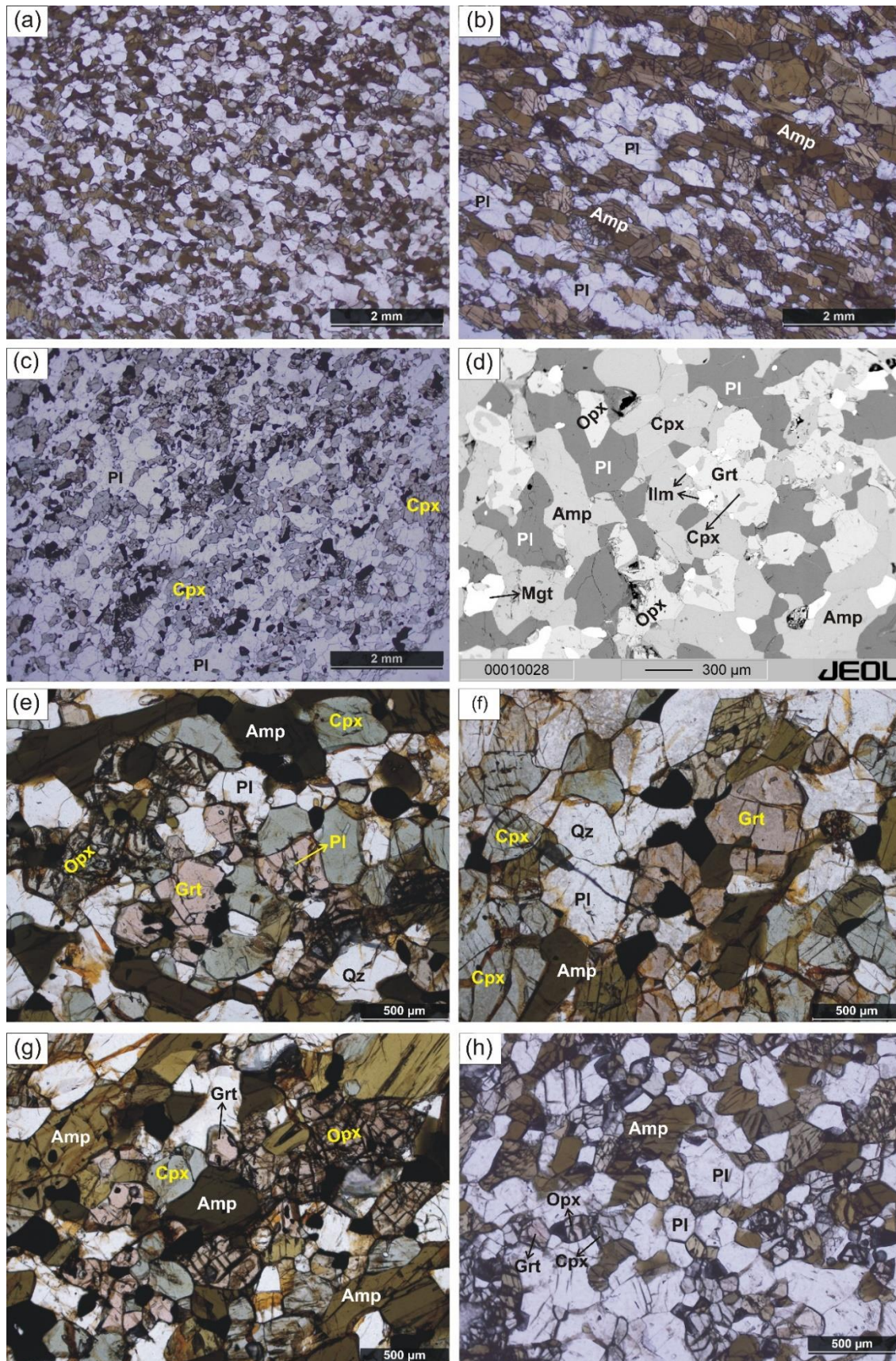


Figure 8.1 (a) Fine-grained rock comprises a mineral assemblage of amphibole, plagioclase, quartz, garnet, and pyroxenes. Phases exhibit prominent grain orientation. (b) Amp is dominant over Cpx and Opx. Pl and Amp form alternate bands, and grains are oriented. (c) Pyroxene is dominant in this domain and Amp almost absent. Pyroxene crystals are deformed and oriented. (d) Garnet contains Cpx inclusions. Ilm and Mgt are present in the rock matrix. (e) Garnet shares a non-reactive straight boundary with Cpx. Grt contains Pl inclusion. (f) Garnet shares a similar straight boundary with Amp, but Amp is replacing Cpx. (g) Cpx, Pl, and Amp in a fine-grained matrix share a 120° dihedral angle contact. (h) Amp is replacing the Pl in the rock matrix.

in some locales, pyroxene dominates over amphibole (Fig. 4.1.c), while in other places, pyroxene is almost absent (Fig. 4.1.b).

Small garnet grains with pyroxene and amphibole are present in the rock matrix (Fig. 4.1.d-g). In a few instances, Garnet contains inclusions of clinopyroxene and plagioclase (Fig. 4.1.d-e). Amphibole replaces pyroxenes along the grain boundary, often resulting in complete replacement (Fig. 4.1.e-h). Amphibole is present in the rock matrix around plagioclase by rimming them partially to completely (Fig. 4.1.b, h). Ilmenite and magnetite are often associated with the pyroxenes and often exhibit relict interlocking texture (Fig. 4.1.d). In the recrystallised matrix, garnet often forms straight boundary with amphibole and pyroxene (Fig. 4.1.e-g).

8.2 Phase chemistry:

At the University of Cologne in Germany, the chemical compositions of the minerals were ascertained using a JEOL EPMA JAX 8900RL electron microprobe. The setup for the instrument was 2 µm beam diameter, 15 nA current, and 15 kV accelerating voltage. Fe³⁺ is estimated using the cation recalculation scheme of Droop (1987). Amphibole cation recalculation is performed using the classification scheme of Leake et al. (1997). Mineral abbreviations are used in phase chemistry, and the following sections are after Whitney and Evans (2010). The salient features of phase compositions are presented in the following section. Representative phase compositions are presented in Table 8.1-8.5.

Garnet:

The almandine component governs the garnet composition (Table 8.1) (**Alm₆₀₋₆₂ Py₁₄₋₁₅ Grs₁₉₋₂₀ Sps₄₋₅**). X_{Mg} ($=Mg/(Mg+Fe^{2+})$) of garnet ranges between 0.19-0.20. Garnet compositional range is fairly restricted and exhibits no core rim compositional variation.

Pyroxene:

Clinopyroxenes are diopsidic in composition (Fig. 8.2.a; Table 8.2), with X_{Mg} varying between **0.61-0.67**. Clinopyroxene inclusions in garnet are slightly more magnesian ($X_{Mg}= 0.61-0.63$) than the matrix clinopyroxene ($X_{Mg}= 0.64-0.67$). Orthopyroxene composition (Table) plots in the field of ferrosilite ($X_{Mg}= 0.48-0.49$) (Fig. 8.2.a). Neither Opx nor Cpx exhibits any core rim compositional variation.

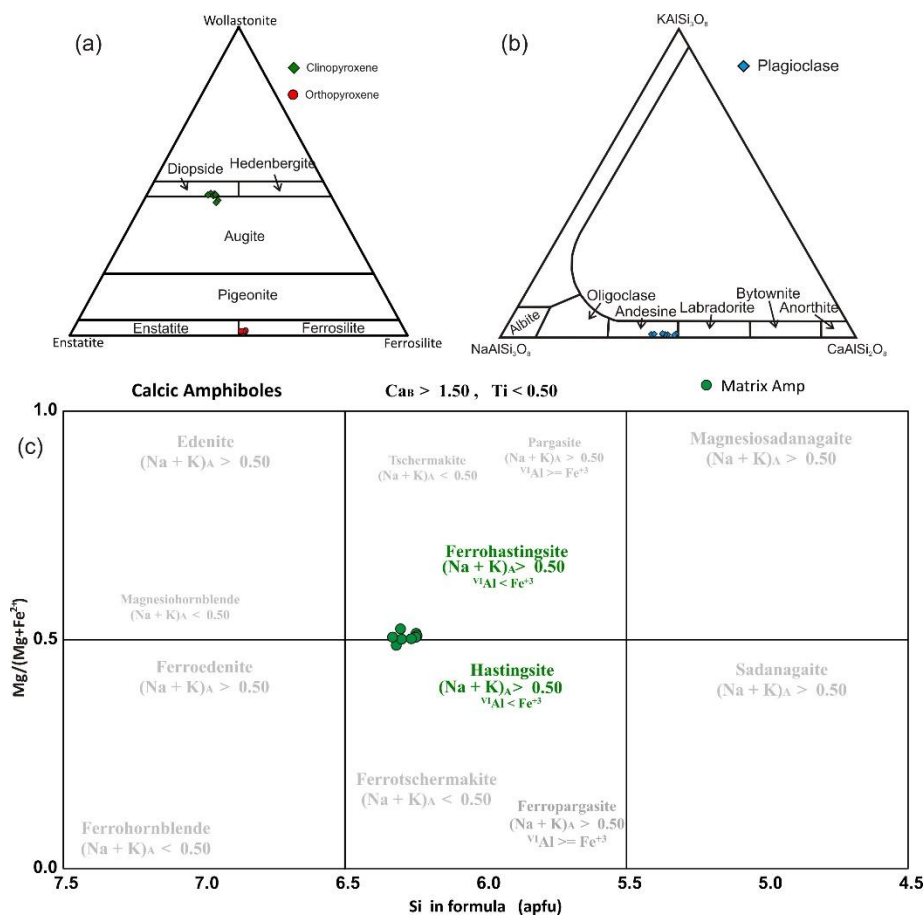


Figure 8.2 (a) The Wo-En-Fs ternary diagram shows that Cpx is diopsidic in composition and Opx composition is in the En-Fs boundary. (b) Pl composition typically plots in the andesine field in the ternary feldspar diagram. (c) According to the classification scheme of Leake et al. (1997), Amp plots are in the Hastingsite and Ferrohastingsite fields.

Table 8.1: Representative microprobe analyses of garnet and cation calculations based on 12 oxygens (oxide data given as wt%)

Point No.	47/1	53/1	54/1	67/1	63/1	70/1	76/1
Texture	core	core	core	rim	rim	rim	rim
SiO ₂	37.54	37.62	37.63	36.98	37.04	37.12	37.17
TiO ₂	0.02	0.03	0.04	0.03	0.05	0.06	0.03
Al ₂ O ₃	20.63	20.93	21.17	20.53	20.44	20.51	20.76
Cr ₂ O ₃	0.03	<d.l.	0.02	0.07	0.02	0.01	0.02
FeO	30.02	30.18	30.31	30.12	30.14	29.80	30.23
MgO	3.73	3.68	3.71	3.65	3.68	3.68	3.78
CaO	7.04	6.81	6.93	7.04	6.85	6.81	6.73
MnO	2.01	1.96	2.09	1.85	1.94	2.04	1.84
Na ₂ O	0.02	0.01	0.01	<d.l.	<d.l.	<d.l.	0.05
K ₂ O	<d.l.	<d.l.	<d.l.	0.02	<d.l.	<d.l.	0.01
Total	101.4	101.5	102.2	100.7	100.5	100.3	101.0
Si	2.95	2.95	2.93	2.93	2.94	2.95	2.93
Ti	0.00	0.00	0.00	0.00	0.00	0.00	0.00
Al	1.91	1.93	1.94	1.91	1.91	1.92	1.93
Cr	0.00	0.00	0.00	0.00	0.00	0.00	0.00
Fe ⁺³	0.18	0.16	0.19	0.21	0.20	0.18	0.22
Fe ⁺²	1.79	1.82	1.78	1.78	1.80	1.80	1.78
Mg	0.44	0.43	0.43	0.43	0.43	0.43	0.44
Ca	0.59	0.57	0.58	0.60	0.58	0.58	0.57
Mn	0.13	0.13	0.14	0.12	0.13	0.14	0.12
Na	0.00	0.00	0.00	0.00	0.00	0.00	0.01
K	0.00	0.00	0.00	0.00	0.00	0.00	0.00
Total	8.00	8.00	8.00	8.00	8.00	8.00	8.00
X _{Alm}	0.61	0.62	0.61	0.61	0.61	0.61	0.61
X _{Py}	0.15	0.15	0.15	0.15	0.15	0.15	0.15
X _{Grs}	0.20	0.19	0.20	0.20	0.20	0.20	0.20
X _{Sps}	0.05	0.04	0.05	0.04	0.04	0.05	0.04
X _{Mg}	0.20	0.19	0.19	0.19	0.19	0.19	0.20

<d.l.: Below detection limit

* Fe³⁺ recalculated according to the scheme of Droop (1987)

Table 8.2: Representative microprobe analyses of pyroxene and cation calculations based on 6 oxygens (oxide data given as wt%)

Phase	Clinopyroxene				Orthopyroxene		
Point No.	48/1	52/1	50/1	99/1	81/1	89/1	97/1
Texture	Incl. in Grt	core	rim	rim	rim	core	rim
SiO ₂	51.92	50.49	51.05	50.17	49.84	49.73	49.37
TiO ₂	0.15	0.22	0.24	0.29	0.06	0.06	0.07
Al ₂ O ₃	1.64	2.29	2.36	2.66	1.01	0.79	1.05
Cr ₂ O ₃	0.03	0.01	0.02	0.03	<d.l.	<d.l.	<d.l.
FeO	13.09	15.12	14.68	14.17	33.09	33.18	33.15
MgO	11.84	11.46	11.35	10.99	15.97	15.80	15.84
CaO	21.57	19.55	20.20	20.55	0.63	0.61	0.63
MnO	0.32	0.35	0.30	0.35	0.71	0.76	0.83
Na ₂ O	0.44	0.48	0.41	0.51	0.01	<d.l.	0.04
K ₂ O	0.01	<d.l.	<d.l.	0.02	<d.l.	<d.l.	0.01
Total	101.08	100.03	100.61	99.72	101.33	100.92	101.00
Si	1.94	1.92	1.93	1.91	1.92	1.93	1.91
Ti	0.00	0.01	0.01	0.01	0.00	0.00	0.00
Al	0.07	0.10	0.10	0.12	0.05	0.04	0.05
Cr	0.00	0.00	0.00	0.00	0.00	0.00	0.00
Fe ⁺³	0.06	0.08	0.06	0.08	0.11	0.11	0.13
Fe ⁺²	0.35	0.40	0.41	0.37	0.95	0.97	0.94
Mg	0.66	0.65	0.64	0.62	0.92	0.91	0.91
Ca	0.86	0.80	0.82	0.84	0.03	0.03	0.03
Mn	0.01	0.01	0.01	0.01	0.02	0.02	0.03
Na	0.03	0.04	0.03	0.04	0.00	0.00	0.00
K	0.00	0.00	0.00	0.00	0.00	0.00	0.00
Total	4.00	4.00	4.00	4.00	4.00	4.00	4.00
X _{Mg}	0.65	0.62	0.61	0.63	0.49	0.49	0.49

<d.l.: Below detection limit

* Fe³⁺ recalculated according to the scheme of Droop (1987)

Table 8.3: Representative microprobe analyses of plagioclase and cation calculations based on 8 oxygens (oxide data given as wt%)

Point No.	56/1	66/1	75/1	80/1	82/1	93/1	100/1
Texture	core	rim	core	rim	core	rim	rim
SiO ₂	55.06	55.55	55.63	55.34	56.05	54.73	55.67
TiO ₂	0.01	0.01	<d.l.	0.02	0.02	0.02	0.03
Al ₂ O ₃	27.45	27.11	27.22	26.91	26.76	27.39	26.65
Cr ₂ O ₃	0.04	<d.l.	<d.l.	0.01	<d.l.	0.01	<d.l.
FeO	0.25	0.11	0.20	0.13	0.08	0.31	0.15
MgO	<d.l.	<d.l.	0.01	0.05	<d.l.	0.03	0.00
CaO	9.80	9.53	9.58	9.35	8.82	9.93	9.04
MnO	<d.l.	<d.l.	<d.l.	0.01	0.06	<d.l.	<d.l.
Na ₂ O	6.01	6.01	6.22	6.07	6.45	5.69	6.40
K ₂ O	0.09	0.10	0.12	0.15	0.11	0.07	0.12
Total	98.71	98.42	99.00	98.04	98.39	98.20	98.06
Si	2.51	2.54	2.53	2.54	2.56	2.51	2.55
Ti	0.00	0.00	0.00	0.00	0.00	0.00	0.00
Al	1.48	1.46	1.46	1.45	1.44	1.48	1.44
Cr	0.00	0.00	0.00	0.00	0.00	0.00	0.00
Fe ⁺²	0.01	0.00	0.01	0.00	0.00	0.01	0.01
Mg	0.00	0.00	0.00	0.00	0.00	0.00	0.00
Ca	0.48	0.47	0.47	0.46	0.43	0.49	0.44
Mn	0.00	0.00	0.00	0.00	0.00	0.00	0.00
Na	0.53	0.53	0.55	0.54	0.57	0.51	0.57
K	0.01	0.01	0.01	0.01	0.01	0.00	0.01
Total	5.02	5.00	5.02	5.01	5.01	5.00	5.02
X _{An}	0.47	0.46	0.46	0.46	0.43	0.49	0.44
X _{Ab}	0.52	0.53	0.54	0.54	0.57	0.51	0.56
X _{Or}	0.01	0.01	0.01	0.01	0.01	0.00	0.01

<d.l.: Below detection limit

Table 8.4: Representative microprobe analyses of amphibole and cation calculations based (after Leake et al., 1997) on 23 oxygens (oxide data given as wt%)

Point No.	60/1	65/1	71/1	78/1	84/1	86/1	95/1
Texture	core	core	core	core	rim	rim	rim
SiO ₂	42.26	42.71	42.48	41.90	42.32	41.94	42.21
TiO ₂	2.02	1.94	1.97	2.05	1.86	2.01	2.07
Al ₂ O ₃	11.51	11.73	11.51	11.74	11.31	11.81	11.80
Cr ₂ O ₃	0.06	0.01	0.05	0.02	0.04	0.00	0.04
FeO	20.06	19.59	20.14	20.11	19.92	20.33	20.18
MgO	8.99	9.73	9.34	9.25	9.28	9.17	9.32
CaO	10.88	10.85	11.03	10.84	10.84	10.81	10.92
MnO	0.20	0.13	0.17	0.17	0.19	0.19	0.22
Na ₂ O	2.06	2.15	2.26	1.91	2.05	2.02	2.24
K ₂ O	0.81	0.74	0.61	0.79	0.71	0.71	0.72
F	0.00	0.00	0.00	0.00	0.00	0.00	0.00
Cl	0.05	0.04	0.04	0.05	0.05	0.05	0.04
Total	98.89	99.63	99.58	98.82	98.57	99.02	99.77
Si	6.32	6.30	6.30	6.25	6.33	6.24	6.25
Al (IV)	1.68	1.70	1.70	1.75	1.67	1.76	1.75
Ti	0.00	0.00	0.00	0.00	0.00	0.00	0.00
Sum T	8.00	8.00	8.00	8.00	8.00	8.00	8.00
Al (VI)	0.35	0.34	0.31	0.31	0.32	0.32	0.31
Ti	0.23	0.22	0.22	0.23	0.21	0.22	0.23
Cr ⁺³	0.01	0.00	0.01	0.00	0.00	0.00	0.00
Fe ⁺³	0.41	0.47	0.45	0.57	0.47	0.57	0.49
Mg	2.00	2.14	2.06	2.05	2.07	2.03	2.06
Fe ⁺²	2.01	1.83	1.96	1.84	1.92	1.86	1.92
Mn	0.00	0.00	0.00	0.00	0.00	0.00	0.00
Li	0.00	0.00	0.00	0.00	0.00	0.00	0.00
Sum C	5.00	5.00	5.00	5.00	5.00	5.00	5.00
Mg	0.00	0.00	0.00	0.00	0.00	0.00	0.00
Fe ⁺²	0.09	0.12	0.10	0.10	0.10	0.11	0.10
Mn	0.03	0.02	0.02	0.02	0.02	0.02	0.03
Li	0.00	0.00	0.00	0.00	0.00	0.00	0.00
Ca	1.74	1.72	1.75	1.73	1.74	1.72	1.73
Na	0.14	0.15	0.13	0.14	0.14	0.15	0.14
Sum B	2.00	2.00	2.00	2.00	2.00	2.00	2.00
Ca	0.00	0.00	0.00	0.00	0.00	0.00	0.00
Na	0.46	0.46	0.52	0.41	0.46	0.44	0.50
K	0.15	0.14	0.11	0.15	0.14	0.14	0.14
Sum A	0.61	0.60	0.63	0.56	0.59	0.57	0.64
Total	15.61	15.60	15.63	15.56	15.59	15.57	15.64

Table 8.5: Representative microprobe analyses of ilmenite, magnetite and apatite; cation calculations based on 3, 4, and 13 oxygens (oxide data given as wt%)

Phase	Ilm		Mgt			Ap	
Point No.	68/1	72/1	62/1	91/1		61/1	92/1
SiO ₂	0	0	0.06	0.08	SiO ₂	0.106	0.074
TiO ₂	49.69	49.71	0.16	0.19	TiO ₂	0.011	0.003
Al ₂ O ₃	0.03	0.00	0.30	0.57	Al ₂ O ₃	0.004	0.011
Cr ₂ O ₃	0.02	0.01	0.09	0.12	Cr ₂ O ₃	0	0.036
FeO	50.23	49.78	95.83	93.37	FeO	0.238	0.291
MgO	0.65	0.45	0.00	0.01	MgO	0.013	0.013
CaO	0.01	0.02	0.08	0.00	CaO	54.266	53.321
MnO	0.43	0.55	0.05	0.00	MnO	0	0.026
Na ₂ O	0.00	0.00	0.07	0.00	Na ₂ O	0	0.025
K ₂ O	0.03	0.01	0.00	0.01	K ₂ O	0	0.001
Total	101.15	100.52	96.64	94.34	P ₂ O ₅	39.855	39.925
Si	0.00	0.00	0.00	0.00	F	1.294	1.21
Ti	0.92	0.93	0.00	0.01	Cl	0.162	0.15
Al	0.00	0.00	0.00	0.00	Total	95.367	94.543
Cr	0.00	0.00	0.01	0.03	O=F	0.54	0.51
Fe ⁺³	0.15	0.14	1.98	1.95	O=Cl	0.04	0.03
Fe ⁺²	0.89	0.90	0.99	1.01	Revised SUM	95.37	94.54
Mg	0.02	0.02	0.00	0.00	Si	0.01	0.01
Ca	0.00	0.00	0.00	0.00	Ti	0.00	0.00
Mn	0.01	0.01	0.00	0.00	Al	0.00	0.00
Na	0.00	0.00	0.00	0.00	Cr	0.00	0.00
K	0.00	0.00	0.00	0.00	Fe ⁺²	0.02	0.02
Total	2.00	2.00	3.00	3.00	Mg	0.00	0.00
					Mn	0.00	0.00
					Ca	4.81	4.76
					Na	0.00	0.00
					K	0.00	0.00
					P	2.79	2.81
					F	0.34	0.32
					Cl	0.02	0.02
					SUM	7.99	7.95
					OH	1.64	1.66
<d.l.: Below detection limit					Rev. Sum	9.63	9.61

<d.l.: Below detection limit

* Fe³⁺ recalculated according to the scheme of Droop (1987)

Plagioclase:

Albite and anorthite end members dominate the plagioclase composition (Table 8.3) with negligible orthoclase component (<1%). In the ternary feldspar diagram, plagioclase composition (**An₄₃₋₄₉ Ab₅₀₋₅₇ Or_{<1}**) plots in the field of andesine near the andesine-labradorite boundary (Fig. 8.2.b). Plagioclase does not show any core rim compositional variation. Though the overall compositional range is minimal, the plagioclase adjacent to garnet and amphibole tends to be slightly more anorthitic than the plagioclase near pyroxene.

Amphibole:

In the studied metamafic dyke, amphiboles do not show any compositional variation. According to the classification scheme of Leake et al. (1997), amphibole composition (Table 8.4) is calcic and straddles the boundary between hastingsite and magnesio hastingsite (**X_{Mg} = 0.49-0.52**) (Fig. 8.2.c). Amphibole has a TiO₂ content between 1.86 – 2.07 wt%.

Accessory phase:

Ilmenite and apatite are in the rock matrix (Table 8.5). MnO content in ilmenite is negligible (<1wt%). F and Cl are present in apatite, but F content (1.21-1.29 wt%) is higher than Cl (0.15-0.16 wt%).

8.3 Mineral evolution during metamorphism:

The detailed petrographic study combined with texture-coordinated phase composition is crucial in understanding the metamorphic evolution of the metamafic dyke. Due to intense metamorphism and deformation, preservation of prior mineral assemblage is poor. It is evident from the lack of compositional variability apart from some inclusion phases. Pyroxene and plagioclase inclusions within garnet exhibit slight compositional variation, giving a glimpse of the protolith. The slight compositional variation between matrix and inclusion Cpx demonstrates two possibilities: (a) these Cpx formed along the prograde metamorphic part, or (b) these Cpx originate during the magmatic crystallisation history. The association of Ilm, Mgt with the pyroxene grains (exhibiting relict interlocking texture) suggest a probable igneous protolith assemblage of Cpx-Opx-Pl-Ilm-Mgt.

Nevertheless, the inclusion of Cpx and Pl can act as crucial reactant phases in garnet formation (Eckert et al. 1991), and pressure increase primarily governs such garnet formation during metamorphism (Eckert et al. 1991).

Amp is replacing the pyroxenes in the rock matrix, but it does not share any similar relation with Grt. Amp in the rock matrix rims and replaces Pl, which acts as the primary source of Al in Amp formation. An increase in amphibole abundance is associated with a decrease in pyroxene content. It indicates that amphibole is primarily replacing pyroxene. Significant variation in Amp abundance within a few centimetres shows probable fluid (primarily H₂O) availability variability during metamorphism. In a few locales, lack of hydration resulted in the complete absence of amphibole. So, fluid presence determines the relative proportion between Amp and Cpx-Opx in forming peak metamorphic assemblage.

Grt is associated with Opx, Cpx and Amp in the fine-grained, deformed and metamorphosed rock. Garnet exhibits a straight boundary with amphibole and pyroxene in the recrystallised fine-grained rock matrix, demonstrating equilibrium phase assemblage. So, Grt and Amp form in the rock during deformation and metamorphism, and the relict igneous assemblage is also reequilibrating to the changing physical conditions of metamorphism. Thus, the petrographic study suggests that the assemblage of Grt+Cpx+Opx+Amp+Ilm+Qz comprises the peak metamorphic mineral assemblage. Formation of Garnet and amphibole during metamorphism constrains a metamorphic facies of amphibolite granulite transition.

8.4 Physical condition of metamorphism:

Estimation of physical conditions of metamorphism is crucial in understanding a metamorphic event. P-T condition of metamorphism of the studied rock is constrained by compositional and textural attributes of various phases in the metamafic dyke. Conventional thermobarometry and phase equilibria modelling methods are used to constrain the physical conditions of metamorphism.

8.4.1 Conventional thermobarometry:

Considering the metamorphic assemblage that developed in the studied rock, a number of thermobarometers are used to estimate the P-T parameters. Details of P-T estimations from various thermobarometers are provided in Table 8.6.

Garnet-clinopyroxene (GC) (Ellis and Green 1979) and garnet-orthopyroxene (GO) (Bhattacharya et al. 1991) ion exchange thermometers yield a temperature range of 650-700 °C and 675-700°C respectively. Garnet-clinopyroxene-plagioclase-quartz (GCPQ) (Eckert et al. 1991) and garnet-orthopyroxene-plagioclase-quartz (GOPQ) (Bhattacharya et al. 1991) barometers estimate a pressure range of 6.5-7 kbar and 6.5-6.7 kbar respectively.

Table 8.6: P-T estimates through conventional thermobarometric calculations

Assemblage		Thermometry			Barometry	
		P (kbar, ref)	T (°C)		T (°C, ref)	P (kbar)
Grt-Cpx-Pl-Qz	GC	7	650-700	GCPQ	700	6.5-7
Grt-Opx-Pl-Qz	GO	7	675-700	GOPS	700	6.5-6.7
Grt-Amp-Pl-Qz	GA	600-650		GAPQ		6.6-6.8
				Al in Amp1		6.7 ± 0.13
				Al in Amp2		6.4 ± 0.15

GC: Garnet – clinopyroxene geothermometer (Ellis and Green, 1979).

GCPQ: Garnet – clinopyroxene – plagioclase – quartz barometer (Eckert et al., 1991).

GO: Garnet - orthopyroxene geothermometer (Bhattacharya et al., 1991).

GOPS: Garnet - orthopyroxene - plagioclase - quartz barometer (Eckert et al., 1991).

GA: Garnet - Amphibole thermometer (Graham and Powell, 1984).

GAPQ: Garnet - orthopyroxene - plagioclase - quartz barometer (Kohn and Spear, 1991).

Al in Amp1: Al in amphibole barometer (Schmidt, 1992)

Al in Amp2: Al in amphibole barometer (Hammarstrom and Zen, 1986)

Al in amphibole barometer yields an average pressure estimate of 6.7 ± 0.13 kbar (Schmidt 1992) and 6.4 ± 0.15 kbar (Hammarstrom and Zen 1986). Pressure from Al in Amp barometer is identical to the pressure estimates from GCPQ and GOPQ barometers. Al in amphibole barometer has an uncertainty of ± 2 (Hammarstrom and Zen 1986). Similarly, the garnet-amphibole-plagioclase-quartz (GAPQ) barometer (Kohn and Spear 1991) also estimates an average pressure of 6.8 kbar and this barometer is more robust compared to Al in Amp with an uncertainty of ± 1 (Kohn and Spear 1991). The garnet-amphibole (GA) ion exchange thermometer (Graham and Powell 1984) calibrates a temperature range of 600-650 °C. Though the estimated temperature from the GA thermometer is slightly lower than GC and GO thermometers, it is well within the general uncertainty limits of ± 50 °C.

8.4.2 Phase equilibria modelling:

Phase equilibria modelling is an essential tool in understanding the formation of metamorphic mineral assemblage in the studied metamafic dykes. In NCKFMASHT ($\text{Na}_2\text{O}-\text{K}_2\text{O}-\text{CaO}-\text{FeO}-\text{MgO}-\text{Al}_2\text{O}_3-\text{SiO}_2-\text{H}_2\text{O}-\text{TiO}_2$) components system, numerically simulated phase equilibria modelling (pseudosection) of the studied metamafic dyke is calculated (Fig. 8.3).

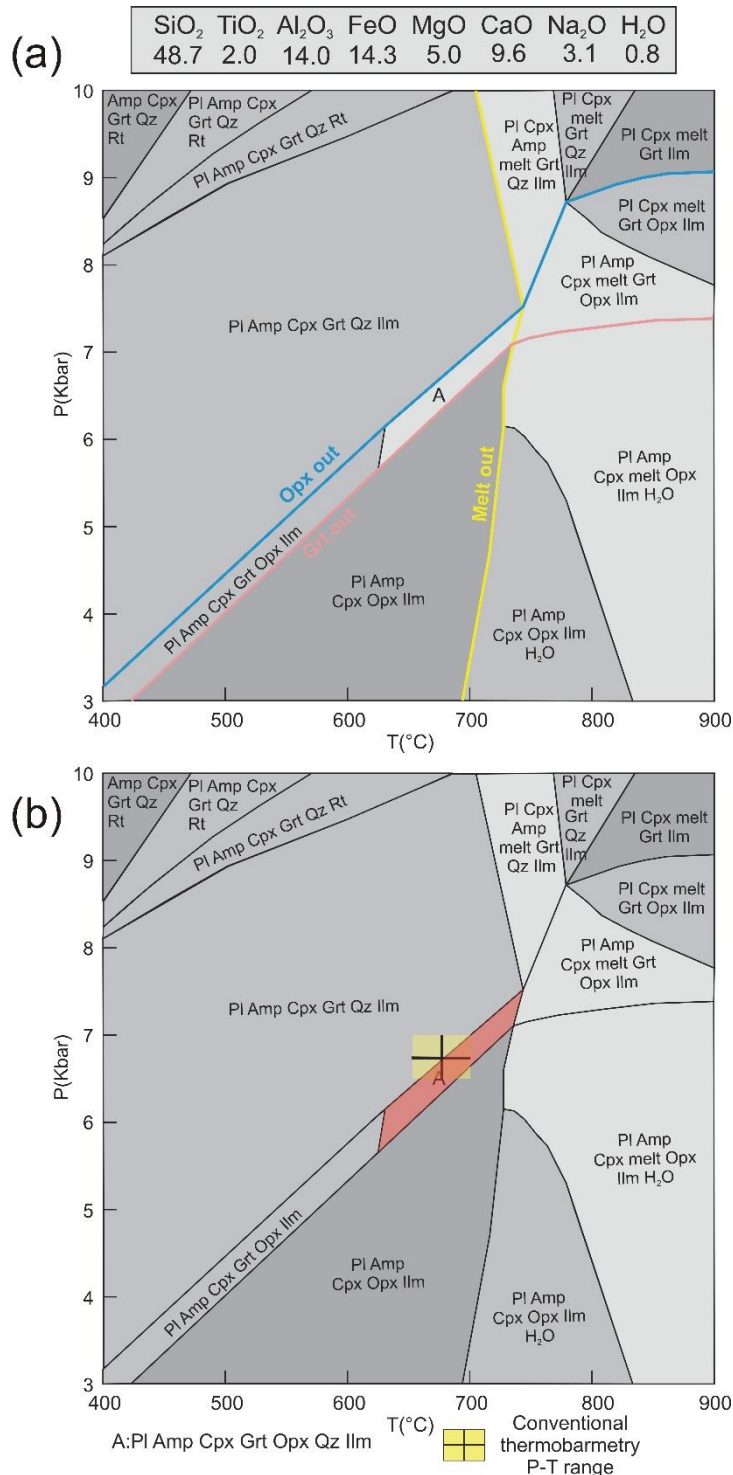


Figure 8.3 (a) Pseudosection is computed in NCKFMASHT ($\text{Na}_2\text{O}-\text{K}_2\text{O}-\text{CaO}-\text{FeO}-\text{MgO}-\text{Al}_2\text{O}_3-\text{SiO}_2-\text{H}_2\text{O}-\text{TiO}_2$) components system with the representative bulk composition. Opx, Grt and melt stability limits are demarcated in the pseudosection. (b) P-T is constrained based on the metamorphic mineral assemblage and it correlates well with conventional thermobarometry data.

Determining the representative bulk composition is crucial in pseudosection construction. Since the rock is fine-grained and lacks mesoscopic heterogeneity, measured bulk composition from the studied rock sample (SD-19) is used as representative bulk composition. Major oxide bulk composition is analysed in the X-ray fluorescence laboratory of the National Centre for Earth Science Studies (NCESS), India. Bruker S4 Pioneer sequential wavelength-dispersive X-ray spectrometer is used for the analysis. A detailed analytical technique has already been discussed in the Appendix. Fluid is considered as pure H₂O in the representative bulk composition. While free H₂O is typically negligible, H₂O is typically found within mineral structures or in the melt phase at deep crustal settings. The water content of the metamafic dyke is evaluated in such a way that free fluid is absent in the presence of a melt phase.

The pseudosections are calculated with the internally consistent thermodynamic dataset of Holland and Powell 2011 (TC-DS633), using the programme PerpleX (ver. 7.0.11; Connolly 2005). MnO is not considered for modelling as it is primarily found in garnet (only 1-2% of the garnet composition), and present in negligible amounts in the bulk composition. For the pseudosection computation, activity models of phases clinopyroxene, orthopyroxene, garnet, melt (Holland et al. 2018), clino-amphibole (Diener and Powell 2012) and feldspars (Holland and Powell 2003) are used. Other pure endmember phases in the modelling comprise quartz, rutile, titanite and ilmenite. To further refine the estimated P-T conditions of the rock, compositional isopleths for garnet are computed in the relevant assemblage fields.

Results: As the rock does not develop any melt phase, temperature is mainly restricted below 700°C (Fig. 8.3.a). Opx-out and Grt-out lines further restrict the PT condition in the phase diagram (Fig. 8.3.a). The phase assemblage of Cpx-Opx-Grt-Pl-Qz-Ilm determined by the petrographic study constrains the P-T range of 600-700°C and 6.5-7 kbar pressure (Fig. 8.3.b). The evaluated P-T range of metamorphism is quite identical to various conventional thermobarometry (Fig. 8.3.b).

Reference:

Bhattacharya, A., Krishnakumar, K.R., Raith, M., and Sen, S.K. (1991) An improved set of a-X parameters for Fe-Mg-Ca garnets and refinements of the orthopyroxene-garnet thermometer and the orthopyroxene-garnet-plagioclase-quartz barometer. *Journal of*

Petrology, 32, 629–656.

- Bhui, U.K., Sengupta, Pulak, and Sengupta, Pranesh (2007) Phase relations in mafic dykes and their host rocks from Kondapalle, Andhra Pradesh, India: Implications for the time–depth trajectory of the Palaeoproterozoic (late Archaean?) granulites from southern Eastern Ghats Belt. *Precambrian Research*, 156, 153–174.
- Bleeker, W., and Ernst, R. (2006) Short-lived mantle generated magmatic events and their dyke swarms: The key unlocking Earth’s paleogeographic record back to 2.6 Ga. *Dyke Swarms - Time Markers of Crustal Evolution - Proceedings of the 5th International Conference, IDC-5*.
- Connolly, J.A.D. (2005) Computation of phase equilibria by linear programming: A tool for geodynamic modeling and its application to subduction zone decarbonation. *Earth and Planetary Science Letters*, 236, 524–541.
- Diener, J.F.A., and Powell, R. (2012) Revised activity–composition models for clinopyroxene and amphibole. *Journal of Metamorphic Geology*, 30, 131–142.
- Droop, G.T.R. (1987) A general equation for estimating Fe ³⁺ concentrations in ferromagnesian silicates and oxides from microprobe analyses, using stoichiometric criteria. *Mineralogical Magazine*, 51, 431–435.
- Eckert, J.O., Newton, R.C., and Kleppa, O.J. (1991) The ΔH of reaction and recalibration of garnet-pyroxene- plagioclase-quartz geobarometers in the CMAS system by solution calorimetry. *American Mineralogist*, 76, 148–160.
- Ellis, D.J., and Green, D.H. (1979) An experimental study of the effect of Ca upon garnet-clinopyroxene Fe-Mg exchange equilibria. *Contributions to Mineralogy and Petrology*, 71, 13–22.
- Graham, C.M., and Powell, R. (1984) A garnet–hornblende geothermometer: calibration, testing, and application to the Pelona Schist, Southern California. *Journal of Metamorphic Geology*, 2, 13–31.
- Hammarstrom, J.M., and Zen, E. (1986) Aluminum in hornblende: an empirical igneous geobarometer. *American Mineralogist*, 71, 1297–1313.

- Holland, T., and Powell, R. (2003) Activity-compositions relations for phases in petrological calculations: An asymmetric multicomponent formulation. *Contributions to Mineralogy and Petrology*, 145, 492–501.
- Holland, T., Green, E.C.R., and Powell, R. (2018) Melting of peridotites through to granites: A simple thermodynamic model in the system KNCFMASHTOCr. *Journal of Petrology*, 59, 881–900.
- Holland, T.J.B., and Powell, R. (2011) An improved and extended internally consistent thermodynamic dataset for phases of petrological interest, involving a new equation of state for solids. *Journal of Metamorphic Geology*, 29, 333–383.
- Kohn, M.J., and Spear, F.S. (1991) Error propagation for barometers; 1, Accuracy and precision of experimentally located end-member reactions. *American Mineralogist*, 76, 128–137.
- Leake, B.E., Woolley, A.R., Arps, C.E.S., Birch, W.D., Gilbert, M.C., Grice, J.D., Hawthorne, F.C., Kato, A., Kisch, H.J., Krivovichev, V.G., and others (1997) Nomenclature of amphiboles: Report of the subcommittee on amphiboles of the international mineralogical association, commission on new minerals and mineral names. *Canadian Mineralogist*, 35, 219–246.
- Schmidt, M.W. (1992) Amphibole composition in tonalite as a function of pressure: an experimental calibration of the Al-in-hornblende barometer. *Contributions to Mineralogy and Petrology*, 110, 304–310.
- Sengupta, S. (1993) Tectonothermal history recorded in mafic dykes and enclaves of gneissic basement in the Schirmacher Hills, East Antarctica. *Precambrian Research*, 63, 273–291.
- Whitney, D.L., and Evans, B.W. (2010) Abbreviations for Names of Rock-Forming Minerals. *American Mineralogist*, 95, 185–187.

Chapter 9

Discussion

The findings presented in the foregoing sections are synthesized, and their significance is discussed in the context of the evolution of the CGGC. The study area comprises a number of different lithounits, and mutual field relations among them (detailed in Chapter 3) establish a general chronology of these lithounits. The enclave suite mafic granulite (within migmatitic felsic gneiss), bearing discordant (S1) foliation, represents the earliest unit in the litho package of the study area. The migmatitic felsic gneiss (MFG) was intruded by younger metaporphyritic charnockite (PC) and biotite gneiss (BG). The biotite gneiss, present along the boundary of the metaporphyritic charnockite, share a gradational contact with the metaporphyritic charnockite. The entire felsic orthogneiss lithopackge develops a pervasive foliation (S2) that is subsequently cut by intrusive metamafic dykes.

This section comprises three subdivisions. In the first part, salient findings from the different lithounits are described and discussed in various chapters. In the second subdivision, major inferences related to the tectonothermal events from the studied rocks are correlated with other parts of CGGC and a possible crustal evolutionary history is proposed. Finally, in the concluding section, the tectonothermal events of the CGGC are discussed against the backdrop of other Proterozoic Indian landmass and correlated with the Rodinia and Columbia supercontinental cycles.

9.1 Petrogenetic evolution of various lithounits:

9.1.1 Migmatitic felsic gneiss (MFG):

The key findings from the migmatitic felsic gneiss (detailed in Chapter 4) are discussed below.

9.1.1.a The magmatic protolith of MFG:

It is difficult and, at the same time, essential to classify granites based on petrogenetic types (A-, I-, and S- granites). In the classification diagrams of Whalen et al. (1987) (Fig. 9.1), MFG typically concentrates on the I- and S- type fields. The studied granitoids have a comparatively low SiO₂ (Avg. ~70.6 wt%) with respect to a high alkali content (Na₂O+K₂O= Avg. ~7.29 wt%). Most samples have an A/CNK <1.1, and only a few samples have an A/CNK value slightly greater than 1.1. The low concentration of

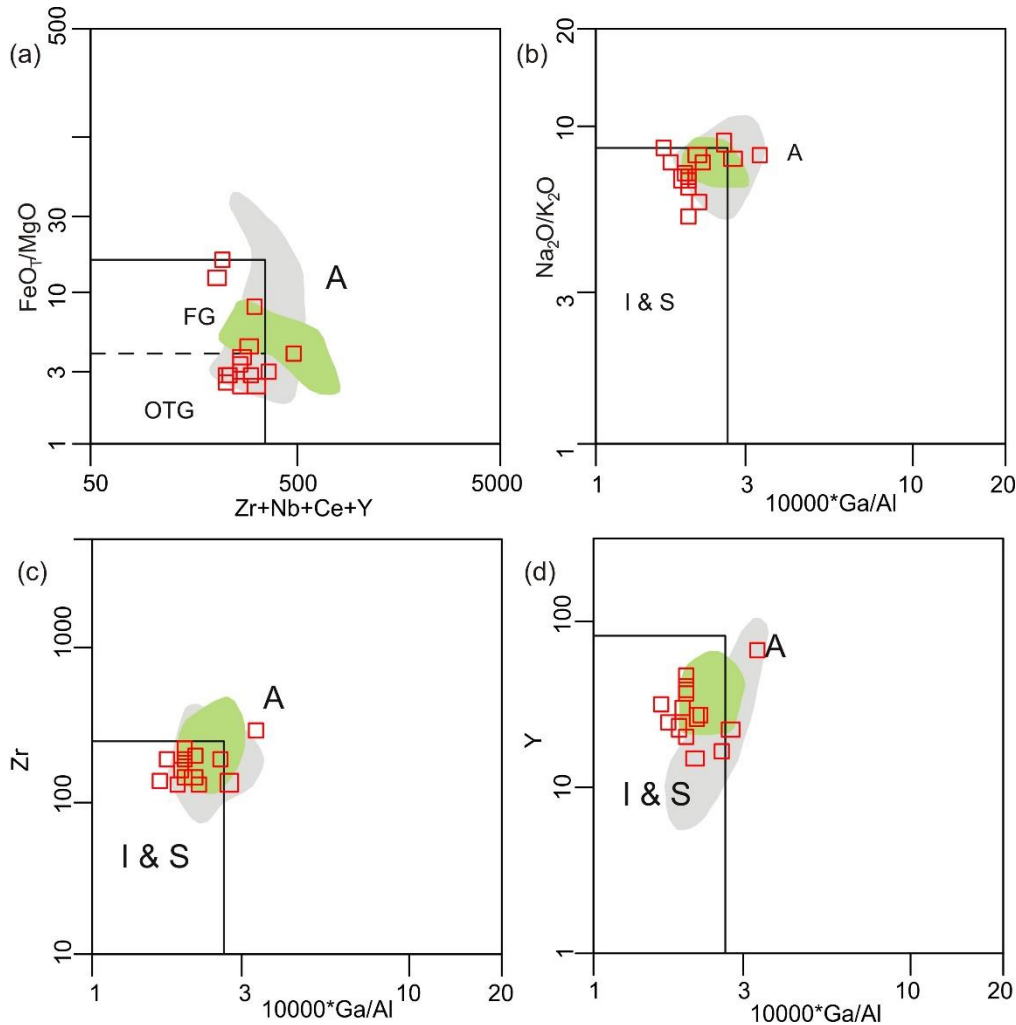


Figure 9.1: In the classification diagrams of Whalen et al. (1987) MFG typically concentrates on the I- and S- type fields. Migmatitic felsic gneiss is compared with felsic orthogneisses from the Dumka-Deoghar (grey) and Bathani (light green) area.

HFSEs (Nb, Ta) and low value of $10000 \cdot \text{Ga}/\text{Al}$, along with the comparatively low magmatic temperature of the studied granitoids, indicate that these are not A-type granites. These geochemical characteristics are primarily consistent with I-type granites (Chappell and White, 1992).

Furthermore, the studied granitoids exhibit a negative correlation between SiO_2 and P_2O_5 , i.e., an increase in SiO_2 results in a decrease in P_2O_5 content (Fig. 9.2). This feature is vital in distinguishing between I- and S- type granites as apatite are quite soluble in strongly peraluminous (S-type) granitic melts. However, it reaches saturation in metaluminous to slightly peraluminous granitic magma systems (Wolf and London 1994).

The low values of X_{Fe} , $\text{Zr}+\text{Ce}+\text{Nb}+\text{Y}$ and $10^3 \cdot \text{Ga}/\text{Al}$, the metaluminous to slightly peraluminous nature of the studied granitoids along with the negative correlation between SiO_2 and P_2O_5 suggests that MFG is typically I-type in nature. Field studies furthermore corroborate this as the MFG is the country rock of the region, and the regional extent of the studied granitoids favours I-type over S-type granites as the latter is generally limited in its extent.

9.1.1.b Mechanism of felsic magma generation:

The magmatic source of voluminous I-type granites is broadly debated contentious issue. Several models are proposed to explain the genesis of this rock that range between these petrologic models,

- (a) Anatexis of crustal rock with variable mantle input is a possible mechanism behind voluminous I-type granite formation (Vielzeuf and Holloway 1988; Clemens 1990; Montel and Vielzeuf 1997). Another potential source for high K-granite is the melting of the tonalitic rock in the lower crust caused by K-rich fluid from mantle melts (Castro 2004).
- (b) Fractionation of basaltic to andesitic melts is also a viable alternative mechanism in I-type granite formation (Jagoutz et al. 2009; Jagoutz 2010; Castro 2014; Moyen et al. 2017).

The generation of voluminous I-type granite from crustal anatexis requires a significant amount of melting of the lower continental crust (Vielzeuf and Holloway 1988;

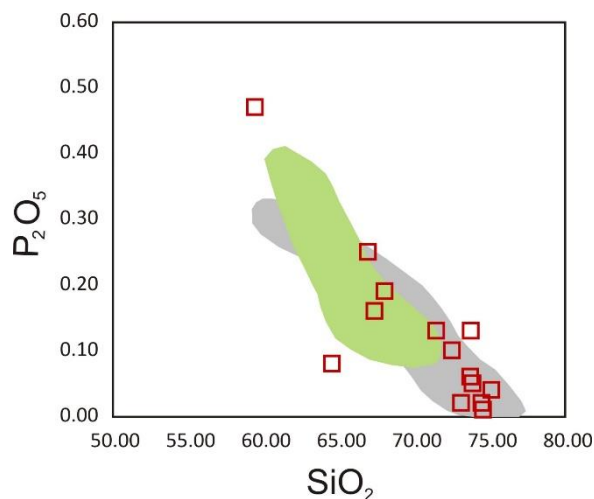


Figure 9.2: The studied granitoids exhibit a negative correlation in the SiO_2 vs. P_2O_5 plot. Migmatitic felsic gneiss is compared with felsic orthogneisses from the Dumka-Deoghar (grey) and Bathani (light green) area.

Clemens 1990; Montel and Vielzeuf 1997). This process requires considerable heat flux by mantle-derived basaltic melts (Vielzeuf and Holloway 1988; Clemens 1990; Montel and Vielzeuf 1997). Thermal modelling studies suggest voluminous I-type granite magmatism requires almost double the amount of basaltic magmatism, which is unlikely in most scenarios (Annen et al. 2006). Furthermore, the lower crustal rocks are majorly granulite facies, much less fertile regarding melt productivity (Vielzeuf and Holloway 1988; Clemens 1990; Montel and Vielzeuf 1997). On the other hand, the partial melting of a metasomatised mantle wedge in a subduction zone generates basaltic or andesitic magma that results in magma accumulation beneath the crust. Fractional crystallisation along with possible crustal assimilation of the accumulated basaltic to andesitic magma is a viable source for I-type magma (Annen et al. 2006; Castro 2014).

The high silica and alkali content, along with the low concentrations of HFSE, and the high $(\text{Pb/Nb})_N$, $(\text{Pb/Ta})_N$ indicate crustal input in the source (Moreno et al. 2016). These suggest the possibility of assimilation between ponded basaltic magma with crustal components. The LREE enrichment and flat HREE pattern, along with the Eu negative anomaly, suggest that though plagioclase was present garnet was absent in the source indicating a relatively shallow depth of the source.

9.1.1.c Probable tectonic setting of magmatism of the MFG protolith

The tectonic setting of magmatism is vital in understanding the petrogenetic history of the studied rock types. The primitive mantle normalised (McDonough and Sun 1995) trace element pattern suggests enrichment of Pb, Rb, and Ba but depletion in Na, Ta, Ti, and P content. The depletion of HFSEs and the LREE enrichment over HREE indicate a typical continental arc setting. This is further established by the tectonic discrimination diagrams of Pearce et al. (1984). The Rb vs. (Y+Nb) and Nb vs. Y diagrams discriminate granites based on the tectonic setting (Fig. 9.3.a-b) (Pearce et al. 1984). The ocean ridge granites (ORG) are associated with mid-ocean ridges and are formed by partial melting of the mantle. Volcanic arc granites (VAG) are found in subduction zones and formed by partially melting the mantle wedge and overlying sediments. Within plate granites (WPG) are not associated with plate boundaries and are thought to be formed by partial melting of the continental crust. Collision granites (COLG) are formed by partially melting crustal rocks involved in collisional events, such as the collision of two continents. The I-type granite magmatism typically plots in the field of volcanic arc granites and predominantly

indicates a convergent tectonic margin along the subduction zone. Th/Hf vs. Ta/Hf diagram (Fig. 9.3.c) further asserts the affinity of arc magmatism (Schandl and Gorton 2002).

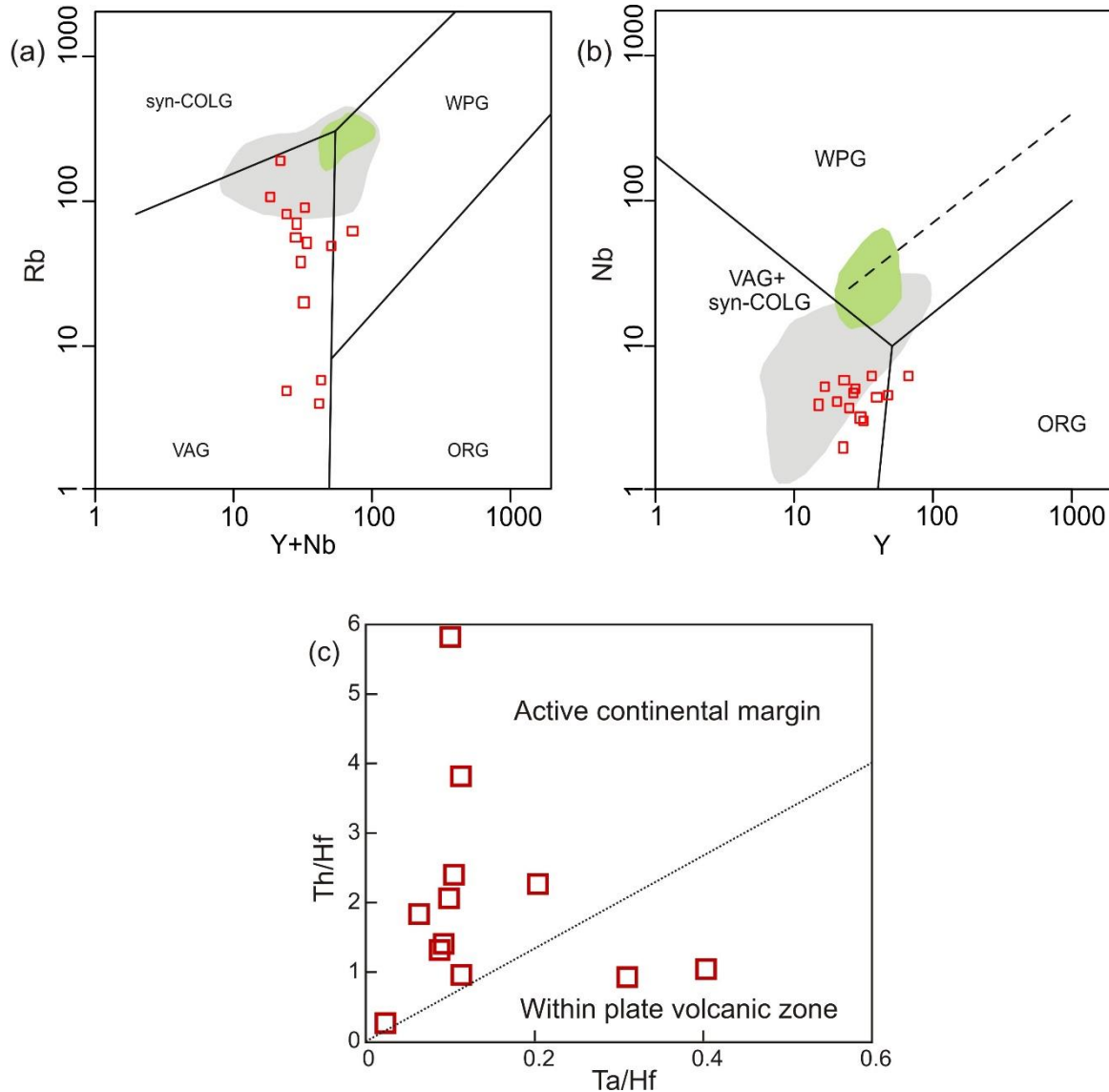


Figure 9.3: (a-b) The tectonic discrimination diagram (Pearce et al. 1984; Pearce 1996) shows the studied granitoids plotted in the volcanic arc granite field (VAG) field. (c) In the Th/Hf vs. Ta/Hf (Schandl and Gorton 2002) diagram most samples plot in the field of active continental margin. Migmatitic felsic gneiss is compared with felsic orthogneisses from the Dumka-Deoghar (grey) and Bathani (light green) areas.

9.1.1.d Metamorphic history of the MFG and its tectonic significance

The interpretation of the reaction textures and the phase equilibria modelling and conventional thermobarometry, a P-T condition of 700-800 °C; 7.5-8 kbar is identified as

the culmination of metamorphism and deformation. The recorded pressure corresponds to a crustal depth of ~26 km. The estimated P-T values are consistent with a geothermal gradient of ~28 °C/km during peak metamorphism. Subsequently, the rock exhumed along a decompressive P-T path till ~6 Kbar (Fig. 9.4). The geometry of the P-T path and inferred geothermal gradient suggest a continent-continent collision setting.

9.1.2 Petrogenesis of the Ferroan granitoids and metamorphic implications:

The metaporphyritic charnockite (PC) and biotite gneiss (BG) intruded the country rock (MFG) and are geochemically characterised as ferroan A-type granitoids. Field relations, petrographic study, mineral chemistry, geochemical features, and phase equilibria modelling of the magmatic system suggest that PC is magmatic charnockite and PC and BG are cogenetic that form by fractional crystallisation of ferroan magma. A detailed study is presented in Chapter 5.

9.1.2.a Magmatic source characterisation of the ferroan granitoids:

The igneous charnockites (metaporphyritic charnockite; PC) and associated granites (now biotite gneiss; BG) are geochemically characterised as ferroan A-type granitoids. Various petrogenetic models have been proposed to explain the source of the ferroan granitoids. Among several models, the origin of A-type granitoids can be majorly restricted to three mechanisms, (a) fractionation of mantle derived mafic magma via anhydrous fractional crystallization (Duchesne and Wilmart 1997; Frost et al. 1999; I. Carl Anderson et al. 2003); (b) high temperature partial melting of the quartzo- feldspathic lower crust (Collins et al. 1982; Anderson 1983; Landenberger and Collins 1996; King et al. 1997; Dall'Agnol et al. 1999b) and (c) a combination of the mantle and crustal sources (Kemp et al. 2005; Montero et al. 2009; Moreno et al. 2014, 2016). The studied ferroan granitoids

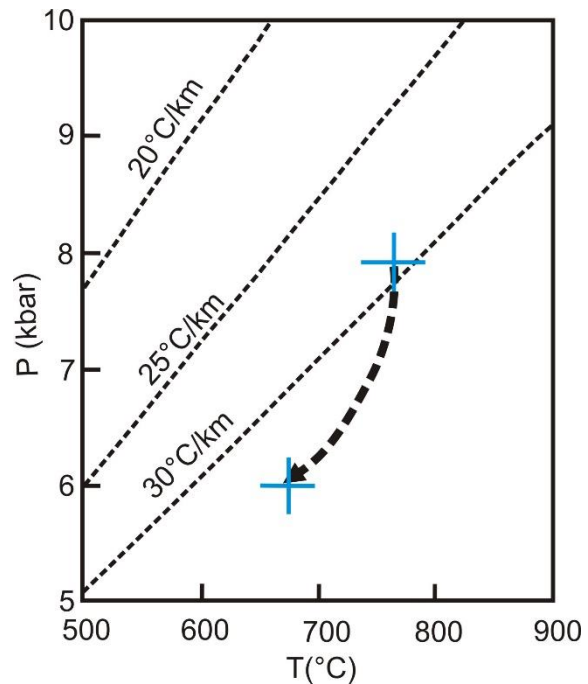


Figure 9.4: P-T path of metamorphism of the migmatitic felsic gneiss.

(both PC and BG) are calc-alkaline granitoids that straddle the metaluminous and peraluminous granitoids field boundary (see Chapter 5; Fig. 5.7) in the aluminium saturation index diagram, which suggests a predominantly crustal source according to the natural and experimental works (Collins et al. 1982; Skjerlie and Johnston 1993; Patiño Douce 1997; King et al. 2001; Dall'Agnol and de Oliveira 2007; Oliveira and Agnol 2009; Frost and Frost 2013).

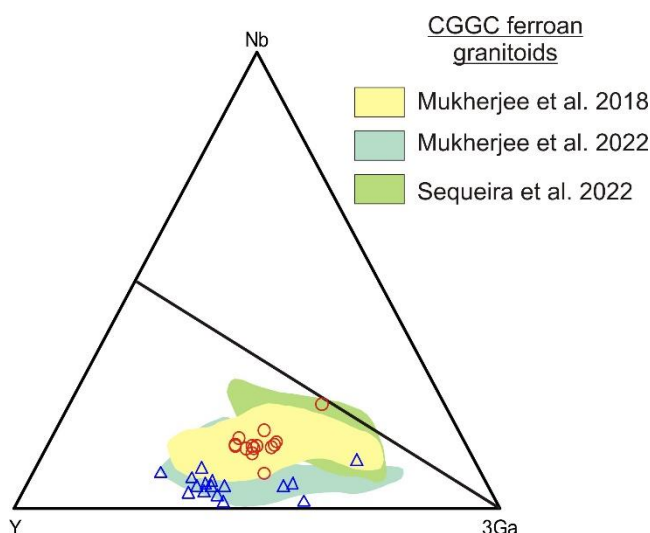


Figure 9.5: Nb-Y-3Ga ternary plot (Eby, 1992) classifies both the studied ferroan rock types as A_2 granitoids.

The detailed geochemical and Lu-Hf isotopic study constrain a predominantly crustal source for the ferroan granitoids from other parts of the CGGC (Mukherjee et al. 2018a, 2022; Sequeira et al. 2022). Resembling the ferroan granitoids from other parts, both PC and BG plot in the A_2 field (Fig. 9.5) (Eby 1992), which further strengthens the dominance of crustal component in the source (Eby 1992; Moreno et al. 2014) as A_2 type granitoids implicate a possible crustal source (Eby 1992) or a mantle source previously metasomatized by crustal fluids (Montero et al. 2009; Moreno et al. 2014).

Experimental studies further demonstrate that orthopyroxene is favoured over clinopyroxene in low pressure (Patiño Douce 1997), and at high pressure, the melt becomes strongly peraluminous (Patiño Douce 1997; Frost and Frost 2011). Mid- to lower crustal voluminous ferroan magmatism requires high temperature (Clemens et al. 1986; King et al. 2001), generally in a fluid-undersaturated condition (Clemens and Vielzeuf 1987). Experimental works suggest such high temperature fluid, absent partial melting at mid to lower crustal depth, requires disintegration of hydrous phases (Clemens and Vielzeuf 1987; Rushmer 1991; Watkins et al. 2007).

Experimental studies show calc-alkaline, meta to peraluminous granitoids, can form from the dehydration melting of both amphibole and biotite (Patiño Douce 1997). Dehydration melting involving biotite and amphibole and their relative fraction in the

source influences the melt composition (Clemens and Stevens 2012). Melting of biotite and amphibole, enriches the melt of K_2O and Na_2O respectively (Patiño Douce and Beard 1995; Watkins et al. 2007). Dehydration melting of these hydrous phases also influences the water activity of the magma (Clemens and Vielzeuf 1987), as the amount of water contained in amphibole (2-3% H_2O) is lower than biotite (3-5% H_2O). Amphibole's dominance over biotite could explain the low H_2O content of the ferroan granitoid magma as constrained from phase equilibria modelling.

9.1.2.b Genesis of igneous charnockite (PC): phase equilibria modelling vs. experimental studies

The open system phase equilibria modelling is calculated at various P-T conditions, bulk H_2O content and oxygen fugacity. Phase equilibria modelling gives a unique opportunity to investigate the role of various parameters in the genesis of magmatic charnockite in CGGC. The information described in the preceding sections provides constraints on the control of physico-chemical factors that presumably created a suitable ambience for the generation of igneous charnockite. The following section describes the relative importance of the various factors deduced from phase equilibrium modelling and compares those with existing studies and experimental works.

Role of pressure and temperature:

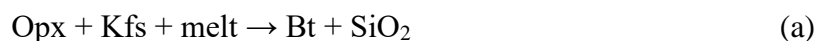
The modelling (Fig. 5.10-11; Chapter 5) reveals that in the ferroan granitoid of the CGGC, orthopyroxene starts to crystallise with temperatures as high as 995°C (at 1% H_2O) to 940°C. Considering the whole range of initial H_2O (from 1 to 2.5 wt%) and pressure (3-5 kbar), Opx is stable in the magma, approximately up to 750°C. Even with only 1% initial H_2O in the bulk, orthopyroxene becomes unstable at around 740°C. Several studies on charnockite plutons also suggest a very high magmatic temperature (950-800°C), often a liquidus temperature of 1000°C or higher (Kilpatrick and Ellis 1992; Young et al. 1997; Frost et al. 1999; Percival and Mortensen 2002). Orthopyroxene in the felsic ferroan (A-type) magma is sensitive to temperature (Naney 1983; Frost and Frost 2008).

Lowering pressure (from 5 to 3 kbar) at a particular bulk composition increases the abundance of Opx in the fractionated crystal system. Similar emplacement depths were also recorded from charnockite plutons from the Sherman batholith and Thor range, recording a pressure range of 2.5 – 5.5 kbar (Frost and Frost, 2008). Experimental studies also confirm

that low pressure favours the stability of Ca-poor orthopyroxene (Naney 1983; Patiño Douce 1997). High pressure favours the stabilisation of Ca-poor plagioclase (Patiño Douce 1997) in the magma system, increasing Ca activity. Thus, high pressure facilitate crystallisation of Ca-rich pyroxenes over Opx.

Role of fluids:

Open system phase equilibria modelling (Fig. 5.10-11; Chapter 5) suggests that H₂O dissolved in the magma can significantly alter Opx's stability. Only with an increase of 1.5% (from 1% to 2.5%) Opx becomes utterly absent from the fractionated crystal system, even though it is one of the initial crystallising phases in the magma. This observation from phase equilibria modelling agrees well with previous works (Naney 1983; Frost and Frost 2008; Zhao et al. 2018, 2023). Phase equilibria modelling in the melt-dominated system demonstrates that the Opx out line is almost synchronous with the biotite in line. In the melt-dominated system (MS), already crystallised Opx starts to get consumed with the appearance of biotite (hydrous ferromagnesian phase) crystallisation. Apart from Opx, biotite crystallisation also decreases the abundance of Kfs in the solid system. The Opx breakdown reaction within the magma chamber is consistent with several other studies (Frost and Frost 2008; Harlov et al. 2013; Zhao et al. 2017).



In the felsic melt system, the crystallisation of anhydrous phases increases the amount of H₂O in the residual melt. Experimental works (Naney 1983) on granitic and granodioritic melts also show that Opx is stable initially in the magma chamber, and its stability decreases with increasing H₂O content of the melt. From the above reaction, it is quite evident that an increase in dissolved H₂O in the residual magma would suddenly favour biotite over orthopyroxene.

Role of oxygen fugacity:

The oxygen fugacity of ferroan granites varies over a wide range, from oxidised to reduced conditions (Dall'Agnol and de Oliveira 2007). Experimental studies have shown that fO₂ strongly influences the geochemistry of A-type granites (Dall'Agnol et al. 1999a). Notably, Frost and Frost (2008) demonstrated that fO₂ conditions of charnockitic plutons stretch from less than FMQ to greater than FMQ+2 buffer. Phase equilibria modelling primarily indicates that increasing fO₂ improves magnetite's stability as the magma Fe³⁺

content expands. It is manifested by the greater abundance of magnetite over ilmenite at the FMQ+2 modelling condition. This is accompanied by a decrease in Opx abundance in the crystal-dominated system and a reduction of Opx stability (Opx absent at 4 kbar at 2% H₂O at FMQ+2). An increase in Fe³⁺/Total Fe content decreases the X_{Fe} (=Fe²⁺/(Fe²⁺+Mg)) of the magma, resulting in more magnesian Opx (X_{Mg} of Opx increases from 0.3 to 0.4). Experimental studies on ferroan granites (Dall'Agnol et al. 1999a) and detailed phase equilibria modelling on metaluminous silicic magma also confirm similar Opx stability enhancement in low fO₂. Both in the modelled system at FMQ buffer and in the petrography of studied granitoids, the abundance of Ilm is more than Mgt. This petrographic similarity, combined with identical Opx composition (X_{Mg} = 0.3), constrains the fO₂ condition of the CGGC charnockites at FMQ. This further attests to the influence of melt composition, particularly X_{Mg} of the melt system, on the stability of orthopyroxene. Increasing magma X_{Mg} increases biotite's stability limits (Frost and Frost, 2008).

9.1.2.c Preservation of magmatic phases:

The widespread occurrence of A-type granitoids from parts of CGGC has been documented extensively by different workers (Mukherjee et al. 2018a, 2022; Sequeira et al. 2022). Charnockites are reported from the Dumka-Deoghar region, located within a few tens of kilometres from the study area but detailed study suggests these orthopyroxenes are of metamorphic origin (Mukherjee et al. 2017, 2018a). This study reports igneous charnockite from the CGGC for the first time. Like its counterpart in other terranes (Table 2 of Zhao et al. 2023), preservation of magmatic orthopyroxene in the studied area, even after high-grade metamorphism, is an enigma and warrants an answer. Based on phase equilibria modelling, the above discussion suggests several physio-chemical parameters (high T., low P, low aH₂O and low fO₂) enhance orthopyroxene stability, but among these aH₂O seems more influential as only a slight increase in bulk H₂O can make Opx unstable drastically. The following sections examine the influence of different factors responsible for maintaining the low aH₂O in the studied rocks.

Infiltration of CO₂ and brine during magmatic and post-magmatic stages:

Infiltration of CO₂ (>10 vol%) in crystal mush during /soon after the crystallization of the magmatic orthopyroxene is a viable mechanism to help preserve orthopyroxene in magmatic charnockite (Frost et al. 2000; Clemens and Birch 2012; Harlov et al. 2013; Scaillet et al. 2016; Zhao et al. 2023). Degassing of deep-seated magma (Yoshimura and

Nakamura 2011) or magmas ponded at the base of the reservoirs (Parmigiani et al. 2016) can act as the source for such CO₂-flushed fluids (Zhao et al. 2023). In an extensive analysis, Zhao et al. (2023) showed that the process of infiltration of CO₂ in crystal mush can only operate in a narrow temperature interval and requires a specific mode of movement of CO₂ through the intergranular spaces of the crystal mush (through bubble channel connectivity) over a large distance. Owing to the higher wetting angle of CO₂ (relative to H₂O or brine) (Newton and Tsunogae 2014; Newton et al. 2014), the efficacy of the process based on fluid inclusion data can be ambiguous (reviewed in Touret et al., 2022). It is well-known that at elevated P-T conditions, dissolved salt (NaCl and others) can drastically reduce the aH₂O of aqueous fluid (Newton and Tsunogae 2014; Newton et al. 2014). Owing to its favourable wetting properties, extensive infiltration (often several tens of square km or more) of brine-rich fluid makes a viable option for creating a low aH₂O environment that renders stability of orthopyroxene over its hydrous counterpart (amphibole and biotite, Touret et al. 2022). Several petrological features corroborate the large-scale infiltration of brine-rich fluid from the mantle through the crustal rocks (Touret et al. 2022). Like CO₂ and brine, halogen in the fluid can influence orthopyroxene stability in felsic magma (Bucher and Frost 2006). However, infiltration of low aH₂O fluid is inconsistent with the preservation of biotite in biotite granitoid that is expected to be converted to orthopyroxene+K-feldspar (Newton et al. 1980; Newton 1992; Raith and Srikantappa 1993).

Separation of hydrous melt from crystal mush:

Separation of an increasingly hydrous melt from an orthopyroxene, feldspar, quartz crystal mush is considered to be a viable mechanism to prevent the back reaction (reaction a) (Harlov et al. 2013; Zhao et al. 2018, 2023) that converts Opx to Bt, described in the above section. Thus, crystal fractionation is crucial in forming magmatic charnockite. Several previous works (Harlov et al. 2013; Zhao et al. 2018, 2023) also assert the importance of fractionation in the petrogenesis of magmatic charnockite. This study showed that hydrous melt (now biotite granitoid) was separated from orthopyroxene – bearing crystal mush during fractionation. However, both the components occur side by side. Similar charnockite-granite association has been reported by several workers from different parts of the world (Frost et al. 2000; Klötzli et al. 2002; Finger et al. 2003; Harlov et al. 2013; Zhao et al. 2017, 2018). Though limited flux of low aH₂O fluid in the magmatic

system cannot be completely ruled out, the physical separation of charnockite crystal mush and hydrous melt seems to be the likely mechanism for the preservation of orthopyroxene in the magmatic charnockite.

Preservation of magmatic features during high-grade metamorphism:

Several studies have recognised the preservation of magmatic mineralogy and textures in high-grade meta-igneous rocks (Bohlen and Essene 1978; Jiang et al. 1988; Clarke et al. 2013; Chapman et al. 2015; Darling and Peck 2016; Dev et al. 2023). Studies have also suggested that even the foliation-defining pyroxene in some high-grade rocks may not originate from metamorphic reactions but represent a recrystallised protolith phase (Clarke et al. 2013; Chapman et al. 2015). Several possible processes can contribute to preserving plutonic assemblage by countering deformation and metamorphism.

- (a) Low water activity in the igneous protolith can be crucial in hindering metamorphic reactions. In mid to lower-crustal rocks, H₂O is generally present as structural water within hydrous phases (e.g., biotite, amphibolite). The lack of such a hydrous phase in the protolith of metaporphyritic charnockite (as suggested by petrographic study and phase equilibria modelling) advocates for the sheer dryness of the rock. This can significantly limit solid-state element mobility required for metamorphic reactions (e.g. garnet formation). Lack of such reaction completion during metamorphism can help preserve the relict magmatic assemblage of the protolith. Separation of hydrous melt contributes to the low aH₂O of the charnockitic pluton.
- (b) Like the magmatic system, CO₂ or brine-enriched fluids infiltration can also produce low water activity during metamorphism (Touret et al. 2022). However, such fluid infiltration would probably convert biotites to Opx in the biotite gneiss (incipient charnockitisation, Newton and Tsunogae, 2014). As such, Opx in biotite gneiss is not observed, CO₂ or brine-enriched fluids infiltration is less likely.

The coarse grain size and interlocking texture of the magmatic charnockite put an additional obstacle to the pervasive fluid during metamorphism (high volume/area ratio).

9.1.2.d Tectonic setting of magmatism of PC and BG protolith:

Magmatic charnockites are reported from a number of tectonic settings, including subduction zones, collisional orogens, and rift settings (Frost and Frost 2008; Rajesh and

Santosh 2012; Zhao et al. 2023). However, the ferroan A-type characters of the studied rock are likely to have formed in an extensional tectonic condition related to a continental or oceanic rift setting (Clemens et al. 1986; Whalen et al. 1987; Eby 1990, 1992; King et al. 1997; Frost and Frost 2008; Dall'Agnol et al. 2012; Moreno et al. 2017; Zhao et al. 2023). This conjecture is further strengthened in the charnockite granite association of

CGGC as both granitoids plot in the “Within plate granite” (WPG) field in the tectonic discrimination diagrams (Fig. 9.6) (Pearce et al. 1984; Pearce 1996). The predominance of crustal components in the source suites continental rift over oceanic rift setting as a favourable tectonic condition. Mid- to lower crustal voluminous ferroan magmatism requires high temperature (Clemens et al. 1986; Klimm et al. 2003), generally in a fluid-undersaturated condition (Clemens et al. 1986). An appreciably high heat supply from a mantle source is reasonably necessary for such voluminous melting in a continental rift setup. Crustal thinning at extensional tectonic setup perturbs the normal geotherm by asthenospheric upwelling, providing heat for the voluminous mid- to lower crustal melting (Bonin 2004).

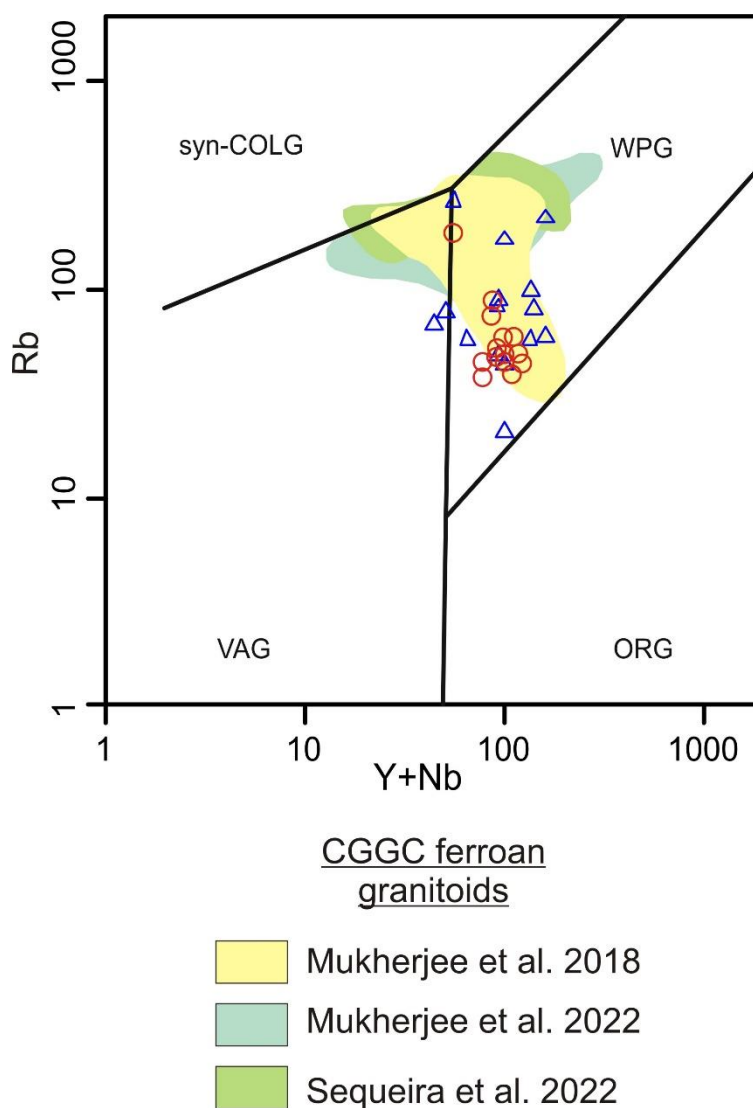


Figure 9.6: The tectonic discrimination diagram (Pearce, 1996) shows the studied granitoids plotted in the WPG (within plate granite) field.

9.1.2.e Geochemical control on Igneous charnockites:

Magmatic charnockites and C-type magma:

Kilpatrick & Ellis (1992) distinguished magmatic charnockites based on specific geochemical characteristics and defined a distinctive magma type called **Charnockite magma** (C-type magma) that forms intrusive charnockitic plutons. The C-type magma is defined by higher abundances of K_2O , P_2O_5 , TiO_2 , and LILE, and a lower abundance of CaO compared to other felsic magma types (I-, S-, A- types). According to Kilpatrick & Ellis, (1992), the Mg# of C-type magma varies in the range of ~25-40. However, in the current study the magmatic charnockite resemble the charectersitics of typical ferroan (A-type) granites.

A compilation of globally published data (Fig. 9.7) of charnockitic plutons (Ormaasen 1977; Kilpatrick and Ellis 1992; Duchesne and Wilmart 1997; Young et al. 1997; Frost et al. 1999; Grantham et al. 2001; Percival and Mortensen 2002; Percival et al. 2003; Tollo et al. 2006; Mikhalsky et al. 2006; Pouclet et al. 2007; Rajesh 2008; Motuza et al. 2008; Scandolara et

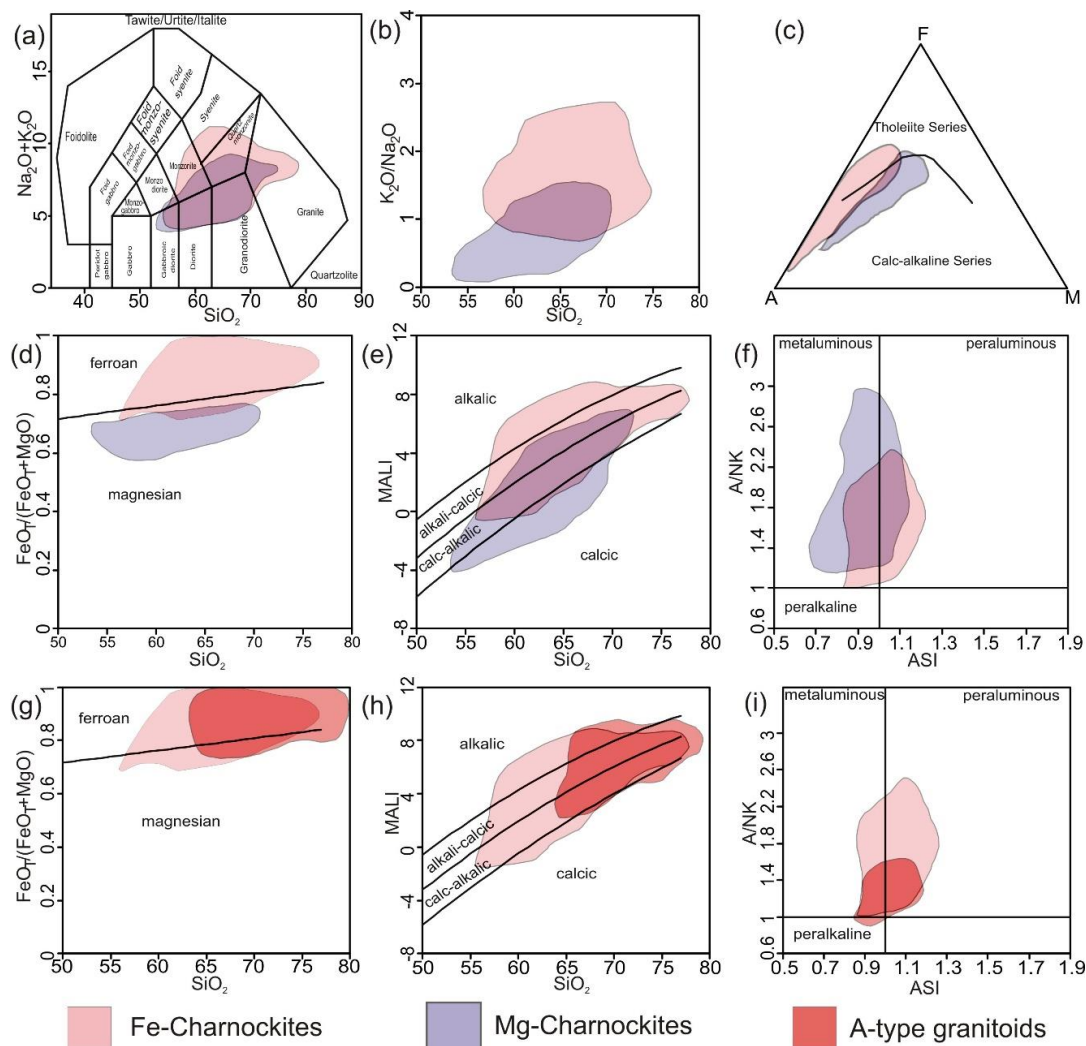


Figure 9.7: Ferroan and magnesian charnockite compositions from published data (Duchesne and Wilmart, 1997; Frost et al., 1999; Grantham et al., 2001; Kilpatrick and Ellis, 1992; Lu et al., 2019; Ma et al., 2013; Melo et al., 2020; Mikhalsky et al., 2006; Motuza et al., 2008; Ormaasen, 1977; Percival et al., 2003; Percival and Mortensen, 2002; Pouclet et al., 2007; Rajesh, 2008; Scandolara et al., 2013; Tollo et al., 2006; Yang et al., 2014; Yang and Santosh, 2015; Young et al., 1997; Zhao et al., 2014) are plotted in (a) the total alkali silica (TAS) diagram of Middlemost, (1994) (b) K_2O/Na_2O vs. SiO_2 plot, (c) AFM diagram, (d-f) Granite classification diagrams (Frost et al., 2001). (g-i) Ferroan charnockite (Duchesne and Wilmart, 1997; Frost et al., 1999; Grantham et al., 2001; Kilpatrick and Ellis, 1992; Melo et al., 2020; Mikhalsky et al., 2006; Motuza et al., 2008; Ormaasen, 1977; Pouclet et al., 2007; Rajesh, 2008; Scandolara et al., 2013; Tollo et al., 2006; Yang et al., 2014; Yang and Santosh, 2015; Zhao et al., 2014) composition is compared with published A-type granite composition (Anderson et al., 2003; Deng et al., 2016; Du et al., 2016; Frost et al., 1999; Goodenough et al., 2000; Jarrar et al., 2008; Katzir et al., 2007; King et al., 1997; Li et al., 2014; Scandolara et al., 2013; Valério et al., 2018; Zhao et al., 2016; Zhu et al., 2020) in granite classification diagrams (Frost et al., 2001); MALI = Modified alkali lime index ($Na_2O + K_2O - CaO$); ASI = molar $Al_2O_3/(Na_2O + K_2O + CaO)$; A/NK = molar $Al_2O_3/(Na_2O + K_2O)$.

al. 2013; Ma et al. 2013; Yang et al. 2014; Zhao et al. 2014; Yang and Santosh 2015; Lu et al. 2019) reveal that the magmatic charnockites show a wide compositional range varying from highly ferroan to magnesian, alkalic to calcic and metaluminous to peraluminous. In the total alkali-silica (TAS) diagram (Fig. 9.7.a), magmatic charnockite composition from published data stretches the fields of granite-monzonite-granodiorite-diorite while the K_2O/Na_2O (Fig. 9.7.b) ranges from <1 to ~ 1 to >1 . This corroborates well with the study of Frost & Frost, (2008), suggesting that magmatic charnockite composition almost entirely covers the whole compositional range of granitoids composition while C-type magma only partially covers the compositional range (Fig. 9.7.d-f) that is intermediate between ferroan and magnesian charnockites. Furthermore, in their attempt to classify C-type magma, Kilpatrick & Ellis, (1992) have considered granitic rocks that are compositionally similar to C-type magma but do not form orthopyroxene, which indicates that orthopyroxene stability in a C-type magma is not completely composition dependent. The fractionation modelling carried out in the current study also suggests that in the stability of the orthopyroxene in the granitic melt, factors such as the H_2O content of the magma or crystal fractionation imparts the primary control and composition dependence is limited (if any). So, classifying magmatic charnockites based on such compositional range is equivocal.

Fe-Charnockites vs A-type granites:

The phase equilibria modelling, coupled with the coupled with experimental study (detailed above in 9.1.2.b), show that low H_2O , fO_2 granites with high magmatic

temperature and shallow depth are most likely to crystallise orthopyroxene as an early crystallising phase. The ferroan A-type granites are characterised by high Fe# (Loiselle and Wones 1979; Whalen et al. 1987), elevated magmatic temperature (Clemens et al. 1986; Klimm et al. 2003) and low water activity (Clemens et al. 1986; Patiño Douce 1997) seems to be suitable for orthopyroxene stability. Figure 9.7.g-i reveals that there is a geochemical similarity between ferroan charnockites (Ormaasen 1977; Kilpatrick and Ellis 1992; Duchesne and Wilmart 1997; Frost et al. 1999; Grantham et al. 2001; Tollo et al. 2006; Mikhalsky et al. 2006; Pouclet et al. 2007; Motuza et al. 2008; Rajesh 2008; Scandolara et al. 2013; Yang et al. 2014; Zhao et al. 2014; Yang and Santosh 2015; Melo et al. 2020) and ferroan (A-type) granites (King et al. 1997; Frost et al. 1999; Goodenough et al. 2000; Anderson et al. 2003; Katzir et al. 2007; Jarrar et al. 2008; Scandolara et al. 2013; Li et al. 2014; Deng et al. 2016; Du et al. 2016; Zhao et al. 2016; Valério et al. 2018; Zhu et al. 2020), but the average SiO₂ content of the Fe-charnockites (SiO₂ = 66.7; n= 232) is considerably lower than the A-type granitoids (SiO₂ = 71.7; n= 262). This suggests that the A-type granitoids are more differentiated than charnockites. This is quite similar to the ferroan charnockites and granites studied here. The ferroan charnockites are less differentiated and correspond to the initial stage of crystal fractionation, while the later stages of fractional crystallisation correlate well with the ferroan granites (A-type).

9.1.2.f Tectonic significance of metamorphism of the Ferroan granitoids:

Detailed petrogenetic evolution of the ferroan granitoids suggests that the studied rocks were subjected to a wide variety of P-T conditions, from magmatic conditions through sub-solidus metamorphism. Igneous charnockites are generally related to low pressure (2-6 kbar) conditions (see review Zhao et al., 2023). The metamorphic garnet formation (750-800°C and 8-8.5 kbar) suggests that the ferroan granitoids were put through

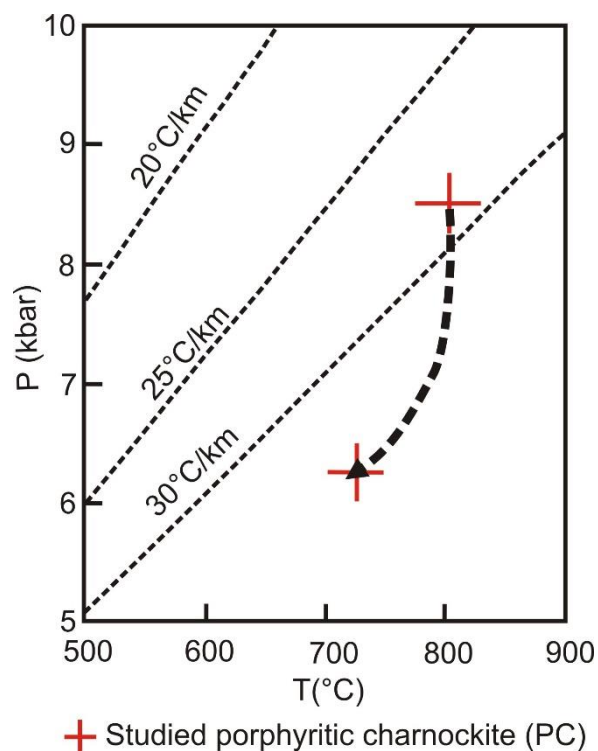


Figure 9.8: P-T condition of metamorphism of the porphyritic charnockite.

burial to a depth of 26-28 km during the granulite facies metamorphism. The peak metamorphic garnet formation is followed by amphibole formation during hydration at 700-750°C and ~6 kbar pressure, which indicates a steep decompressional P-T path of metamorphism. The peak metamorphism along 25-30 km/ °C geothermal gradient (Fig. 9.8) and the steeply decompressive P-T path (clockwise) indicate collisional orogeny (Harley 1989; Brown 2007, 2008, 2014).

9.1.3 Metamorphic evolution of the Mafic granulite:

Intense deformation and metamorphism obliterated most of the magmatic characters. The preserved field and petrographic features cannot confirm(or reject) the idea that some of the pyroxene grains are inherited from the magmatic assemblage. Nevertheless, the preponderance of pyroxenes and development of leucosomes (a product of partial melting) suggest that (a) the protolith of the rock was mafic in composition and (b) the assemblage prior to the granulite facies condition contained amphibole. However, it is not possible to identify if the amphibole was a part of the magmatic assemblage or developed subsequently during an earlier phase of metamorphism.

9.1.3.a Tectonic setting during the metamorphism of mafic granulite:

Peak metamorphic pressure of ~13 kbar corresponds to 800-900 °C in the lower crustal condition. Experimental work on mid oceanic basalts suggests that amphibole dehydration melting reaction is often pressure sensitive, sub-horizontal with a slightly negative slope and represents a P-T condition of 10-14kbar and 800-1000 °C (Vielzeuf and Schmidt 2001). Experimental work by several workers (Beard and Lofgren 1991; Rushmer 1991; Sen and Dunn 1994; Wolf and Wyllie

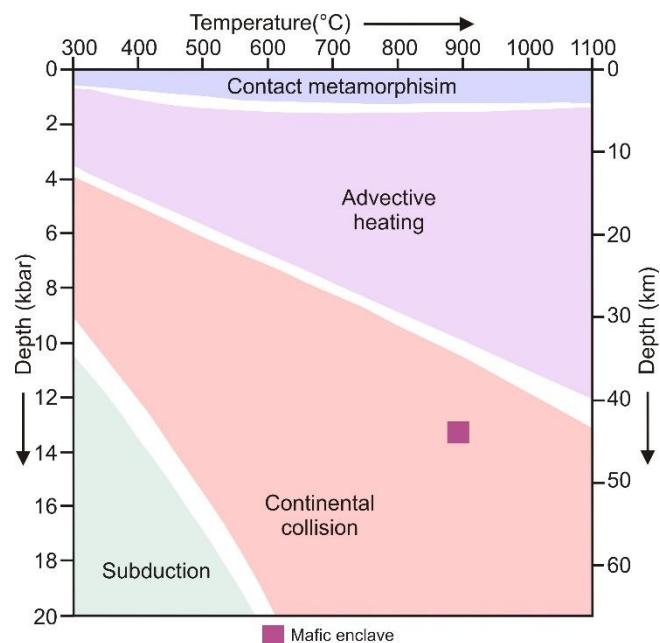


Figure 9.9: Peak metamorphic P-T of the mafic granulite plots well within continental collision field (Brown 2008).

1994; Patiño Douce and Beard 1995; Rapp and Watson 1995) on various basaltic compositions gives a consistent sub-horizontal, slightly negative slope for the reaction. For the forward reaction to produce garnet + clinopyroxene, an increase of pressure is necessary with or without an increase in temperature. The P-T conditions of early retrograde (M_{R1}) assemblage from M_{PK} require a near isothermal decompressive P-T path. M_{R2} assemblage, which re-introduces amphibole in the mafic granulite, indicates a near isobaric cooling path. Reconstructed from mineral assemblages developed at the different stages of metamorphism (M_{PK} to M_{R2}) suggest a clockwise (CW) geometry. The early retrograde near isothermal decompressive P-T path resulted in a pressure drop from 13 kbar to 7 kbar, indicating a rapid exhumation from a depth of lower crust (~43 km) to the middle crust (~23 km). The steeply decompressive retrograde P-T path indicates a post-collisional crustal extension that is common in a continental collisional setup (England and Thompson 1984). CW P-T path in a high pressure metamorphism indicates an event of crustal thickening in a continent-continent collisional tectonic setup (Brown 2008). The estimated peak (M_{PK}) P-T condition (800-900 °C, 13-14 kbar) corresponds to a ~19 °C/km geothermal gradient. The inferred geothermal gradient of ~19 °C/km, is also consistent with a continental collisional tectonic setup (Fig. 9.9) (Brown 2008).

9.1.3.b Composition of the leucosomes and its relation with TTG suites:

Tonalite-trondjemite-granodiorite (TTG) suite of rock accounts for more than 80% of exposed Archean cratons, suggesting these are significant constituents of the Archean continental crust. Despite immense significance in crustal evolution, the origin of these TTG suites of rock is inconclusive (Aranovich et al. 2014). A number of processes have been proposed for the generation of TTG. The major opinions regarding the process (es) of formation of the TTG suites are as follows: (a) Partial melting (reviewed in Moyen and Martin, 2012) (b) fractionation of Amp or Amp-Pl (Johnson et al. 2019; Laurent et al. 2020) from basalt (Jagoutz et al. 2013), diorite (Liou and Guo 2019) or melt derived from enriched lithospheric mantle (Smithies et al. 2019), (c) magma hybridisation during mafic crust partial melting (Hernández-Montenegro et al. 2021), and (d) free fluid flux during metabasalt melting (Tamblyn et al. 2023).

However, anatexis of amphibolites (or hydrated mafic source) appears to be the dominant process (Moyen and Martin 2012; Johnson et al. 2019). One of the major sources of uncertainty regarding the source and process characteristics of the TTG suites is that the

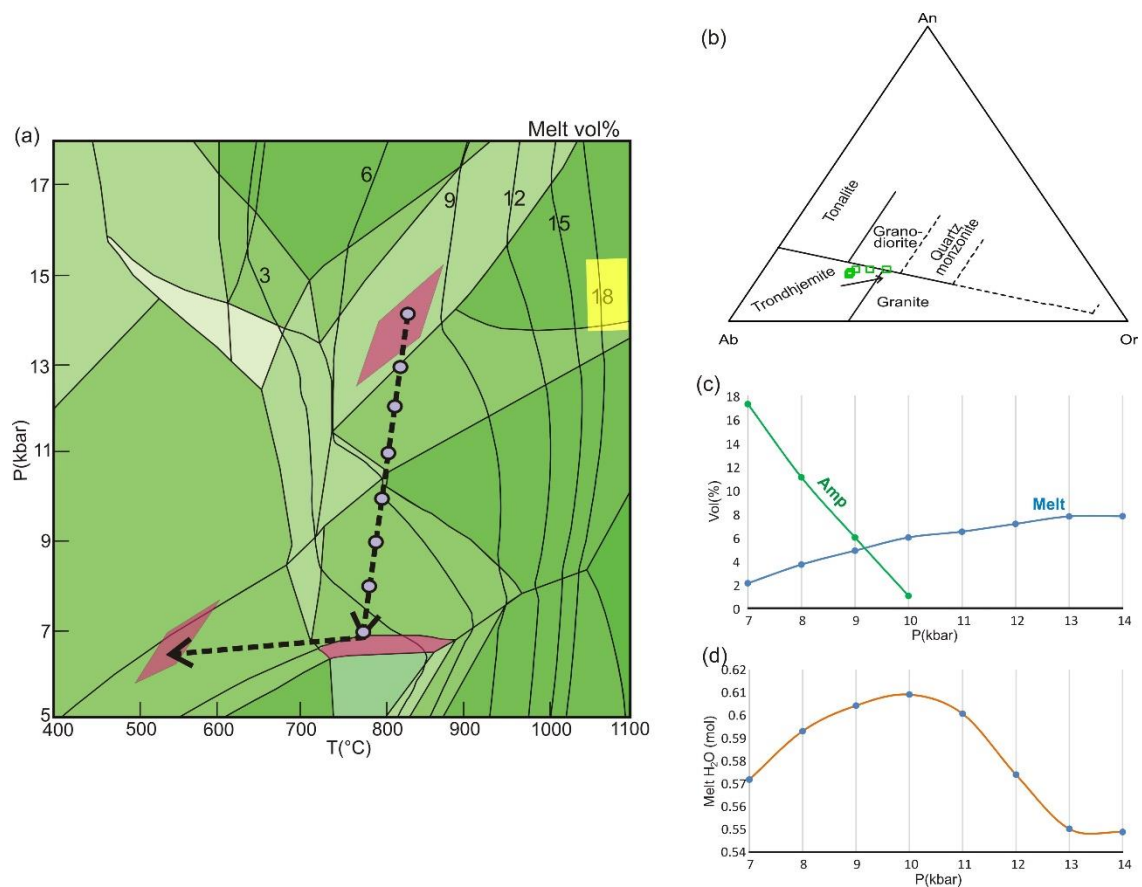


Figure 9.10: (a) P-T pseudosection of the mafic granulite with volume isopleths. Yellow patch marks the T range for melting more than 18 vol% and more. Melt compositions obtained along the decompressive P-T path; compositions are calculated at the blue dots. (b) Melt compositions along the decompressive P-T path plot in the trondhjemite field in the normative Ab-An-Or ternary diagram. (c) From 10 kbar to 7 kbar Amp volume increases from 1 vol% to 18 vol%. From 14 kbar to 7 kbar melt volume gradually decreases. (d) Melt H₂O content increases along the PT path from 14 kbar to 10 kbar; from 10 kbar to 7 kbar, melt H₂O content steadily decreases.

voluminous melt has been segregated from the source, and the source is not exposed. It is shown in the previous sections (Chapter 6) that the leucosomes in the studied rock were derived from the dehydration melting of an amphibolite source. This offers an opportunity to test if the composition of the leucosomal segregation overlaps with the composition of the TTG. Petrographic features do suggest that the leucosome is effectively composed of quartz + plagioclase with a variable proportion of peritectic phases. In view of the intimate association of the peritectic phases and leucosomes, the determination of accurate bulk composition of the latter with conventional methods (namely XRF, ICP) render difficult. To overcome this problem, the quenched melt (leucosome) composition is computed from the P-T pseudosection (Cai et al. 2020). The melt compositions are obtained along the

decompressive P-T path (compositions are calculated at the blue dots; Fig. 9.10.a). These obtained melt compositions plot in the trondjemite field in the normative Ab-An-Or ternary diagram (Fig. 9.10.b).

One of the observations of this study is that garnet, a scavenger of the HREE, is a peritectic phase. Furthermore, phase equilibria modelling (X(Na) isopleth) indicates that with pressure lowering, melt composition moves from trondjemite to granite as potassium content increases with decompression. However, the increase of melt volume with increasing temperature yields a more sodic and ferroan melt that favours the TTG suite of rock formation. The present study does not support large-scale segregation of the partial melt owing to small volume of melt generated (< 15 vol% melt). Volume isoplethed P-T pseudosection (Fig. 9.9.a) suggests that a temperature higher than 1000 °C and beyond is critical for large-scale melting, and this warrants the requirement for a high geothermal gradient for large-scale melting. In the studied mafic granulite, the generation of 18% melt at the peak pressure requires a geothermal gradient of ~25 °C/ km (above ~19 °C/ km of the studied mafic granulites; yellow zone in Fig. 9.10.a). Furthermore, the presence of peritectic garnet in the melting zone will cause the melt to be depleted on HREE, a characteristic of a large proportion of TTG (Moyen and Martin 2012).

This study, therefore, supports the experimental work (Rapp et al. 1991; Wolf and Wyllie 1993) and the view of several workers (reviewed in Moyen and Martin 2012) that partial melting of amphibolites is a viable option for the generation of the TTG suites. Other processes may also be effective in modulating the compositions of the TTG suites. One important factor that controls the large bodies of TTG (relative to the migmatite) seems to be the ambient geothermal gradient. A steep geothermal gradient in the Archaean time could facilitate the melting and fractionation of the melt phase to form large plutons of the TTG. More studies are warranted to understand the genesis of the TTG. Nevertheless, studies on mafic migmatite hold the clue to the genesis of the enigmatic TTG suites.

9.1.3.c Origin of amphibole rich selvages:

Amphibole-rich selvages that develop at the interface between leucosome and melanosome and extensively replace the former warrant an explanation. Growth of such selvage around leucosome in migmatitic rocks is a well-documented phenomenon (Sawyer 2008) and is commonly interpreted as a product of hydration caused by quenching of the felsic melts (leucosome) (Kriegsman and Hensen 1998; Kriegsman 2001; Waters

2001; Brown 2002; White and Powell 2002, 2010). Such hydrous selvage forms by the H_2O released during in-situ crystallisation of anhydrous phases in the leucosomal segregations can form the selvage through back reaction (Kriegsman and Hensen 1998; Kriegsman 2001) or diffusive interaction between melt residue (White and Powell 2010). In the mafic granulite, as melt crystallised in-situ into a relatively anhydrous assemblage, and melt loss (if any) is limited, selvage formation by such a process is quite evident. Melt H_2O content increases along the steeply decompressive PT path (9.10.a) from 14 kbar to 10 kbar (9.10.d); but from 10 kbar to 7 kbar, melt H_2O content steadily decreases (Fig. 9.10.d). This decrease in melt H_2O content at 10 kbar also marks the appearance of Amp (Fig. 9.10.c). From 10 kbar to 7 kbar, the Amp volume increases from 1 vol% to 18 vol%. In the phase equilibria modelling study, the decrease in melt H_2O with the stabilisation of amphibole in the system along the decompressive P-T path also suggests that the melt-released fluid has probably played a role in the formation of amphibole selvage (Fig. 9.10.c-d). However, several features indicate that though crystallization of the precursor melt of the leucosome could form amphibole, an independent hydration event that was caused by infiltration-driven metamorphism seems likely. The features include,

- (a) Selvage formation by melt residue interaction suggests that such extensive amphibole growth is restricted in the melanosome (Kriegsman 2001; Brown 2002; White and Powell 2010), but in the studied area, both metamosome and leucosomes are affected by extensive hydration (amphibole formation).
- (b) Furthermore, amphibole formation is pervasive throughout the mafic granulite (both in melanosome and leucosome) and not restricted to the vicinity of the amphibole-rich selvages selvage.
- (c) Amphiboles do not show any effect of internal deformation and replace recrystallized minerals in both the leucosome and melanosome. This feature suggests that the amphibole formation happened after the solidification and solid-state deformation of the leucosome. In the case of hydration that is triggered by fluid evolved from leucosome, solid state deformation would affect the amphibole in the selvages.
- (d) The proportion of leucosome is small (<15 vol%), and the precursor melt of the same is likely to be undersaturated. Such a small volume of melt is not likely to induce hydration over a large volume of rock (more than the volume of the leucosome)

These features favour probable fluid infiltration from an external source over melt-induced hydration. Fluid infiltration is facilitated along the structurally weak zones (e.g. foliation planes, litho boundaries, cracks etc.). Therefore, the contact between leucosome and melanosome provided a significantly weak zone where the effect of probable fluid infiltration (amphibole formation) would be most prominent. In CGGC, amphibolite facies hydration event by fluid infiltration during the late Tonian period is documented by several studies (Mukherjee et al. 2018b; Dey et al. 2019a). The P-T condition of the hydration event correlates well with the estimated P-T condition of Amp formation during retrogression.

9.1.4 Formation of Ilm-Cpx Symplectite in Mafic granulite:

9.1.4.a Textural modelling of Ilm-Cpx₂symplectite: an algebraic approach

Textural features suggest that the garnet and titanite (\pm rutile) of the primary assemblages in the mafic granulite became unstable and are separated by two types of symplectites. The symplectite of Ilm-Cpx₂(\pm Opx) develops near and variably replaces the titanite. Meanwhile, the symplectite of Cpx₂ + Pl₂ replaces garnet and forms away from the titanite. In another situation, a rind of plagioclase having the same compositions as in Pl₂ develops at the contact of and replaces garnet porphyroblasts. Rutile is found to coexist with garnet but not in the symplectite domains. This raises two possibilities. One likely scenario is that rutile might be consumed during the formation of the Ilm-Cpx₂ symplectite and preserved only where the symplectite did not form. While there exists clinching textural evidence in support of Ilm-Cpx₂ symplectite partially to completely replacing titanite, the role of rutile in the formation of this symplectite remains unclear. In the following section, we will focus on the process that promoted the growth of the Ilm-Cpx₂ and Cpx₂-Plg₂ symplectites after the primary titanite and garnet.

9.1.4.b Formation of symplectites: Solution-precipitation vs volume diffusion:

Two endmember processes, commonly working in tandem, are invoked to explain mineral replacement textures. These are (a) volume diffusion (Lasaga 1981; Ganguly 2002; Watson and Baxter 2007; Chakraborty 2008) and (b) solution reprecipitation (Putnis 2002, 2009; Hellmann et al. 2003; Putnis and Putnis 2007; Ruiz-Agudo et al. 2014). Though both processes can be driven by temperature, each process has its characteristic mechanism of mass transport during the mineral replacement. In the case of the diffusion-driven process, the framework of the mineral being replaced remains essentially intact. Through volume

diffusion, mass transport occurs through the framework during the replacement process (Ganguly 2002; Chakraborty 2008). In the case of a fluid-aided solution and reprecipitation driven process, mineral replacement occurs through the complete destruction of the reactant minerals, and the product phases are formed with new bonds (Putnis 2002, 2009). The replacement process can be isochemical or allochemical (common) depending on the composition of the fluid vis-à-vis the phases being replaced and the ambient physical condition (Putnis and Putnis 2007; Putnis 2009). A number of features suggest that the fluid-mediated solution-reprecipitation process dominated during the formation of Ilm-Cpx₂ symplectite after titanite (with or without rutile). These are:

1. Titanite has triclinic symmetry that is completely different from ilmenite (trigonal) and clinopyroxene (monoclinic). It then follows that the growth of Ilm-Cpx₂ symplectite requires a complete breakdown of all the bonds in the titanite and redistribution of elements, including Ti. The replacement also involves a marked change in chemistry as the reactant titanite contains insignificant FeO and MgO relative to Ilm-Cpx₂. These features are consistent with the fluid-aided solution-reprecipitation process (Putnis and Putnis 2007; Putnis 2009).
2. The original outline of the reactant titanite is conserved during the variable replacement of titanite by Ilm-Cpx₂ symplectite (pseudomorphic replacement). Several studies have demonstrated that pseudomorphic mineral replacement texture is the consequence of the fluid-mediated solution reprecipitation process in which replacement occurs on a nano- to micrometre scale (Putnis 2009; Ruiz-Agudo et al. 2014). The wavy/ bulbous outline of the protruding Ilm-Cpx₂ front into the titanite (Fig. 3a-b) also supports the solution-reprecipitation process.
3. The Ilm-Cpx₂ symplectite contains tiny apatite with significant F and Cl. Since the primary assemblage does not have any sink of P or the halogens, only a fluid-mediated process can explain the texture.
4. The Ilm-Cpx₂ symplectite is commonly associated with Pl₂-Cpx₂ symplectite that preferentially replaces garnet porphyroblasts. Plagioclase in the symplectite contains a significant albite molecule (Ab 15-25%). Since the garnet composition cannot account for the Na in the symplectic plagioclase, Na must be supplied by the fluid.

9.1.4.c Mobility of chemical species during the formation of Ilm-Cpx₂ symplectite:

The mass-balanced reactions (Reaction 1-2; Chapter 7) obtained from textural modelling studies suggest the mobility of several chemical species across the initial boundary between garnet and titanite. In Domain I, wherein Cpx₂ did not develop with Pl₂, the breakdown of garnet to plagioclase rind releases FeO, MgO, and CaO by the reaction (Fig. 9.10.). These chemical species moved to and reacted with the titanite by a fluid-mediated process to produce Ilm-Cpx₂ by reaction (Fig. 9.11.a). This feedback mechanism can explain the complete and partial decomposition of titanite and garnet in Domain I (Fig. 9.11.a). Both reactions (1.a-b; Chapter 7) consume Na₂O. Furthermore, F, Cl-bearing apatite formed as a part of the Ilm-Cpx₂ symplectite. These observations require that the infiltrated fluid also supplied P₂O₅, Na₂O, and halogens.

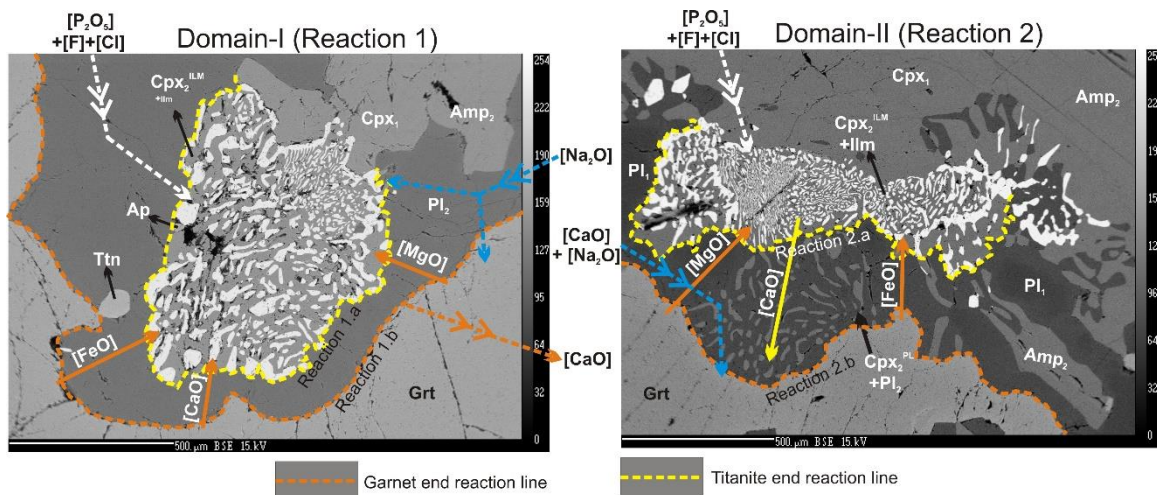


Figure 9.11: (a-b) Textural modelling studies from Domain I-II suggest the mobility of several chemical species across the initial boundary between garnet and titanite. FeO and MgO are moving from the garnet end toward the titanite end in both domains. P₂O₅, Na₂O, F, and Cl come from external sources in both domains. The direction of CaO movement is reversed between Domain I and II. Domain II requires an external source of CaO, while Domain I releases CaO outside.

A similar feedback mechanism also seems to have prevailed in Domain II, where Cpx₂-Pl₂ symplectite formed after garnet (Fig. 9.11.b). However, in contrast to Domain I, CaO in Domain II moved from the titanite end (now completely replaced with Ilm-Cpx₂-Opx intergrowth) to the garnet end (Fig. 9.11.b). Since quartz is present in the rock, it is presumed that the symplectite forming reactions consumed the quartz in Domains I and II.

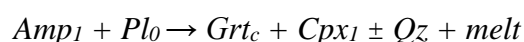
X-ray intensity map of Ti and the modelled symplectite forming reactions in both domains suggest that Ti was not mobile beyond the volume of the initial titanite grain.

However, the lamellar intergrowth of Ilm-Cpx₂ does support that Ti was locally mobile in the scale defined by the interlamellar space (Abart et al. 2012; Remmert et al. 2018) between Ilm lamellae. The interlamellar space between the lamellar ilmenite rods ranges from ~2-55µm in Domains I and II. Coarsening of the fine rods of ilmenite to bigger lamellae further attests to the view that Ti was indeed mobile, but its length scale of mobility was much smaller than the mobility of FeO, MgO, and CaO (Fig. 9.11.a-b). The length scale of mobility of the latter species covered the whole width of the product phases that develop between titanite and garnet (Fig. 9.11.a-b). Owing to the smaller size of the titanite (than garnet) and the length scale of the transport of FeO, MgO, and CaO, completely replaced the titanite with the Ilm-Cpx₂ (±Opx) symplectite in both Domains I and II. The solubility of TiO₂ is low in pure H₂O or even in alkali, silica-bearing hydrous fluids (Audétat and Keppler 2005; Tropper and Manning 2005; Antignano and Manning 2008; Lucassen et al. 2010; Hayden and Manning 2011); however, the presence of halogens can significantly enhance the solubility of TiO₂ in the aqueous fluids (Purtov and Kotel'nikova 1993; Ryzhenko et al. 2006; Antignano and Manning 2008; Rapp et al. 2010; Hayden and Manning 2011; Tanis et al. 2016; Karmakar 2021). The presence of significant F and Cl in apatite granules within Ilm-Cpx₂ symplectite supports the view that segregations of ilmenite in the Ilm-Cpx₂(±Opx) symplectites were formed in the presence of a halogen-bearing fluid. This fluid helped the migration of Ti in the length scale of the interlamellar space of the Ilm rods (Abart et al. 2012; Remmert et al. 2018). Very low concentrations of halogen in secondary amphibole that replaced the Ilm-Cpx₂ symplectite can be explained by the greater affinity of halogens in apatite structure relative to amphibole. The Ti content of amphibole is higher than the two minerals (Cpx and garnet) that it extensively replaces, and textural features (7.2.e-f; Chapter 7) suggest that any one or all of the Ti-bearing accessory phases can be responsible.

9.1.4.d Formation of Ilm-Cpx₂: the control of metamorphic P-T path

The foregoing analyses (physical condition of metamorphism) by different methods of P-T calculations suggest that the primary granoblastic assemblages (including both titanite and rutile) were formed in the realm of high pressure and high temperature (800-850°C and 12-14 kbar) in the presence of partial melt. Studies have shown that melting and accompanying thermal maxima (T_{\max}) in the high- to ultrahigh-pressure metamorphism can occur at a pressure that is significantly lower than the P_{\max} (maximum pressure). The “decompression melting” phenomenon has been documented in several areas (Groppo et

al. 2012; Chen et al. 2017; Deng et al. 2018; Liu and Massonne 2022). It is, therefore, difficult to identify if the pressure of 12-13 kbar represents the P_{\max} or if the primary granuloblastic assemblage achieved this pressure during decompression and melting. High temperature metamorphism in the studied area homogenized the primary porphyroblastic phases. However, the presence of amphibole (Amp_0) and plagioclase (Pl_0) as inclusion phases in garnet and clinopyroxene (Cpx_1) suggests the dehydration melting reaction (detailed in Chapter 6),



This reaction has been inferred to explain the formation of mafic migmatites during high pressure and temperature metamorphism (Vielzeuf and Schmidt 2001; Pattison 2003; Watkins et al. 2007).

If the estimated P-T values of the primary granuloblastic assemblage and the Ilm-Cpx₂ symplectite are joined, a steeply decompressive retrogressed P-T path results. The volume increase (6.5-7.5 %) that is predicted by the texturally modelled chemical reactions (Reaction 1-2; Chapter 7) is consistent with the view that the Ilm-Cpx₂ were formed on the steeply decompressive retrograde P-T path. Though the textural modelling was done with titanite in the chosen microdomains, rutile could also participate in other symplectic domains that are not studied here. The computed pseudosection shows the presence of a melt phase even when the symplectites were formed. Based on textural evidence and the computed phase diagram, it seems likely that the secondary amphibole formed after the formation of the clinopyroxene-bearing symplectite, presumably during cooling. In complete hydration of the granulite facies, assemblage could be governed by several factors, including ease of fluid movement and the abeyant physical conditions.

9.1.5 Metamorphic condition of the metamafic dyke:

Metamafic dyke in continental crust represents an extensional tectonic regime (Condie 1997). Extension of continental crust and the mantle beneath is crucial in generating mafic magma in dyke formation (Condie 1997). Deformation and metamorphism of metamafic dykes signify a change in tectonic regime from extensional to compressional (Barton et al. 1990; Kuehner and Green 1991; Sengupta 1993; Bleeker and Ernst 2006; Bhui et al. 2007; Ernst and Bleeker 2010; Hou 2012). Owing to intense infiltration-driven metamorphism and accompanied deformation, the magmatic assemblage of the dyke has been overprinted

by amphibolite facies metamorphism. The present study suggests that the deformation and metamorphism of the metamafic dykes culminated at 600-700 °C and 6.5-7 kbar pressure that corresponds to the crustal depth 22-24 km and a geothermal gradient of 25-30 km/ °C. This is similar to the metamorphic conditions reported from the adjoining metamorphic rocks.

9.2 Tectono-thermal events in the CGGC in the backdrop of the present study:

Based on the existing geochronological database, the tectonothermal events of CGGC broadly cluster into four segments throughout the Proterozoic eon. These events manifest as major magmatic and metamorphic episodes of the CGGC. This section attempts to correlate the magmatic and metamorphic events recorded from the studied rocks with that from other parts of the CGGC.

9.2.1 Paleoproterozoic era:

9.2.1.a I-type granite magmatism:

Late Palaeoproterozoic time records the oldest tectonothermal event of the CGGC (ca. 1750-1640 Ma; Mallik et al. 1991; Ray Barman et al. 1994; Chatterjee and Ghose 2011; Rekha et al. 2011; Saikia et al. 2017; Dey et al. 2019c; Mukherjee et al. 2019). Saikia et al. (2017) documented widespread felsic magmatism from the Bathani Volcano-sedimentary Sequence (BVSS) in the NW part of the terrain between ~1750-1660 Ma. The north-eastern part of the terrain (Dumka-Deoghar) also records Paleoproterozoic felsic magmatism between ~1710-1635 Ma. (Mukherjee et al. 2019a). Geochemical features constrain this as I-type granite magmatism from a crustal source at shallow depth in a continental arc setting (Saikia et al. 2017; Mukherjee et al. 2019a). Acharyya (2003) reported similar ages (1624 ± 5 Ma) for the hypersthene gneiss from the study area. Geochemically, these rocks are similar to the migmatitic felsic gneiss (MFG) studied here, which also indicates I-type granite magmatism with similar source characteristics in a continental arc setup.

9.2.1.b High grade metamorphism (M1):

Coeval metamorphic events (M1; ~1650 Ma.) accompany this widespread Paleoproterozoic magmatism (Mallik et al. 1991; Chatterjee and Ghose 2011; Rekha et al. 2011; Sanyal and Sengupta 2012; Dey et al. 2019c). In the northeastern fringe of the CGGC, the Paleoproterozoic metamorphic imprints have been documented only in the metapelitic enclaves but not in the host felsic orthogneisses (Dey et al. 2019c). Dey et al. (2019b) associated the burial of ~1700-1680 Ma supracrustals (Dey et al. 2017) to a significant crustal depth with the continental collisional event during the Paleoproterozoic (1580-1680 Ma) high temperature (>850 °C) metamorphic event (M1). Asthenospheric upwelling by the delamination of the mantle lithosphere during the waning stage of the continental collision was inferred to have provided the necessary heat for this high temperature metamorphism (Dey et al. 2019c). High-grade metamorphism of the pelitic lithounits at ~1638 Ma from the Daltonganj region located in the northwestern fringe of the terrain also demonstrates continent-continent collision tectonic setup (Kumar et al. 2022a). Similarly, the mafic granulites studied here are present as enclaves within the felsic orthogneisses and bear foliation (S1) that truncate the regional fabric of host felsic orthogneiss (S2-S3), suggesting preservation of an older metamorphic and deformation event (before S2 formation). The steeply decompressive CW P-T path and the inferred peak metamorphic geothermal gradient of ~19 °C/km indicate continent-continent collision that correlates well with the inferred Paleoproterozoic continental collisional event. Nevertheless, the tectonic setup is consistent with an active convergent margin of the Paleoproterozoic I-type magmatism.

9.2.2 Mesoproterozoic era: A-type granite magmatism

Emplacement of the Bankura anorthosite (1550 ±12 Ma, U-Pb zircon age) near the SE margin of the terrain (Domain IA) is inferred as post-orogenic magmatism (Chatterjee et al. 2008). From the north eastern fringe (Dumka-Deoghar; Domain IB) of the terrain, intrusion of ferroan (A-type) granites (~1450 Ma, U-Pb zircon age) within the Paleoproterozoic crust has been documented (Mukherjee et al. 2017, 2018a). A syenite body revealing an intrusion age of 1457±63 Ma has also been reported close to Dumka (Ray Barman et al. 1994). A widespread intrusion of ferroan (A-type) granitoids expanding from Domain IB, Domain II and Domain III has been reported by Sequeira et al. (2022). The charnockite-granite association from the study area is surrounded by a vast area of ferroan granite batholiths (Mukherjee et al. 2018a, 2022; Sequeira et al. 2022). The ferroan

granitoids (metaporphyrific charnockite and biotite gneiss) studied here, also intrude the arc granites (I-type granites) and bear profound similarity in geochemical signatures with the A-type granites from the other parts of the terrain. Resembling ferroan granitoids from other parts of CGGC, both metaporphyrific charnockite and biotite gneiss, assert the dominance of crustal components in the source. Post-emplacement crystal fractionation played a major role in generating ferroan igneous charnockites (metaporphyrific charnockite) and associated ferroan granites (biotite gneiss) in the study area. A similar influence of crystal fractionation on A-type granites is evident from the other parts (Mukherjee et al. 2018a, 2022; Sequeira et al. 2022). Similar Mesoproterozoic age (1515 ± 5 Ma) from charnockites are reported from the study area (Acharyya 2003). In accordance with other parts of the CGGC, the studied ferroan granitoid vouches for a widespread extensional tectonic regime manifested by continental rift setup magmatism during the Mesoproterozoic times.

9.2.3 Neoproterozoic era:

9.2.3.a Early Neoproterozoic metamorphism (M2):

The third major tectonothermal event of CGGC is represented by the high-grade granulite facies metamorphism (M2). The high grade M2 metamorphism is the most pervasive metamorphic event documented from various parts of the CGGC during the early Neoproterozoic (ca. 1000-950 Ma; Chatterjee et al. 2010; Chatterjee and Ghose 2011; Karmakar et al. 2011; Mukherjee et al. 2017; Dey et al. 2019b, 2019a; Kumar et al. 2022b; Roy Choudhury et al. 2023). In the study area, M2 metamorphism is manifested by the development of pervasive E-W trending

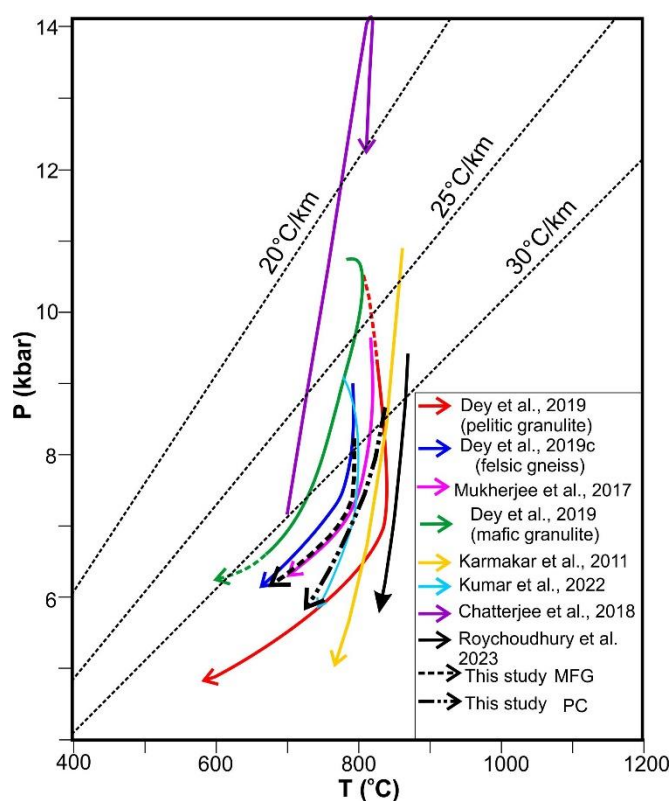


Figure 9.12: Metamorphic P-T path of metaporphyrific charnockite (PC) and migmatitic felsic gneiss (MFG) exhibit similar P-T conditions that have been constrained for the ~950 Ma M2 metamorphism from various parts of CGGC.

S2 fabric that prevails in all the felsic orthogneisses documented in the study area. In the migmatitic felsic gneiss, M2 metamorphism corresponds to high-grade granulite facies metamorphism (defined by the anhydrous phase assemblage of Grt-Opx and leucosomal segregations along S2) at peak metamorphic P-T condition of 700-800 °C; 7.5-8 kbar along 26-28 °C/km geothermal gradient followed by decompression. Similarly, M2 metamorphism in the ferroan granitoids corresponds to granulite facies conditions of 750-800°C and 8-8.5 kbar along 25-30 km/ °C geothermal gradient, which is followed by steep decompression. The metamorphic conditions correspond to continental collisional orogeny. Similar CW P-T paths (Fig. 9.12) and tectonic setups have been constrained for the ~950 Ma M2 metamorphism from various parts

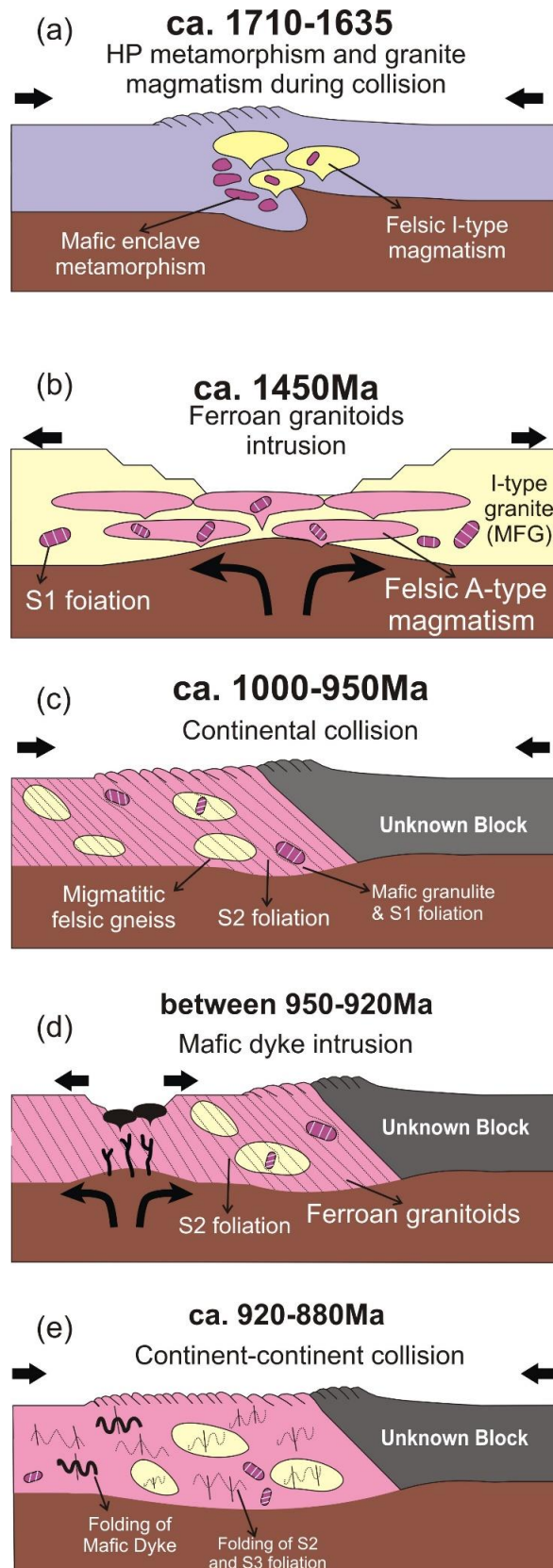


Figure 9.13: Schematic diagram describing the tectonic evolution of the CGGC. (a) Paleoproterozoic tectonic convergence resulted in arc magmatism, mafic granulite metamorphism, and S1 fabric generation. (b) Mesoproterozoic tectonic extension resulting in felsic ferroan magmatism. (c) Early Neoproterozoic continental collision and S2 fabric generation. (d) Brief Neoproterozoic extension resulted in mafic dyke intrusion. (e) Late Neoproterozoic continental collision and folding of S2, generating S3 fabric.

of CGGC (Chatterjee et al. 2010; Chatterjee and Ghose 2011; Karmakar et al. 2011; Mukherjee et al. 2017; Chatterjee 2018; Dey et al. 2019b, 2019a; R. R. Kumar et al. 2022b; Roy Choudhury et al. 2023a).

9.2.3.b Neoproterozoic Magmatism:

In the study area, Neoproterozoic magmatism is manifested by intrusive mafic dykes that intruded the crust after the granulite grade M2 metamorphism. Similar mafic dyke intrusion in the post-Grenvillian times is reported from the NE (Dumka-Deoghar; Mukherjee et al. 2018b) and SW (Simdega area; D. Kumar et al. 2022) parts of the terrain. A similar extension-related Neoproterozoic magmatism of nepheline syenite between 950-900 Ma was reported from the NPSZ (Das et al. 2019). Peralkaline anorogenic granitoid intrusion (~966 Ma) is also reported from the NPSZ (Chakraborty et al. 2022). Apart from these, relatively older (~1000 Ma) syn-collisional S-type granites are reported from the SE region of the terrain. Calc-alkaline lamprophyre intrusion is documented from the Simdega area of CGGC at ~944 Ma (Kumar et al. 2023).

9.2.3.c Late Neoproterozoic metamorphism (M3):

The last major tectonothermal event in the CGGC is the M3 metamorphism during the late Tonian period. The metamorphic conditions of M3 culminate at amphibolite facies conditions (Mukherjee et al. 2018b; Dey et al. 2019b, 2019a; Roy Choudhury et al. 2023b). From the Dumka-Deoghar sector, Mukherjee et al. (2018b) constrained the amphibolite facies metamorphism (M3) at ~902 Ma and similar age of M3 metamorphic event is documented from several parts of the CGGC (Karmakar et al. 2011; Dey et al. 2019c; D. Kumar et al. 2022). A ~870-780 Ma event, characterized by high-pressure metamorphism and N-S foliation along the eastern boundary of the CGGC and NSFB, has also been constrained as the "Eastern Indian Tectonic Zone" (EITZ) by Chatterjee, 2018; Chatterjee et al., 2010. In the Dumka Deoghar sector, M3 metamorphism resulted in the amphibolite facies metamorphism of the mafic dykes (Mukherjee et al. 2018b). M3 event has also been associated with fluid-infiltration driven metamorphism that led to the formation of garnet-vesuvianite assemblage (Dey et al. 2019b), as well as the enrichment of titanites by Al, F in the calc-silicate rocks (Roy Choudhury et al. 2023b) in this sector. M3 metamorphism has also been documented from the mafic granulites and felsic orthogneisses from the Dumka Deoghar region. These studies constrain a P-T condition of 600-700°C and 6-7 kbar

pressure. Mafic dykes from the Simdega area in the southwestern part of CGGC also manifest similar P-T conditions of M3 metamorphism (D. Kumar et al. 2022). Mukherjee et al. (2018b) associated the M3 metamorphism with continent-continent collisional setup having a peak metamorphic geothermal gradient of $\sim 25\text{-}30^\circ\text{C}/\text{km}$. In the present study area, the deformation related to M3 metamorphism resulted in the folding of the pervasive S2 fabric and the formation of S3 foliation parallel to the E-W trending axial plane. S3 foliation is defined by hydrous phases (e.g. amphibole and biotite). It also resulted in the folding and deformation of the intrusive mafic dykes. In the Metamafic dykes, M3 is characterised by amphibolite facies ($600\text{-}700^\circ\text{C}$, 6.5-7 kbar) metamorphism that overprinted the Cpx-Opx bearing magmatic assemblage with dominant amphibole and minor garnet. The peak metamorphic geothermal gradient of $25\text{-}30^\circ\text{C}/\text{km}$ indicates a possible continental collisional setting. The M3 event also resulted in the hydration (M_{R2}) of the mafic granulite that resulted in pervasive growth of amphibole in the mafic granulite at $\sim 600^\circ\text{C}$ and 6.5-7 kbar pressure. P-T conditions of amphibole formation in mafic granulites and intrusive metamafic dykes are the same. M3 metamorphic event culminating in the amphibolite facies metamorphism represents continental collisional tectonic setup.

9.3 Correlation between CGGC and Proterozoic Indian landmass in context with supercontinental cycle:

9.3.1 Paleoproterozoic CGGC and adjacent terrains: Implication for Columbia assembly

The Paleoproterozoic crustal evolution of the CGGC is predominantly represented by continental collisional orogeny, UHT metamorphism (during the waning stage of orogeny) and arc magmatism. Contemporaneous arc magmatism (ca. 1750 Ma.) has been reported from the Mahakoshal belt (Bora et al. 2013) and the Makrohar granulite belt (Chakrabarty et al. 2023) in CGGC. Paleoproterozoic high-grade metamorphism has also been documented from the Mahakoshal belt ($\sim 1800\text{-}1600$ Ma; Deshmukh et al. 2017) and Balaghat-Bhandara Granulite Belt (~ 1600 Ma; Bhowmik et al. 2005; Bhandari et al. 2011) of CITZ.

Late Palaeoproterozoic (ca. 1.8-1.6 Ga) tectonothermal events have been reported from the Shillong Meghalaya gneissic complex (SMGC). The intrusion of ~1780-1630 Ma granitoids has been reported from Rongjeng and Guwahati area (Kumar et al. 2017). Geochemical characters indicate syn-collisional magmatism of the dominant crustal source (Kumar et al. 2017). Concurrent high-grade metamorphism (850°C and 7-8 Kbar) has also been reported from the pelitic enclaves during ~1600 Ma from SMGC (Chatterjee et al. 2007; Chatterjee and Ghose 2011). In coherence with CGGC and SMGC, the basement rocks of the Bengal basin record ~1700-1650 Ma felsic magmatism with predominant subduction to syn-collisional affinity (Ameen et al. 2007, 2022; Hossain et al. 2007).

Palaeoproterozoic arc magmatism has also been reported from the Aravalli-Delhi fold belt between ~1860- 1810 Ma from a dominant Archean source (Kaur et al. 2009, 2017). Evidence of granulite grade metamorphism, which took place at approximately 1740-1580 Ma, is preserved in the Sandmata complex of the Aravalli Delhi fold belt (Roy et al. 2006; Buick et al. 2010). The terrane is intruded by pre to synchronous calc-alkaline granitic magmatism (Wiedenbeck et al. 1996; Biju-Sekhar et al. 2003; Roy et al. 2006; Bhowmik et al. 2010; Erickson et al. 2015). Eastern Ghats Mobile Belt (EGMB) also records

Palaeoproterozoic magmatism of arc setting between 1750 and 1710 Ma from the Ongole domain (Sarkar et al. 2015). Similar to CGGC, the Ongole domain records UHT metamorphism at ca. 1610 Ma (Sengupta et al. 1999; Sarkar and Schenk 2014; Sarkar et al. 2014).

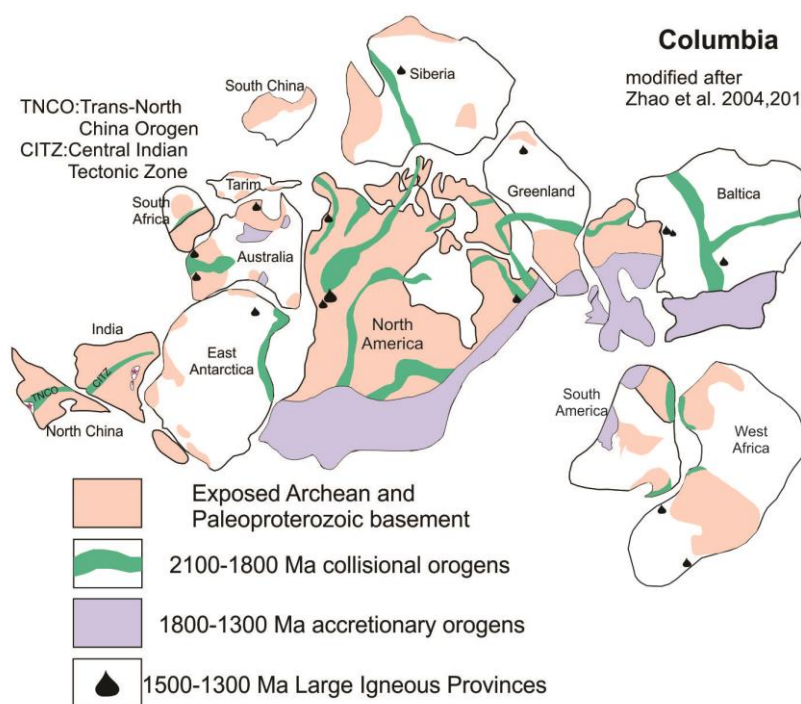


Figure 9.14 Configuration of the columbia supercontinent

Felsic to intermediate arc-affinity magmatism was attested during 1791-1771 Ma

from the Vinjamuru domain (Vadlamani et al. 2013). Late Palaeoproterozoic arc magmatism from different parts of the Lower Lesser Himalayas reveal intrusion ages between 1880-1740 Ma. and constrain an arc affinity of magmatism (Miller et al. 2000; Richards et al. 2005; Chambers et al. 2008; Kohn et al. 2010; Rameshwar Rao and Sharma 2011).

Similar temporal and tectonic settings in the aforementioned terrain support the view that the north and south Indian landmasses merged to form the unified "Greater Indian Landmass," at least from the late Palaeoproterozoic (~1700-1600 Ma). Contemporaneous orogenic imprints have also been identified from Kemp land of Antarctica (Kelly et al. 2002; Halpin et al. 2005, 2007a). The existence of coeval orogenic fronts in parts of East Antarctica and India suggests that the East Antarctica blocks were juxtaposed against the amalgamated north and south Indian blocks during the Paleoproterozoic times. The Paleoproterozoic arc magmatism is correlated with the assembly of the Columbia supercontinent by several studies (Kohn et al. 2010; Rameshwar Rao and Sharma 2011; Chakrabarty et al. 2023). The widespread Paleoproterozoic events from different parts of the world (Australia, Antarctica and southwest Africa; summarized in Sarkar and Schenk 2016) in combination with India, east Antarctica advocates for the assembly of the Columbia supercontinent (Zhao et al. 2011).

9.3.2 Mesoproterozoic CGGC and adjacent terrains: Implication for Columbia breakup

Mesoproterozoic ferroan magmatism of CGGC suggests a widespread extensional tectonic regime during the time. Apart from the widespread occurrence in CGGC, the Mesoproterozoic ferroan magmatism is scarce and reported primarily from the western margin of the Eastern Ghats belt and recently from a few localities of the CITZ. Emplacement of A-type granites and alkaline rocks have been constrained between ~1590-1350 Ma (Dobmeier et al. 2006; Upadhyay and Raith 2006; Vijaya Kumar et al. 2007) in the western margin of the Eastern Ghats belt. Mesoproterozoic ferroan magmatism is also reported from the Makrohar granulite belt (Yadav et al. 2023) and Sauser belt (Bose et al. 2023) in the CITZ at 1498 ± 38 Ma and 1322 ± 3 Ma respectively. The Mesoproterozoic ferroan magmatism is widely reported worldwide and linked with the disintegration of the

Columbia supercontinent (Dall'Agnol et al. 2012; Frost and Frost 2013). The Mesoproterozoic ferroan magmatism in the CGGC and CITZ are also correlated to the extensional regime that prevailed during Columbia breakdown by several studies (Mukherjee et al. 2018a; Sequeira et al. 2022; Bose et al. 2023; Yadav et al. 2023).

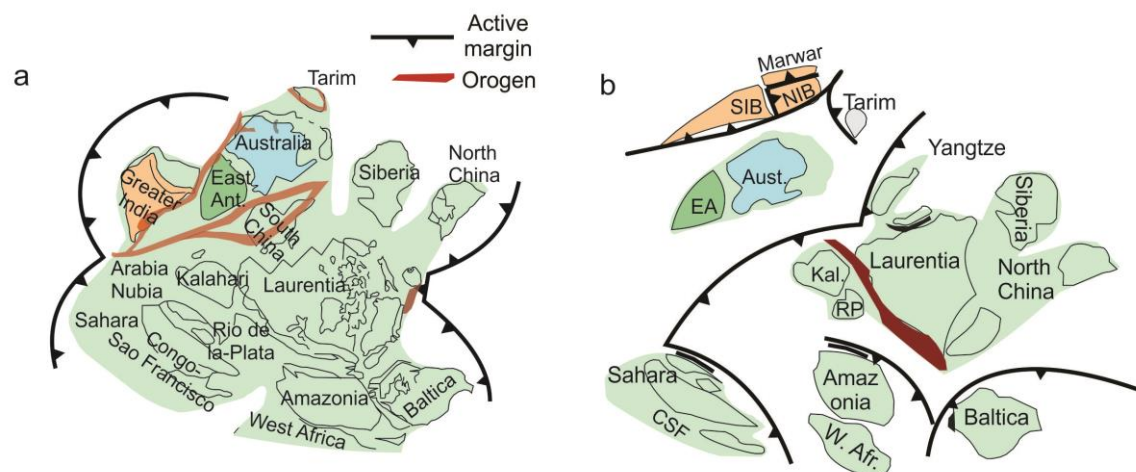


Figure 9.15 Configuration of the Rodinia supercontinent modified after Zhao et al. 2004

9.3.3 Neoproterozoic CGGC and adjacent terrains: Implication for Rodinia assembly

The early Neoproterozoic tectonothermal event (M2) in CGGC is characterised by high-grade metamorphism and steeply decompressive CW PT path that is inferred to be a continental collisional setting. A slightly younger (late Tonian) amphibolite facies collisional orogeny in CGGC (M3) is punctuated by a brief period of extension that resulted in the Mafic dyke intrusion in the study area as well as in the other parts (Mukherjee et al. 2018b; D. Kumar et al. 2022). The Neoproterozoic orogenic imprints are also widely reported from adjacent terrains. Contemporaneous clockwise P-T path within a continent-continent collisional setting has been documented in the different parts of the CITZ including the Sausar mobile belt (~1060-940 Ma), the Gavligarh–Tan Shear Zone (~1000-950 Ma), the Ramakona-Katangi granulite belt (~1040-940 Ma) and the Makrohar Granulite Belt (~974-913 Ma) (Bhandari et al. 2011; Bhowmik et al. 2012; Chattopadhyay et al. 2015; Deshmukh and Prabhakar 2020; Chakrabarty et al. 2022). Coeval (~1000-900 Ma) high pressure granulite facies metamorphism in continental collisional orogeny has been reported in the EGMB (Das et al. 2011; Korhonen et al. 2013; Enakshi et al. 2017;

Mitchell et al. 2019) Late Tonian (~900-800 Ma) collisional imprints are also documented from the EGMB (Dobmeier and Simmat 2002; Simmat and Raith 2008; Korhonen et al. 2013; Chattopadhyay et al. 2015) and Aravalli-Delhi fold Belt (~910-810 Ma) (Bhowmik et al. 2010; Chattopadhyay et al. 2017; Dasgupta et al. 2017).

Apart from the adjacent terrains, similar contemporaneous orogenic imprints are widely reported from the Rayner complex in east Antarctica (Dunkley et al. 2002; Kelly et al. 2002; Kelly and Harley 2004; Halpin et al. 2005, 2007b, 2007a). Both early and late Tonian metamorphism are reported from the Rayner Complex (Kelly et al. 2002; Asami et al. 2005; Shiraishi et al. 2008). Integrating all the available information, it is evident that the Stenian-Tonian orogenic events that encompass the Proterozoic terranes of ADFB, EGMB, CITZ and CGGC demarcate the final amalgamation of the northern and southern Indian blocks during the accretion of Rodinia supercontinent. The Neoproterozoic P-T paths documented from various crustal segments of the Indian shield and east Antarctica show a remarkable similarity. These characteristics provide credence to the notion that the Indian shield (comprising the CGGC, CITZ and EGMB) and east Antarctica formed a coherent landmass during the assembly of the Rodinia supercontinent (Dasgupta et al. 2017; Mukherjee et al. 2019b).

References

- Abart, R., Petrishcheva, E., and Joachim, B. (2012) Thermodynamic model for growth of reaction rims with lamellar microstructure. *American Mineralogist*, 97, 231–240.
- Acharyya, S.K. (2003) The Nature of Mesoproterozoic Central Indian Tectonic Zone with Exhumed and Reworked Older Granulites. *Gondwana Research*, 6, 197–214.
- Ameen, S.M.M., Wilde, S.A., Kabir, M.Z., Akon, E., Chowdhury, K.R., and Khan, M.S.H. (2007) Paleoproterozoic granitoids in the basement of Bangladesh: A piece of the Indian shield or an exotic fragment of the Gondwana jigsaw? *Gondwana Research*, 12, 380–387.
- Ameen, S.M.M., Wilde, S.A., Hossain, M.S., Das, S.C., Tapu, A.-T., Zaman, M.N., and Sarma, D.S. (2022) Episodic Proterozoic magmatism in Northwest Bangladesh: Implications for Columbia/Nuna and Rodinia reconstructions. *Lithos*, 412–413, 106586.
- Anderson, I.Carl, Frost, C.D., and Frost, B.R. (2003) Petrogenesis of the Red Mountain pluton, Laramie anorthosite complex, Wyoming: implications for the origin of A-type

- granite. *Precambrian Research*, 124, 243–267.
- Anderson, I. Carl, Frost, C.D., and Frost, B.R. (2003) Petrogenesis of the Red Mountain pluton, Laramie anorthosite complex, Wyoming: Implications for the origin of A-type granite. *Precambrian Research*, 124, 243–267.
- Anderson, J.L. (1983) Proterozoic anorogenic granite plutonism of North America. *Geological Society of America Memoir*, 161, 133–154.
- Annen, C., BLUNDY, J.D., and SPARKS, R.S.J. (2006) The Genesis of Intermediate and Silicic Magmas in Deep Crustal Hot Zones. *Journal of Petrology*, 47, 505–539.
- Antignano, A., and Manning, C.E. (2008) Rutile solubility in H₂O, H₂O-SiO₂, and H₂O-NaAlSi₃O₈ fluids at 0.7-2.0 GPa and 700-1000 °C: Implications for mobility of nominally insoluble elements. *Chemical Geology*, 255, 283–293.
- Aranovich, L.Y., Makhluif, A.R., Manning, C.E., and Newton, R.C. (2014) Dehydration melting and the relationship between granites and granulites. *Precambrian Research*, 253, 26–37.
- Asami, M., Suzuki, K., and Grew, E. (2005) Monazite and Zircon Dating by the Chemical Th-U-Total Pb Isochron Method (CHIME) from Alasheyev Bight to the Sør Rondane Mountains, East Antarctica: A Reconnaissance Study of the Mozambique Suture in Eastern Queen Maud Land. *Journal of Geology - J GEOL*, 113, 59–82.
- Audétat, A., and Keppler, H. (2005) Solubility of rutile in subduction zone fluids, as determined by experiments in the hydrothermal diamond anvil cell. *Earth and Planetary Science Letters*, 232, 393–402.
- Barton, J.M., van Reenen, D.D., and Roering, C. (1990) The significance of 3000 Ma granulite-facies mafic dikes in the central zone of the Limpopo belt, southern Africa. *Precambrian Research*, 48, 299–308.
- Beard, J.S., and Lofgren, G.E. (1991) Dehydration melting and water-saturated melting of basaltic and andesitic greenstones and amphibolites at 1, 3, and 6. 9 kb. *Journal of Petrology*, 32, 365–401.
- Bhandari, A., Chandra Pant, N., Bhowmik, S.K., and Goswami, S. (2011) ~1.6 Ga ultrahigh-temperature granulite metamorphism in the Central Indian Tectonic Zone: insights from metamorphic reaction history, geothermobarometry and monazite chemical ages. *Geological Journal*, 46, 198–216.
- Bhowmik, S.K., Sarbadhikari, A.B., Spiering, B., and Raith, M.M. (2005) Mesoproterozoic Reworking of Palaeoproterozoic Ultrahigh-temperature Granulites in the Central Indian Tectonic Zone and its Implications. *Journal of Petrology*, 46, 1085–1119.

- Bhowmik, S.K., Bernhardt, H.-J., and Dasgupta, S. (2010) Grenvillian age high-pressure upper amphibolite-granulite metamorphism in the Aravalli-Delhi Mobile Belt, Northwestern India: New evidence from monazite chemical age and its implication. *Precambrian Research*, 178, 168–184.
- Bhowmik, S.K., Wilde, S.A., Bhandari, A., Pal, T., and Pant, N.C. (2012) Growth of the Greater Indian Landmass and its assembly in Rodinia: Geochronological evidence from the Central Indian Tectonic Zone. *Gondwana Research*, 22, 54–72.
- Bhui, U.K., Sengupta, Pulak, and Sengupta, Pranesh (2007) Phase relations in mafic dykes and their host rocks from Kondapalle, Andhra Pradesh, India: Implications for the time–depth trajectory of the Palaeoproterozoic (late Archaean?) granulites from southern Eastern Ghats Belt. *Precambrian Research*, 156, 153–174.
- Biju-Sekhar, S., Yokoyama, K., Pandit, M.K., Okudaira, T., Yoshida, M., and Santosh, M. (2003) Late Paleoproterozoic magmatism in Delhi Fold Belt, NW India and its implication: evidence from EPMA chemical ages of zircons. *Journal of Asian Earth Sciences*, 22, 189–207.
- Bleeker, W., and Ernst, R. (2006) Short-lived mantle generated magmatic events and their dyke swarms: The key unlocking Earth’s paleogeographic record back to 2.6 Ga. Dyke Swarms - Time Markers of Crustal Evolution - Proceedings of the 5th International Conference, IDC-5.
- Bohlen, S.R., and Essene, E.J. (1978) Igneous pyroxenes from metamorphosed anorthosite massifs. *Contributions to Mineralogy and Petrology*, 65, 433–442.
- Bonin, B. (2004) Do coeval mafic and felsic magmas in post-collisional to within-plate regimes necessarily imply two contrasting, mantle and crustal, sources? A review. *Lithos*, 78, 1–24.
- Bora, S., Kumar, S., Yi, K., Kim, N., and Lee, T.H. (2013) Geochemistry and U–Pb SHRIMP zircon chronology of granitoids and microgranular enclaves from Jhirkadandi Pluton of Mahakoshal Belt, Central India Tectonic Zone, India. *Journal of Asian Earth Sciences*, 70–71, 99–114.
- Bose, S., Anand, R., D’Souza, J., Hartnady, M., Kirkland, C., and Kooijman, E. (2023) Zircon UPb and Hf isotope insights into the Mesoproterozoic breakup of supercontinent Columbia from the Sausar Belt, Central Indian Tectonic Zone. *Geochemistry*, 126054.
- Brown, M. (2002) Retrograde processes in migmatites and granulites revisited. *Journal of Metamorphic Geology*, 20, 25–40.

- Brown, M. (2007) Metamorphic Conditions in Orogenic Belts: A Record of Secular Change. *International Geology Review*, 49, 193–234.
- Brown, M. (2008) Characteristic thermal regimes of plate tectonics and their metamorphic imprint throughout earth history: when did earth first adopt a plate tectonics mode of behavior? *Special Paper of the Geological Society of America*, 440, 97–128.
- (2014) The contribution of metamorphic petrology to understanding lithosphere evolution and geodynamics. *Geoscience Frontiers*, 5, 553–569.
- Bucher, K., and Frost, B.R. (2006) Fluid Transfer in High-grade Metamorphic Terrains Intruded by Anorogenic Granites: The Thor Range, Antarctica. *Journal of Petrology*, 47, 567–593.
- Buick, I.S., Clark, C., Rubatto, D., Hermann, J., Pandit, M., and Hand, M. (2010) Constraints on the Proterozoic evolution of the Aravalli–Delhi Orogenic belt (NW India) from monazite geochronology and mineral trace element geochemistry. *Lithos*, 120, 511–528.
- Cai, J., Liu, F., and Liu, C. (2020) A unique Paleoproterozoic HP–UHT metamorphic event recorded by the Bengbu mafic granulites in the southwestern Jiao–Liao–Ji Belt, North China Craton. *Gondwana Research*, 80, 244–274.
- Castro, A. (2004) The source of granites: inferences from the Lewisian complex. *Scottish Journal of Geology*, 40, 49–65.
- (2014) The off-crust origin of granite batholiths. *Geoscience Frontiers*, 5, 63–75.
- Chakrabarty, A., Karmakar, S., Mukherjee, S., Roy Choudhury, S., Maiti, P., Sanyal, S., and Sengupta, P. (2022) Neoproterozoic reworking of a Mesoproterozoic magmatic arc from the north-eastern part of the Central Indian Tectonic Zone: Implication for the growth and disintegration of the Indian shield in the Proterozoic supercontinental cycles. *Precambrian Research*, 378, 106758.
- Chakrabarty, A., Mukherjee, S., Karmakar, S., Sanyal, S., and Sengupta, P. (2023) Petrogenesis and in situ U–Pb zircon dates of a suite of granitoid in the northern part of the Central Indian tectonic Zone: Implications for prolonged arc magmatism during the formation of the Columbia supercontinent. *Precambrian Research*, 387, 106990.
- Chakraborty, K., Ray, A., Chakraborti, T.M., Deb, G.K., Mandal, A., Kimura, K., and Mukhopadhyay, S. (2022) Petrology, geochemistry and U–Pb zircon geochronology of alkali granites of Jhalda, eastern India and their possible linkage to Rodinia Supercontinent. *Journal of Earth System Science*, 131, 253.
- Chakraborty, S. (2008) Diffusion in solid silicates: A tool to track timescales of processes

- comes of age. *Annual Review of Earth and Planetary Sciences*, 36, 153–190.
- Chambers, J.A., Argles, T.W., Horstwood, M.S.A., Harris, N.B.W., Parrish, R.R., and Ahmad, T. (2008) Tectonic implications of Palaeoproterozoic anatexis and Late Miocene metamorphism in the Lesser Himalayan Sequence, Sutlej Valley, NW India. *Journal of the Geological Society*, 165, 725–737.
- Chapman, T., Clarke, G.L., Daczko, N.R., Piazzolo, S., and Rajkumar, A. (2015) Orthopyroxene–omphacite- and garnet–omphacite-bearing magmatic assemblages, Breaksea Orthogneiss, New Zealand: Oxidation state controlled by high-P oxide fractionation. *Lithos*, 216–217, 1–16.
- Chatterjee, N. (2018) An assembly of the Indian Shield at c . 1 . 0 Ga and shearing at c . 876 – 784 Ma in Eastern India : Insights from contrasting P-T paths , and burial and exhumation rates of metapelitic granulites. *Precambrian Research*, 317, 117–136.
- Chatterjee, N., and Ghose, N.C. (2011) Extensive Early Neoproterozoic high-grade metamorphism in North Chotanagpur Gneissic Complex of the Central Indian Tectonic Zone. *Gondwana Research*, 20, 362–379.
- Chatterjee, N., Mazumdar, A.C., Bhattacharya, A., and Saikia, R.R. (2007) Mesoproterozoic granulites of the Shillong–Meghalaya Plateau: Evidence of westward continuation of the Prydz Bay Pan-African suture into Northeastern India. *Precambrian Research*, 152, 1–26.
- Chatterjee, N., Crowley, J.L., and Ghose, N.C. (2008) Geochronology of the 1.55Ga Bengal anorthosite and Grenvillian metamorphism in the Chotanagpur gneissic complex, eastern India. *Precambrian Research*, 161, 303–316.
- Chatterjee, N., Banerjee, M., Bhattacharya, A., and Maji, A.K. (2010) Monazite chronology, metamorphism–anatexis and tectonic relevance of the mid-Neoproterozoic Eastern Indian Tectonic Zone. *Precambrian Research*, 179, 99–120.
- Chattopadhyay, A., Chatterjee, A., Das, K., and Sarkar, A. (2017) Neoproterozoic transpression and granite magmatism in the Gavilgarh-Tan Shear Zone, central India: Tectonic significance of U-Pb zircon and U-Th-total Pb monazite ages. *Journal of Asian Earth Sciences*, 147, 485–501.
- Chattopadhyay, S., Upadhyay, D., Nanda, J.K., Mezger, K., Pruseth, K.L., and Berndt, J. (2015) Proto-India was a part of Rodinia: Evidence from Grenville-age suturing of the Eastern Ghats Province with the Paleoproterozoic Singhbhum Craton. *Precambrian Research*, 266, 506–529.
- Chen, Y.X., Zhou, K., and Gao, X.Y. (2017) Partial melting of ultrahigh-pressure

- metamorphic rocks during continental collision: Evidence, time, mechanism, and effect. *Journal of Asian Earth Sciences*, 145, 177–191.
- Clarke, G.L., Daczko, N.R., and Miescher, D. (2013) Identifying Relic Igneous Garnet and Clinopyroxene in Eclogite and Granulite, Breaksea Orthogneiss, New Zealand. *Journal of Petrology*, 54, 1921–1938.
- Clemens, J.D. (1990) The Granulite — Granite Connexion BT - Granulites and Crustal Evolution. In D. Vielzeuf and P. Vidal, Eds., pp. 25–36. Springer Netherlands, Dordrecht.
- Clemens, J.D., and Birch, W.D. (2012) Assembly of a zoned volcanic magma chamber from multiple magma batches: The Cerberean Cauldron, Marysville Igneous Complex, Australia. *Lithos*, 155, 272–288.
- Clemens, J.D., and Stevens, G. (2012) What controls chemical variation in granitic magmas ? *Lithos*, 135, 317–329.
- Clemens, J.D., and Vielzeuf, D. (1987) Constraints on melting and magma production in the crust. *Earth and Planetary Science Letters*, 86, 287–306.
- Clemens, J.D., Holloway, J.R., and White, A.J.R. (1986) Origin of an A-type granite : Experimental constraints. *American Mineralogist*, 71, 317–324.
- Collins, W.J., Beams, S.D., White, A.J.R., and Chappell, B.W. (1982) Nature and origin of A-type granites with particular reference to southeastern Australia. *Contributions to Mineralogy and Petrology*, 80, 189–200.
- Condie, K.C. (1997) Sources of Proterozoic mafic dyke swarms: constraints from Th/Ta and La/Yb ratios. *Precambrian Research*, 81, 3–14.
- Dall’Agnol, R., and de Oliveira, D.C. (2007) Oxidized, magnetite-series, rapakivi-type granites of Carajás, Brazil: Implications for classification and petrogenesis of A-type granites. *Lithos*, 93, 215–233.
- Dall’Agnol, R., Scaillet, B., and Pichavant, M. (1999a) An Experimental Study of a Lower Proterozoic A-type Granite from the Eastern Amazonian Craton, Brazil. *Journal of Petrology*, 40, 1673–1698.
- Dall’Agnol, R., Rämö, O.T., De Magalhães, M.S., and Macambira, M.J.B. (1999b) Petrology of the anorogenic, oxidised Jamon and Musa granites, Amazonian Craton: Implications for the genesis of Proterozoic A-type granites. *Lithos*, 46, 431–462.
- Dall’Agnol, R., Frost, C.D., and Rämö, O.T. (2012) IGCP Project 510 “A-type Granites and Related Rocks through Time”: Project vita, results, and contribution to granite research. *Lithos*, 151, 1–16.

-
- Darling, R.S., and Peck, W.H. (2016) Metamorphic Conditions of Adirondack Rocks. *Adirondack Journal of Environmental Studies*, 21.
- Das, K., Bose, S., Karmakar, S., Dunkley, D., and Dasgupta, S. (2011) Multiple tectonometamorphic imprints in the lower crust: First evidence of ca. 950Ma (zircon U-Pb SHRIMP) compressional reworking of UHT aluminous granulites from the Eastern Ghats Belt, India. *Geological Journal*, 46, 217–239.
- Das, S., Sanyal, S., Karmakar, S., Sengupta, S., and Sengupta, P. (2019) Do the deformed alkaline rocks always serve as a marker of continental suture zone? A case study from parts of the Chotanagpur Granite Gneissic complex, India. *Journal of Geodynamics*, 129, 59–79.
- Dasgupta, S., Bose, S., Bhowmik, S., and Sengupta, P. (2017) The Eastern Ghats Belt, India, in the context of supercontinent assembly. *Geological Society London Special Publications*, 457.
- Deng, L.P., Liu, Y.C., Gu, X.F., Groppo, C., and Rolfo, F. (2018) Partial melting of ultrahigh-pressure metamorphic rocks at convergent continental margins: Evidences, melt compositions and physical effects. *Geoscience Frontiers*, 9, 1229–1242.
- Deng, X., Peng, T., and Zhao, T. (2016) Geochronology and geochemistry of the late Paleoproterozoic aluminous A-type granite in the Xiaoqinling area along the southern margin of the North China Craton: Petrogenesis and tectonic implications. *Precambrian Research*, 285, 127–146.
- Deshmukh, T., and Prabhakar, N. (2020) Linking collision, slab break-off and subduction polarity reversal in the evolution of the Central Indian Tectonic Zone. *Geological Magazine*, 157, 340–350.
- Deshmukh, T., Prabhakar, N., Bhattacharya, A., and Madhavan, K. (2017) Late Paleoproterozoic clockwise P–T history in the Mahakoshal Belt, Central Indian Tectonic Zone: Implications for Columbia supercontinent assembly. *Precambrian Research*, 298, 56–78.
- Dev, S.G.D., Shaji, E., Santosh, M., Tsunogae, T., and Prasanth, R.S. (2023) Mesoarchean charnockites from the Coorg Block, Southern India: Petrology, geochemistry and tectonic implications. *Geosystems and Geoenvironment*, 2, 100134.
- Dey, A., Mukherjee, S., Sanyal, S., and Sengupta, P. (2017) Deciphering Sedimentary Provenance and Timing of Sedimentation From a Suite of Metapelites From the Chotanagpur Granite Gneissic Complex , India : Implications for Proterozoic Tectonics in the East-Central Part of the Indian Shield, 453–486 p.

- Dey, A., Karmakar, S., Mukherjee, S., Sanyal, S., Dutta, U., and Sengupta, P. (2019a) High pressure metamorphism of mafic granulites from the Chotanagpur Granite Gneiss Complex, India: Evidence for collisional tectonics during assembly of Rodinia. *Journal of Geodynamics*, 129, 24–43.
- Dey, A., Roy Choudhury, S., Mukherjee, S., Sanyal, S., and Sengupta, P. (2019b) Origin of vesuvianite-garnet veins in calc-silicate rocks from part of the Chotanagpur Granite Gneiss Complex, East Indian Shield: The quantitative P - T - X CO₂ topology in parts of the system CaO-MgO-SiO₂-H₂O-Co₂(+Fe₂O₃,F). *American Mineralogist*, 104, 744–760.
- Dey, A., Karmakar, S., Ibanez-Mejia, M., Mukherjee, S., Sanyal, S., and Sengupta, P. (2019c) Petrology and geochronology of a suite of pelitic granulites from parts of the Chotanagpur Granite Gneiss Complex, eastern India: Evidence for Stenian - Tonian reworking of a late Paleoproterozoic crust. *Geological Journal*, 55, 2851–2880.
- Dobmeier, C., and Simmat, R. (2002) Post-Grenvillean transpression in the Chilka Lake area, Eastern Ghats Belt—implications for the geological evolution of peninsular India. *Precambrian Research*, 113, 243–268.
- Dobmeier, C., Lütke, S., Hammerschmidt, K., and Mezger, K. (2006) Emplacement and deformation of the Vinukonda meta-granite (Eastern Ghats, India)—Implications for the geological evolution of peninsular India and for Rodinia reconstructions. *Precambrian Research*, 146, 165–178.
- Du, L., Yang, C., Wyman, D.A., Nutman, A.P., Lu, Z., Song, H., Xie, H., Wan, Y., Zhao, L., Geng, Y., and others (2016) 2090–2070Ma A-type granitoids in Zanhuang Complex: Further evidence on a Paleoproterozoic rift-related tectonic regime in the Trans-North China Orogen. *Lithos*, 254–255, 18–35.
- Duchesne, J.C., and Wilmart, E. (1997) Igneous charnockites and related rocks from the Bjerkreim-Sokndal layered intrusion (Southwest Norway): A jotunite (hypersthene monzodiorite)-derived A-type granitoid suite. *Journal of Petrology*, 38, 337–369.
- Dunkley, D.J., Clarke, G.L., and White, R.W. (2002) Structural and metamorphic evolution of the Mid-Late Proterozoic Rayner Complex, Cape Bruce, East Antarctica. *Royal Society of New Zealand, New Zealand*.
- Eby, G.N. (1990) The A-type granitoids: A review of their occurrence and chemical characteristics and speculations on their petrogenesis. *Lithos*, 26, 115–134.
- Eby, G.N. (1992) Chemical subdivision of the A-type granitoids: petrogenetic and tectonic implications. *Geology*, 20, 641–644.

- Enakshi, D., Subrata, K., Anindita, D., Shreya, K., and Pulak, S. (2017) Reaction textures, pressure–temperature paths and chemical dates of monazite from a new suite of sapphirine–spinel granulites from parts of the Eastern Ghats Province, India: insights into the final amalgamation of India and East Antarctica during the for. Geological Society, London, Special Publications, 457, 141–170.
- England, P.C., and Thompson, A.B. (1984) Pressure - temperature - time paths of regional metamorphism I. heat transfer during the evolution of regions of thickened continental crust. *Journal of Petrology*, 25, 894–928.
- Erickson, T.M., Pearce, M.A., Taylor, R.J.M., Timms, N.E., Clark, C., Reddy, S.M., and Buick, I.S. (2015) Deformed monazite yields high-temperature tectonic ages. *Geology*, 43, 383–386.
- Ernst, R., and Bleeker, W. (2010) Large igneous provinces (LIPs), giant dyke swarms, and mantle plumes: significance for breakup events within Canada and adjacent regions from 2.5 Ga to the Present This article is one of a selection of papers published in this Special Issue on the the them. *Canadian Journal of Earth Sciences*, 47, 695–739.
- Finger, F., Doblmayr, P., Friedl, G., Gerdes, A., Krenn, E., and von Quadt, A. (2003) Petrology of the Weinsberg granite in the South Bohemian Batholith: New data from the mafic end members. *Journal of the Czech Geological Society*, 48, 46–47.
- Frost, B.R., and Frost, C.D. (2008) On charnockites. *Gondwana Research*, 13, 30–44.
- Frost, B.R., Frost, C.D., Hulsebosch, T.P., and Swapp, S.M. (2000) Origin of the Charnockites of the Louis Lake Batholith, Wind River Range, Wyoming. *Journal of Petrology*, 41, 1759–1776.
- Frost, C.D., and Frost, B.R. (2011) On Ferroan (A-type) Granitoids : their Compositional Variability and Modes of Origin Fe-index. *Journal of Petrology*, 0, 1–15.
- (2013) Proterozoic ferroan feldspathic magmatism. *Precambrian Research*, 228, 151–163.
- Frost, C.D., Frost, B.R., Chamberlain, K.R., and Edwards, B.R. (1999) Petrogenesis of the 1.43 Ga Sherman Batholith, SE Wyoming, USA : a reduced, Rapakivi-type anorogenic granite, 1771–1802 p. *Journal of Petrology* Vol. 40.
- Ganguly, J. (2002) Diffusion kinetics in minerals: Principles and applications to tectono-metamorphic processes. *European Mineralogical Union Notes in Mineralogy*, 4, 271–309.
- Goodenough, K.M., Upton, B.G.J., and Ellam, R.M. (2000) Geochemical evolution of the Ivigtut granite, South Greenland: a fluorine-rich “A-type” intrusion. *Lithos*, 51, 205–

221.

- Grantham, G., Eglington, B., Thomas, B., and Mendonidis, P. (2001) The nature of the Grenville-age charnockitic A-type magmatism from the Natal, Namaqua and Maud Belts of southern Africa and Western Dronning Maud Land, Antarctica. *Memoirs of the National Institute of Polar Research*, 55, 59–81.
- Groppo, C., Rolfo, F., and Indares, A. (2012) Partial melting in the higher Himalayan crystallines of Eastern Nepal: The effect of decompression and implications for the “channel flow” model. *Journal of Petrology*, 53, 1057–1088.
- Halpin, J.A., Gerakiteys, C.L., Clarke, G.L., Belousova, E.A., and Griffin, W.L. (2005) In-situ U–Pb geochronology and Hf isotope analyses of the Rayner Complex, east Antarctica. *Contributions to Mineralogy and Petrology*, 148, 689–706.
- Halpin, J.A., Clarke, G.L., White, R.W., and Kelsey, D.E. (2007a) Contrasting P–T–t paths for Neoproterozoic metamorphism in MacRobertson and Kemp Lands, east Antarctica. *Journal of Metamorphic Geology*, 25, 683–701.
- Halpin, J.A., White, R.W., Clarke, G.L., and Kelsey, D.E. (2007b) The Proterozoic P–T–t Evolution of the Kemp Land Coast, East Antarctica; Constraints from Si-saturated and Si-undersaturated Metapelites. *Journal of Petrology*, 48, 1321–1349.
- Harley, S.L. (1989) The origins of granulites: A metamorphic perspective. *Geological Magazine*, 126, 215–247.
- Harlov, D.E., Van Den Kerkhof, A., and Johansson, L. (2013) The Varberg–Torpa Charnockite–Granite Association, SW Sweden: Mineralogy, Petrology, and Fluid Inclusion Chemistry. *Journal of Petrology*, 54, 3–40.
- Hayden, L.A., and Manning, C.E. (2011) Rutile solubility in supercritical NaAlSi₃O₈–H₂O fluids. *Chemical Geology*, 284, 74–81.
- Hellmann, R., Penisson, J.M., Hervig, R.L., Thomassin, J.H., and Abrioux, M.F. (2003) An EFTEM/HRTEM high-resolution study of the near surface of labradorite feldspar altered at acid pH: Evidence for interfacial dissolution-reprecipitation. *Physics and Chemistry of Minerals*, 30, 192–197.
- Hernández-Montenegro, J.D., Palin, R.M., Zuluaga, C.A., and Hernández-Urbe, D. (2021) Archean continental crust formed by magma hybridization and voluminous partial melting. *Scientific Reports*, 11, 5263.
- Hossain, I., Tsunogae, T., Rajesh, H.M., Chen, B., and Arakawa, Y. (2007) Palaeoproterozoic U–Pb SHRIMP zircon age from basement rocks in Bangladesh: A possible remnant of the Columbia supercontinent. *Comptes Rendus Geoscience*, 339,

- 979–986.
- Hou, G. (2012) Mechanism for three types of mafic dyke swarms. *Geoscience Frontiers*, 3, 217–223.
- Jagoutz, O., Schmidt, M.W., Enggist, A., Burg, J.-P., Hamid, D., and Hussain, S. (2013) TTG-type plutonic rocks formed in a modern arc batholith by hydrous fractionation in the lower arc crust. *Contributions to Mineralogy and Petrology*, 166, 1099–1118.
- Jagoutz, O.E. (2010) Construction of the granitoid crust of an island arc. Part II: a quantitative petrogenetic model. *Contributions to Mineralogy and Petrology*, 160, 359–381.
- Jagoutz, O.E., Burg, J.-P., Hussain, S., Dawood, H., Pettke, T., Iizuka, T., and Maruyama, S. (2009) Construction of the granitoid crust of an island arc part I: geochronological and geochemical constraints from the plutonic Kohistan (NW Pakistan). *Contributions to Mineralogy and Petrology*, 158, 739–755.
- Jarrar, G.H., Manton, W.I., Stern, R.J., and Zachmann, D. (2008) Late Neoproterozoic A-type granites in the northernmost Arabian-Nubian Shield formed by fractionation of basaltic melts. *Geochemistry*, 68, 295–312.
- Jiang, J., Clayton, R.N., and Newton, R.C. (1988) Fluids in Granulite Facies Metamorphism: A Comparative Oxygen Isotope Study on the South India and Adirondack High-Grade Terrains. *The Journal of Geology*, 96, 517–533.
- Johnson, T.E., Kirkland, C.L., Gardiner, N.J., Brown, M., Smithies, R.H., and Santosh, M. (2019) Secular change in TTG compositions: Implications for the evolution of Archaean geodynamics. *Earth and Planetary Science Letters*, 505, 65–75.
- Karmakar, S. (2021) Formation of clinohumite \pm spinel in dolomitic marbles from the Makrohar Granulite Belt, Central India: Evidence of Ti mobility during metamorphism. *American Mineralogist*, 106, 1818–1827.
- Karmakar, S., Bose, S., Sarbadhikari, A.B., and Das, K. (2011) Evolution of granulite enclaves and associated gneisses from Purulia, Chhotanagpur Granite Gneiss Complex, India: Evidence for 990-940Ma tectonothermal event(s) at the eastern India cratonic fringe zone. *Journal of Asian Earth Sciences*, 41, 69–88.
- Katzir, Y., Eyal, M., Litvinovsky, B.A., Jahn, B.M., Zandvilevich, A.N., Valley, J.W., Beerli, Y., Pelly, I., and Shimshilashvili, E. (2007) Petrogenesis of A-type granites and origin of vertical zoning in the Katharina pluton, Gebel Mussa (Mt. Moses) area, Sinai, Egypt. *Lithos*, 95, 208–228.
- Kaur, P., Chaudhri, N., Raczek, I., Kröner, A., and Hofmann, A.W. (2009) Record of

- 1.82 Ga Andean-type continental arc magmatism in NE Rajasthan, India: Insights from zircon and Sm–Nd ages, combined with Nd–Sr isotope geochemistry. *Gondwana Research*, 16, 56–71.
- Kaur, P., Zeh, A., and Chaudhri, N. (2017) Palaeoproterozoic continental arc magmatism, and Neoproterozoic metamorphism in the Aravalli-Delhi orogenic belt, NW India: New constraints from in situ zircon U–Pb–Hf isotope systematics, monazite dating and whole-rock geochemistry. *Journal of Asian Earth Sciences*, 136, 68–88.
- Kelly, N.M., and Harley, S.L. (2004) Orthopyroxene–Corundum in Mg–Al-rich Granulites from the Oygarden Islands, East Antarctica. *Journal of Petrology*, 45, 1481–1512.
- Kelly, N.M., Clarke, G.L., and Fanning, C.M. (2002) A two-stage evolution of the Neoproterozoic Rayner Structural Episode: new U–Pb sensitive high resolution ion microprobe constraints from the Oygarden Group, Kemp Land, East Antarctica. *Precambrian Research*, 116, 307–330.
- Kemp, A.I.S., Wormald, R.J., Whitehouse, M.J., and Price, R.C. (2005) HF isotopes in zircon reveal contrasting sources and crystallization histories for alkaline to peralkaline granites of Temora, southeastern Australia. *Geology*, 33, 797–800.
- Kilpatrick, J.A., and Ellis, D.J. (1992) C-type magmas: igneous charnockites and their extrusive equivalents. *Earth and Environmental Science Transactions of The Royal Society of Edinburgh*, 83, 155–164.
- King, P.L., White, A.J.R., Chappell, B.W., and Allen, C.M. (1997) Characterization and origin of aluminous A-type granites from the Lachlan Fold Belt, Southeastern Australia. *Journal of Petrology*, 38, 371–391.
- King, P.L., Chappell, B.W., Allen, C.M., and White, A.J.R. (2001) Are A-type granites the high-temperature felsic granites? Evidence from fractionated granites of the Wangrah Suite. *Australian Journal of Earth Sciences*, 501–514.
- Klimm, K., Holtz, F., Johannes, W., and King, P.L. (2003) Fractionation of metaluminous A-type granites: an experimental study of the Wangrah Suite, Lachlan Fold Belt, Australia. *Precambrian Research*, 124, 327–341.
- Klötzli, U.S., KOLLER, F., SCHARBERT, S., and HÖCK, V. (2002) Cadomian Lower-crustal Contributions to Variscan Granite Petrogenesis (South Bohemian Pluton, Austria): a Reply. *Journal of Petrology*, 43, 1783–1786.
- Kohn, M.J., Paul, S.K., and Corrie, S.L. (2010) The lower Lesser Himalayan sequence: A Paleoproterozoic arc on the northern margin of the Indian plate. *GSA Bulletin*, 122, 323–335.

- Korhonen, F.J., Clark, C., Brown, M., Bhattacharya, S., and Taylor, R. (2013) How long-lived is ultrahigh temperature (UHT) metamorphism? Constraints from zircon and monazite geochronology in the Eastern Ghats orogenic belt, India. *Precambrian Research*, 234, 322–350.
- Kriegsman, L.M. (2001) Partial melting, partial melt extraction and partial back reaction in anatectic migmatites. *Lithos*, 56, 75–96.
- Kriegsman, L.M., and Hensen, B.J. (1998) Back reaction between restite and melt: Implications for geothermobarometry and pressure-temperature paths. *Geology*, 26, 1111–1114.
- Kuehner, S.M., and Green, D.H. (1991) Uplift history of the East Antarctic Shield: constraints imposed by high-pressure experimental studies of Proterozoic mafic dykes. In *International symposium on Antarctic earth sciences*. 5 pp. 1–6.
- Kumar, D., Rao, N.V.C., Prabhat, P., Chatterjee, A., and Rahaman, W. (2022) Petrochemistry and Sr-Nd isotopes of post-collisional Neoproterozoic (ca. 950 Ma) amphibolite dykes of continental flood basalt affinity from the Simdega area: Implications for the geodynamic evolution of the Chhotanagpur Gneissic Complex, Eastern India. *Lithos*, 428–429, 106810.
- Kumar, D., Rao, N.V.C., Tripathi, A., Belyatsky, B., Prabhat, P., Rahaman, W., and Satyanarayanan, M. (2023) U-Pb Neoproterozoic age and petrogenesis of a calc-alkaline shoshonitic lamprophyre from Simdega area, Chhotanagpur Gneissic Complex (Eastern India): Implication for the evolution of the Central Indian Tectonic Zone and Rodinia tectonics. *Chemical Geology*, 631, 121512.
- Kumar, R.R., Kawaguchi, K., Dwivedi, S.B., and Das, K. (2022a) Metamorphic evolution of the pelitic and mafic granulites from Daltonganj, Chhotanagpur Granite Gneiss Complex, India: Constraints from zircon U–Pb age and phase equilibria modelling. *Geological Journal*, 57, 1284–1310.
- Kumar, R.R., Dwivedi, S.B., and Pathak, P. (2022b) Phase equilibria modelling and geochemistry of high-grade gneiss from the Chhotanagpur Granite Gneiss Complex, eastern India: Implications for tectono-metamorphic evolution. *Geosystems and Geoenvironment*, 1, 100082.
- Kumar, S., Rino, V., Hayasaka, Y., Kimura, K., Raju, S., Terada, K., and Pathak, M. (2017) Contribution of Columbia and Gondwana Supercontinent assembly- and growth-related magmatism in the evolution of the Meghalaya Plateau and the Mikir Hills, Northeast India: Constraints from U-Pb SHRIMP zircon geochronology and

- geochemistry. *Lithos*, 277, 356–375.
- Landenberger, B., and Collins, W.J. (1996) Derivation of A-type Granites from a Dehydrated Charnockitic Lower Crust: Evidence from the Chaelundi Complex, Eastern Australia. *Journal of Petrology*, 37, 145–170.
- Lasaga, A.C. (1981) Atomistic basis of kinetics: defects in minerals. *Reviews in Mineralogy & Geochemistry*, 8, 261–316.
- Laurent, O., Björnsen, J., Wotzlaw, J.-F., Bretscher, S., Pimenta Silva, M., Moyen, J.-F., Ulmer, P., and Bachmann, O. (2020) Earth's earliest granitoids are crystal-rich magma reservoirs tapped by silicic eruptions. *Nature Geoscience*, 13, 163–169.
- Li, H., Ling, M., Ding, X., Zhang, H., Li, C., Liu, D., and Sun, W. (2014) The geochemical characteristics of Haiyang A-type granite complex in Shandong, eastern China. *Lithos*, 200–201, 142–156.
- Liou, P., and Guo, J. (2019) Generation of Archaean TTG Gneisses Through Amphibole-Dominated Fractionation. *Journal of Geophysical Research: Solid Earth*, 124, 3605–3619.
- Liu, P., and Massonne, H.J. (2022) High-pressure granulite facies re-equilibration and zoisite–biotite dehydration melting during decompression of an ultrahigh-pressure garnet clinopyroxenite from the island of Fjærtoft, Norway. *Journal of Metamorphic Geology*, 40, 887–918.
- Loiselle, M.C., and Wones, D.R. (1979) Characteristics and origin of anorogenic granites. *Geological Society of America, Abstracts with Programs*, 11, 468.
- Lu, L., Zhang, K.-J., Jin, X., Zeng, L., Yan, L.-L., and Santosh, M. (2019) Crustal Thickening of the Central Tibetan Plateau prior to India–Asia Collision: Evidence from Petrology, Geochronology, Geochemistry and Sr–Nd–Hf Isotopes of a K-rich Charnockite–Granite Suite in Eastern Qiangtang. *Journal of Petrology*, 60, 827–854.
- Lucassen, F., Franz, G., Rhede, D., and Wirth, R. (2010) Ti–Al zoning of experimentally grown titanite in the system CaO–Al₂O₃–TiO₂–SiO₂–NaCl–H₂O–(F): Evidence for small-scale fluid heterogeneity. *American Mineralogist*, 95, 1365–1378.
- Ma, L., Wang, Q., Wyman, D.A., Li, Z.-X., Jiang, Z.-Q., Yang, J.-H., Gou, G.-N., and Guo, H.-F. (2013) Late Cretaceous (100–89Ma) magnesian charnockites with adakitic affinities in the Milin area, eastern Gangdese: Partial melting of subducted oceanic crust and implications for crustal growth in southern Tibet. *Lithos*, 175–176, 315–332.
- Mallik, A.K., Gupta, S.N., and Barman, T.R.. (1991) Dating of early Precambrian granite greenstone complex of the eastern India Precambrian shield with special reference to

- Chotonagpur Granite gneiss complex. Records of the Geological Survey of India, 124, 20–21.
- McDonough, W.F., and Sun, S. s. (1995) The composition of the Earth. *Chemical Geology*, 120, 223–253.
- Melo, M.G. de, Lana, C., Stevens, G., Hartwig, M.E., Pimenta, M.S., and Nalini, H.A. (2020) Deciphering the source of multiple U–Pb ages and complex Hf isotope composition in zircon from post-collisional charnockite-granite associations from the Araçuaí orogen (southeastern Brazil). *Journal of South American Earth Sciences*, 103, 102792.
- Mikhalsky, E. V, Sheraton, J.W., and Hahne, K. (2006) Charnockite composition in relation to the tectonic evolution of East Antarctica. *Gondwana Research*, 9, 379–397.
- Miller, C., Urs, K., Frank, W., Thöni, M., and Grasemann, B. (2000) Proterozoic crustal evolution in the NW Himalaya (India) as recorded by circa 1.80 Ga mafic and 1.84 Ga granitic magmatism. *Precambrian Research - PRECAMBRIAN RES*, 103, 191–206.
- Mitchell, R.J., Johnson, T.E., Clark, C., Gupta, S., Brown, M., Harley, S.L., and Taylor, R. (2019) Neoproterozoic evolution and Cambrian reworking of ultrahigh temperature granulites in the Eastern Ghats Province, India. *Journal of Metamorphic Geology*, 37, 977–1006.
- Montel, J.-M., and Vielzeuf, D. (1997) Partial melting of metagreywackes, Part II. Compositions of minerals and melts. *Contributions to Mineralogy and Petrology*, 128, 176–196.
- Montero, P., Bea, F., Corretgé, L.G., Floor, P., and Whitehouse, M.J. (2009) U-Pb ion microprobe dating and Sr and Nd isotope geology of the Galiñeiro Igneous Complex. A model for the peraluminous/peralkaline duality of the Cambro-Ordovician magmatism of Iberia. *Lithos*, 107, 227–238.
- Moreno, J.A., Molina, J.F., Montero, P., Abu Anbar, M., Scarrow, J.H., Cambeses, A., and Bea, F. (2014) Unraveling sources of A-type magmas in juvenile continental crust: Constraints from compositionally diverse Ediacaran post-collisional granitoids in the Katerina Ring Complex, southern Sinai, Egypt. *Lithos*, 192–195, 56–85.
- Moreno, J.A., Molina, J.F., Bea, F., Abu Anbar, M., and Montero, P. (2016) Th-REE- and Nb-Ta-accessory minerals in post-collisional Ediacaran felsic rocks from the Katerina Ring Complex (S. Sinai, Egypt): An assessment for the fractionation of Y/Nb, Th/Nb, La/Nb and Ce/Pb in highly evolved A-type granites. *Lithos*, 258–259, 173–196.

- Moreno, J.A., Baldim, M.R., Semprich, J., Oliveira, E.P., Verma, S.K., and Teixeira, W. (2017) Geochronological and geochemical evidences for extension-related Neoproterozoic granitoids in the southern São Francisco Craton, Brazil. *Precambrian Research*, 294, 322–343.
- Motuzas, G., Motuzas, V., Salnikova, E., and Kotov, A. (2008) Extensive charnockitic-granitic magmatism in the crystalline crust of West Lithuania. *Geologija*, 61, 1–16.
- Moyen, J.-F., and Martin, H. (2012) Forty years of TTG research. *Lithos*, 148, 312–336.
- Moyen, J.-F., Laurent, O., Chelle-Michou, C., Couzinié, S., Vanderhaeghe, O., Zeh, A., Villaros, A., and Gardien, V. (2017) Collision vs. subduction-related magmatism: Two contrasting ways of granite formation and implications for crustal growth. *Lithos*, 277, 154–177.
- Mukherjee, S., Dey, A., and Sanyal, S. (2017) Petrology and U – Pb geochronology of zircon in a suite of charnockitic gneisses from parts of the Chotanagpur Granite Gneiss Complex (CGGC): evidence for the reworking of a Mesoproterozoic basement during the formation of the Rodinia supercontinent. Geological Society, London, Special Publications, 457.
- Mukherjee, S., Dey, A., Ibanez-mejia, M., Sanyal, S., and Sengupta, P. (2018a) Geochemistry , U-Pb geochronology and Lu-Hf isotope systematics of a suite of ferroan (A-type) granitoids from the CGGC : Evidence for Mesoproterozoic crustal extension in the east Indian shield. *Precambrian Research*, 305, 40–63.
- Mukherjee, S., Dey, A., Sanyal, S., and Sengupta, P. (2018b) Tectonothermal imprints in a suite of mafic dykes from the Chotanagpur Granite Gneissic complex (CGGC), Jharkhand, India: Evidence for late Tonian reworking of an early Tonian continental crust. *Lithos*, 320–321, 490–514.
- Mukherjee, S., Dey, A., Sanyal, S., Ibanez, M., and Pulak, M. (2019a) Bulk rock and zircon geochemistry of granitoids from the Chotanagpur Granite Gneissic Complex (CGGC): implications for the late Paleoproterozoic continental arc magmatism in the East Indian Shield. *Contributions to Mineralogy and Petrology*, 174, 1–17.
- Mukherjee, S., Dey, A., Sanyal, S., and Sengupta, P. (2019b) Proterozoic crustal evolution of the Chotanagpur granite Gneissic Complex, Jharkhand-Bihar-West Bengal, India: Current status and future prospect. *Springer Geology*, 7–54.
- Mukherjee, S., Dey, A., Choudhury, S.R., and Mayne, M.J. (2022) Effect of source heterogeneity, melt extraction and crystal separation on the composition of a suite of ferroan (A-type) granites from parts of the Chotanagpur Granite Gneissic Complex

- (CGGC), India. *Lithos*, 430–431, 106875.
- Naney, M.T. (1983) Phase equilibria of rock-forming ferromagnesian silicates in granitic systems. *American journal of science*, 283, 993–1033.
- Newton, R.C. (1992) Charnockitic alteration: evidence for CO₂ infiltration in granulite facies metamorphism. *Journal of Metamorphic Geology*, 10, 383–400.
- Newton, R.C., and Tsunogae, T. (2014) Incipient charnockite: Characterization at the type localities. *Precambrian Research*, 253, 38–49.
- Newton, R.C., Smith, J. V, and Windley, B.F. (1980) Carbonic metamorphism, granulites and crustal growth. *Nature*, 288, 45–50.
- Newton, R.C., Touret, J.L.R., and Aranovich, L.Y. (2014) Fluids and H₂O activity at the onset of granulite facies metamorphism. *Precambrian Research*, 253, 17–25.
- Oliveira, D.C. De, and Agnol, R.D. (2009) Geology , Geochemistry and magmatic evolution of the paleoproterozoic, anorogenic oxidised A-type Redencao granoite of the Jamon suite, eastern Amazonian craton, Brazil. *The Canadian Mineralogist*, 47, 1441–1468.
- Ormaasen, D.E. (1977) Petrology of the Hopen mangerite-charnockite intrusion, Lofoten, north Norway. *Lithos*, 10, 291–310.
- Parmigiani, A., Faroughi, S., Huber, C., Bachmann, O., and Su, Y. (2016) Bubble accumulation and its role in the evolution of magma reservoirs in the upper crust. *Nature*, 532, 492–495.
- Patiño Douce, A.E. (1997) Generation of metaluminous A-type granites by low-pressure melting of calc-alkaline granitoids. *Geology*, 743–746.
- Patiño Douce, A.E., and Beard, J.S. (1995) Dehydration-melting of biotite gneiss and quartz amphibolite from 3 to 15 kbar. *Journal of Petrology*, 36, 707–738.
- Pattison, D.R.M. (2003) Petrogenetic significance of orthopyroxene-free garnet + clinopyroxene + plagioclase \pm quartz-bearing metabasites with respect to the amphibolite and granulite facies. *Journal of Metamorphic Geology*, 21, 21–34.
- Pearce, J. (1996) Sources and settings of granitic rocks. *International Union of Geological Sciences*, 19, 120–125.
- Pearce, J.A., Harris, N.B.W., and Tindle, A.G. (1984) Trace Element Discrimination Diagrams for the Tectonic Interpretation of Granitic Rocks. *Journal of Petrology*, 25, 956–983.
- Percival, J., and Mortensen, J. (2002) Water-deficient Calc-alkaline Plutonic Rocks of Northeastern Superior Province, Canada: Significance of Charnockitic Magmatism.

- Journal of Petrology, 43.
- Percival, J., Stern, R.A., and Rayner, N. (2003) Archean adakites from the Ashuanipi complex, eastern Superior Province, Canada: geochemistry, geochronology and tectonic significance. *Contributions to Mineralogy and Petrology*, 145, 265–280.
- Pouclet, A., Tchameni, R., Mezger, K., Vidal, M., Nsifa, E., Shang, C., and Penaye, J. (2007) Archaean crustal accretion at the northern border of the Congo Craton (South Cameroon). The charnockite-TTG link. *Bulletin De La Societe Geologique De France - BULL SOC GEOL FR*, 178.
- Purtov, V.K., and Kotel'nikova, A.L. (1993) Solubility of titanium in chloride and fluoride hydrothermal solutions. *International Geology Review*, 35, 279–287.
- Putnis, A. (2002) Mineral replacement reactions: from macroscopic observations to microscopic mechanisms. *Mineralogical Magazine*, 66, 689–708.
- Putnis, A. (2009) Mineral replacement reactions. *Reviews in Mineralogy and Geochemistry*, 70, 87–124.
- Putnis, A., and Putnis, C. V. (2007) The mechanism of reequilibration of solids in the presence of a fluid phase. *Journal of Solid State Chemistry*, 180, 1783–1786.
- Raith, M., and Srikantappa, C. (1993) Arrested charnockite formation at Kottavattam, southern India. *Journal of Metamorphic Geology*, 11, 815–832.
- Rajesh, H.M. (2008) Petrogenesis of two granites from the Nilgiri and Madurai blocks, southwestern India: Implications for charnockite–calc-alkaline granite and charnockite–alkali (A-type) granite link in high-grade terrains. *Precambrian Research*, 162, 180–197.
- Rajesh, H.M., and Santosh, M. (2012) Charnockites and charnockites. *Geoscience Frontiers*, 3, 737–744.
- Rameshwar Rao, D., and Sharma, R. (2011) Arc magmatism in eastern Kumaun Himalaya, India: A study based on geochemistry of granitoid rocks. *Island Arc*, 20, 500–519.
- Rapp, J.F., Klemme, S., Butler, I.B., and Harley, S.L. (2010) Extremely high solubility of rutile in chloride and fluoride-bearing metamorphic fluids: An experimental investigation. *Geology*, 38, 323–326.
- Rapp, R.P., and Watson, E.B. (1995) Dehydration melting of metabasalt at 8–32 kbar: Implications for continental growth and crust-mantle recycling. *Journal of Petrology*, 36, 891–931.
- Rapp, R.P., Watson, E.B., and Miller, C.F. (1991) Partial melting of amphibolite/eclogite and the origin of Archean trondhjemites and tonalites. *Precambrian Research*, 51, 1–

25.

- Ray Barman, T., Bishui, P.K., Mukhopadhyay, K., and Ray, J.N. (1994) Rb-Sr geochronology of the high-grade rocks from Purulia, West Bengal and Jamua-Dumka sector, Bihar. *Indian Minerals*, 48, 45–60.
- Rekha, S., Upadhyay, D., Bhattacharya, A., Kooijman, E., Goon, S., Mahato, S., and Pant, N.C. (2011) Lithostructural and chronological constraints for tectonic restoration of Proterozoic accretion in the Eastern Indian Precambrian shield. *Precambrian Research*, 187, 313–333.
- Remmert, P., Heinrich, W., Wunder, B., Morales, L., Wirth, R., Rhede, D., and Abart, R. (2018) Synthesis of monticellite–forsterite and merwinite–forsterite symplectites in the CaO–MgO–SiO₂ model system: influence of temperature and water content on microstructure evolution. *Contributions to Mineralogy and Petrology*, 173, 1–17.
- Richards, A., Argles, T., Harris, N., Parrish, R., Ahmad, T., Darbyshire, F., and Draganits, E. (2005) Himalayan architecture constrained by isotopic tracers from clastic sediments. *Earth and Planetary Science Letters*, 236, 773–796.
- Roy, Abhijit, Kagami, H., Yoshida, M., Roy, Abhinaba, Bandyopadhyay, B.K., Chattopadhyay, A., Khan, A.S., Huin, A.K., and Pal, T. (2006) Rb–Sr and Sm–Nd dating of different metamorphic events from the Sausar Mobile Belt, central India: implications for Proterozoic crustal evolution. *Journal of Asian Earth Sciences*, 26, 61–76.
- Roy Choudhury, S., Dey, A., Mukherjee, S., Sengupta, S., Sanyal, S., Karmakar, S., and Sengupta, P. (2023a) Formation of aluminous clinopyroxene-ilmenite-spinel symplectic assemblage in a regionally metamorphosed calc-silicate granulite from the Chotanagpur Granite Gneiss Complex, East Indian shield. *Lithos*, 442–443, 107058.
- Roy Choudhury, S., Dey, A., Mukherjee, S., Sanyal, S., Karmakar, S., and Sengupta, P. (2023b) On the factors controlling the incorporation of aluminium within titanites: a case study from medium pressure calc-silicate granulites in parts of the East Indian shield. *Mineralogy and Petrology*, 117, 1–16.
- Ruiz-Agudo, E., Putnis, C. V., and Putnis, A. (2014) Coupled dissolution and precipitation at mineral-fluid interfaces. *Chemical Geology*, 383, 132–146.
- Rushmer, T. (1991) Partial melting of two amphibolites: contrasting experimental results under fluid-absent conditions. *Contributions to Mineralogy and Petrology*, 107, 41–59.
- Ryzhenko, B.N., Kovalenko, N.I., and Prisyagina, N.I. (2006) Titanium complexation in

- hydrothermal systems. *Geochemistry International*, 44, 879–895.
- Saikia, A., Bibhuti, G., Tatiana, K., Liudmila, L., Tamara, B., and Mansoor, A. (2017) Geochemical and U–Pb zircon age characterization of granites of the Bathani Volcano Sedimentary sequence, Chotanagpur Granite Gneiss Complex, eastern India: vestiges of the Nuna supercontinent in the Central Indian Tectonic Zone. *Geological Society, London, Special Publications*, 457, 233–252.
- Sanyal, S., and Sengupta, P. (2012) Metamorphic evolution of the Chotanagpur Granite Gneiss Complex of the East Indian Shield: current status. *Geological Society, London, Special Publications*, 365, 117–145.
- Sarkar, T., and Schenk, V. (2014) Two-stage granulite formation in a Proterozoic magmatic arc (Ongole domain of the Eastern Ghats Belt, India): Part 1. Petrology and pressure–temperature evolution. *Precambrian Research*, 255, 485–509.
- Sarkar, T., and Schenk, V. (2016) Early Mesoproterozoic (1.6–1.5 Ga) granulite facies events in the Ongole domain: geodynamic significance and global correlation. *Journal of Metamorphic Geology*, 34, 765–784.
- Sarkar, T., Schenk, V., Appel, P., Berndt, J., and Sengupta, P. (2014) Two-stage granulite formation in a Proterozoic magmatic arc (Ongole domain of the Eastern Ghats Belt, India): Part 2. LA-ICP-MS zircon dating and texturally controlled in-situ monazite dating. *Precambrian Research*, 255, 467–484.
- Sarkar, T., Schenk, V., and Berndt, J. (2015) Formation and evolution of a Proterozoic magmatic arc: geochemical and geochronological constraints from meta-igneous rocks of the Ongole domain, Eastern Ghats Belt, India. *Contributions to Mineralogy and Petrology*, 169, 5.
- Sawyer, E.W. (2008, January 1) *Atlas of Migmatites*. Canadian Science Publishing.
- Scaillet, B., Holtz, F., and Pichavant, M. (2016) Experimental Constraints on the Formation of Silicic Magmas. *Elements*, 12, 109–114.
- Scandolara, J., Fuck, R., Dall’Agnol, R., and Dantas, E. (2013) Geochemistry and origin of the early Mesoproterozoic mangerite-charnockite-rapakivi granite association of the Serra da Providência suite and associated gabbros, central-eastern Rondônia, SW Amazonian Craton, Brazil. *Journal of South American Earth Sciences*, 45, 166–193.
- Schandl, E.S., and Gorton, M.P. (2002) APPLICATION OF HIGH FIELD STRENGTH ELEMENTS TO DISCRIMINATE TECTONIC SETTINGS IN VMS ENVIRONMENTS. *Economic Geology*, 97, 629–642.
- Sen, C., and Dunn, T. (1994) Dehydration melting of a basaltic composition amphibolite at

- 1.5 and 2.0 GPa: implications for the origin of adakites. *Contributions to Mineralogy and Petrology*, 117, 394–409.
- Sengupta, P., Sen, J., Dasgupta, S., Raith, M., Bhui, U.K., and Ehl, J. (1999) Ultra-high Temperature Metamorphism of Metapelitic Granulites from Kondapalle, Eastern Ghats Belt: Implications for the Indo-Antarctic Correlation. *Journal of Petrology*, 40, 1065–1087.
- Sengupta, S. (1993) Tectonothermal history recorded in mafic dykes and enclaves of gneissic basement in the Schirmacher Hills, East Antarctica. *Precambrian Research*, 63, 273–291.
- Sequeira, N., Bhattacharya, A., and Bell, E. (2022) The ~1.4 Ga A-type granitoids in the “Chottanagpur crustal block” (India), and its relocation from Columbia to Rodinia? *Geoscience Frontiers*, 13, 1138.
- Shiraishi, K., Dunkley, D., Hokada, T., Fanning, C., Kagami, H., and Hamamoto, T. (2008) Geochronological constraints on the Late Proterozoic to Cambrian crustal evolution of eastern Dronning Maud Land, East Antarctica: A synthesis of SHRIMP U-Pb age and Nd model age data. *Geological Society, London, Special Publications*, 308, 21–67.
- Simmat, R., and Raith, M.M. (2008) U–Th–Pb monazite geochronometry of the Eastern Ghats Belt, India: Timing and spatial disposition of poly-metamorphism. *Precambrian Research*, 162, 16–39.
- Skjerlie, K.P., and Johnston, A.D. (1993) Fluid-Absent Melting Behavior of an F-Rich Tonalitic Gneiss at Mid-Crustal Pressures: Implications for the Generation of Anorogenic Granites. *Journal of Petrology*, 34.
- Smithies, R.H., Lu, Y., Johnson, T.E., Kirkland, C.L., Cassidy, K.F., Champion, D.C., Mole, D.R., Zibra, I., Gessner, K., Sapkota, J., and others (2019) No evidence for high-pressure melting of Earth’s crust in the Archean. *Nature Communications*, 10, 5559.
- Tamblyn, R., Hermann, J., Hasterok, D., Sossi, P., Pettke, T., and Chatterjee, S. (2023) Hydrated komatiites as a source of water for TTG formation in the Archean. *Earth and Planetary Science Letters*, 603, 117982.
- Tanis, E.A., Simon, A., Zhang, Y., Chow, P., Xiao, Y., Hanchar, J.M., Tschauner, O., and Shen, G. (2016) Rutile solubility in NaF–NaCl–KCl-bearing aqueous fluids at 0.5–2.79 GPa and 250–650 °C. *Geochimica et Cosmochimica Acta*, 177, 170–181.
- Tollo, R.P., Aleinikoff, J.N., Borduas, E.A., Dickin, A.P., McNutt, R.H., and Fanning, C.M. (2006) Grenvillian magmatism in the northern Virginia Blue Ridge: Petrologic

- implications of episodic granitic magma production and the significance of postorogenic A-type charnockite. *Precambrian Research*, 151, 224–264.
- Touret, J.L.R., Santosh, M., and Huizenga, J.M. (2022) Composition and evolution of the continental crust: Retrospect and prospect. *Geoscience Frontiers*, 13, 101428.
- Tropper, P., and Manning, C.E. (2005) Very low solubility of rutile in H₂O at high pressure and temperature, and its implications for Ti mobility in subduction zones. *American Mineralogist*, 90, 502–505.
- Upadhyay, D., and Raith, M.M. (2006) Intrusion age, geochemistry and metamorphic conditions of a quartz-monzosyenite intrusion at the craton–Eastern Ghats Belt contact near Jojuru, India. *Gondwana Research*, 10, 267–276.
- Vadlamani, R., Kröner, A., Vasudevan, D., Wendt, I., Tobschall, H., and Chatterjee, C. (2013) Zircon evaporation ages and geochemistry of metamorphosed volcanic rocks from the Vinjamuru domain, Krishna Province: evidence for 1.78 Ga convergent tectonics along the southeastern margin of the Eastern Dharwar Craton. *Geological Journal*, 48, 293–309.
- Valério, C. da S., Macambira, M.J.B., Souza, V. da S., Dantas, E.L., and Nardi, L.V.S. (2018) 1.88Ga São Gabriel AMCG association in the southernmost Uatumã-Anauá Domain: Petrological implications for post-collisional A-type magmatism in the Amazonian Craton. *Lithos*, 300–301, 291–313.
- Vielzeuf, D., and Holloway, J.R. (1988) Experimental determination of the fluid-absent melting relations in the pelitic system. *Contributions to Mineralogy and Petrology*, 98, 257–276.
- Vielzeuf, D., and Schmidt, M.W. (2001) Melting relations in hydrous systems revisited: Application to metapelites, metagreywackes and metabasalts. *Contributions to Mineralogy and Petrology*, 141, 251–267.
- Vijaya Kumar, K., Frost, C.D., Frost, B.R., and Chamberlain, K.R. (2007) The Chimakurti, Errakonda, and Uppalapadu plutons, Eastern Ghats Belt, India: An unusual association of tholeiitic and alkaline magmatism. *Lithos*, 97, 30–57.
- Waters, D. (2001) The significance of prograde and retrograde quartz-bearing intergrowth microstructures in partially melted granulite-facies rocks. *Lithos*, 56, 97–110.
- Watkins, J.M., Clemens, J.D., and Treloar, P.J. (2007) Archaean TTGs as sources of younger granitic magmas: Melting of sodic metatonalites at 0.6–1.2 GPa. *Contributions to Mineralogy and Petrology*, 154, 91–110.
- Watson, E.B., and Baxter, E.F. (2007) Diffusion in solid-Earth systems. *Earth and*

- Planetary Science Letters, 253, 307–327.
- Whalen, J.B., Currie, K.L., and Chappell, B.W. (1987) A-type granites: geochemical characteristics, discrimination and petrogenesis. *Contributions to Mineralogy and Petrology*, 95, 407–419.
- White, R.W., and Powell, R. (2002) Melt loss and the preservation of granulite facies mineral assemblages. *Journal of Metamorphic Geology*, 20, 621–632.
- (2010) Retrograde melt–residue interaction and the formation of near-anhydrous leucosomes in migmatites. *Journal of Metamorphic Geology*, 28, 579–597.
- Wiedenbeck, M., Goswami, J.N., and Roy, A.B. (1996) Stabilization of the Aravalli Craton of northwestern India at 2.5 Ga: An ion microprobe zircon study. *Chemical Geology*, 129, 325–340.
- Wolf, M.B., and London, D. (1994) Apatite dissolution into peraluminous haplogranitic melts: An experimental study of solubilities and mechanisms. *Geochimica et Cosmochimica Acta*, 58, 4127–4145.
- Wolf, M.B., and Wyllie, P.J. (1993) Garnet Growth during Amphibolite Anatexis: Implications of a Garnetiferous Restite. *The Journal of Geology*, 101, 357–373.
- Wolf, M.B., and Wyllie, P.J. (1994) Dehydration-melting of amphibolite at 10 kbar: the effects of temperature and time. *Contributions to Mineralogy and Petrology*, 115, 369–383.
- Yadav, B.S., Ahmad, T., Bhutani, R., Kaulina, T., and Bayanova, T. (2023) Geochronological and geochemical constraints on the petrogenesis of alkali granites from the Makrohar Granulite Belt: Evidence for Mesoproterozoic extensional regime in the eastern Central Indian Shield. *Geological Journal*, 58, 563–582.
- Yang, Q.-Y., and Santosh, M. (2015) Charnockite magmatism during a transitional phase: Implications for late Paleoproterozoic ridge subduction in the North China Craton. *Precambrian Research*, 261, 188–216.
- Yang, Q.-Y., Santosh, M., Rajesh, H.M., and Tsunogae, T. (2014) Late Paleoproterozoic charnockite suite within post-collisional setting from the North China Craton: Petrology, geochemistry, zircon U–Pb geochronology and Lu–Hf isotopes. *Lithos*, 208–209, 34–52.
- Yoshimura, S., and Nakamura, M. (2011) Carbon dioxide transport in crustal magmatic systems. *Earth and Planetary Science Letters*, 307, 470–478.
- Young, D.N., Zhao, J., Ellis, D.J., and McCulloch, M.T. (1997) Geochemical and Sr–Nd isotopic mapping of source provinces for the Mawson charnockites, east Antarctica:

- implications for Proterozoic tectonics and Gondwana reconstruction. *Precambrian Research*, 86, 1–19.
- Zhao, G., Li, S., Sun, M., and Wilde, S.A. (2011) Assembly, accretion, and break-up of the Palaeo-Mesoproterozoic Columbia supercontinent: record in the North China Craton revisited. *International Geology Review*, 53, 1331–1356.
- Zhao, J.-L., Qiu, J.-S., Liu, L., and Wang, R.-Q. (2016) The Late Cretaceous I- and A-type granite association of southeast China: Implications for the origin and evolution of post-collisional extensional magmatism. *Lithos*, 240–243, 16–33.
- Zhao, K., Xu, X., and Erdmann, S. (2017) Crystallization conditions of peraluminous charnockites: constraints from mineral thermometry and thermodynamic modelling. *Contributions to Mineralogy and Petrology*, 172, 26.
- (2018) Thermodynamic modeling for an incrementally fractionated granite magma system: Implications for the origin of igneous charnockite. *Earth and Planetary Science Letters*, 499, 230–242.
- Zhao, K., Xu, X., Klemd, R., He, Z., and Zhang, X. (2023) A review of the genetic mechanisms generating igneous charnockite: CO₂ flushing and crystal-melt segregation in mushy reservoirs. *Earth-Science Reviews*, 237, 104295.
- Zhao, L., Zhou, X., Zhai, M., Santosh, M., Ma, X., Shan, H., and Cui, X. (2014) Paleoproterozoic tectonic transition from collision to extension in the eastern Cathaysia Block, South China: Evidence from geochemistry, zircon U–Pb geochronology and Nd–Hf isotopes of a granite–charnockite suite in southwestern Zhejiang. *Lithos*, 184–187, 259–280.
- Zhu, W.-G., Zhong, H., Chen, X., Huang, H.-Q., Bai, Z.-J., Yao, J.-H., Wang, Y.-J., and Hu, P.-C. (2020) The earliest Jurassic A-type rhyolites and high-Mg andesites–dacites in southern Jiangxi Province, southeast China: Evidence for delamination of a flat-slab? *Lithos*, 358–359, 105403.

Appendix

Analytical techniques of whole rock geochemistry:

The major oxides were analysed in the X-Ray Fluorescence laboratory of the National Centre for Earth Science Studies (NCESS), India, using a Bruker S4 Pioneer sequential wavelength-dispersive X-ray spectrometer. Fused glass discs were used for major oxide analysis. In order to create the glass discs, a Claisse Fluxer was used to fuse 1 g of finely powdered material with 5 g of lithium tetra-metaborate flux at 1100 °C in a platinum crucible. During the analyses, the following standards were used: G2, GSP2, STM1, SARM1, SARM2, SY3, RGM, GA, GH, GS-N, AC-E, MDOG, ISHG, VS-N, JG-1, JG-2, JG-3, JR-3 and JSY-1. During analysis the major oxide detection limits was ~0.01% and the analytical accuracy was more than 1%.

The trace element analyses were carried out in the Department of Earth Sciences at Indian Institute of Technology, Kanpur. Trace elements were analysed using an Agilent Triple Quadrupole Inductively Coupled Plasma Mass Spectrometer (QQQ-ICP-MS). During the sample preparation, ~0.05 g of sampler powder was initially digested using a 4 mL mixture containing concentrated HCL (1 part), concentrated HF (1 part) and concentrated HNO₃ (2 parts) in pre-cleaned Teflon beakers (Savillex) at 130 ± 5 °C for 48 hours. After the initial digestion procedure is completed, the acid is slowly evaporated at 80 ± 5 °C. Again, during secondary digestion, the samples were redissolved in 3 mL of Aqua Regia acid (2 parts concentrated HNO₃ + 1 part concentrated HCl) for 24 hours. The samples were dried after the Aqua Regia digestion process and redissolved in 2% HNO₃. Only when digestion was not complete were the acid digestion steps repeated. Trace element grade pure acid and 18.2 MΩ cm water from a Millipore water purification system were utilised for all analytical procedures. In the Department of Earth Sciences, sub-boiling distillation utilising the PicoTrace Cupola Still system was used to create pure acids. Trace element concentrations were measured at 500 ppm total dissolved solid solutions, but for the REEs, it was determined at ~2000 ppm total dissolved solid solutions. Following the same procedures, reference materials SBC-1 (shale standard,

USGS) and AGV-2 (Andesite, USGS) were digested along with three blanks. While SBC-1 and AGV-2 were analysed as unknown to assess the data quality, blanks were analysed to quantify the total procedural blank. To create a calibration curve, a Sigma-Aldrich multi-element standard solution at a concentration of 10 g/g was diluted to 7 suitable concentrations (0.1 ng/g, 1 ng/g, 10 ng/g, 20 ng/g, 50 ng/g, 75 ng/g, and 100 ng/g). The calibration curve was used to determine trace element concentrations. All the samples and standards were spiked with 5 ppb In solution, which was employed as an internal standard because rock-matrix matching reference materials were unavailable. Using In as an internal standard, the intensities were corrected for the matrix effect. To optimise the separation of measured isotopes from interfering polyatomic interferences during analysis, ICP-MS was run both with no gas and with reaction gases, namely oxygen and helium. To check the reproductibility, duplicate samples were also run, and the numbers were well produced. The matrix effect was corrected by normalisation, and the final concentrations were blank-corrected using the procedural blank concentrations. All the elements were in agreement with their certified values.

Supplementary Material

Supplementary Table 1: Composition of the melt system (ms) and solid (extracted bulk) system (ss) as predicted by the phase equilibria modelling during fractional crystallisation of the ferroan bulk at 1% dissolved H₂O and FMQ buffer along cooling path

Phase	Pressure (kbar)	Temperature (°C)	Na ₂ O	MgO	Al ₂ O ₃	SiO ₂	K ₂ O	CaO	TiO ₂	FeO	H ₂ O
Bulk_ss	5	895	3.85	0.90	14.90	67.35	1.88	4.00	1.22	5.77	0.00
Bulk_ss	5	740	2.60	0.56	12.25	71.21	6.14	0.66	0.00	6.04	0.54
Bulk_ss	5	665	4.20	0.10	13.09	74.78	5.30	0.23	0.00	2.11	0.19
Bulk_ss	4	870	3.90	0.95	15.00	66.60	1.83	4.04	1.21	6.34	0.00
Bulk_ss	4	715	2.53	0.45	12.07	72.67	6.32	0.54	0.00	4.95	0.49
Bulk_ss	4	670	4.04	0.06	12.81	76.31	5.36	0.18	0.00	1.13	0.10
Bulk_ss	3	840	3.95	0.99	15.05	66.00	1.78	4.04	1.20	6.87	0.00
Bulk_ss	3	690	2.77	0.26	12.13	74.98	6.30	0.38	0.00	2.91	0.29
Bulk_ss	3	685	3.66	0.03	12.51	77.28	5.72	0.16	0.00	0.59	0.06

Supplementary Table 2: Composition of the melt system (ms) and solid (extracted bulk) system (ss) as predicted by the phase equilibria modelling during fractional crystallisation of the ferroan bulk at 1.5% dissolved H₂O and FMQ buffer along cooling path

Phase	Pressure (kbar)	Temperature (°C)	Na ₂ O	MgO	Al ₂ O ₃	SiO ₂	K ₂ O	CaO	TiO ₂	FeO	H ₂ O
Bulk_ss	5	835	3.77	0.97	14.73	66.79	1.88	3.98	1.20	6.56	0.00
Bulk_ss	5	675	2.83	0.37	12.60	72.76	6.27	0.58	0.00	4.18	0.41
Bulk_ss	5	665	4.58	0.02	13.35	76.40	5.08	0.16	0.00	0.37	0.04
Bulk_ss	4	810	3.84	1.00	14.85	66.17	1.81	4.02	1.20	7.00	0.00
Bulk_ss	4	680	2.89	0.25	12.48	74.62	6.32	0.44	0.00	2.73	0.27
Bulk_ss	4	675	3.75	0.03	12.79	77.02	5.82	0.19	0.00	0.37	0.03
Bulk_ss	4	670	4.98	0.03	13.32	76.50	4.58	0.05	0.00	0.49	0.05
Bulk_ss	4	665	4.91	0.01	13.95	76.29	4.43	0.04	0.00	0.36	0.00
Bulk_ss	3	780	3.90	1.02	14.98	65.64	1.82	4.02	1.19	7.31	0.00
Bulk_ss	3	690	2.80	0.19	12.20	76.05	6.38	0.35	0.00	1.85	0.19
Bulk_ss	3	685	3.98	0.03	12.64	77.25	5.40	0.12	0.00	0.54	0.05
Bulk_ss	3	680	4.62	0.02	12.97	77.02	4.64	0.05	0.00	0.65	0.02
Bulk_ss	3	675	4.64	0.02	13.88	76.57	4.52	0.03	0.00	0.33	0.02

Supplementary Table 3: Composition of the melt system (ms) and solid (extracted bulk) system (ss) as predicted by the phase equilibria modelling during fractional crystallisation of the ferroan bulk at 2% dissolved H₂O and FMQ buffer along cooling path

Phase	Pressure (kbar)	Temperature (°C)	Na ₂ O	MgO	Al ₂ O ₃	SiO ₂	K ₂ O	CaO	TiO ₂	FeO	H ₂ O
Bulk_ss	5	795	3.65	0.96	14.52	66.56	2.10	3.81	1.13	6.71	0.44
Bulk_ss	5	670	3.39	0.21	12.89	74.37	5.99	0.41	0.00	2.50	0.24
Bulk_ss	5	665	4.88	0.02	13.41	76.39	4.79	0.09	0.00	0.38	0.04
Bulk_ss	5	660	5.31	0.01	13.99	75.83	4.42	0.05	0.00	0.35	0.04
Bulk_ss	4	785	3.71	1.01	14.71	65.81	1.92	3.98	1.18	7.10	0.46
Bulk_ss	4	680	2.88	0.23	12.48	74.69	6.36	0.43	0.00	2.67	0.26
Bulk_ss	4	670	4.35	0.03	13.06	76.76	5.21	0.12	0.00	0.43	0.04
Bulk_ss	3	760	3.79	1.03	14.87	65.16	1.94	3.98	1.17	7.44	0.50
Bulk_ss	3	690	2.82	0.14	12.16	76.61	6.31	0.35	0.00	1.46	0.15
Bulk_ss	3	685	3.99	0.03	12.65	77.22	5.38	0.12	0.00	0.56	0.05
Bulk_ss	3	680	4.61	0.02	13.02	76.99	4.64	0.06	0.00	0.64	0.01
Bulk_ss	3	675	4.67	0.02	13.74	76.56	4.51	0.04	0.00	0.44	0.01

Supplementary Table 4: Composition of the melt system (ms) and solid (extracted bulk) system (ss) as predicted by the phase equilibria modelling during fractional crystallisation of the ferroan bulk at 2.5% dissolved H₂O and FMQ buffer along cooling path

Phase	Pressure (kbar)	Temperature (°C)	Na ₂ O	MgO	Al ₂ O ₃	SiO ₂	K ₂ O	CaO	TiO ₂	FeO	H ₂ O
Bulk_ss	5	770	3.61	1.04	14.51	65.71	1.92	3.96	1.18	7.43	0.51
Bulk_ss	5	670	3.45	0.12	13.05	75.39	6.05	0.40	0.00	1.39	0.14
Bulk_ss	5	665	4.84	0.02	13.41	76.42	4.82	0.10	0.00	0.36	0.04
Bulk_ss	5	660	5.31	0.01	14.09	75.75	4.41	0.05	0.00	0.32	0.07
Bulk_ss	4	745	3.70	1.05	14.68	65.21	1.93	3.96	1.18	7.65	0.53
Bulk_ss	4	680	2.95	0.09	12.53	76.61	6.36	0.41	0.00	0.95	0.10
Bulk_ss	4	675	3.89	0.02	12.92	76.89	5.68	0.19	0.00	0.37	0.04
Bulk_ss	4	670	4.91	0.03	13.27	76.54	4.63	0.06	0.00	0.51	0.05
Bulk_ss	4	665	4.90	0.01	14.15	76.22	4.43	0.04	0.00	0.25	0.00
Bulk_ss	3	715	3.78	1.06	14.87	64.72	1.94	3.98	1.17	7.81	0.55
Bulk_ss	3	690	3.15	0.04	12.27	77.82	6.09	0.26	0.00	0.35	0.04
Bulk_ss	3	685	3.79	0.07	12.58	76.90	5.51	0.16	0.00	0.89	0.09
Bulk_ss	3	680	4.40	0.03	12.97	77.02	4.94	0.07	0.00	0.55	0.02

Supplementary Table 5. Orthopyroxene composition in the extracted solid system as predicted by the phase equilibria modelling during isobaric cooling of the ferroan bulk at 1-2% dissolved H₂O (FMQ)

Bulk H ₂ O	1% H ₂ O	1% H ₂ O	1% H ₂ O	1.5% H ₂ O	1.5% H ₂ O	1.5% H ₂ O	2% H ₂ O	2% H ₂ O
Phase	Opx	Opx	Opx	Opx	Opx	Opx	Opx	Opx
Pressure (kbar)	5	4	3	5	4	3	5	4
Temperature (°C)	895	870	840	835	810	780	795	785
SiO ₂	48.00	48.08	48.14	47.85	47.84	47.96	47.78	47.95
TiO ₂	0.00	0.00	0.00	0.00	0.00	0.00	0.00	0.00
Al ₂ O ₃	1.57	1.30	1.04	1.47	1.30	1.04	1.47	1.21
FeO	39.82	40.29	40.86	40.83	41.36	41.68	41.19	41.31
MgO	9.58	9.30	8.96	8.92	8.68	8.52	8.74	8.71
CaO	0.96	0.96	0.95	0.86	0.76	0.76	0.76	0.76
Na ₂ O	0.00	0.00	0.00	0.00	0.00	0.00	0.00	0.00
K ₂ O	0.00	0.00	0.00	0.00	0.00	0.00	0.00	0.00
Total	99.92	99.93	99.95	99.93	99.93	99.95	99.93	99.95
Si	1.95	1.96	1.97	1.95	1.96	1.97	1.95	1.96
Ti	0.00	0.00	0.00	0.00	0.00	0.00	0.00	0.00
Al	0.07	0.06	0.05	0.07	0.06	0.05	0.07	0.06
Fe ^{3+*}	0.02	0.02	0.02	0.02	0.02	0.02	0.02	0.02
Fe ²⁺	1.33	1.35	1.38	1.37	1.40	1.41	1.39	1.40
Mg	0.58	0.56	0.55	0.54	0.53	0.52	0.53	0.53
Ca	0.04	0.04	0.04	0.04	0.03	0.03	0.03	0.03
Na	0.00	0.00	0.00	0.00	0.00	0.00	0.00	0.00
K	0.00	0.00	0.00	0.00	0.00	0.00	0.00	0.00
X _{Mg}	0.30	0.29	0.28	0.28	0.28	0.27	0.28	0.28
X _{Al}	0.03	0.02	0.02	0.03	0.02	0.02	0.03	0.02

*Fe³⁺ is recalculated after the scheme of Droop (1987)

Publication

Published paper

Chatterjee, S., Karmakar, S., Mukherjee, S., Sanyal, S. & Sengupta, P. (2023). Origin of clinopyroxene-ilmenite symplectites in mafic granulites from eastern parts of the Chotanagpur granite gneissic complex, East Indian shield. *American Mineralogist*, 108(12), 2308-2322. <https://doi.org/10.2138/am-2022-8715>

Das, E., Karmakar, S., **Chatterjee, S.,** Karmakar, S., and Sengupta, P. (2020) First comprehensive characterization of osumilite from India (Eastern Ghats Province): Physicochemical characteristics, stability of the mineral and its breakdown products. *Lithos* (352-355)
<https://doi.org/10.1016/j.lithos.2019.105315>

Abstracts in International Conference

Chatterjee, S., Mukherjee, S., Karmakar, S., Sanyal, S., and Sengupta, S. (2019) Metamorphic P-T evolution of the porphyritic granitoids from eastern part of the Chotanagpur Granite Gneiss Complex, East Indian Shield. Humboldt Kolleg 2020 on “Food, Livelihood, Opportunities and Wood ‘FLOW’”

Chatterjee, S., Mukherjee, S., Karmakar, S., Sanyal, S., and Sengupta, S. (2020) Origin of ferroan-granitoids from a part of the Chotanagpur Granite Gneissic Complex (CGGC), East Indian Shield. 36th International Geological Congress, Abstract no. 4106-3484